ADVANCED NANOMATERIALS FOR PHOTOTHERMAL AGENTS

EDITED BY: Bo Li, Guanjie He and Ming Ma

PUBLISHED IN: Frontiers in Bioengineering and Biotechnology

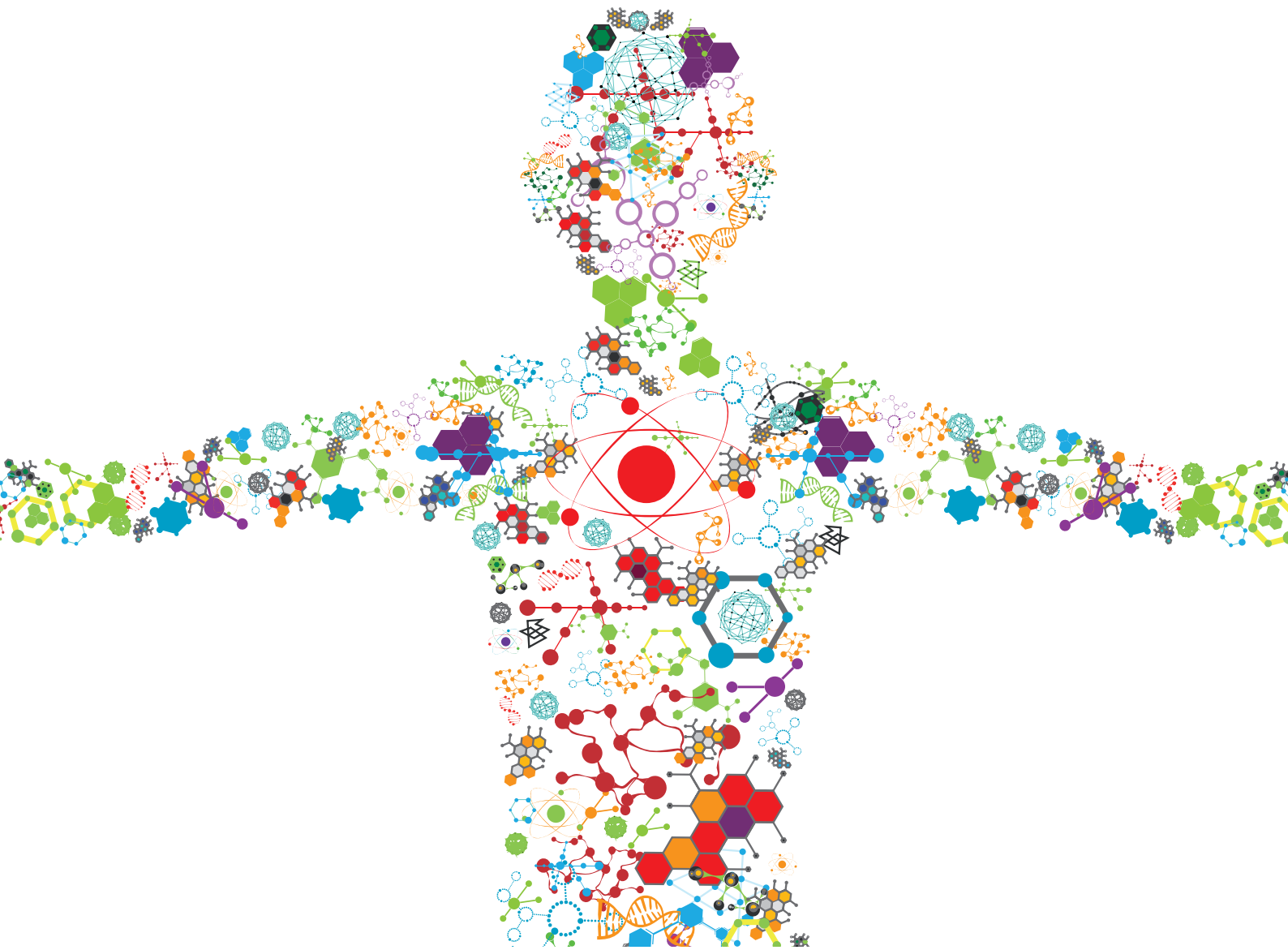

frontiers Research Topics

ISSN 1664-8714
ISBN 978-2-88971-384-4
DOI 10.3389/978-2-88971-384-4

About Frontiers

Frontiers is more than just an open-access publisher of scholarly articles: it is a pioneering approach to the world of academia, radically improving the way scholarly research is managed. The grand vision of Frontiers is a world where all people have an equal opportunity to seek, share and generate knowledge. Frontiers provides immediate and permanent online open access to all its publications, but this alone is not enough to realize our grand goals.

Frontiers Journal Series

The Frontiers Journal Series is a multi-tier and interdisciplinary set of open-access, online journals, promising a paradigm shift from the current review, selection and dissemination processes in academic publishing. All Frontiers journals are driven by researchers for researchers; therefore, they constitute a service to the scholarly community. At the same time, the Frontiers Journal Series operates on a revolutionary invention, the tiered publishing system, initially addressing specific communities of scholars, and gradually climbing up to broader public understanding, thus serving the interests of the lay society, too.

Dedication to Quality

Each Frontiers article is a landmark of the highest quality, thanks to genuinely collaborative interactions between authors and review editors, who include some of the world's best academicians. Research must be certified by peers before entering a stream of knowledge that may eventually reach the public - and shape society; therefore, Frontiers only applies the most rigorous and unbiased reviews.
Frontiers revolutionizes research publishing by freely delivering the most outstanding research, evaluated with no bias from both the academic and social point of view. By applying the most advanced information technologies, Frontiers is catapulting scholarly publishing into a new generation.

What are Frontiers Research Topics?

Frontiers Research Topics are very popular trademarks of the Frontiers Journals Series: they are collections of at least ten articles, all centered on a particular subject. With their unique mix of varied contributions from Original Research to Review Articles, Frontiers Research Topics unify the most influential researchers, the latest key findings and historical advances in a hot research area! Find out more on how to host your own Frontiers Research Topic or contribute to one as an author by contacting the Frontiers Editorial Office: frontiersin.org/about/contact

ADVANCED NANOMATERIALS FOR PHOTOTHERMAL AGENTS

Topic Editors:
Bo Li, Shanghai Jiao Tong University, China
Guanjie He, University of Lincoln, United Kingdom
Ming Ma, Chinese Academy of Sciences (CAS), China

Citation: Li, B., He, G., Ma, M., eds. (2021). Advanced Nanomaterials for Photothermal Agents. Lausanne: Frontiers Media SA. doi: 10.3389/978-2-88971-384-4

Table of Contents

frontiers in Materials

ORIGINAL RESEARCH
published: 26 November 2019
doi: 10.3389/fmats.2019.00286

Cobalt/Manganese Oxides as Theragnosis Nanoplatforms With Magnetic Resonance/Near-Infrared Imaging for Efficient Photothermal Therapy of Tumors

Jichun Liu[1†], Genfa Wu[1†], Zhiyong Tang[1], Qi Sun[1], Jianxin Wu[2] and Renfa Lv[1*]*

[1] Department of Orthopedics, 908th Hospital of the PLA, Yingtan, China, [2] Department of Orthopedics, Shanghai Changhai Hospital, Shanghai, China

OPEN ACCESS

Edited by:
Bo Li,
Shanghai Jiao Tong University, China

Reviewed by:
Kaibing Xu,
Donghua University, China
Jingyi Zhu,
Nanjing Tech University, China

***Correspondence:**
Jianxin Wu
wujx1978@163.com
Renfa Lv
ytlrf@163.com

[†]These authors have contributed equally to this work

Specialty section:
This article was submitted to Biomaterials, a section of the journal Frontiers in Materials

Received: 27 September 2019
Accepted: 24 October 2019
Published: 26 November 2019

Citation:
Liu J, Wu G, Tang Z, Sun Q, Wu J and Lv R (2019) Cobalt/Manganese Oxides as Theragnosis Nanoplatforms With Magnetic Resonance/Near-Infrared Imaging for Efficient Photothermal Therapy of Tumors. Front. Mater. 6:286. doi: 10.3389/fmats.2019.00286

The combination of near-infrared (NIR) response and imaging response is a hot research area in which the functions of nanomaterials are maximized. However, the types of such materials reported so far present problems such as requiring complex synthesis. In this study, hydrophilic, porous, and hollow cobalt/manganese oxide (CMO) nanocrystals (NCs) were successfully prepared via a facile and green hydrothermal route. The CMO NCs show strong near-infrared (NIR) absorption, which results from their defect structure due to the coexistence of Co^{2+} and Co^{3+} in the as-prepared CMO NCs. Thus, the CMO NCs exhibit excellent photothermal performance, showing photothermal efficiency of up to 43.2%. In addition, the CMO NCs possess good magnetic resonance (MR) imaging performance, with longitudinal relaxivity (r_1) of up to 3.48 mM^{-1} s^{-1}. Finally, for the first time, we prove that the CMO nanocrystals are a promising photothermal agent. Our work provides insights into the application of Mn-based control agents and photothermal agents for photothermal theragnosis therapy.

Keywords: cobalt/manganese oxides, photothermal agents, near-infrared absorption, photothermal theragnosis therapy, magnetic resonance imaging

INTRODUCTION

Photothermal therapy (PTT), a promising approach to cancer treatment (Li et al., 2010, 2013; Hessel et al., 2011; Tian et al., 2011), has attracted widespread attention recently because of its superior advantages over traditional treatments such as chemotherapy, surgery, and radiation therapy. The key to the success of photothermal therapy is the development of photothermal agents. Currently, various kinds of photothermal agents are being been explored, including metal nanoparticles (Lee et al., 2019; Zhang D. et al., 2019), carbon-based nanomaterials (Wang et al., 2016; Sobhani et al., 2017), semiconductors (Mou et al., 2015; Zhang X. et al., 2019), and organic compounds (Zha et al., 2013). However, PTT alone is not enough, because contemporary medical diagnosis and treatment require accurate and detailed information on the cancers (i.e., their shape, location, and size). Thus, contrast agents must be introduced. Therefore, nanomaterials that couple near-infrared absorption and imaging properties are much more fit for treating cancers (Hahn et al., 2010; Lee et al., 2012). However, multifunctional nano-biomaterials are mainly composite materials

[for example, MnSe@Bi_2Se_3 (Song et al., 2015) and Fe_3O_4 @$Cu_{2-x}S$ nanoparticles (Tian et al., 2013)], which usually have a rather complicated and cumbersome preparation procedure, resulting in low productivity and heterogeneity. Therefore, a single material that combines NIR and imaging properties [such as Cu_3BiS_3 (Liu et al., 2016), Cu-Fe-S (Zhao et al., 2016), and WO_{3-x} (Chen et al., 2013)] is preferable for photothermal theragnosis therapy, and great efforts have been made in this respect.

Manganese-based oxide nanomaterials (Chen et al., 2014; Song et al., 2015) have been proved to be a promising substitute for gadolinium nanomaterials (Jao et al., 2010; Chen et al., 2014) and have been clinically used as imaging contrast agents for MR imaging. Moreover, manganese is an essential element of the human body. However, manganese-based nanomaterials that have been previously reported (such as MnSe and MnO_2) have very poor absorption properties in the NIR range and thus cannot be used as photothermal agents (Song et al., 2016). One possible solution is to develop a manganese-based nanomaterial with a porous structure in which the photothermal efficiency can be improved (Dong et al., 2013).

In this work, we report the application of hydrophilic porous and hollow cobalt/manganese oxide (CMO) nanocrystals (NCs) as photothermal and T_1-MR imaging control agents. This work, as far as we know, is the first report in which CMO NCs are used as photothermal agents, a functionality that results from their unique porous and hollow structure. These NCs also possess impressive T_1-MR imaging performance, with the longitudinal relaxivity (r_1) up to 3.48 mM^{-1} s^{-1}. Due to the coexistence of Co^{2+} and Co^{3+} in the as-prepared CMO NCs, the resulting NCs exhibit very intense NIR absorption due to electron transitions between Co^{2+} and Co^{3+}. Therefore, the hydrophilic CMO NCs can be used as an excellent NIR-induced photothermal agent. Furthermore, the hydrophilic CMO NCs show excellent biocompatibility.

RESULTS AND DISCUSSION

Synthesis and Characterization

Hydrophilic porous and hollow CMO NCs were synthesized via a simple hydrothermal method by the reaction of $Co(NO_3)_2$ with $KMnO_4$ in a DMF solution at 120°C for 24 h. During preparation, polyvinylpyrrolidone (PVP) was added into the reaction as a surface ligand to improve their biocompatibility, and this coating was determined by FTIR (**Figure S1**). Thus, the CMO NCs are hydrophilic and can be used as photothermal agents without any further modification. Scanning electron microscope (SEM, **Figure 1A**) and transmission electron microscopy (TEM, **Figure 1B**) images demonstrate that the as-prepared products were porous and hollow. The size of the NCs was found to be 80 nm based on the TEM and SEM images (**Figure S2**). Furthermore, the size of the NCs in buffer solution (such as PBS) as determined by dynamic light scattering (DLS) shows almost no change over time, confirming that they have excellent dispersion (**Figure S3**). X-ray photoelectron spectroscopy (XPS, **Figure S4**) revealed the composition and elemental state of the as-prepared products. It showed that the products mainly contain the elements O, Mn, and Co, with no other impurities. We also analyzed the valency state of Mn and Co in the CMO NCs. **Figure 1C** shows the Mn 2p spectrum for the CMO NCs. The binding energy of Mn $2p_{1/2}$ (653.7 eV) and Mn $2p_{3/2}$ (641.6 eV) can be assigned to Mn (IV) coordinated to Mn in CMO (Wang et al., 2003). Also, the binding energy of Co (**Figure 1D**) in the peaks at 779.9 and 795.0 eV, as well as two shakeup satellites demonstrated that there was a mixed cobalt oxidation state, i.e., Co^{2+} and Co^{3+} (Tang et al., 2016), indicating a defect structure in the CMO NCs. The CMO NCs obtained were further characterized by X-ray powder diffraction (XRD) (**Figure S5**). It was seen that the crystal phase of the nanocrystals consisted of Co_3O_4 and MnO_2, confirming the formation of CMO. According to the above results, it can be concluded that porous and hollow CMO NCs were successfully formed.

Photothermal Performance

Photothermal agents with intense NIR absorption are necessary to realize photothermal therapy. The general wavelengths of NIR laser sources that emit photothermal agents include 808, 915, 980, and 1064 nm. As shown in **Figure 2A**, the as-prepared MCO NCs show strong absorption from 700 to 1,000 nm due to the defect structure resulting from the coexistence of Co^{2+} and Co^{3+} in as-prepared CMO NCs. By measuring the CMO NC concentration via inductively-coupled plasma atomic-emission spectroscopy (ICP-AES), the excitation coefficient of CMO NCs was determined to be 12.8 $Lg^{-1}cm^{-1}$. This value is higher than those of CuS and Au nanostructures (Tian et al., 2011; Zhang D. et al., 2019). Thus, the CMO NCs may possess good photothermal performance. The general wavelengths of NIR laser sources that emit photothermal agents include 808, 915, 980, and 1,064 nm. The NIR absorption intensity at 808 nm of the as-prepared nanocrystals is higher than those at other general wavelengths of NIR laser sources, which leads to higher photothermal conversion efficiency. Thus, 808 nm lasers were chosen to evaluate the photothermal performance of CMO NCs. Various concentrations (i.e., 0, 25, 50, and 100 ppm) of CMO NCs were exposed to an 808 nm laser (0.3 W cm^{-2}) to evaluate their photothermal effect. As expected, the CMO NCs showed good photothermal conversion performance, with a concentration-dependent photothermal effect (**Figure 2B**).

The NIR-driven photothermal conversion efficiency of the CMO NCs (50 ppm) was also measured by a modified method similar to that reported by Roper et al. (2007). An aqueous dispersion of CMO NCs was continuously exposed to an 808 nm laser with a power of 0.189 W for 300 s. When the temperature of the system reached a steady state, the 808 nm laser was shut off. The temperature change during cooling was monitored to confirm the rate of heat transfer of the system (**Figure 2C**). Based on Roper's work, the photothermal conversion efficiency (Roper et al., 2007), η_T, was calculated by the following Equation (1):

$$\eta_T = \frac{\mathrm{hA}(\mathrm{T_{max}} - \mathrm{T}_{amb}) - Q_0}{I(1 - 10^{-A_\lambda})} \quad (1)$$

where A is the surface area of the container, h is the heat transfer coefficient, T_{amb} is the temperature of the ambient surroundings,

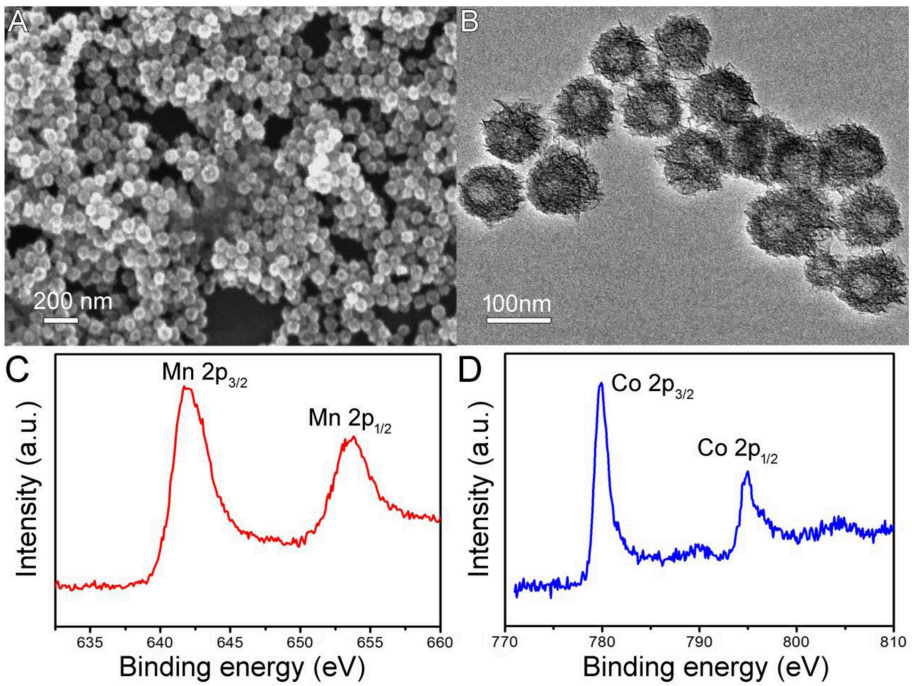

FIGURE 1 | (A) SEM image and **(B)** TEM image of the as-prepared CMO nanocrystals. XPS spectra of **(C)** Mn 2p and **(D)** Co 2p.

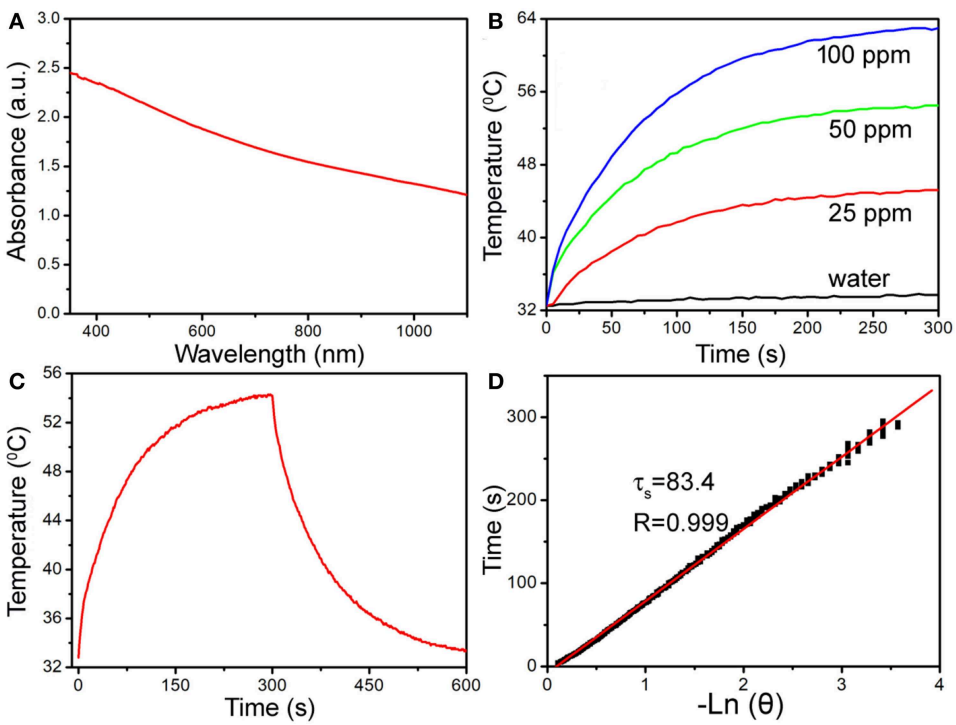

FIGURE 2 | (A) UV-vis-NIR absorbance spectrum of CMO NCs dispersed in water. **(B)** Temperature change of CMO NCs in water at various Mn^{2+} concentrations (i.e., 0, 25, 50, and 100 ppm) as a function of irradiation time. **(C)** Photothermal effect of CMO NCs (50 ppm). **(D)** Time constant of CMO NCs from the system. The laser is an 808 nm laser with a power of 189 mW.

T_{max} is the maximum system temperature, and (T_{max} – T_{amb}) was 21.4°C according to **Figure 2C**. Q_0 is the rate of heat input (mW), A_λ is the absorbance intensity (1.53509) at 808 nm, and I is the laser power used (mW, 189 mW). The value of hA can be obtained from **Figure 2D** and can be derived using the following Equation (2):

$$\tau_s = \frac{m_D C_D}{hA} \quad (2)$$

where m_D and C_D are the mass of water (0.1 g) and heat capacity (4.2 J g^{-1}) of water, respectively, and τ_s is the time constant. Q_0 was tested to be 27.7 mW. Based on the data recorded, the NIR-driven photothermal conversion efficiency (η_T) of the CMO NCs was calculated to be 43.2%, which is high enough for photothermal therapy of cancers.

In vitro Photothermal Therapy

The excellent photothermal performance of MCO NCs indicates that these NCs have great potential to be used as phototherapy agents. Before the realization of photothermal therapy with MCO NCs *in vivo*, their cytotoxicity was measured through a CCK-8 assay with Saos-2 cells. From **Figure S6A**, we can see that these MCO NCs appeared to have very low toxicity. The *in vitro* phototherapy therapy effect of MCO NCs to Saos-2 cells was then studied. After the different treatments indicated in **Figure S6B**, a CCK-8 evaluation was first used to judge the cell mortality rate. The resulted of CCK-8 assay demonstrated that the laser or MCO NCs alone could not kill the cells but that the cell mortality rate for the MCO NCs at 50 ppm combined with 808-nm-laser irradiation was ∼95%, indicating a significantly photothermal effect *in vitro*. Moreover, to visualize the *in vitro* phototherapeutic effect of CMO NCs, Saos-2 cells after the indicated treatments were co-stained with propidium iodide (PI) and calcein-AM. The result of live/dead cell staining analysis (**Figure 3**) matched well with those of CCK-8 evaluation, further confirming an efficient *in vitro* photothermal effect.

MR Imaging

In addition to serving as photothermal agents, CMO NCs can also serve as an imaging contrast agent. Phantom imaging and proton T_1 relaxation tests were carried out on CMO NCs at varied Mn concentrations. As shown in **Figure 4A**, the T_1-weighted MR imaging signal intensity was increased with an increase in the concentration of CMO nanocrystals. The longitudinal relaxivity (r_1) value of the CMO NCs was calculated to be 3.48 mM^{-1} s^{-1}, indicating that they are an efficient MRI contrast agent (**Figure 4B**).

We then evaluated the T_1-weighted MRI signal of CMO NCs in animal experiments. From **Figure 4C**, we can see that the signal in tumor sites increased over time after intravenous injection of a PBS solution of CMO NCs due to the enhanced permeability and retention (EPR) effect. Therefore, CMO NCs can serve as an efficient T_1-weighted MR imaging contrast agent.

In vivo Photothermal Therapy

We then evaluated photothermal therapy of cancers *in vivo*. First, the mice were divided into four groups, referred to as (a) CMO NC injection + 808-nm laser irradiation (Group 1, Treatment), (b) PBS + 808 nm laser irradiation (Group 2, Laser), (c) saline injection (Group 3, Saline), and (d) CMO NC injection (Group 4, NCs). An infrared thermal camera was applied to measure the temperature change at tumor sites. Due to the excellent photothermal effect of CMO NCs, infrared thermal images with obvious contrast were achieved (inset in **Figure 5A**). As we can see in **Figure 5A**, the temperatures of the tumor surface could increase dramatically from ∼31 to 62°C due to the excellent photothermal effect of CMO NCs.

After the indicated treatment, the tumor sizes and body weights in each group were recorded every 2 days. As shown in **Figure 5B**, the tumors of mice in the treatment group disappeared, and no reoccurrence was observed (**Figure 5B**, **Figure S7**). In marked contrast, the tumors gradually increased in the three control groups and did not differ between those groups. In addition, there was no obvious difference in body weight among the four groups of mice (**Figure 5C**), indicating that the given conditions did not produce obvious toxic effects.

Hematoxylin and eosin (H&E) staining analysis of tumor slices from each group was also conducted to evaluate the photothermal therapy effect. The morphology and size of tumor cells in the three control groups (Groups 2–4) showed little change, while the tumor cells in the experimental group (Group 1) showed obvious necrosis (**Figure 5D**). These results are matched well with the tumor growth data. Therefore, CMO NCs can be used as efficient photothermal theragnosis agents with the irradiation of an 808-nm laser.

Finally, the *in vivo* long-term toxicity of the as-prepared CMO NCs was evaluated by histological examination of major organs to observe the shape and the size of cells after intravenous injection of CMO NCs at a dosage of 15 mg/kg. The organs included the lung, heart, spleen, liver, and kidney. As shown in **Figure 6**, there is no tissue damage or adverse effect compared with those of the control groups. This suggests that these CMO NCs, under the given conditions, are not obviously toxic.

CONCLUSION

In conclusion, CMO NCs with a porous and hollow structure, as a new imaging-guided photothermal therapy agent, have been successfully prepared by a simple hydrothermal route. The as-prepared CMO NCs have good dispersion and show intense NIR absorption owning to their defect structure, and thus exhibit excellent photothermal conversion performance. They are also effective for MR imaging *in vivo*. Furthermore, the *in vitro* and *in vivo* toxicity results indicate their excellent biocompatibility. With the exposure to NIR light and an external magnetic field, the CMO NCs can be used as theragnosis nanoplatforms with MR/NIR imaging for efficient photothermal theragnosis therapy.

EXPERIMENTAL SECTIONS

Synthesis of Hydrophilic CMO NCs

First, 1 mmol $Co(NO_3)_2$ and 0.25 mmol $KMnO_4$ were consecutively dissolved in 40 mL N, N-dimethylformamide (DMF). Next, 500 mg of poly (vinyl pyrrolidone) (PVP) was added. The reaction was then kept at 120°C for 24 h in a

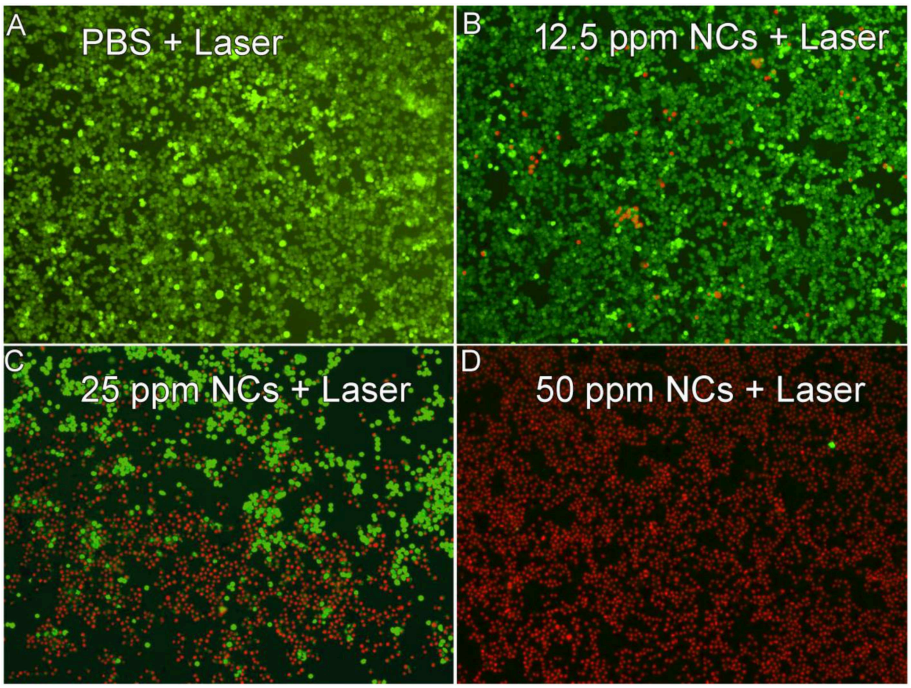

FIGURE 3 | Live/dead cell staining analysis after incubation with CMO NCs at indicated concentrations: **(A)** PBS, **(B)** 12.5 ppm, **(C)** 25 ppm, **(D)** 50 ppm, and then under the exposure of an 808 nm (0.3 W/cm^{-2}) for 5 min. Magnification: 100 times.

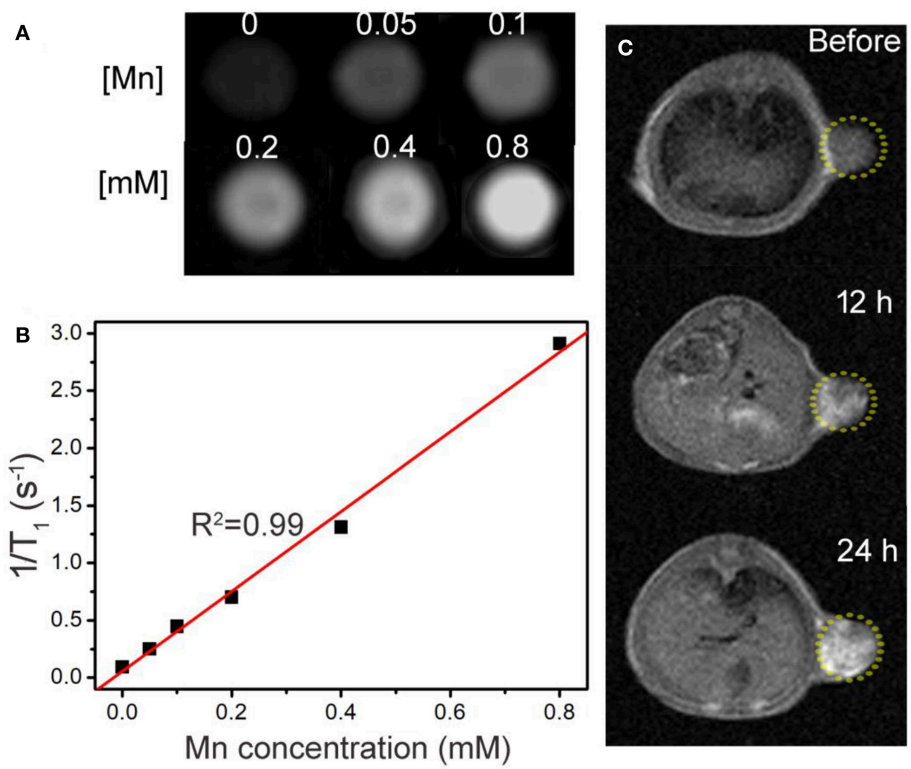

FIGURE 4 | (A) Phantom images of the CMO NCs. **(B)** Proton T_1 relaxation measurements at varied Mn concentrations **(C)** T_1-weighted MR imaging *in vivo* of a tumor-bearing mouse before and after intravenous injection of a solution of CMO NCs. The position of the tumor is marked by yellow dotted circles.

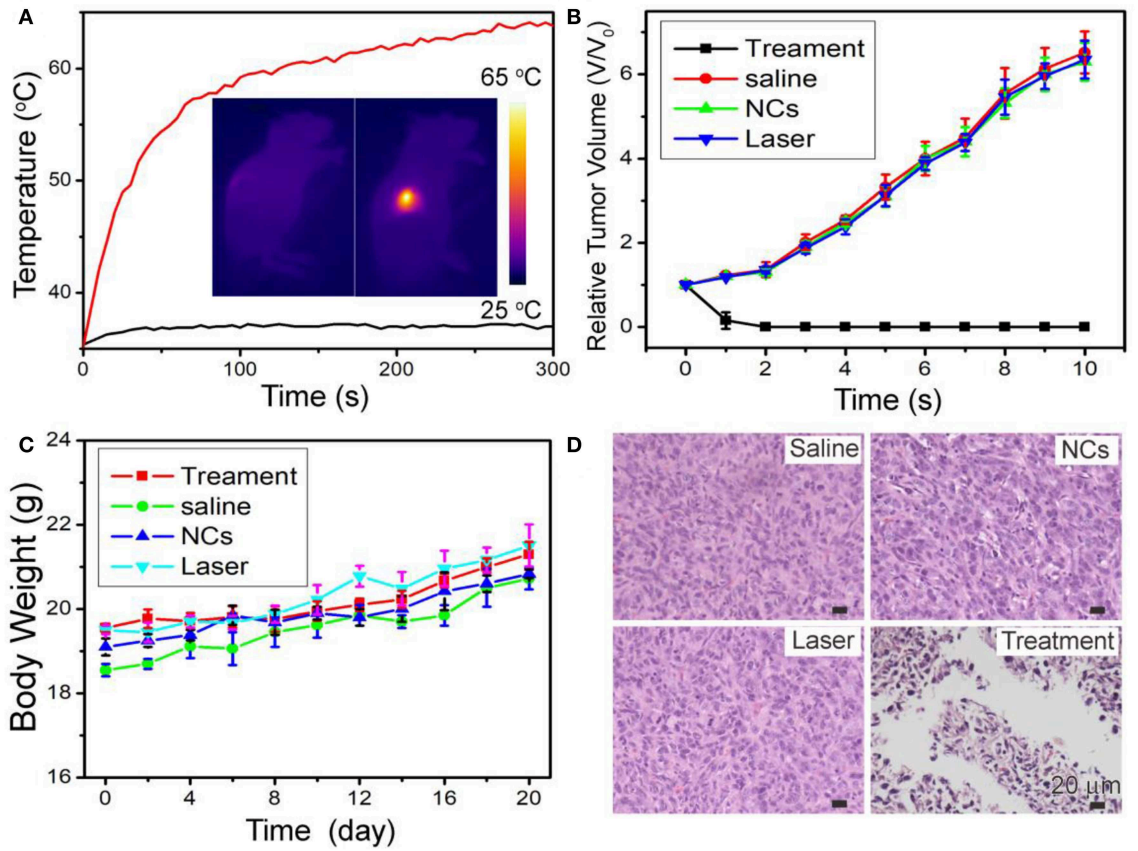

FIGURE 5 | (A) Temperature curves of tumors as a function of irradiation time. Insert: Full-body infrared thermal images of two Saos-2 tumor-bearing mice injected with saline (left) or MCO NCs (right) by intravenous injection, respectively, and irradiated with an 808-nm laser (0.7 W cm^{-2}) for 5 min. **(B)** Growth curves of tumors in the four groups after the indicated treatments. **(C)** Body-weight curves as a function of time in the four groups. **(D)** Representative H&E-stained histological images of the tumor sections after the indicated treatments.

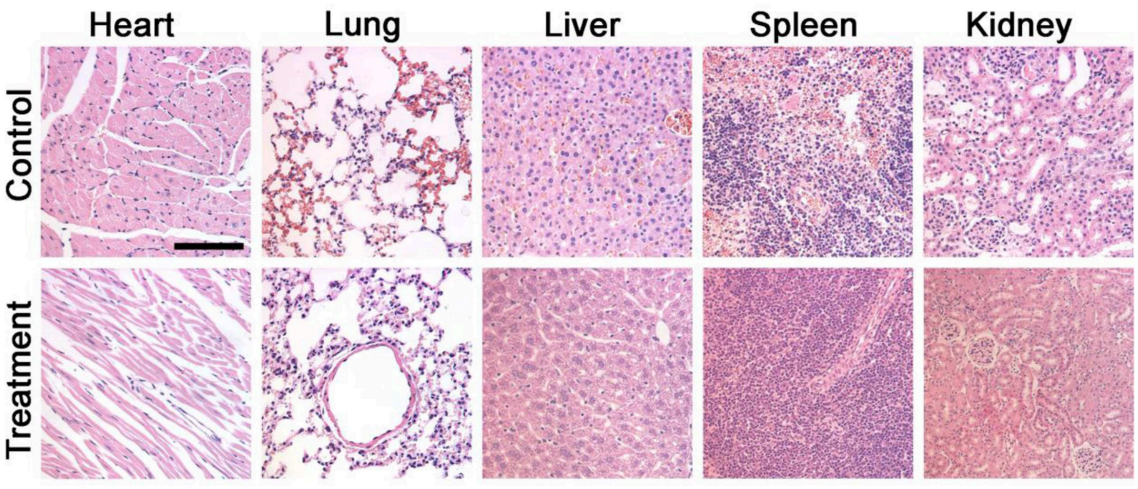

FIGURE 6 | Hematoxylin- and Eosin-stained tissue sections from the two groups of mice to evaluate the histological changes in heart, lung, liver, spleen, and kidney of the mice one month after a single intravenous injection of CMO NC solution. Scale bar: 100 μm.

stainless steel autoclave. The products were collected through centrifugation and were finally washed with ethanol and deionized water three times.

Characterization

The morphology and the size of the NCs was determined by TEM (JEM-2100F, JEOL, Japan). UV-Vis-NIR absorbance spectra were obtained with a UV-Visible-NIR spectrophotometer (UV-1902PC, Phenix) at room temperature. The crystal phase of CMO NCs was measured by XRD (Rigaku D/Max-2550 V, Geigerflex). The oxidation state of the CMO NCs was measured through X-ray photoelectron spectra (XPS, ESCA-Lab 250Xi). The concentration of Mn ions released from CMO NCs was tested by ICP-AES (Leeman Laboratories Prodigy).

Measurement of the Photothermal Effect of CMO NCs

For the evaluation of the photothermal performance of CMO NCs, 100 μL of CMO NCs dispersed in deionized water at various concentrations was exposed to irradiation from an 808 nm laser. The temperature change was recorded by a thermal imaging camera.

In vitro Cellular Experiment of CMO NCs

Saos-2 cells were used as the model of cancer cells to assess the biocytotoxicity of the CMO NCs. Saos-2 cells were cultured in Dulbecco's modified Eagle's medium (DMEM) combined with 5% CO_2 at 37°C prior to use. For cytotoxicity evaluation *in vitro*, Saos-2 cells (1×10^4 cells per well) were seeded in 96-well plates. After cultivation for 24 h, the upper layer of the DMEM medium was removed through a straw and was washed several times by PBS. CMO NCs dispersed in DMEM at varied concentrations were then added into the wells. After 24 h, a CCK8 (Dojindo Laboratories, Kumamoto) assay was used to measure cell viability. For photothermal therapy of Saos-2 cells *in vitro*, the cell suspension was dispensed in 200 μL centrifuge tubes (1×10^5 cells every tube) and incubated with CMO NCs. These Saos-2 cells were then irradiated with an 808 nm laser (0.3 W cm^{-2}) for 5 min. After that, the Saos-2 cells were co-stained with propidium iodide (PI) and calcein-AM. The live/dead fluorescence images were taken with a fluorescence microscope (Leica DMi8). All of the experiments were carried out four times.

MR Imaging

The dispersions of CMO NCs with varied Mn concentrations (0–0.8 mM) were scanned at room temperature via an animal MR imaging scanner, using a 0.5 T MRI scanner at room temperature. All animal procedures were agreed on with the institutional animal use and care committee at Shanghai Changhai Hospital and were carried out ethically and humanely. For MR imaging *in vivo*, mice were scanned with the same MR scanner with the same parameters after intravenous injection with the CMO NC dispersion (100 μL, 15 mg/kg).

In vivo Photothermal Therapy

The nude mice were subcutaneously injected with Saos-2 cells (5×10^6 per mouse) into the right thigh to establish the tumor models. After the tumor volumes reached about ∼100 mm^3, Saos-2 tumor-bearing mice were then divided into four groups (six mice in each group). CMO NC solution (100 μL, 100 ppm) or PBS solution were intravenously injected in the tumor sites of the nude mice. The nude mice without or with the CMO NC injection were exposed to an 808 nm laser (0.7 W cm^{-2}) for 5 min. The temperature of the tumor surface was monitored with an infrared thermal camera. The tumor size and body weight were measured every two days after treatment. Relative tumor volumes were calculated as V/V_0, where V_0 was the initial tumor volume before the therapy.

Histological Examination

For histological examination of the tumors, one mouse in each group was killed under anesthesia after the indicated treatment. The tumors were then harvested, sectioned into 4 μm slices using a conventional microtome, and finally stained with H&E. The slices were examined by microscope.

DATA AVAILABILITY STATEMENT

All datasets generated for this study are included in the article/**Supplementary Material**.

ETHICS STATEMENT

The animal study was reviewed and approved by the ethics committee of Shanghai Changhai hospital.

AUTHOR CONTRIBUTIONS

JW and RL designed the project. JL, GW, ZT, and QS carried out the experiment and performed the experimental data analysis. JL and GW wrote the paper. All of the authors contributed to discussion of the results.

SUPPLEMENTARY MATERIAL

The Supplementary Material for this article can be found online at: https://www.frontiersin.org/articles/10.3389/fmats.2019.00286/full#supplementary-material

REFERENCES

Chen, Y., Ye, D. L., Wu, M. Y., Chen, H. R., Zhang, L. L., Shi, J. L., et al. (2014). Break-up of two-dimensional MnO_2 nanosheets promotes ultrasensitive pH-triggered theranostics of cancer. *Adv. Mater.* 26, 7019–7026. doi: 10.1002/adma.201402572

Chen, Z., Wang, Q., Wang, H., Zhang, L., Song, G., Song, L., et al. (2013). Ultrathin PEGylated W18O49 nanowires as a new 980 nm-laser-driven photothermal agent for efficient ablation of cancer cells *in vivo*. *Adv. Mater.* 25, 2095–2100. doi: 10.1002/adma.201204616

Dong, K., Liu, Z., Li, Z., Ren, J., and Qu, X. (2013). Hydrophobic anticancer drug delivery by a 980 nm laser-driven photothermal vehicle for efficient

synergistic therapy of cancer cells *in vivo*. *Adv. Mater.* 25, 4452–4458. doi: 10.1002/adma.201301232

Hahn, M. A., Singh, A. K., Sharma, P., Brown, S. C., and Moudgil, B. M. (2010). Nanoparticles as contrast agents for *in-vivo* bioimaging: current status and future perspectives. *Anal. Bioanal. Chem.* 399, 3–27. doi: 10.1007/s00216-010-4207-5

Hessel, C. M., Pattani, V. P., Rasch, M., Panthani, M. G., Koo, B., Tunnell, J. W., et al. (2011). Copper selenide nanocrystals for photothermal therapy. *Nano Lett.* 11, 2560–2566. doi: 10.1021/nl201400z

Jao, S. Y., Yang, B. Y., Weng, H. H., Yeh, C. H., and Lee, L. W. (2010). Evaluation of gadolinium-enhanced T1-weighted magnetic resonance imaging in the preoperative assessment of local staging in rectal cancer. *Colorectal Dis.* 12, 1139–1148. doi: 10.1111/j.1463-1318.2009.01959.x

Lee, D.-E., Koo, H., Sun, I.-C., Ryu, J. H., Kim, K., and Kwon, I. C. (2012). Multifunctional nanoparticles for multimodal imaging and theragnosis. *Chem. Soc. Rev.* 41, 2656–2672. doi: 10.1039/C2CS15261D

Lee, S. B., Lee, J. E., Cho, S. J., Chin, J., Kim, S. K., Lee, I. K., et al. (2019). Crushed gold shell nanoparticles labeled with radioactive iodine as a theranostic nanoplatform for macrophage-mediated photothermal therapy. *Nano Micro Lett.* 11:36. doi: 10.1007/s40820-019-0266-0

Li, W., Zamani, R., Rivera Gil, P., Pelaz, B., Ibanez, M., Cadavid, D., et al. (2013). CuTe nanocrystals: shape and size control, plasmonic properties, and use as SERS probes and photothermal agents. *J. Am. Chem. Soc.* 135, 7098–7101. doi: 10.1021/ja401428e

Li, Y., Lu, W., Huang, Q., Huang, M., Li, C., and Chen, W. (2010). Copper sulfide nanoparticles for photothermal ablation of tumor cells. *Nanomedicine* 5, 1161–1171. doi: 10.2217/nnm.10.85

Liu, J., Wang, P., Zhang, X., Wang, L., Wang, D., Gu, Z., et al. (2016). Rapid degradation and high renal clearance of Cu_3BiS_3 nanodots for efficient cancer diagnosis and photothermal therapy *in vivo*. *ACS Nano* 10, 4587–4598. doi: 10.1021/acsnano.6b00745

Mou, J., Liu, C., Li, P., Chen, Y., Xu, H., Wei, C., et al. (2015). $Cu_{2-x}S$ MRI and infrared thermal/photoacoustic multimodal imaging. *Biomaterials* 57, 12–21. doi: 10.1016/j.biomaterials.2015.04.020

Roper, D. K., Ahn, W., and Hoepfner, M. (2007). Microscale heat transfer transduced by surface plasmon resonant gold nanoparticles. *J. Phys. Chem. C* 111, 3636–3641. doi: 10.1021/jp064341w

Sobhani, Z., Behnam, M. A., Emami, F., Dehghanian, A., and Jamhiri, I. (2017). Photothermal therapy of melanoma tumor using multiwalled carbon nanotubes. *Int. J. Nanomed.* 12, 4509–4517. doi: 10.2147/IJN.S134661

Song, G., Liang, C., Gong, H., Li, M., Zheng, X., Cheng, L., et al. (2015). Core-shell MnSe@Bi_2Se_3 fabricated via a cation exchange method as novel nanotheranostics for multimodal imaging and synergistic thermoradiotherapy. *Adv. Mater.* 27, 6110–6117. doi: 10.1002/adma.201503006

Song, M. L., Liu, T., Shi, C. R., Zhang, X. Z., and Chen, X. Y. (2016). Bioconjugated manganese dioxide nanoparticles enhance chemotherapy response by priming tumor-associated macrophages toward M1-like phenotype and attenuating tumor hypoxia. *ACS Nano* 10, 633–647. doi: 10.1021/acsnano.5b06779

Tang, J. H., Ge, Y. C., Shen, J. F., and Ye, M. X. (2016). Facile synthesis of $CuCo_2S_4$ as a novel electrode material for ultrahigh supercapacitor performance. *Chem. Commun.* 52, 1509–1512. doi: 10.1039/C5CC09402J

Tian, Q., Hu, J., Zhu, Y., Zou, R., Chen, Z., Yang, S., et al. (2013). Sub-10 nm Fe_3O_4@$Cu_{2-x}S$ core-shell nanoparticles for dual-modal imaging and photothermal therapy. *J. Am. Chem. Soc.* 135, 8571–8577. doi: 10.1021/ja4013497

Tian, Q., Tang, M., Sun, Y., Zou, R., Chen, Z., Zhu, M., et al. (2011). Hydrophilic flower-like CuS superstructures as an efficient 980 nm laser-driven photothermal agent for ablation of cancer cells. *Adv. Mater.* 23, 3542–3547. doi: 10.1002/adma.201101295

Wang, L. Z., Omomo, Y., Sakai, N., Fukuda, K., Nakai, I., Ebina, Y., et al. (2003). Fabrication and characterization of multilayer ultrathin films of exfoliated MnO_2 nanosheets and polycations. *Chem. Mater.* 15, 2873–2878. doi: 10.1021/cm034191r

Wang, S., Shang, L., Li, L., Yu, Y., Chi, C., Wang, K., et al. (2016). Metal-organic-framework-derived mesoporous carbon nanospheres containing porphyrin-like metal centers for conformal phototherapy. *Adv. Mater.* 28, 8379–8387. doi: 10.1002/adma.201602197

Zha, Z., Yue, X., Ren, Q., and Dai, Z. (2013). Uniform polypyrrole nanoparticles with high photothermal conversion efficiency for photothermal ablation of cancer cells. *Adv. Mater.* 25, 777–782. doi: 10.1002/adma.201202211

Zhang, D., Qin, X., Wu, T., Qiao, Q., Song, Q., and Zhang, Z. (2019). Extracellular vesicles based self-grown gold nanopopcorn for combinatorial chemo-photothermal therapy. *Biomaterials* 197, 220–228. doi: 10.1016/j.biomaterials.2019.01.024

Zhang, X., Liu, J. C., Yang, X. R., He, G. J., Li, B., Qin, J. B., et al. (2019). $CuCo_2S_4$ nanocrystals as a nanoplatform for photothermal therapy of arterial inflammation. *Nanoscale* 11, 9733–9742. doi: 10.1039/C9NR00772E

Zhao, Q., Yi, X., Li, M., Zhong, X., Shi, Q., and Yang, K. (2016). High near-infrared absorbing Cu5FeS4 nanoparticles for dual-modal imaging and photothermal therapy. *Nanoscale* 8, 13368–13376. doi: 10.1039/C6NR04444A

Conflict of Interest: The authors declare that the research was conducted in the absence of any commercial or financial relationships that could be construed as a potential conflict of interest.

frontiers in Materials

ORIGINAL RESEARCH
published: 03 December 2019
doi: 10.3389/fmats.2019.00316

Magnetic Iron Sulfide Nanoparticles as Thrombolytic Agents for Magnetocaloric Therapy and Photothermal Therapy of Thrombosis

Dapeng Fu[1,2†], *Junle Liu*[2†], *Qilong Ren*[3], *Jinhui Ding*[2*], *Heyi Ding*[2], *Xuan Chen*[2] and *Xiaohu Ge*[1,4*]

[1] Xinjiang Medical University, Urumqi, China, [2] Department of Vascular Surgery, Karamay Central Hospital, Karamay, China, [3] Material Science and Engineering School, Donghua University, Shanghai, China, [4] Department of Vascular Surgery, The People's Hospital of Xinjiang Uygur Autonomous Region, Urumqi, China

OPEN ACCESS

Edited by:
Ming Ma,
Shanghai Institute of Ceramics (CAS), China

Reviewed by:
Xijian Liu,
Shanghai University of Engineering Sciences, China
Jinbao Qin,
Shanghai Ninth People's Hospital, China

***Correspondence:**
Jinhui Ding
2817602110@qq.com
Xiaohu Ge
549468587@qq.com

[†]These authors have contributed equally to this work

Specialty section:
This article was submitted to Biomaterials, a section of the journal Frontiers in Materials

Received: 15 October 2019
Accepted: 20 November 2019
Published: 03 December 2019

Citation:
Fu D, Liu J, Ren Q, Ding J, Ding H, Chen X and Ge X (2019) Magnetic Iron Sulfide Nanoparticles as Thrombolytic Agents for Magnetocaloric Therapy and Photothermal Therapy of Thrombosis. Front. Mater. 6:316. doi: 10.3389/fmats.2019.00316

Non-invasive removal of thrombosis is a difficult problem in clinical vascular disease. Herein, we reported magnetic hyperthermia combined photothermal therapy for celiac vein thrombosis using Fe_3S_4 nanoparticles as thrombolytic agents under the stimulation of a near infrared (NIR) laser and an external alternating magnetic field (AMF). Fe_3S_4 nanoparticles showed excellent magnetothermal conversion performance under the continuous stimulation of an AMF and very good photothermal conversion performance under the irradiation of a NIR laser. Moreover, Fe_3S_4 nanoparticles exhibited a synergistic thermal conversion effect under the co-stimulation of NIR and AMF. In addition, the Fe_3S_4 nanoparticles possess the ability for magnetic resonance (MR) imaging with the transverse relaxivity (r_2) is up to 53.1 mM^{-1} s^{-1}. Finally, we, for the first time, proved the Fe_3S_4 nanoparticles as a promising thrombolytic agent for both photothermal thrombolytic capacity and magnetothermal thrombolytic ability. Our work provides the insight of hyperthermia for removal of the thrombosis.

Keywords: photothermal therapy, magnetocaloric therapy, thrombosis, iron sulfide, magnetic resonance imaging

INTRODUCTION

Cardiovascular disease is one of the main causes of harm to human health (Mackman, 2008; Engelmann and Massberg, 2013). Because the blood vessels are aging and the blood vessel wall is damaged, it is easy to form the thromboses in the blood vessel, and it is also more likely to suffer from diseases such as hypertension and arteriosclerosis. Surgery and chemotherapy are still the main treatment options for thrombosis. Surgical treatment causes great pain to the patient's body; chemotherapy is non-targeting and belongs to systemic administration, which has great side effects (Voros et al., 2015). Traditional treatments often treat known thrombi, but may cause new problems for blood vessels. Older people with thrombosis often do not dare to use thrombolytic drugs. Therefore, it is of great significance to develop an efficient and accurate thrombosis treatment system for non-invasive and precise treatment of thrombosis.

Clinically approved thrombolytic agents are characterized by short half-life, short blood flow life and damage to local bleeding (Hacke et al., 2008; Derex and Nighoghossian, 2009). Nanoparticles have proven to be promising diagnostic agents for the treatment of a

variety of diseases and have relatively long blood circulation agents (Vogel and Venugopalan, 2003; Mahmoudi et al., 2011; Li et al., 2017). At present, it has been reported that hyperthermia can achieve a good thrombolytic effect (Voros et al., 2015; Wang X. et al., 2017). Hyperthermia methods include photothermal therapy and magnetic hyperthermia (Dai et al., 2019). Photothermal therapy is the treatment through heat generated by near-infrared (NIR) light-induced photothermal reagents (Fang et al., 2012; Zhang et al., 2013; Chen et al., 2014; Li et al., 2014, 2015, 2017). Wang et al. prove that heat generated by the photothermal effect of gold can achieve the purpose of thrombolysis (Wang X. et al., 2017). Magnetic hyperthermia is a way in which a magnetothermal conversion reagent generates heat to treat a disease under the action of an external alternating magnetic field (AMF) (Wang F. et al., 2017; Li et al., 2018; Dai et al., 2019). The magnetocaloric effect of iron oxide has been shown to accelerate the dissolution of blood clots in Voros et al.' report (Voros et al., 2015). However, there are more or less defects in the way of thrombolysis. In the photothermal treatment, due to the poor penetration of light, it is impossible to treat deep thrombus, such as celiac vein thrombosis. In the case of iron oxide magnetothermal treatment of thrombus, it causes certain side effects due to the long-term presence of iron oxide in the body. Therefore, there is a great of necessary and importance to adjust the current strategy for treating thrombosis to treat thrombosis.

Fe_3S_4 nanoparticles have similar properties to iron oxide (Liu et al., 2014). It has been revealed that Fe_3S_4 nanoparticles have a very good magnetocaloric effect which could be used in magnetic hyperthermia for deep thrombosis (Guan et al., 2018; Moore et al., 2019). Moreover, Fe_3S_4 nanoparticles have been shown to degrade rapidly *in vivo* (Guan et al., 2018). Therefore, Fe_3S_4 nanoparticles show great potential for the magnetic hyperthermia for deep thrombosis. Herein, we reported hyperthermia for celiac vein thrombosis using Fe_3S_4 nanoparticles as a thrombolytic reagent under the stimulation of a NIR laser and an AMF. Fe_3S_4 nanoparticles show a synergistic thermal transition effect under the co-action of a NIR laser and an AMF. In addition, the Fe_3S_4 nanoparticles possess the ability for magnetic resonance (MR) imaging with the transverse relaxivity (r_2) is up to 53.1 mM^{-1} s^{-1}. Finally, we, for the first time, proved the Fe_3S_4 nanoparticles as a promising thrombolytic agent for magnetic hyperthermia for celiac vein thrombosis.

RESULTS AND DISCUSSION

Synthesis and Characterization of Fe_3S_4 Nanoparticles

Hydrophilic Fe_3S_4 nanoparticles were synthesized via a simple hydrothermal method by reaction the $FeSO_4$ with L-Cysteine in water at 220°C for 20 h. During the preparation, the polyvinylpyrrolidone (PVP) was added into the reaction as surface ligand to improve their biocompatibility. Thus, the Fe_3S_4 nanoparticles are capped by PVP (demonstrated by FTIR, **Figure S1**) and hydrophilic, and can be used as thrombolytic agents without any further modification. As shown in **Figure 1A**, transmission electron microscopy (TEM) image demonstrated that the as-prepared products were highly dispersible nanoparticles. The size of NCs was found to be 17.7 nm based on the TEM images (**Figure S2**). More microstructure information can be achieved from high resolution TEM (**Figure 1B**). It shows an interplanar spacing of 0.298 nm, which can be indexed to (220) planes of greigite structured Fe_3S_4. As shown in **Figure 1C**, X-ray diffraction (XRD) pattern of the products could be well-matched with that of greigite structured Fe_3S_4 (JCPDS file no.: 16-0713), indicating that we obtained pure greigite structured Fe_3S_4 with high crystallinity. X-ray photoelectron spectroscopy (XPS) revealed the composition and element state of the as-prepared products (**Figure S3**). It showed that the products mainly contain Fe and S elements with no other impurities. We analyzed the valency state of Fe in Fe_3S_4 nanoparticles. **Figure 1D** shows Fe 2p spectrum for the Fe_3S_4 nanoparticles. It was demonstrated that there was a mixed Fe oxidation state, i.e., Fe^{2+} and Fe^{3+} (Guan et al., 2018), indicating a defect structure in Fe_3S_4 nanoparticles. According to the above results, it can be concluded that the pure Fe_3S_4 nanoparticles with high crystallinity was successfully formed.

Magnetocaloric Conversion Performance of Fe_3S_4 Nanoparticles

Figures 2A,B shows the magnetocaloric conversion performance of Fe_3S_4 nanoparticles. Under the continuous simulation of AMF (4.2×10^9 A m^{-1} s^{-1}), the temperature of Fe_3S_4 nanoparticles with a concentration of 0.5 mg/mL can increase by 12.8°C, while the temperature change of pure water is not obvious. When the concentration is increased to 1.0 mg/mL, the temperature of Fe_3S_4 nanoparticle dispersion can be raised by 20°C which is high enough to dissolve thrombus. **Figure 2C** shows the thermal imaging of pure water and Fe_3S_4 nanoparticles (1.0 mg/mL) under the action of an AMF for 5 min, respectively. As we can see from **Figure 2D**, a high contrast image was obtained. These results indicated that Fe_3S_4 nanoparticles showed an excellent magnetocaloric conversion performance.

Photothermal Conversion Performance of Fe_3S_4 Nanoparticles

We also measured the UV-vis absorbance spectrum of the Fe_3S_4 nanoparticles, which is important for photothermal performance. From **Figure 3A**, we can see that the Fe_3S_4 nanoparticles showed a strong absorption in the NIR region from 700 to 1,000 nm, resulted from the defect structure in Fe_3S_4 nanoparticles. Then varied concentrations (0–0.5 mg/mL) of Fe_3S_4 nanoparticles were exposed to an 808 nm (0.33 W cm^{-2}) laser to evaluate the photothermal effect. As expected, the Fe_3S_4 nanoparticles showed a good photothermal conversion performance with concentration-dependent photothermal effect (**Figure 3B**). Fe_3S_4 nanoparticles with a concentration at 0.5 mg/mL, the temperature can increase by about 30°C, while the temperature of pure water showed little change. The photothermal performance of Fe_3S_4 nanoparticles ensured the potential of Fe_3S_4 nanoparticles as a thrombolytic reagent.

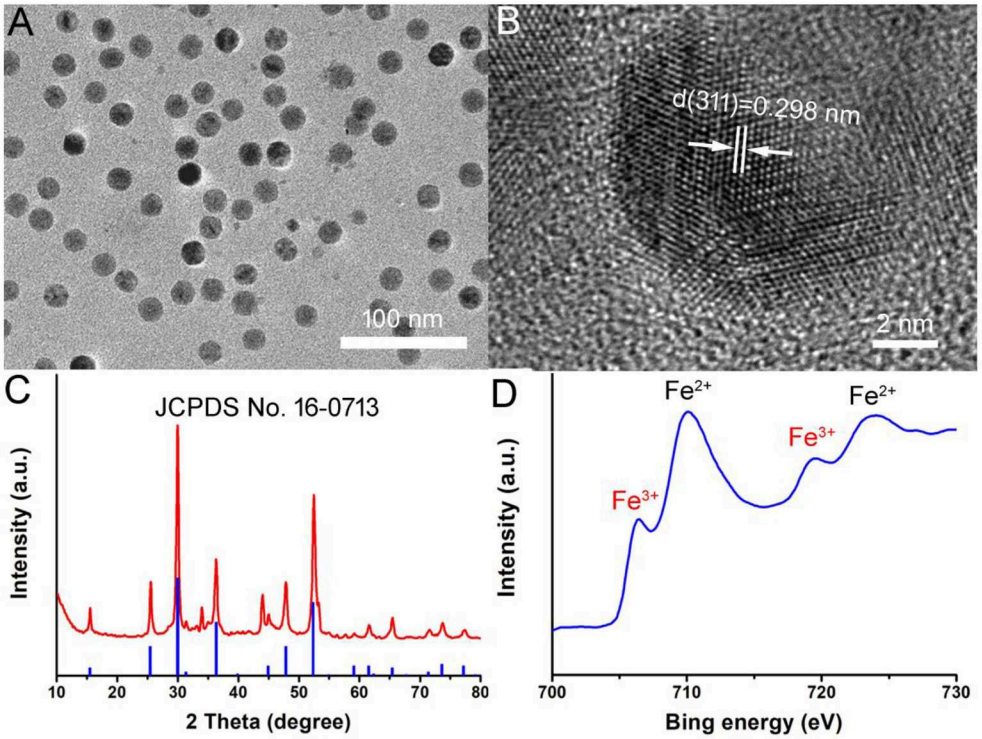

FIGURE 1 | (A) TEM image of as-prepared Fe_3S_4 nanoparticles. **(B)** High resolution TEM image of Fe_3S_4 nanoparticles. **(C)** XRD pattern of Fe_3S_4 nanoparticles. **(D)** High resolution XPS spectra of Fe in Fe_3S_4 nanoparticles.

Synergistic Thermal Conversion Effect

To test the synergistic thermal conversion effect of Fe_3S_4 nanoparticles, Fe_3S_4 nanoparticles (500 ppm, 100 μL) was assessed under the simultaneous stimulation including a NIR (808 nm, 0.33 W cm^{-2}) laser and an AMF (4.2×10^9 A m^{-1} s^{-1}) for 5 min. Temperature change was recorded by a thermal imaging camera. It was found that the temperature elevation can reach 37.1°C under the co-stimulation of NIR and AMF (**Figure 4A**). From **Figure 4B**, we can see that the temperature change from the co-stimulation of NIR and AMF was much higher the that from the single stimulation of NIR or AMF, indicating a synergistic thermal conversion effect.

Combined Therapy of Thrombotic *in vitro*

Due to the excellent thermal conversion performance of Fe_3S_4 nanoparticles, we measured the *in vitro* thrombolytic capacity of Fe_3S_4 nanoparticles under an 808 nm (0.33 W cm^{-2}) laser and/or an AMF (4.2×10^9 A m^{-1} s^{-1}). Thrombosis was obtained 1 week after ligation of the abdominal vena cava in mice using the surgical suture. A thrombus block was placed in a 20 mL glass vial followed by a 5 mL Fe_3S_4 nanoparticle solution. Finally, it was irradiated by an 808 nm (0.33 W cm^{-2}) laser and/or an AMF (4.2×10^9 A m^{-1} s^{-1}) for *in vitro* thrombolysis. As a control, the thrombus block in another bottle containing nanoparticle solution wasn't stimulated by NIR laser. It showed that the thrombus can be partially dissolved under the stimulation of NIR or AMF combined with Fe_3S_4 nanoparticles. Moreover, when co-stimulated by NIR and AMF, the thrombus was almost disappeared (**Figure S4**). However, the thrombus in the control showed little change. Therefore, Fe_3S_4 nanoparticles can be used as a thrombolytic agent under the stimulation of NIR or/and AMF.

MR Imaging Guided Thrombotic *in vivo*

Fe_3S_4 nanoparticles can be served for imaging guided magnetic hyperthermia of thrombosis. We established a model of deep vein thrombosis using black C57 mice, and the penetration depth of the laser did not reach the lesions. Moreover, the temperature of the hair of the C57 mice increased after laser irradiation to cause burntness. So we use magnetic hyperthermia to dissolve the thrombus. First, Fe_3S_4 nanoparticle' phantom images and proton T_2 relaxation test at varied Fe concentrations were measured. As shown in **Figure 5A**, T_2-weighted MR imaging signal intensity was increased with the increase of the concentration of Fe_3S_4 nanoparticle. The transverse relaxivity (r_2) value of the CMO NCs was calculated to be 53.1 mM^{-1} s^{-1}, indicating an efficient MRI contrast agent (**Figure 5B**). We then evaluated animal experiments on the T_2-weighted MR imaging guided magnetic hyperthermia of thrombosis. From **Figure 5C**, we can see that the signal in thrombosis sites (left) was light white. Under the action of Fe_3S_4 nanoparticles combined with AMF, light white region in thrombosis sites (right) obviously decreased. Therefore, Fe_3S_4

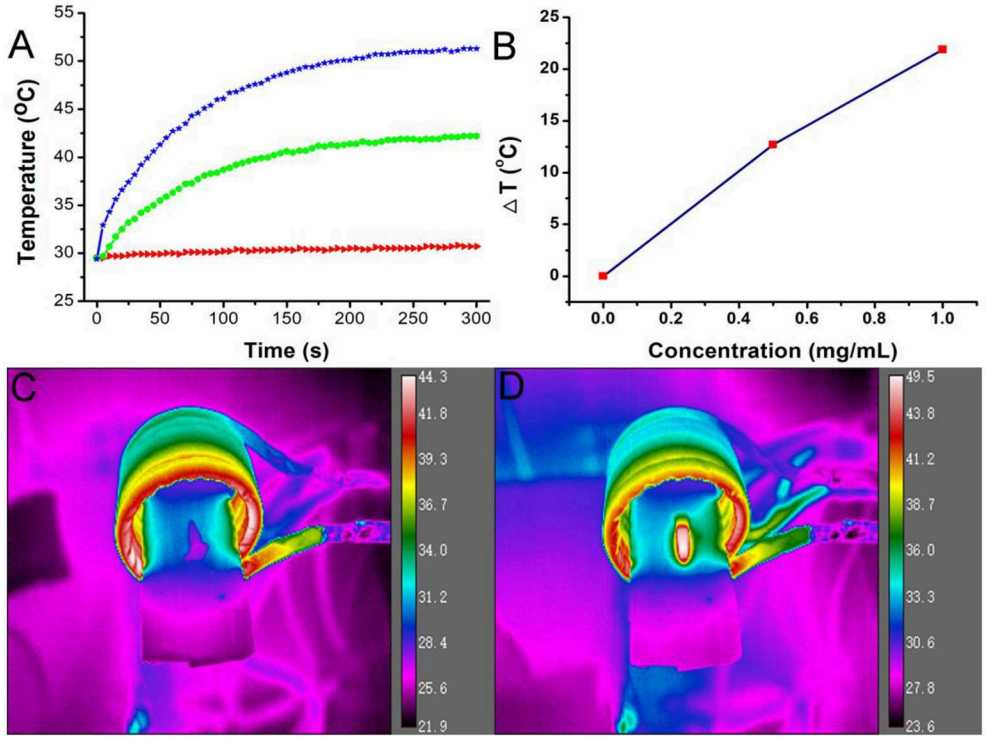

FIGURE 2 | (A) Temperature change of the Fe_3S_4 nanoparticles in water at varied concentrations of Fe^{2+} (i.e., 0, 0.5, and 1.0 mg/mL) as a function of magnetic field action time. **(B)** Plot of temperature change over 300s vs. the concentration of Fe_3S_4 nanoparticles. Thermal imaging of **(C)** pure water and **(D)** Fe_3S_4 nanoparticles (1.0 mg/mL) under the action of an AMF for 5 min.

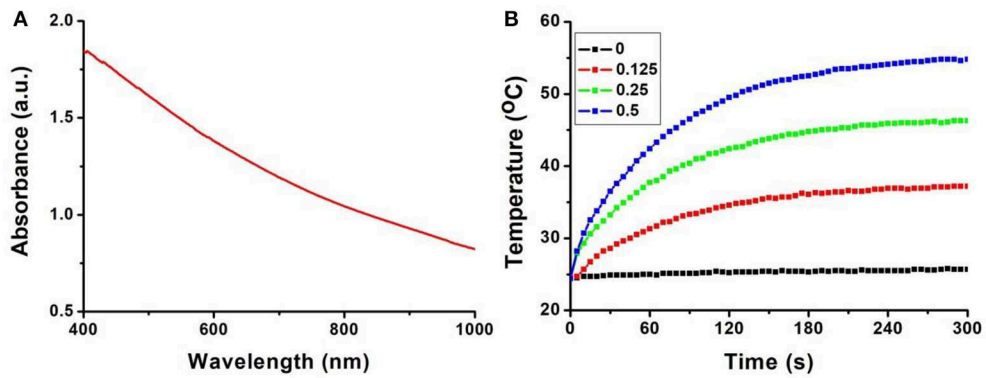

FIGURE 3 | (A) UV-vis absorbance spectrum of the Fe_3S_4 nanoparticles. **(B)** Temperature change of the Fe_3S_4 nanoparticles in water at varied concentrations (i.e., 0, 0.125, 0.25, and 0.5 mg/mL) as a function of the irradiation time of an 808 nm laser (0.33 W cm^{-2}).

nanoparticles can be served as an efficient thrombolytic agent *in vivo*.

Biomaterials must have good biocompatibility in clinical applications. Then *in vivo* long-term toxicity of the as-prepared Fe_3S_4 nanoparticles was evaluated by blood bioanalysis and hematoxylin and Eosin analysis, respectively. There was no obvious difference detected in alanine aminotransferase (ALT) and aspartate aminotransferase (AST) (**Figures 6A,B**), which indicated that Fe_3S_4 nanoparticles have good biocompatibility to the liver and heart (Zhang et al., 2018). Then histological examination analysis for main organs was performed to observe the shape and the size of cells after the intravenous injection of Fe_3S_4 nanoparticles at a dosage of 12 mg/kg. The organs included the heart, kidney, liver, lung, and spleen. As shown in **Figure 6C**, there is no tissue damage or adverse effect compared with those of control groups. This suggests

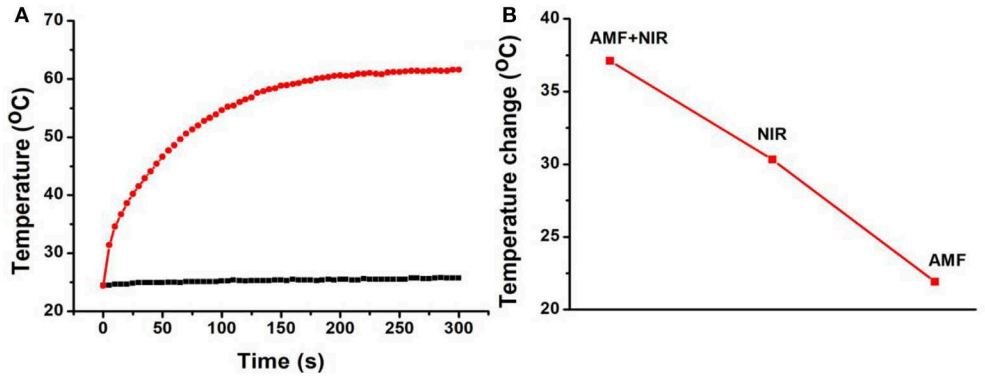

FIGURE 4 | (A) Temperature change of Fe_3S_4 nanoparticles under co-stimulation of NIR and AMF for 5 min. **(B)** Comparison of the temperature change from the indicated conditions. Fe_3S_4 nanoparticles: 0.5 mg/mL; NIR: 808 nm, 0.33 W cm^{-2}; AMF: 4.2 × 10^9 A m^{-1} s^{-1}.

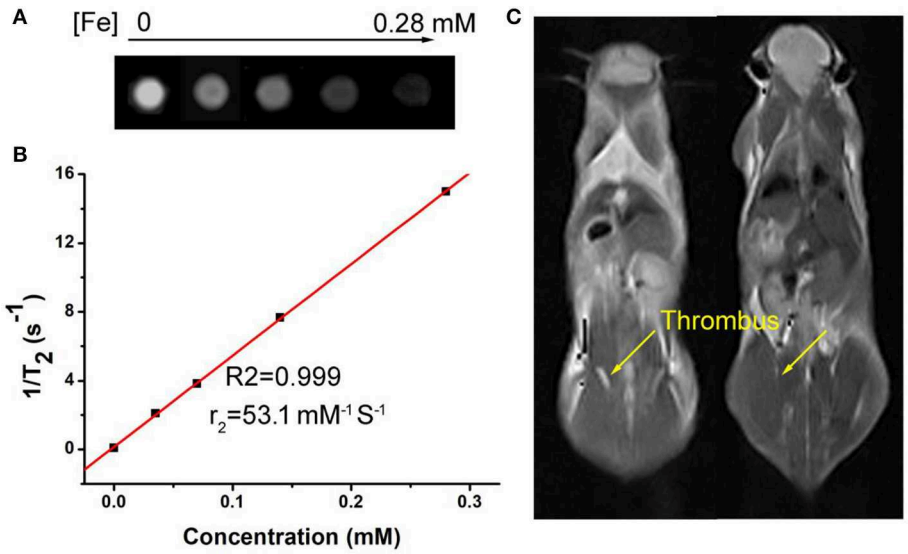

FIGURE 5 | (A) Phantom images of the Fe_3S_4 nanoparticles. **(B)** Proton T_2 relaxation measurements at varied Fe concentrations **(C)** T_2-weighted MR imaging *in vivo* of a mouse with celiac vein thrombosis before (left) and after (right) an intravenous injection of a solution of the Fe_3S_4 nanoparticles followed by the simulation of AMF.

that these Fe_3S_4 nanoparticles at the given dose are not obviously toxic.

It was reported that inorganic nanoparticles (quantum dots used as a model system) with relatively large sizes would accumulate in reticuloendothelial systems (RES) such as liver and spleen for long periods of time (Choi et al., 2007). Ideally, it would be the best to make Fe_3S_4 nanoparticles quickly excreted from the normal organs of the body, while being able to effectively accumulate and retain in lesions. A study from guan reported that the clearance of Fe_3S_4 nanoparticles was quickly post intravenous injection (Guan et al., 2018). We also studied the distribution and metabolism of the Fe_3S_4 nanoparticles, mice were intravenously injected with 12 mg·kg^{-1} of the Fe_3S_4 nanoparticles. At different intervals of time (i.e., 1, 3, 7, and 10 days, $n = 3$ at each time point), mice were sacrificed to obtain major organs including kidney, spleen, heart, liver, and lung. These organs were digested and solubilized. An ICP-MS analysis was used to determine Fe content in each organ. It was (**Figure S5**) found that the Fe_3S_4 nanoparticles mainly accumulate at spleen and liver, indicating that Fe_3S_4 nanoparticles was mainly degraded in these two organs.

CONCLUSION

In conclusion, Fe_3S_4 nanoparticles, as a new imaging-guided thrombolytic agent, have been successfully prepared by a simple hydrothermal route. The as-prepared Fe_3S_4 nanoparticles have a good dispersity and show an excellent magnetothermal conversion performance and photothermal effect, and exhibited a synergistic thermal conversion effect under the co-stimulation of NIR and AMF. They also possess an effective MR imaging *in vivo*. Furthermore, the *in vivo* toxicity results indicate their excellent biocompatibility. With the stimulation of an external AMF and

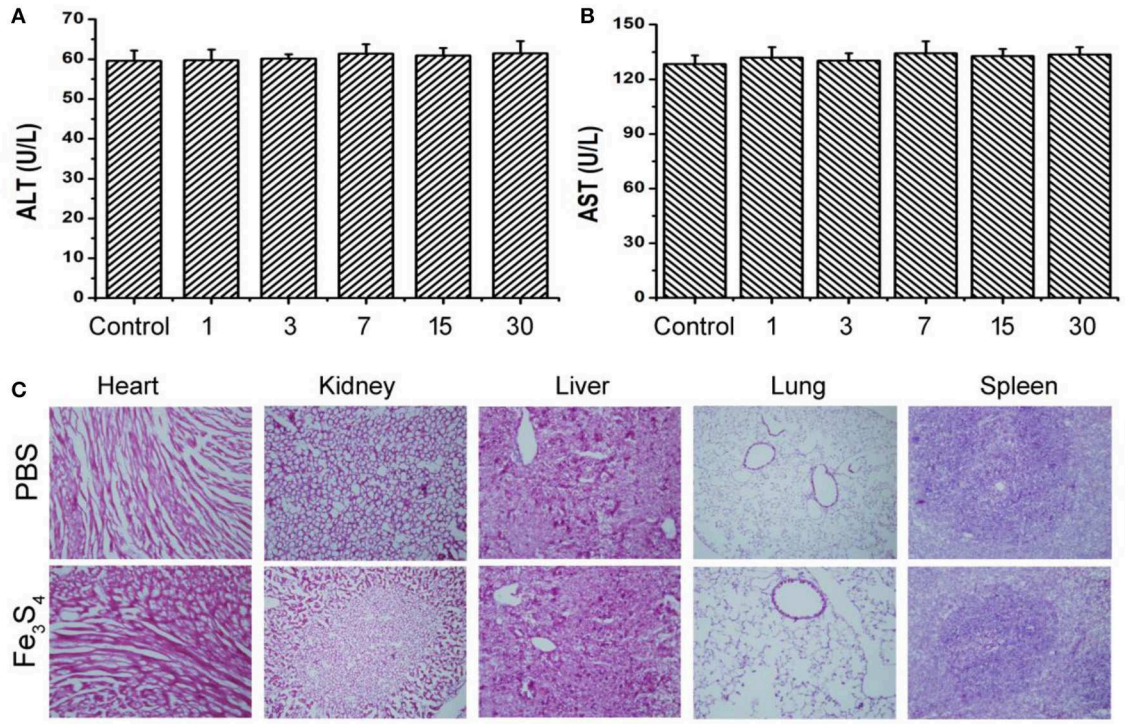

FIGURE 6 | Blood bioanalysis of mice in control group and Fe_3S_4 group at different time points (1, 3, 7, 15, and 30 days), including **(A)** alanine aminotransferase (ALT) and **(B)** aspartate aminotransferase (AST). **(C)** Hematoxylin and Eosin stained tissue sections from the mice to monitor the histological changes in heart, kidney, liver, lung, and spleen of the mice 1 month after a single intravenous injection of the Fe_3S_4 nanoparticle' solution. Scale bar: 100 μm.

a NIR laser, the Fe_3S_4 nanoparticles can be used as thrombolytic agents with MR imaging guided hyperthermia of thrombosis.

EXPERIMENTAL SECTIONS

Synthesis of Fe_3S_4 Nanoparticles

One millimole of $FeSO_4$ and 1 mmol L-cysteine were consecutively dissolved in 40 mL water. Seven hundred milligram of poly (vinyl pyrrolidone) (PVP) was then added. Then the reaction was kept at 220°C for 24 h in a stainless steel autoclave. The products were collected through centrifugation and finally washed with ethanol and deionized water for three times.

Characterization

The morphology as well as the size of nanoparticles was achieved by TEM (JEOL JEM-2010F, Japan). The crystal phase of Fe_3S_4 nanoparticles was measured by XRD (Bruker D4). The oxidation state analysis of Fe_3S_4 nanoparticles was measured by X-ray photoelectron spectra (XPS, ESCA-Lab 250Xi). Concentration of Fe ions released from Fe_3S_4 nanoparticles was tested by ICP-AES (Leeman Laboratories Prodigy).

Measurement of Magnetocaloric Conversion Performance of Fe_3S_4 Nanoparticles

For the evaluation of the magnetocaloric conversion performance of Fe_3S_4 nanoparticles, 100 μL of Fe_3S_4 nanoparticles dispersed in deionized water at varied concentrations was simulated under the external AMF (4.2 $\times$ 10^9 A m^{-1} s^{-1}). Temperature change was recorded by a thermal imaging camera.

Measurement of Photothermal Effect of Fe_3S_4 Nanoparticles

For the evaluation of the photothermal performance of Fe_3S_4 nanoparticles, 100 μL of Fe_3S_4 nanoparticles dispersed in deionized water at varied concentrations was exposed upon the irradiation of an 808 nm laser. Temperature change was recorded by a thermal imaging camera.

Thrombotic Animal Model

All animal experiments were approved by the Animal Ethics Committee of Karamay central hospital. 8-week-old C57 mice were anesthetized and laparotomy, the inferior vena cava was separated, and the inferior vena cava was ligated under the left renal vein with a surgical line (Kyogashima et al., 1999).

Hyperthermia of Thrombosis *in vitro*

To evaluate *in vitro* thrombolytic capacity of Fe_3S_4 nanoparticles under the irradiation of a NIR laser or/and AMF, thromboses was obtained 1 week after ligation of the abdominal vena cava in mice using a surgical line. A thrombus block was placed in a 20 mL glass vial followed by a 5 mL Fe_3S_4 nanoparticle solution. Finally, it was irradiated by an 808 nm laser or/and AMF for *in vitro* thrombolysis. As a control, the thrombus block in another

bottle containing nanoparticle solution wasn't stimulated by the 808 nm laser or/and AMF.

MR Imaging Guided Hyperthermia of Thrombosis *in vivo*

The Fe_3S_4 nanoparticle dispersions with varied Fe concentrations (0–0.28 mM) were scanned at room temperature via the animal MR imagine scanner under a 0.5 T MRI scanner at room temperature. Before *in vivo* MR imaging guided magnetic hyperthermia of thrombosis, thrombosis model mouse were scanned with the same MR scanner with the same parameters to be a control. After intravenous injection with the Fe_3S_4 nanoparticle dispersion (100 μL, 12 mg/kg) followed by stimulation under an AMF, the thrombosis model mouse were scanned again with the MR scanner.

Histological Examination Analysis and Blood Analysis

As for the histological examination, one mouse in each group was killed under anesthesia after the indicated treatment. Then the organs included the heart, kidney, liver, lung, and spleen were harvested, and then sectioned into 4 μm slices using a conventional microtome, finally stained with H&E. The slices were examined via a microscope. Also, the blood from mice in control group and Fe_3S_4 group was collected to test the biocompatibility of Fe_3S_4 nanoparticle to major organs.

DATA AVAILABILITY STATEMENT

All datasets generated for this study are included in the article/**Supplementary Material**.

ETHICS STATEMENT

The animal study was reviewed and approved by the Animal Ethics Committee of Karamay Central Hospital.

AUTHOR CONTRIBUTIONS

DF, JD, and XG designed the project. DF, QR, JL, and HD carried out the experiment and performed the experimental data analysis. DF and XC wrote the paper. All the authors contributed to discussion of the results.

FUNDING

This work was supported by Xinjiang Uygur Autonomous Region Natural Science Fund (2019D01A08).

SUPPLEMENTARY MATERIAL

The Supplementary Material for this article can be found online at: https://www.frontiersin.org/articles/10.3389/fmats.2019.00316/full#supplementary-material

REFERENCES

Chen, Q., Wang, C., Zhan, Z., He, W., Cheng, Z., Li, Y., et al. (2014). Near-infrared dye bound albumin with separated imaging and therapy wavelength channels for imaging-guided photothermal therapy. *Biomaterials* 35, 8206–8214. doi: 10.1016/j.biomaterials.2014.06.013

Choi, H. S., Liu, W., Misra, P., Tanaka, E., Zimmer, J. P., Itty Ipe, B., et al. (2007). Renal clearance of quantum dots. *Nat. Biotechnol.* 25, 1165–1170. doi: 10.1038/nbt1340

Dai, C., Wang, C., Hu, R., Lin, H., Liu, Z., Yu, L., et al. (2019). Photonic/magnetic hyperthermia-synergistic nanocatalytic cancer therapy enabled by zero-valence iron nanocatalysts. *Biomaterials*, 219:119374. doi: 10.1016/j.biomaterials.2019.119374

Derex, L., and Nighoghossian, N. (2009). Thrombolysis, stroke-unit admission and early rehabilitation in elderly patients. *Nat. Rev. Neurol.* 5, 506–511. doi: 10.1038/nrneurol.2009.127

Engelmann, B., and Massberg, S. (2013). Thrombosis as an intravascular effector of innate immunity. *Nat. Rev. Immunol.* 13, 34–45. doi: 10.1038/nri3345

Fang, W., Yang, J., Gong, J., and Zheng, N. (2012). Photo- and pH-triggered release of anticancer drugs from mesoporous silica-coated Pd@Ag nanoparticles. *Adv. Funct. Mater.* 22, 842–848. doi: 10.1002/adfm.201101960

Guan, G., Wang, X., Li, B., Zhang, W., Cui, Z., Lu, X., et al. (2018). "Transformed" Fe_3S_4 tetragonal nanosheets: a high-efficiency and body-clearable agent for magnetic resonance imaging guided photothermal and chemodynamic synergistic therapy. *Nanoscale* 10, 17902–17911. doi: 10.1039/C8NR06507A

Hacke, W., Kaste, M., Bluhmki, E., Brozman, M., Dávalos, A., Guidetti, D., et al. (2008). Thrombolysis with alteplase 3 to 4.5 hours after acute ischemic stroke. *N. Engl. J. Med.* 359, 1317–1329. doi: 10.1056/NEJMoa0804656

Kyogashima, M., Onaya, J., Miyauchi, S., Arai, M., Shibata, Y., Suda, A., et al. (1999). Antithrombotic activity of avian crown dermatan sulfate. *Thromb. Res.* 96, 459–465. doi: 10.1016/S0049-3848(99)00138-3

Li, B., Wang, Q., Zou, R., Liu, X., Xu, K., Li, W., et al. (2014). Cu7.2S4 nanocrystals: a novel photothermal agent with a 56.7% photothermal conversion efficiency for photothermal therapy of cancer cells. *Nanoscale* 6, 3274–3282. doi: 10.1039/c3nr06242b

Li, B., Ye, K., Zhang, Y., Qin, J., Zou, R., Xu, K., et al. (2015). Photothermal theragnosis synergistic therapy based on bimetal sulphide nanocrystals rather than nanocomposites. *Adv. Mater. Weinheim.* 27, 1339–1345. doi: 10.1002/adma.201404257

Li, B., Yuan, F., He, G., Han, X., Wang, X., Qin, J., et al. (2017). Ultrasmall $CuCo_2S_4$ nanocrystals: all-in-one theragnosis nanoplatform with magnetic resonance/near-infrared imaging for efficiently photothermal therapy of tumors. *Adv. Funct. Mater.* 27:1606218. doi: 10.1002/adfm.201606218

Li, M., Bu, W., Ren, J., Li, J., Deng, L., Gao, M., et al. (2018). Enhanced synergism of thermo-chemotherapy for liver cancer with magnetothermally responsive nanocarriers. *Theranostics* 8, 693–709. doi: 10.7150/thno.21297

Liu, X., Feng, C., Bi, N., Sun, Y., Fan, J., Lv, Y., et al. (2014). Synthesis and electromagnetic properties of Fe_3S_4 nanoparticles. *Ceramics Int.* 40, 9917–9922. doi: 10.1016/j.ceramint.2014.02.087

Mackman, N. (2008). Triggers, targets and treatments for thrombosis. *Nature* 451, 914–918. doi: 10.1038/nature06797

Mahmoudi, M., Sant, S., Wang, B., Laurent, S., and Sen, T. (2011). Superparamagnetic iron oxide nanoparticles (SPIONs): development, surface modification and applications in chemotherapy. *Adv. Drug Deliv. Rev.* 63, 24–46. doi: 10.1016/j.addr.2010.05.006

Moore, J., Nienhuis, E., Ahmadzadeh, M., and McCloy, J. (2019). Synthesis of greigite (Fe_3S_4) particles via a hydrothermal method. *AIP Adv.* 9:035012. doi: 10.1063/1.5079759

Vogel, A., and Venugopalan, V. (2003). Mechanisms of pulsed laser ablation of biological tissues. *Chem. Rev.* 103, 577–644. doi: 10.1021/cr010379n

Voros, E., Cho, M. J., Ramirez, M., Palange, A. L., De Rosa, E., Key, J., et al. (2015). TPA immobilization on iron oxide nanocubes and localized magnetic

hyperthermia accelerate blood clot lysis. *Adv. Funct. Mater.* 25, 1709–1718. doi: 10.1002/adfm.201404354

Wang, F., Yang, Y., Ling, Y., Liu, J., Cai, X., Zhou, X., et al. (2017). Injectable and thermally contractible hydroxypropyl methyl cellulose/Fe_3O_4 for magnetic hyperthermia ablation of tumors. *Biomaterials* 128, 84–93. doi: 10.1016/j.biomaterials.2017.03.004

Wang, X., Wei, C., Liu, M., Yang, T., Zhou, W., Liu, Y., et al. (2017). Near-infrared triggered release of uPA from nanospheres for localized hyperthermia-enhanced thrombolysis. *Adv. Funct. Mater.* 27:1701824. doi: 10.1002/adfm.201701824

Zhang, W., Deng, G., Li, B., Zhao, X., Ji, T., Song, G., et al. (2018). Degradable rhenium trioxide nanocubes with high localized surface plasmon resonance absorbance like gold for photothermal theranostics. *Biomaterials* 159, 68–81. doi: 10.1016/j.biomaterials.2017.12.021

Zhang, Z., Wang, J., and Chen, C. (2013). Near-infrared light-mediated nanoplatforms for cancer thermo-chemotherapy and optical imaging. *Adv. Mater. Weinheim.* 25, 3869–3880. doi: 10.1002/adma.201301890

Conflict of Interest: The authors declare that the research was conducted in the absence of any commercial or financial relationships that could be construed as a potential conflict of interest.

frontiers in Bioengineering and Biotechnology

ORIGINAL RESEARCH
published: 18 February 2020
doi: 10.3389/fbioe.2020.00021

Cu_5FeS_4 Nanoparticles With Tunable Plasmon Resonances for Efficient Photothermal Therapy of Cancers

Lei Yuan[1], *Weiwei Hu*[2], *Hui Zhang*[1], *Long Chen*[1], *Jianyu Wang*[1] *and Qiang Wang*[1]*

[1] Xuzhou Cancer Hospital, Xuzhou, China, [2] The Affiliated Hospital of Xuzhou Medical University, Xuzhou, China

Localized surface plasmon resonances (LSPRs) in heavily doped copper chalcogenides are unique because LSPR energy can be adjusted by adjusting doping or stoichiometry. However, there are few investigations on the LSPRs of bimetal copper-based chalcogenides. Herein, bimetal Cu_5FeS_4 (CFS) nanoparticles were synthesized by a facile hot injection of a molecular precursor. The tunable plasmon resonance absorption of CFS nanoparticles is achieved by the decrease of the ratio of copper to iron and the treatment of n-dodecylphosphoric acid (DDPA). After surface modification with polyethylene glycol (PEG), the CFS nanoparticles with a plasmon resonance absorption peak at 764 nm can serve as promising photothermal agents, showing good biocompatibility and excellent photothermal performance with a photothermal conversion efficiency of up to 50.5%, and are thus used for photothermal therapy of cancers under the irradiation of an 808-nm laser. Our work provides insight into bimetal copper-based chalcogenides to achieve tunable LSPRs, which opens up the possibility of rationally designing plasmonic bimetal copper-based chalcogenides.

Keywords: Cu_5FeS_4 nanoparticles, plasmon resonances, bimetal copper-based chalcogenides, photothermal agents, photothermal therapy

OPEN ACCESS

Edited by:
Bo Li,
School of Medicine, Shanghai Jiao Tong University, China

Reviewed by:
Xijian Liu,
Shanghai University of Engineering Sciences, China
Jianqiang Liu,
Guangdong Medical University, China

***Correspondence:**
Qiang Wang
doctorwang618@126.com

Specialty section:
This article was submitted to Biomaterials, a section of the journal Frontiers in Bioengineering and Biotechnology

Received: *09 December 2019*
Accepted: *10 January 2020*
Published: *18 February 2020*

Citation:
Yuan L, Hu W, Zhang H, Chen L, Wang J and Wang Q (2020) Cu_5FeS_4 Nanoparticles With Tunable Plasmon Resonances for Efficient Photothermal Therapy of Cancers. Front. Bioeng. Biotechnol. 8:21. doi: 10.3389/fbioe.2020.00021

INTRODUCTION

Localized surface plasmon resonances (LSPRs) of nanostructures contribute to enhanced tunable optical absorption in the near-infrared (NIR) region, which is great for the improvement of the photothermal performance of photothermal nanoagents (Luther et al., 2011; Manthiram and Alivisatos, 2012; Yang et al., 2013; Li et al., 2015). As noble metals are stable under various conditions and have high carrier densities, most reports of LSPRs have been performed on them (Huang et al., 2011a,b; Manthiram and Alivisatos, 2012). There are also reports of LSPRs in doped semiconductor nanostructures, including copper chalcogenides (Liu et al., 2013; Balitskii et al., 2014), tin oxides (Kanehara et al., 2009; Garcia et al., 2011), and zinc oxide (Buonsanti et al., 2011). LSPRs in heavily doped copper chalcogenides are unique because LSPR energy can be adjusted by adjusting doping or stoichiometry (Luther et al., 2011; Tian et al., 2011; Li et al., 2015). There have been a few reports on copper chalcogenides with enhanced photothermal performance by adjusting doping for photothermal therapy of cancers (Hessel et al., 2011; Tian et al., 2013; Li et al., 2014a, 2015).

The LSPRs of copper-based chalcogenide compounds is an important factor affecting their photothermal conversion efficiency. As the plasmon resonance absorption of gold nanostructures is much higher than the inter-band absorption of organic materials, the photothermal conversion efficiency of gold nanostructures is one of the currently reported high photothermal conversion

materials (Yavuz et al., 2009; Tang et al., 2012). The hole-doped copper-based chalcogenides have a high extinction coefficient similar to that of the metal plasmon resonance absorption. Tian et al. developed a novel hole-doped semiconductor photothermal conversion material, i.e., Cu_9S_5 disk-shaped nanocrystals (Tian et al., 2011). The extinction coefficient and photothermal conversion efficiency of this Cu_9S_5 nanocrystal at 980 nm are as high as $\sim 1.2 \times 10^9$ M^{-1} cm^{-1} and 25.7%, respectively, which are higher than the extinction coefficient ($\sim 1.1 \times 10^9$ M^{-1} cm^{-1}) and the photothermal conversion efficiency (23.7%) of gold nanorods under the same test conditions. Therefore, the photothermal conversion efficiency of the hole-doped semiconductor can be improved by regulating the plasmon resonance absorption. Zhao et al. and Luther et al. have demonstrated that the plasmon resonance absorption of hole-doped copper-based chalcogenides depends on the carrier concentration in the doped semiconductor (Zhao et al., 2009; Luther et al., 2011). Therefore, the plasmon resonance absorption of hole-doped copper-based chalcogenide is different from that of metals. It can control the position and intensity of the plasmon resonance absorption peak not only by changing the morphology and particle size of the semiconductor, but also by changing its structure and composition. For a hole-doped alloy copper-based chalcogenide [such as $Cu_{2-x}S_ySe_{1-y}$, $Cu_{2-x}S_yTe_{1-y}$ ($0 \leq x, y \leq 1$)] compound, the bandgap can be controlled by tuning the ratio of chalcogen (S and Se, Te) (Wang et al., 2011; Liu et al., 2013), and it is also possible to increase the hole density by increasing the Cu defect to achieve the regulation of the position and intensity of local surface plasmon resonance absorption (Dorfs et al., 2011; Garcia et al., 2011; Hsu et al., 2011; Scotognella et al., 2011). Wang et al. have prepared $Cu_{2-x}S_ySe_{1-y}$ compounds by a simple one-step synthesis method and have realized the effective regulation of plasmon resonance absorption by regulating the composition and structure of the compounds (Wang et al., 2011). Many groups have reported hole-doped plasma resonance absorption effect of copper chalcogenides. Recently, it has been reported that the doping of indium can change the particle size, morphology, and crystal phase of $Cu_{2-x}S$ nanocrystals, which in turn affects its plasmon resonance absorption (Wang and Swihart, 2015). In addition, the synthesized copper chalcogenide compounds can still achieve the regulation of plasma absorption by oxidation or reduction (Kriegel et al., 2012). Balitskii et al. have reported an interesting phenomenon: They synthesized oleylamine-coated $Cu_{2-x}Se$ nanocrystals, and then partially exchanged the oleylamine ligand with n-dodecylphosphoric acid (DDPA) or 1-dodecanethiol (DDT) to blue or red shift the plasma absorption of the $Cu_{2-x}Se$ nanocrystals (Balitskii et al., 2014). Therefore, plasma absorption can also be adjusted by changing the surface ligand. In summary, the plasmon resonance absorption of copper chalcogenides can be changed and improved by controlling the doping, morphology, structure, composition, particle size, and surface ligand of the hole-doped copper chalcogenide compounds, thereby improving the photothermal conversion efficiency. However, there are few investigations on the LSPRs of bimetal copper-based chalcogenides.

In this work, we report Cu_5FeS_4 (CFS) nanoparticles as a promising photothermal agent for efficient photothermal therapy of cancers. The plasmon resonance absorption of CFS nanoparticles could be tuned by the increase of the ratio of iron to copper during the reaction leading to the increased defect structure in CFS. The plasma absorption of CFS nanoparticles could also be tuned by exchanging the oleylamine ligand with n-dodecylphosphoric acid (DDPA). The CFS nanoparticles with a plasmon resonance absorption peak at 764 nm can be used as the 808-nm laser-driven photothermal agents for the photothermal therapy of cancers after surface modification by polyethylene glycol (PEG). To the best of our knowledge, this work is the first report on the tunable plasmon resonance of CFS.

MATERIALS AND METHODS

Synthesis of Molecular Precursor

$CuCl_2 \cdot 2H_2O$ and $FeCl_3 \cdot 6H_2O$ were fully dissolved in water, and then a solution of sodium diethyldithiocarbamate (SDEDTC) was added and stirred for 1 h. The brown products were then filtered, washed with water several times, and then dried at room temperature before use.

Synthesis of CFS Nanoparticles

Twenty-five milliliters of oleylamine (Aladdin) was added in a flask, and then heated to 120°C within under the magnetic stirring with a continuous flow of dry argon gas. The solution was then heated to 300°C and kept for 30 min. Subsequently, another 5 ml of oleylamine containing the molecular precursors was injected into the above hot solution. The reaction was kept for 10 min. After cooling to room temperature, the end products were collected via centrifugation and washed with ethanol twice.

DDPA Treatment

Three hundred microliters of the resulting solution containing about 4 mg of CFS nanoparticles was mixed with 4 ml of 0–20 mM DDPA in toluene. The solution was then sonicated for about 15 min.

Surface Modification

Two milligrams of PEG-NH_2 was added in 4 ml of the resulting solution containing about 10 mg of CFS nanoparticles in toluene. The resulting solution was then sonicated for 10 min. Thereafter, 10 ml of deionized water was added in the above solution and sonicated for another 10 min. The products were obtained by centrifugal collection and washed with ethanol twice.

Characterization

TEM (JEOL JEM-2010F, Japan) was used to measure the morphology and size of the CFS nanoparticles. UV-Vis-NIR absorbance spectra of CFS nanoparticles were obtained through a UV-Visible spectrophotometer (UV-1900, Phenix) at room temperature. X-ray photoelectron spectra (XPS, ESCA-Lab 250Xi) were used to test the oxidation state analysis of CFS nanoparticles. XRD (Bruker D4) was used to measure the crystal phase of CFS nanoparticles. ICP-AES (Leeman Laboratories Prodigy) was used to measure the concentration of ions released from CFS nanoparticles.

Photothermal Effect

To measure the photothermal effect of the CFS nanoparticles, CFS nanoparticles with different concentrations dispersed in deionized water were irradiated under an 808-nm laser (0.5 W cm^{-2}) for 5 min. Temperature change of CFS nanoparticles was monitored and recorded by an infrared thermal camera.

Cellular Experiment *in vitro*

K7M2 cells were used as a model to assess the cytotoxicity of the CFS nanoparticles to cancer cells. K7M2 cells were cultured in Roswell Park Memorial Institute (RPMI-1640) and incubated at 37°C in the presence of 5% CO_2. For cytotoxicity evaluation of the CFS nanoparticles *in vitro*, K7M2 cells were seeded in the 96-well-plates at a density of 1×10^4 cells every well. After cultivation for 24 h, the suspension medium was aspirated by pipette and washed with PBS three times. CFS nanoparticles dispersed in RPMI-1640 with different concentrations were added into the wells one by one. After co-culture 24 h, a standard CCK8 evaluation was used to investigate the cell viability of CFS nanoparticles to K7M2 cells. For photothermal therapy effect of K7M2 cells *in vitro* using CFS nanoparticles, K7M2 cells were cultured CFS nanoparticles in RPMI-1640 for 24 h. These cells were then irradiated upon an 808-nm laser at a power density of 0.5 W cm^{-2} for 5 min. After then, the K7M2 cells were stained with both calcein AM and PI and then imaged by a Leica DMi8 fluorescence microscope. All of the tests were measured three times.

Photothermal Therapy *in vivo*

The immunodeficiency nude mice were subcutaneously injected by K7M2 cells (4×10^6 cells for each mouse) into the left thigh to obtain the desired tumor model. K7M2 model mice were then divided randomly into four groups (six mice for each group) when the tumor volumes reached about ∼100 mm^3. PBS solution containing CFS nanoparticles (50 ppm, 100 μl) or PBS solution alone was injected intravenously into the tumor sites of the nude mice. The mice with or without the CFS nanoparticle's injection were then irradiated to an 808-nm laser with a power density at 0.5 W cm^{-2} for 5 min. During the treatment, the temperature changes of tumor surface were monitored and recorded by a NIR thermal medical camera. After the indicated treatments, we recorded the body weight and tumor size of the mice in four groups every 2 days to evaluate the photothermal therapy effect. Relative tumor volumes were calculated as V/V_0, where V_0 was the initial tumor volume before the therapy.

Long-Term Toxicity Analysis

As for the tumors' histological examination analysis, a mouse from the each group was sacrificed under anesthesia after the indicated treatment. Then, the tumors from the sacrificed mice were harvested, sectioned into 4-μm slices, and stained with hematoxylin and eosin (H&E). The slices were examined via a microscope. Mice were sacrificed to collect blood sample for blood biochemistry and complete blood panel analysis after intervals of 3, 6, 9, and 12 days, respectively.

RESULTS AND DISCUSSION

Oleylamine-capped CFS nanoparticles were synthesized by a facile hot injection of a molecular precursor. The molecular precursors were obtained by reacting $CuCl_2{\cdot}2H_2O$ as well as a certain molar ratio of $FeCl_3{\cdot}6H_2O$ with sodium diethyldithiocarbamate (SDEDTC). **Figure 1A** presents the transmission electron microscopy (TEM) image of CFS nanoparticles obtained from the reaction with a ratio of 20% for iron source to copper source. One can see that the as-prepared CFS products showed very good dispersion from the TEM image. The size of CFS nanoparticles was found to be 18.2 nm based on the statistics of 100 nanoparticles from the TEM images (**Figure S1**). **Figure 1B** showed more microstructure information from the high-resolution TEM; an interplanar spacing of 0.194 nm was observed, assigned to (110) planes of bornite structured Cu_5FeS_4. In addition, selected area electron diffraction of the individual CFS nanoparticles from the high-resolution TEM can be indexed to the [110] zone axis of bornite structured Cu_5FeS_4, which indicated the single-crystalline nature of these nanoparticles (**Figure S2**). As shown in **Figure 1C**, all of the main peaks of X-ray XRD pattern of the CFS products can be matched well with those of bornite structured Cu_5FeS_4 (JCPDS file no. 24-0050), showing a high crystallinity for pure CFS. XPS results (**Figure S3**) demonstrated that the obtained products mainly contain Cu, Fe, and S elements. We also analyzed the valency state of Cu and Fe in CFS nanoparticles. In **Figure 1D**, it exhibited the high-resolution Cu 2p spectrum (red line) and Fe 2p spectrum (blue line) for the CFS nanoparticles. The binding energy peaks at 931.8 and 951.7 eV could belong to Cu (I) coordinated to Cu in CFS nanoparticles (Chang et al., 2013). Generally speaking, the existence of Cu(II) in copper-based photothermal agents could contribute to the defect structure, thus resulting in NIR absorption (Li et al., 2015). However, no binding energy peak at around 940 eV was detected, indicating that there was no Cu (II) existing in CFS nanoparticles (Chang et al., 2013). Therefore, no copper defect structure was found in CFS obtained from the reaction with a ratio of 20% for iron source to copper source. In addition, the binding energy peaks at 711.2 and 724.1 eV could be assigned to Fe(III) coordinated to Fe in CFS nanoparticles (Guan et al., 2018). Based on the obtained results, we can conclude that CFS nanoparticles with high purity and crystallinity were achieved.

The optical absorption spectrum of CFS nanoparticles, obtained from the reaction with a ratio of 20% for iron source to copper source, showed a peak around 1,100 nm. The NIR absorption may be attributed to 3d electronic transitions from the valence band to an intermediate band, similar to $CuFeS_2$ nanocrystals (Ghosh et al., 2016) and $CuCo_2S_4$ nanocrystals (Li et al., 2017). The ratio of Cu to Fe was found to be 4.99, confirmed by ICP-AES. Interestingly, the ratio of 4.82, 4.75, 4.71, and 4.67 for Cu to Fe can also be obtained by the addition of precursors with the ratio of 22, 24, 26, and 28% for iron source to copper source, respectively, indicating different copper deficiencies. The high-resolution XPS spectra of Fe 2p and Cu 2p in CFS nanoparticles obtained from the reaction with a ratio of 28% for iron source to copper source are given in **Figure S4**.

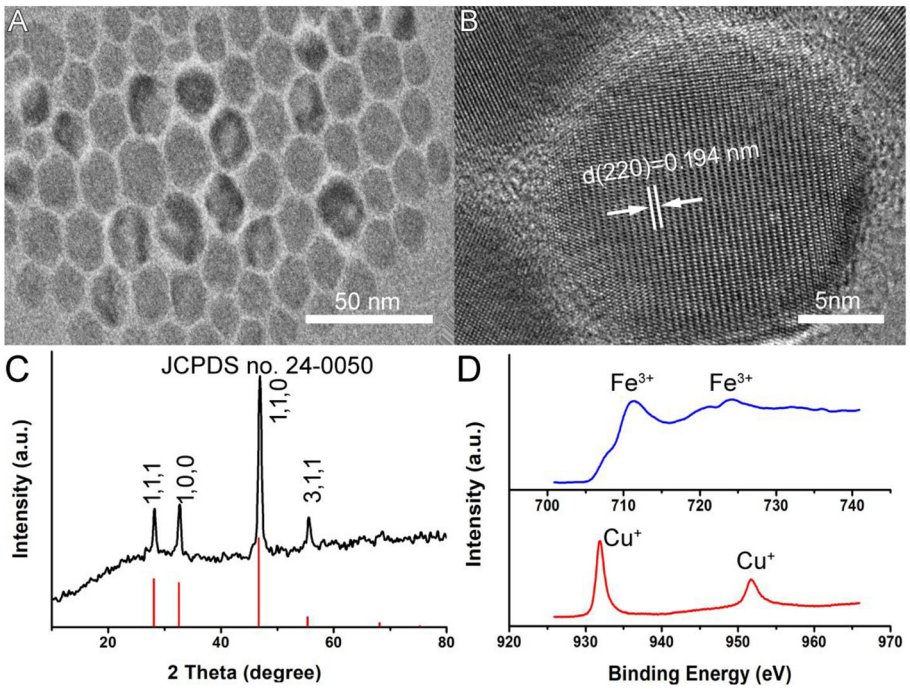

FIGURE 1 | (A) A typical TEM image of CFS nanoparticles. **(B)** The high-resolution TEM image of CFS nanoparticles. **(C)** XRD patterns of CFS nanoparticles. **(D)** The high-resolution XPS spectra of Fe 2p (blue line) and Cu 2p (red line) in CFS nanoparticles.

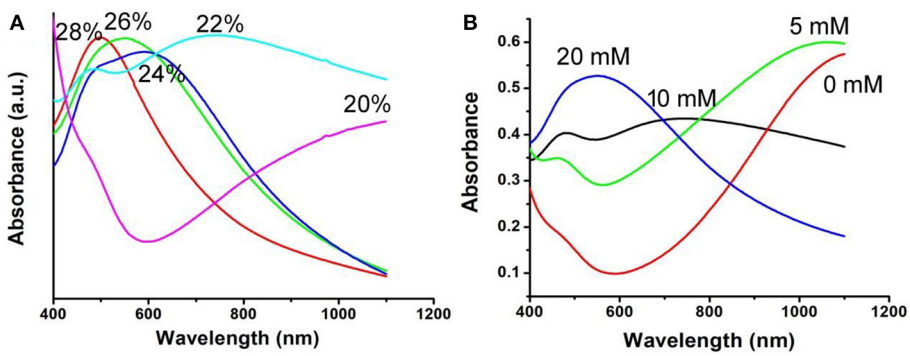

FIGURE 2 | (A) UV-vis-NIR spectra of the CFS nanoparticles obtained from the addition of precursors with different ratios for iron source to copper source. **(B)** UV-vis-NIR spectra of the CFS nanoparticles after the treatment of DDPA.

It was found that the peaks of Cu^{2+} and Fe^{2+} were detected, further indicating the formation of defect structures (Chang et al., 2013; Guan et al., 2018). Previous work has demonstrated that the plasmon resonance absorption peak will shift blue as the copper defects increase (Balitskii et al., 2014). In order to verify it, we measured the optical absorption spectrum of CFS nanoparticles with different ratios of Cu to Fe. As expected, there was a blue shift with the increase of copper deficiencies (**Figure 2A**). It has been revealed that copper deficiency could be achieved by oxidizing copper in the crystal. When the CFS was prepared from the reaction with a ratio of 20% for iron source to copper source, the obtained CFS products were processed with DDPA to achieve CFS with different deficiencies. When treating the CFS nanoparticle solution with DDPA, a blue shift was observed (**Figure 2B**). The blue shift up to 500 nm was achieved when the concentration of DDPA was increased to 20 mM. After the treatment by 20 mM, the CFS nanoparticles showed little change, which can be confirmed from the TEM image and XRD pattern of CFS nanoparticles (**Figure S5**). Therefore, the LSPRs of CFS nanoparticles can be tuned by the addition of precursors with different ratios for iron source to copper source and the treatment of DDPA, respectively.

In general, both 980-nm light and 808-nm light have been used as laser sources for the photo-responsive imaging and treatments of tumors due to their security and deep tissue penetration (Smith et al., 2009). However, as the main constituent

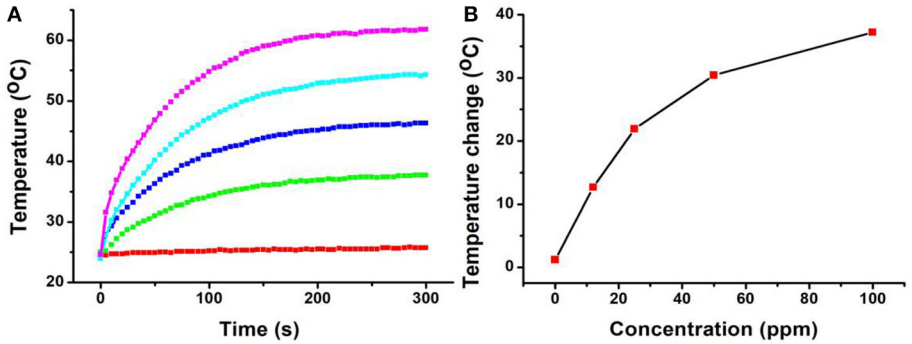

FIGURE 3 | (A) The temperature changes of the CFS nanoparticles dispersed in water with different concentrations of Cu^{2+} (0–100 ppm) vs. the irradiation time of the 808-nm laser. **(B)** Relationship curves of temperature change as a function of the concentration of CFS nanoparticles.

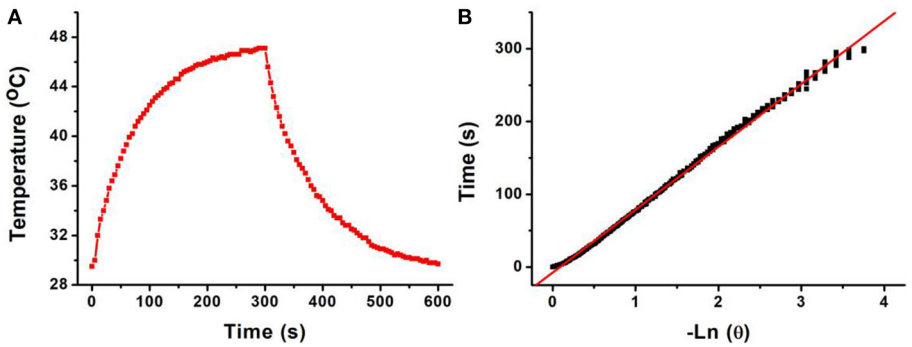

FIGURE 4 | (A) Photothermal effect of CFS nanoparticles under the irradiation of an 808-nm laser for 300 s; then, the laser was shut off and the temperature was recorded for another 300 s. **(B)** Time constant of CFS NCs from the system. $\tau_s = 73.2$ s.

of living organisms, the absorption intensity of the water at 980 nm is confirmed to be 30 times higher than that at 808 nm (Li et al., 2014b). It has been proved that a 980-nm laser irradiation at a power intensity of 0.72 W/cm^2 can make the temperature of the pure water increase by 15.1°C, while only 3.0°C for an 808-nm laser in the same conditions (Li et al., 2014b). This means that the 808-nm laser exhibits deeper tissue penetration and less photo-damage to the surrounding healthy tissues compared to the 980-nm laser (Wu and Butt, 2016). In our experiments, The CFS nanoparticles, obtained from the reaction with a ratio of 22% for iron source to copper source, showed a plasmon resonance absorption peak at 764 nm, which is close to 808 nm. Therefore, an 808-nm laser was used as the excitation source for photothermal therapy. Photothermal agents should be hydrophilic before realizing their biological application; thus, a ligand exchange process was performed to modify the CFS nanoparticles' surface property using PEG. We then measured the photothermal effect of PEG-coated CFS nanoparticles. As shown in **Figure 3**, CFS nanoparticles exhibited a concentration-dependent photothermal effect. As a control, the pure water showed almost no temperature raise under the exposure of an 808-nm laser (0.5 W cm^{-2}). However, with the increase of the concentration of CFS nanoparticles (i.e., 12, 25, 50, and 100 ppm), the temperature was increased by 12.7–37.2°C, indicating that CFS nanoparticles can efficiently convert NIR light energy to heat energy.

The 808-nm laser-driven photothermal conversion efficiency of the CFS nanoparticles was also measured and calculated by Roper et al.'s reported method (Roper et al., 2007). The CFS nanoparticles with a concentration of 50 ppm were exposed to the 808-nm laser (0.192 W) for 300 s. The laser was shut off when the temperature of the system reached a steady state (**Figure 4A**). Cooling time constant was measured to confirm system's rate of heat transfer (**Figure 4B**). Then, the photothermal conversion efficiency (η_T) of CFS nanoparticles could be calculated by the following:

$$\eta_T = \frac{Q_1 - Q_0}{I(1 - 10^{A_\lambda})} \tag{1}$$

In which Q_1 and Q_0 are the rate of heat input (in units of mW) of the solvent with and without CFS nanoparticles. I is the laser power (in units of mW, 192 mW). A_λ is the absorbance (0.8345) at irradiation wavelength (808 nm). The value of Q_1 and Q_0 are derived according to:

$$Q = hA(T_{\max} - T_{amb}) \tag{2}$$

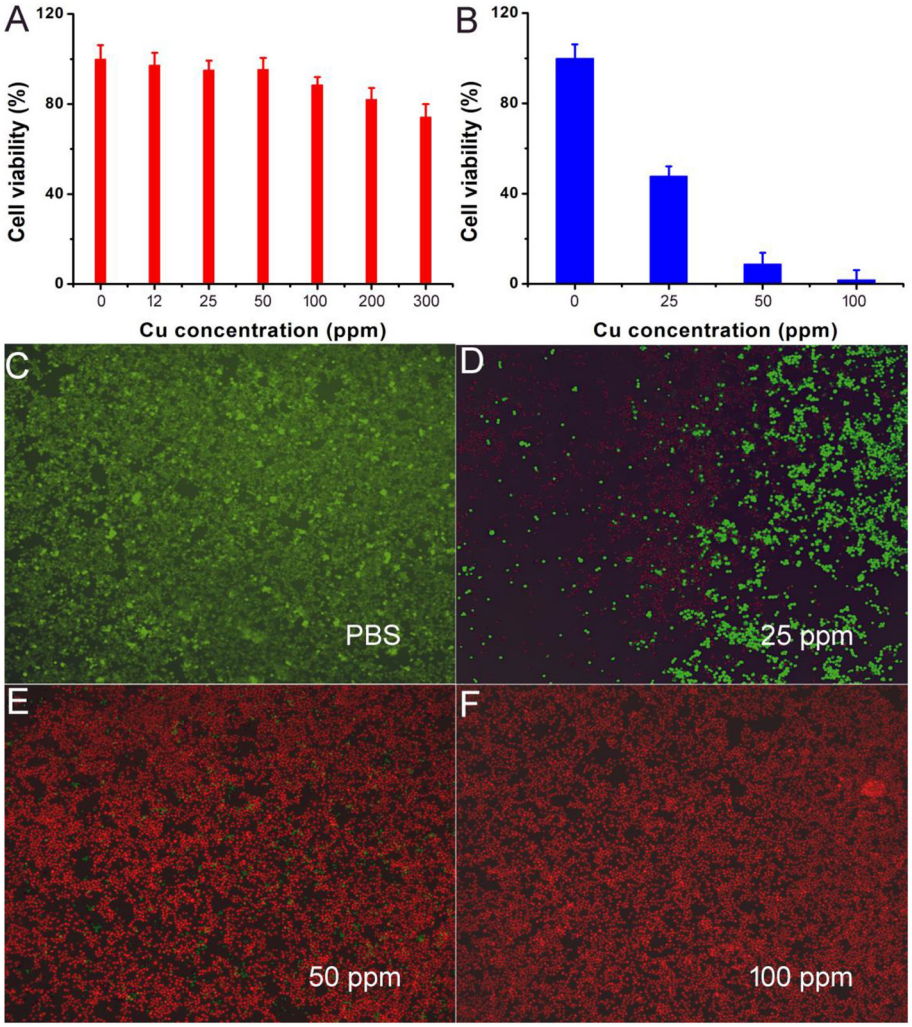

FIGURE 5 | (A) Cell viability incubated with different concentrations of CFS nanoparticles. **(B)** Cell viability after the indicated photothermal treatments. **(C–F)** Live/dead cell staining analysis after photothermal therapy with CFS nanoparticles at different concentrations. Magnification: 100 times.

h is the heat transfer coefficient, and A is the container's surface area. T_{amb} is the ambient surrounding temperature, T_{max} is the maximum temperature of the system, and (T_{max} – T_{amb}) was 17.6°C obtained from **Figure 4A**. The Q_0 was independently measured with a quartz cuvette cell containing pure water and calculated to be 18.7 mW. The value of hA can be calculated from:

$$hA = \frac{m_D c_D}{\tau_s} \tag{3}$$

where m_D and c_D are the mass (0.1 g) and heat capacity (4.2 J g^{-1}) of pure water, which was used as solvent, respectively. τ_s is the sample system time constant. According to the achieved data, the 808-nm laser-driven photothermal conversion efficiency (η_T) of the CFS nanoparticles was calculated to be 50.5%, indicating the promising potential for photothermal therapy of cancers. To evaluate the NIR photostability of the CFS nanoparticles, the aqueous dispersion (50 ppm) was irradiated with 808-nm laser (1.0 W cm^{-2}) for 10 min (LASER ON, **Figure S6**), respectively, followed by naturally cooling to room temperature for 30 min (without irradiation, LASER OFF). It was shown that there was little loss of the maximum temperature elevation after four cycles of LASER ON/OFF. The result indicated that the CFS nanoparticles showed good NIR photostability.

Motivated by the excellent photothermal performance of CFS nanoparticles, we evaluated the potential of these nanoparticles as photothermal agents. Before realization of their biological application, the cytotoxicity of CFS nanoparticles was evaluated by a standard CCK-8 assay method with K7M2 cells (**Figure 5A**). It can be seen that these CFS nanoparticles appeared to be very low toxicity. With a concentration up to 200 ppm, the cell viability can still be up 80%. The *in vitro* photothermal therapy to K7M2 cells using CFS nanoparticles was then studied. After the treatment with varied concentration of CFS nanoparticles, a standard CCK-8 evaluation was used to test the cell viability (**Figure 5B**). The cell mortality rate increased with the increase of the concentration. The cell mortality rate

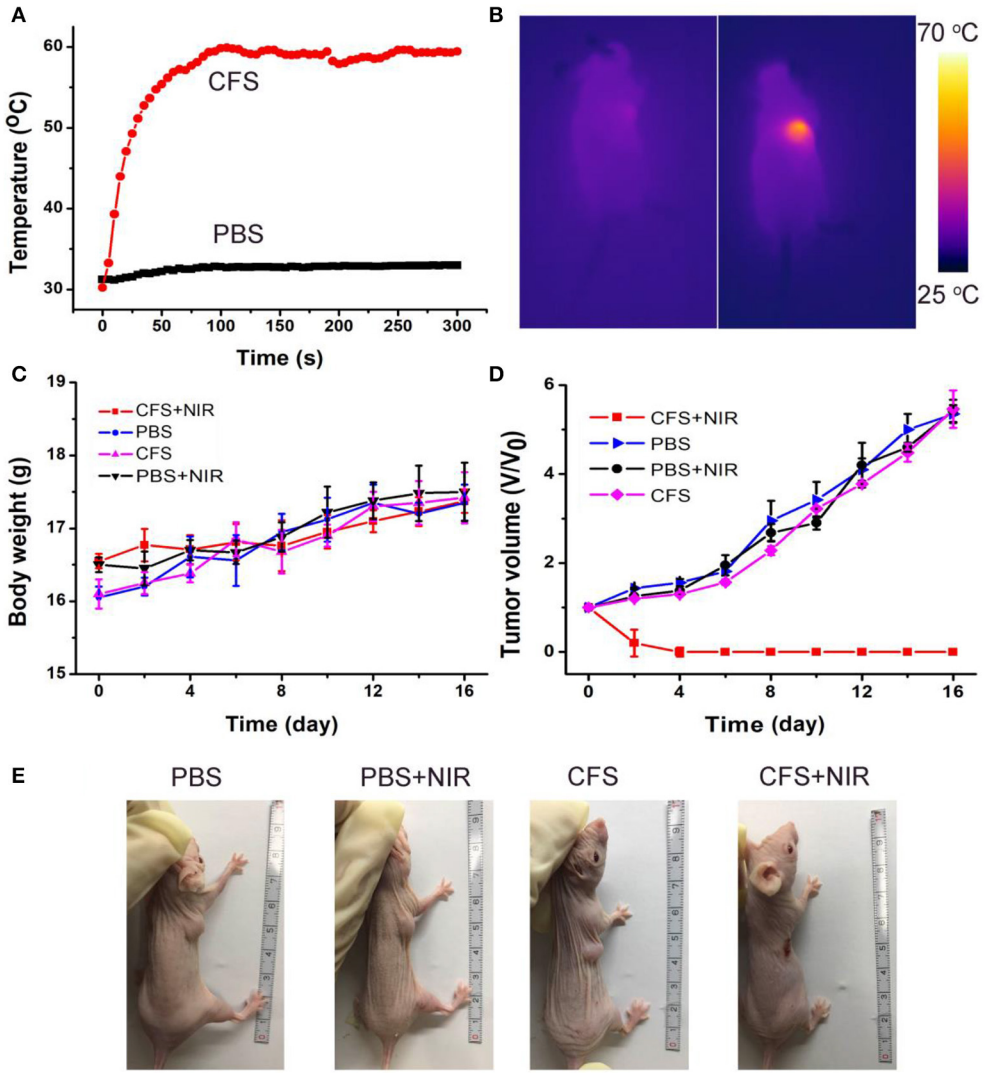

FIGURE 6 | (A) Temperature curves of tumors as a function of irradiation time of an 808-nm laser. **(B)** The infrared thermal images of the tumor-bearing mice intravenously injected with the PBS (the left mouse) or CFS nanoparticles (the right mouse), respectively. **(C)** Body weight curves over time in the four groups after indicated treatments. **(D)** Growth curves of tumors over time in the four groups after indicated treatments. **(E)** Photographs of mice in the four groups after the indicated photothermal treatments for 14 days.

of the treatment combined CFS nanoparticles (50 ppm) and the irradiation of an 808-nm laser was ∼92%, demonstrating an excellent photothermal effect *in vitro*. When the concentration of nanoparticles was increased to 100 ppm, the cell death rate was increased by 7%. Thus, the optimized concentration should be 50 ppm. In addition, to visualize the *in vitro* photothermal therapy effect of CFS nanoparticles, K7M2 cells after the showing treatments were co-stained with calcein-AM and propidium iodide. The results (**Figures 5C–F**) were consistent with the result of the CCK-8 assay, demonstrating the efficient photothermal effect *in vitro*.

The photothermal therapy effect of cancers *in vivo* was evaluated. The tumor-bearing mice were divided randomly into four groups: (a) CFS nanoparticle injection + 808-nm laser irradiation (CFS+NIR); (b) PBS + 808-nm laser irradiation (PBS+NIR); (c) PBS injection (PBS); and (d) CFS nanoparticle (CFS). The temperatures of tumor surface injected with CFS nanoparticles could dramatically increase from ∼30 to ∼59°C, resulting from the photothermal effect of CFS nanoparticles (**Figure 6A**). As a control, the temperatures of tumor surface injected with PBS solution only increased by less than 3°C. During the treatment, a medical thermal camera was used to monitor and record the temperature change of tumor sites. As expected, infrared thermal images with a high contrast were achieved (**Figure 6B**), indicating that CFS nanoparticles still showed excellent photothermal effect *in vivo*.

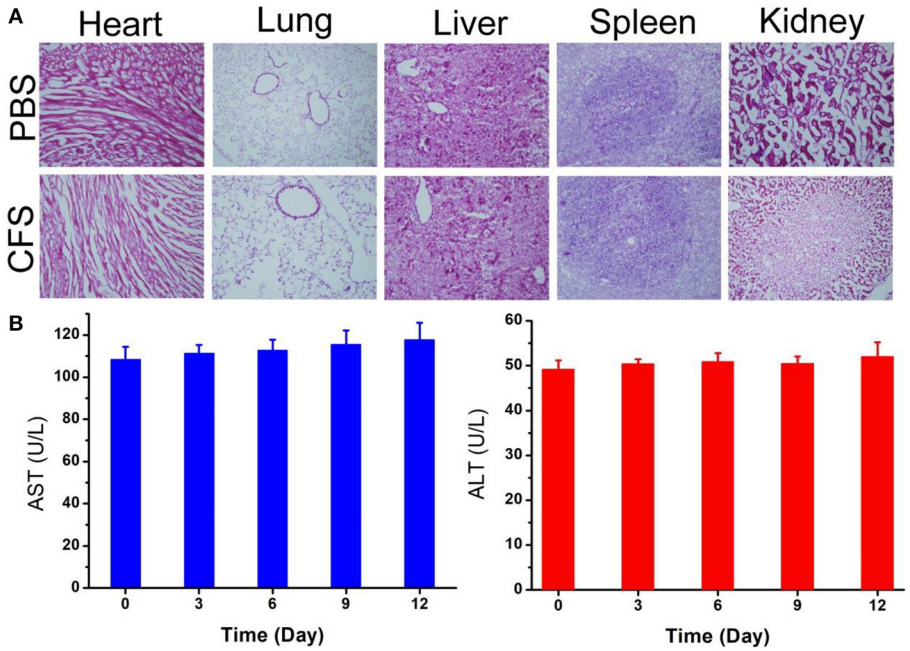

FIGURE 7 | (A) H&E-stained slices of main organs. Magnification: 100 times. **(B)** Blood biochemistry of mice receiving intravenous injection of CFS at different time points. The examined parameters include aspartate aminotransferase (AST, left) and alanine aminotransferase (ALT, right).

After the indicated treatment, the body weights and tumor sizes from each group were recorded every 2 days. We can see that there was almost no difference in body weight among the four groups of mice (**Figure 6C**), indicating the low toxicity of CFS at the given conditions. In addition, tumors of mice in group (a) disappeared and there was no reoccurrence observed (**Figures 6D,E**), while the tumors gradually increased and showed no difference in the three control groups. H&E staining analysis was also analyzed immediately after treatment to evaluate the photothermal therapy effect after the CFS/NIR laser treatment. The tumor cells in the three control groups showed very little change in morphology and size, while those in the experimental group (CFS+NIR) showed obvious necrosis, such as nuclear condensation, shrinkage of the malignant cells, lysis, and fragmentation (**Figure S7**). Therefore, CFS nanoparticles showed great potential for photothermal therapy of cancers.

As *in vivo* biosafety of nanomedicines is always of great concern for application in photothermal therapy, further biosafety experiment on histological examination analysis with H&E staining for the main organs was conducted to observe the size, shape, and number of cells after the intravenous injection of CFS nanoparticles (10 mg/kg). From the HE staining of the major organs, including heart, kidney, spleen, liver, and lung, no inflammation or damage is observed (**Figure 7A**). The parameters related to the serum biochemistry (**Figure 7B**) showed no meaningful changes. The evidence further confirmed that the CFS nanoparticles have promising potential for photothermal therapy. However, deep systematic studies of pharmacokinetics and pharmacodynamics are still pretty important for future clinical application of such a material. This kind of material may also have other specific potential, such as magnetic resonance imaging, that can further transform the platform for multiple use to promote its clinical translation.

CONCLUSION

In conclusion, hydrophilic Cu_5FeS_4 nanoparticles with a plasmon resonance absorption peak at 764 nm that served as an efficient photothermal agent have been successfully prepared by a facile thermal decomposition route and, subsequently, a surface modification process. The plasmon resonance absorption of Cu_5FeS_4 nanoparticles could be tuned by the decrease of the ratio of copper to iron and the treatment of DDPA leading to the formation of defect structures. Moreover, CFS nanoparticles showed excellent biocompatibility, demonstrated by the *in vitro* and *in vivo* toxicity results. With the exposure of the NIR light, the Cu_5FeS_4 nanoparticles can be used for efficient photothermal therapy of cancers.

DATA AVAILABILITY STATEMENT

All datasets generated for this study are included in the article/**Supplementary Material**.

ETHICS STATEMENT

This study was carried out in accordance with the principles of the Basel Declaration and recommendations of the Institutional

Animal Care and Use Committee of the Affiliated Hospital of Xuzhou Medical University. The protocol was approved by the Affiliated Hospital of Xuzhou Medical University.

AUTHOR CONTRIBUTIONS

LY and QW designed the project. LY, WH, and HZ carried out the experiment and performed the experimental data analysis. LY, LC, and JW wrote the paper. All authors contributed to discussion of the results.

FUNDING

This work was financially supported by six top talent projects in Jiangsu Province (YY-156).

SUPPLEMENTARY MATERIAL

The Supplementary Material for this article can be found online at: https://www.frontiersin.org/articles/10.3389/fbioe.2020.00021/full#supplementary-material

REFERENCES

Balitskii, O. A., Sytnyk, M., Stangl, J., Primetzhofer, D., Groiss, H., and Heiss, W. (2014). Tuning the localized surface plasmon resonance in Cu(2-x)Se nanocrystals by postsynthetic ligand exchange. *ACS Appl. Mater. Interfaces* 6, 17770–17775. doi: 10.1021/am504296y

Buonsanti, R., Llordes, A., Aloni, S., Helms, B. A., and Milliron, D. J. (2011). Tunable infrared absorption and visible transparency of colloidal aluminum-doped zinc oxide nanocrystals. *Nano Lett.* 11, 4706–4710. doi: 10.1021/nl203030f

Chang, J. Y., Lin, J. M., Su, L. F., and Chang, C. F. (2013). Improved performance of $CuInS_2$ quantum dot-sensitized solar cells based on a multilayered architecture. *ACS Appl. Mater. Interfaces* 5, 8740–8752. doi: 10.1021/am402547e

Dorfs, D., Hartling, T., Miszta, K., Bigall, N. C., Kim, M. R., Genovese, A., et al. (2011). Reversible tunability of the near-infrared valence band plasmon resonance in $Cu_{2-x}Se$ nanocrystals. *J. Am. Chem. Soc.* 133, 11175–11180. doi: 10.1021/ja2016284

Garcia, G., Buonsanti, R., Runnerstrom, E. L., Mendelsberg, R. J., Llordes, A., Anders, A., et al. (2011). Dynamically modulating the surface plasmon resonance of doped semiconductor nanocrystals. *Nano Lett.* 11, 4415–4420. doi: 10.1021/nl202597n

Ghosh, S., Avellini, T., Petrelli, A., Kriegel, I., Gaspari, R., Almeida, G., et al. (2016). Colloidal $CuFeS_2$ nanocrystals: intermediate fe d-band leads to high photothermal conversion efficiency. *Chem. Mater.* 28, 4848–4858. doi: 10.1021/acs.chemmater.6b02192

Guan, G., Wang, X., Li, B., Zhang, W., Cui, Z., Lu, X., et al. (2018). "Transformed" Fe3S4 tetragonal nanosheets: a high-efficiency and body-clearable agent for magnetic resonance imaging guided photothermal and chemodynamic synergistic therapy. *Nanoscale* 10, 17902–17911. doi: 10.1039/c8nr06507a

Hessel, C. M., Pattani, V. P., Rasch, M., Panthani, M. G., Koo, B., Tunnell, J. W., et al. (2011). Copper selenide nanocrystals for photothermal therapy. *Nano Lett.* 11, 2560–2566. doi: 10.1021/nl201400z

Hsu, S. W., On, K., and Tao, A. R. (2011). Localized surface plasmon resonances of anisotropic semiconductor nanocrystals. *J. Am. Chem. Soc.* 133, 19072–19075. doi: 10.1021/ja2089876

Huang, X., Tang, S., Liu, B., Ren, B., and Zheng, N. (2011a). Enhancing the photothermal stability of plasmonic metal nanoplates by a core-shell architecture. *Adv. Mater. Weinheim.* 23, 3420–3425. doi: 10.1002/adma.201100905

Huang, X., Tang, S., Mu, X., Dai, Y., Chen, G., Zhou, Z., et al. (2011b). Freestanding palladium nanosheets with plasmonic and catalytic properties. *Nat. Nanotechnol.* 6, 28–32. doi: 10.1038/nnano.2010.235

Kanehara, M., Koike, H., Yoshinaga, T., and Teranishi, T. (2009). Indium tin oxide nanoparticles with compositionally tunable surface plasmon resonance frequencies in the near-IR region. *J. Am. Chem. Soc.* 131, 17736–17737. doi: 10.1021/ja9064415

Kriegel, I., Jiang, C., Rodríguez-Fernández, J., Schaller, R. D., Talapin, D. V., da Como, E., et al. (2012). Tuning the excitonic and plasmonic properties of copper chalcogenide nanocrystals. *J. Am. Chem. Soc.* 134, 1583–1590. doi: 10.1021/ja207798q

Li, B., Wang, Q., Zou, R., Liu, X., Xu, K., Li, W., et al. (2014a). $Cu_{7.2}S_4$ nanocrystals: a novel photothermal agent with a 56.7% photothermal conversion efficiency for photothermal therapy of cancer cells. *Nanoscale* 6, 3274–3282. doi: 10.1039/c3nr06242b

Li, B., Ye, K., Zhang, Y., Qin, J., Zou, R., Xu, K., et al. (2015). Photothermal theragnosis synergistic therapy based on bimetal sulphide nanocrystals rather than nanocomposites. *Adv. Mater. Weinheim.* 27, 1339–1345. doi: 10.1002/adma.201404257

Li, B., Yuan, F., He, G., Han, X., Wang, X., Qin, J., et al. (2017). Ultrasmall $CuCo_2S_4$ nanocrystals: all-in-one theragnosis nanoplatform with magnetic resonance/near-infrared imaging for efficiently photothermal therapy of tumors. *Adv. Funct. Mater.* 27:1606218. doi: 10.1002/adfm.201606218

Li, B., Zhang, Y., Zou, R., Wang, Q., Zhang, B., An, L., et al. (2014b). Self-assembled WO_{3-x} hierarchical nanostructures for photothermal therapy with a 915 nm laser rather than the common 980 nm laser. *Dalton Trans.* 43, 6244–6250. doi: 10.1039/c3dt53396d

Liu, X., Wang, X., and Swihart, M. T. (2013). $Cu_{2-x}S_{1-y}Se_y$ alloy nanocrystals with broadly tunable near-infrared localized surface plasmon resonance. *Chem. Mater.* 25, 4402–4408. doi: 10.1021/cm402848k

Luther, J. M., Jain, P. K., Ewers, T., and Alivisatos, A. P. (2011). Localized surface plasmon resonances arising from free carriers in doped quantum dots. *Nat. Mater.* 10, 361–366. doi: 10.1038/nmat3004

Manthiram, K., and Alivisatos, A. P. (2012). Tunable localized surface plasmon resonances in tungsten oxide nanocrystals. *J. Am. Chem. Soc.* 134, 3995–3998. doi: 10.1021/ja211363w

Roper, D. K., Ahn, W., and Hoepfner, M. (2007). Microscale heat transfer transduced by surface plasmon resonant gold nanoparticles. *J. Phys. Chem. C* 111, 3636–3641. doi: 10.1021/jp064341w

Scotognella, F., Della Valle, G., Srimath Kandada, A. R., Dorfs, D., Zavelani-Rossi, M., Conforti, M., et al. (2011). Plasmon dynamics in colloidal Cu2-xSe nanocrystals. *Nano Lett.* 11, 4711–4717. doi: 10.1021/nl202390s

Smith, A. M., Mancini, M. C., and Nie, S. M. (2009). Bioimaging second window for *in vivo* imaging. *Nat Nanotech* 4, 710–711. doi: 10.1038/nnano.2009.326

Tang, H., Shen, S., Guo, J., Chang, B., Jiang, X., and Yang, W. (2012). Gold nanorods@$mSiO_2$ with a smart polymer shell responsive to heat/near-infrared light for chemo-photothermal therapy. *J. Mater. Chem.* 22:16095. doi: 10.1039/c2jm32599c

Tian, Q., Hu, J., Zhu, Y., Zou, R., Chen, Z., Yang, S., et al. (2013). Sub-10 nm Fe_3O_4@$Cu_{2-x}S$ core-shell nanoparticles for dual-modal imaging and photothermal therapy. *J. Am. Chem. Soc.* 135, 8571–8577. doi: 10.1021/ja4013497

Tian, Q., Jiang, F., Zou, R., Liu, Q., Chen, Z., Zhu, M., et al. (2011). Hydrophilic Cu_9S_5 nanocrystals: a photothermal agent with a 25.7% heat conversion efficiency for photothermal ablation of cancer cells *in vivo*. *ACS Nano* 5, 9761–9771. doi: 10.1021/nn203293t

Wang, J. J., Xue, D. J., Guo, Y. G., Hu, J. S., and Wan, L. J. (2011). Bandgap engineering of monodispersed $Cu_{2-x}S_ySe_{1-y}$ nanocrystals through chalcogen ratio and crystal structure. *J. Am. Chem. Soc.* 133, 18558–18561. doi: 10.1021/ja208043g

Wang, X., and Swihart, M. T. (2015). Controlling the size, shape, phase, band gap, and localized surface plasmon resonance of $Cu_{2-x}S$ and Cu_xIn_yS nanocrystals. *Chem. Mater.* 27, 1786–1791. doi: 10.1021/cm504626u

Wu, S., and Butt, H. J. (2016). Near-infrared-sensitive materials based on upconverting nanoparticles. *Adv. Mater. Weinheim.* 28, 1208–1226. doi: 10.1002/adma.201502843

Yang, C., Ma, L., Zou, X., Xiang, G., and Chen, W. (2013). Surface plasmon-enhanced Ag/CuS nanocomposites for cancer treatment. *Cancer Nanotechnol.* 4, 81–89. doi: 10.1007/s12645-013-0039-2

Yavuz, M. S., Cheng, Y., Chen, J., Cobley, C. M., Zhang, Q., Rycenga, M., et al. (2009). Gold nanocages covered by smart polymers for controlled release with near-infrared light. *Nat. Mater.* 8, 935–939. doi: 10.1038/nmat2564

Zhao, Y., Pan, H., Lou, Y., Qiu, X., Zhu, J., and Burda, C. (2009). Plasmonic Cu(2-x)S nanocrystals: optical and structural properties of copper-deficient copper(I) sulfides. *J. Am. Chem. Soc.* 131, 4253–4261. doi: 10.1021/ja805655b

Conflict of Interest: The authors declare that the research was conducted in the absence of any commercial or financial relationships that could be construed as a potential conflict of interest.

frontiers in Bioengineering and Biotechnology

ORIGINAL RESEARCH
published: 17 March 2020
doi: 10.3389/fbioe.2020.00170

Efficient Delivery of Triptolide Plus a miR-30-5p Inhibitor Through the Use of Near Infrared Laser Responsive or CADY Modified MSNs for Efficacy in Rheumatoid Arthritis Therapeutics

Xiaonan Zhang[1], Xin Zhang[2], Xipeng Wang[1], Tao Wang[1], Bin Bai[1], Na Zhang[1], Yanjiao Zhao[1], Yang Yu[1] and Bing Wang[1]**

[1] Institute of Biochemistry and Molecular Biology, College of Life and Health Sciences, Northeastern University, Shenyang, China, [2] Department of Rheumatology and Immunology, China-Japan Union Hospital of Jilin University, Changchun, China

OPEN ACCESS

Edited by:
Bo Li,
Shanghai Jiao Tong University, China

Reviewed by:
Kaibing Xu,
Donghua University, China
Haijun Wu,
University of Science and Technology of China, China

***Correspondence:**
Yang Yu
yuyang2013@mail.neu.edu.cn
Bing Wang
wangbing@mail.neu.edu.cn

Specialty section:
This article was submitted to Biomaterials, a section of the journal Frontiers in Bioengineering and Biotechnology

Received: 11 January 2020
Accepted: 19 February 2020
Published: 17 March 2020

Citation:
Zhang X, Zhang X, Wang X, Wang T, Bai B, Zhang N, Zhao Y, Yu Y and Wang B (2020) Efficient Delivery of Triptolide Plus a miR-30-5p Inhibitor Through the Use of Near Infrared Laser Responsive or CADY Modified MSNs for Efficacy in Rheumatoid Arthritis Therapeutics. Front. Bioeng. Biotechnol. 8:170. doi: 10.3389/fbioe.2020.00170

Rheumatoid arthritis (RA) is a chronic autoimmune inflammatory disease for which treatment focuses on suppressing an overactive immune system and maintaining the physiological balance of synovial fibroblasts (SFs). We found that miR-30-5p was highly expressed in rheumatoid arthritis synovial fibroblasts (RASFs). Subsequently, we predicted that phosphatidylinositol 3-kinase regulatory subunit 2 (PIK3R2) might be a putative target of miR-30-5p. Recent studies have reported that PIK3R2 can maintain the physiological homeostasis of RASFs. Therefore, miR-30-5p inhibitor has the potential to be used in the treatment of RA, but low levels of miR-30-5p inhibitor internalization affect its application. Triptolide (TP) is an effective drug in the treatment of RA but induces severe toxicity and has a narrow therapeutic window. In this study, the cell internalization performance of miR-30-5p inhibitor was improved by loading it into cell membrane penetrating peptide (CADY)-modified mesoporous silica nanoparticles (MSNs), and the toxicity of TP was decreased by loading it into a controlled drug release system based on MSNs. The nanodrug carrier was constructed by filling a phase-change material (PCM) of 1-tetradecanol and drugs into MSNs that could be triggered by an NIR laser with thermo-chemo combination RA therapy. Our results show that the miR-30-5p inhibitor-loaded MSNs@CADY significantly inhibited RASF proliferation and increased apoptosis. In addition, MSNs@PCM@TP under 808 nm laser irradiation were effective in downregulating immune system activation in an RA rat model. Finally, the results of a pharmacodynamics study showed that the combination of MSNs@CADY@miR-30-5p inhibitor and MSNs@PCM@TP under 808 nm laser significantly increased the effectiveness of RA treatment. These findings provide a novel understanding of RA pathogenesis and a theoretical basis for RA treatment.

Keywords: rheumatoid arthritis, triptolide, miR-30-5p, NIR laser-responsive, mesoporous silica nanoparticles

INTRODUCTION

Rheumatoid arthritis (RA) is a complex autoimmune disorder with two main characteristics: hyperactivity of the immune system and abnormal proliferation of synovial fibroblasts (SFs) (Zwerina et al., 2005; Onozaki, 2009; Mullen and Saag, 2015; Collison, 2016). Current treatment for RA mainly focuses on maintaining the physiological homeostasis of synovial cells and suppressing the activity of the immune system. It is believed that damage to articular cartilage and bone tissue in RA is mainly caused by the activation and proliferation of synovial cells. The activation and proliferation of synoviocytes are closely related to apoptosis. The PI3K/AKT signaling pathway activity is prominent in SFs, and its abnormal activation can create an imbalance between SF proliferation and apoptosis (Qu et al., 2019).

PIK3R2 is a negative regulator of the PI3K/AKT signaling pathway. In 2016, Zhao et al. reported that miR-126 targeting of PIK3R2 promotes the proliferation of rheumatoid arthritis synovial fibroblasts (RASFs) and resistance to apoptosis by regulating PI3K/AKT (Gao et al., 2016). Downregulation of miR-126 may indirectly inhibit the PI3K/AKT signaling pathway by targeting PIK3R2, disrupting the balance between RASF survival and death. It has been suggested that PIK3R2, which maintains the physiological homeostasis of SFs (Gao et al., 2016), may be a potential target for the treatment of RA.

Many Chinese herbal medicines, such as Tripterygium Wilfordii Hook F (TWHF), which is the most prominent, have been reported to be effective in treating RA (Fan et al., 2018). Triptolide (TP), an epoxy diterpenoid lactone compound, is considered an important anti-inflammatory and immune inhibitory component of TWHF. The anti-arthritis activity of TP has also been reported (Kong et al., 2013; Li et al., 2014; Fan et al., 2016). Many clinical trials have also confirmed that TP has a good anti-inflammatory effect, especially in RA. Unfortunately, the hepatotoxic, nephrotoxic, and hematological toxic effects of TP limit its clinical applicability (Xue et al., 2011; Zhang et al., 2012).

Mesoporous silica nanoparticles (MSNs) have been widely used as pharmaceutical carriers, and the surface of MSNs can be easily modified by polypeptides or other functional groups. For example, cell penetrating peptides such as CADY have been widely used to modify MSNs to facilitate the effective entry of drug carriers into cells (Cai et al., 2017; Dowaidar et al., 2017). The porous structure of MSNs enhances their release performance and their drug load capacity, the effect of which prevents the side effects caused by locally high drug concentrations administered in a short time, which can be problematic when drugs are administered alone (Jeong et al., 2015).

Drug release can be controlled by using photothermal materials, such as near infrared response photothermal controlled-release drug carriers by irradiating the material with near infrared laser, and the side effects of the loaded drug can be reduced. Indocyanine green (ICG) is a drug approved by Food and Drug Administration (FDA) and widely used in clinical liver and kidney function evaluation with relatively high safety (Saxena et al., 2004; Manchanda et al., 2010). ICG has been used as a photothermal material in RA treatment (Tang et al., 2017). Phase-change materials (PCMs) are a kind of material with great latent heat hat and can change between solid and liquid at a relatively constant temperature (Choi et al., 2010). In this study, 1-tetradecanol was selected as the photothermal response phase change material. The melting point of tetradecanol is 38–39°C (Moon et al., 2011). Moreover, the material has good biocompatibility and low oral toxicity.

The drug TP was blended with ICG, which exerts photothermal effects into tetradecanol, and the tetradecanol blends were loaded into the channels and internal cavities of MSNs at a temperature higher than that of tetradecanol to form a laser responsive drug controlled-release system. Because tetradecanol (hereinafter referred to as PCM) is solid at normal temperature, the adriamycin and ICG loaded into the system are "solidified" in tetradecanol, and thus, the controlled-release system is characterized by of "zero drug release" during the delivery process. When the system is irradiated by near-infrared laser (808 nm), the indocyanine green in the system will produce heat and melt the tetradecanol, thus releasing TP and finally fulfilling the purpose of photothermal controlled-release of drugs.

Here, miR-30-5p was identified to be overexpressed in 80% (32 of 40) of the clinical RA tissues examined and verified that the miR-30-5p inhibitor was a potent reagent that relieved RA through PIK3R2 pathways. Furthermore, we combined a miR-30-5p inhibitor with TP, a traditional drug for treatment of RA, and delivered a miR-30-5p inhibitor with a CADY-modified MSNs to deliver TP with near infrared response photothermal controlled-release MSNs. We ultimately obtained an outstanding result: the combination of the MSNs@CADY@miR-30-5p inhibitor and MSNs@PCM@TP under 808 nm laser significantly reduced the symptoms of RA in the joints of rats. These findings provide a novel understanding of RA pathogenesis and a theoretical basis for RA treatment.

MATERIALS AND METHODS

Ethics Statement

The patients included in the present study provided written informed consent. The study was approved by the Ethical Board of China-Japan Union Hospital of Jilin University.

Sample Preparation and Cell Culture

Forty consecutively RA patients (28 females and 12 males; aged 29–59 years) treated at the Immuno-Rheumatology Clinic from January 1 to December 31, 2018, and 15 volunteers were joined the study. The inclusion criteria were as follows: patient participation was approved by the Hospital Human Ethics Committee, and each participant signed an informed written consent; all patients with RA fulfilled the criteria of the American College of Rheumatology (Altman et al., 1986; Arnett et al., 1988); the average time of clinical treatment was 7.45 $\pm$ 3.26 days; according to the Larsen classification

system (Larsen et al., 1977), weight-bearing anteroposterior and lateral X-ray photos of the affected knee were taken, the patients we selected were all candidates for early synovectomy, and all radiographs were evaluated by the same experienced orthopedists; no contraindication to anesthesia or surgery; and no other major diseases. All volunteers were patients with joint injury who were admitted to China–Japan Union Hospital of Jilin University for joint repair, aged 34–48 years (mean age of 39.9 years). Exclusion criteria were patients who had ever been treated with disease-modifying antirheumatic drug trerapy, absence of joint swelling and limited range of motion, or above Larsen stage II in the operated knee joint.

Rheumatoid arthritis synovial fibroblasts were obtained during arthroplasty or synovectomy from forty patients with RA following the method described below. The synovial tissue specimens were washed five times with Hank's buffer (pH 7.5) 5 min and then minced and placed in a 10 cm^2 culture flask with 4 ml of DMEM (Gibco BR) and 120 μl of type II collagenase, and then incubated at 37°C for 6 h. Then, 3 ml of trypsin without EDTA was used to detach the cells from the flask for subsequent screening. Cultured RASFs from passages 4–10 were used for experiments in this study.

The human fibroblast-like synoviocyte cell line (HFLS) was obtained from Cell Applications, Inc. (San Diego, CA, United States). A human renal epithelial cell line (293 cells) and a human hepatocyte cell line (HL-7702 cells) were purchased from Feng Hui Biotechnology, Co., Ltd. The cells were cultured in DMEM (HyClone, Thermo Fisher) supplemented with 10% FBS (HyClone, Thermo Fisher), 1% penicillin streptomycin (1000 U/ml) (Gibco, Invitrogen). All cell lines were cultured in a cell incubator at 37°C under 5% CO_2

RNA Isolation and qRT-PCR

TRIzol reagent (Thermo Fisher Scientific) was used for total RNA extraction. One milliliter of Trizol was added to selected cells, and the mixture was shaken violently and then let stand for 5 min at 25°C. Next, 200 μl of chloroform was added, and the mixture was shaken violently, then place the mixture at 25°C for 5 min, after 12,000 rpm centrifuging at 4°C for 15 min. 500 mL of supernatant and 300 μl of isopropanol was gently mixed, then place the mixture for 10 min at 25°C, and centrifuged at 12,000 rpm at 4°C for 15 min, the supernatant was then discarded. Next, 1 mL 75% alcohol was added to the centrifuge tube, which was gently shaken, then place the mixture for 5 min at 25°C, and centrifuged at 7500 rpm at 4°C for 15 min, the supernatant was discarded. RNA free water (15 μL) was added to the centrifuge tube, and the precipitate was gently blown for dissolution. The reverse transcription procedure was 42°C for 2 min, 50°C for 15 min, and 85°C for 2 min. After the reaction, the cDNA was stored at −80°C. cDNA was synthesized through reverse transcription using an RT reagent kit (BEENbio, Shanghai, China). The mRNA levels of the genes were analyzed by qRT-PCR using a 2 × SYBR qPCR kit (BEENbio, Shanghai, China), as described in the manufacturer's protocols. Data in all panels are representative of three independent experiments with six replicates per detection. The results were analyzed according to the $2^{-\Delta\Delta Ct}$ formula. The primers used in this paper are shown in **Supplementary Table 1**.

Western Blot Analysis

Fifty micrograms of protein was resolved on 10% SDS-PAGE gels and transferred to PVDF membranes (Millipore, Billerica, MA, United States). The membranes were incubated with primary antibodies and a secondary antibody labeled with HRP. The following primary antibodies were used: rabbit anti-PIK3R2 (PA5-84807, Thermo Fisher, United States), anti-PI3K (3811S, CST, United States), anti-p-PI3K (4228S, Cell Signaling Technology, United States), anti-AKT (4691S, CST, United States), anti-p-AKT (4060S, CST, United States), anti-β-actin (4970S, CST, United States), and rabbit anti-human PTPN22 (ab182239, Abcam, United States).

Enzyme Linked Immunosorbent Assay

After various treatments, serum was extracted from the fresh blood of the experimental and control rats. The samples were diluted in 1 × dilution buffer to be in the range of concentrations used in the assay. IL-2 enzyme linked immunosorbent assay (ELISA) was performed using an ELISA kit from R&D Systems (D2050), and IL-6 and TNF-α ELISA were performed follow the kit instruction (ab46027 and ab181421). The levels of IL-2, IL-6 and TNF-α released into the supernatant were analyzed by ELISA, as described in the manufacturer's instructions. All ELISA measurements were performed in triplicate.

Cell Proliferation Assay

MTT assay was used to detect the cell proliferation. Briefly, the cells were seeded in 96-well plates 5×10^3 per well. All cell groups were incubated for 24, 48, or 72 h. MTT was added to each well, and the cells were sustained and incubated at 37°C for 4 h with 5% CO_2. The solution was then discarded, 300 μl of dimethyl sulfoxide (DMSO) was added to each well, and the cells were shaken for 15 min at 25°C to dissolve the crystals. The absorbance of the samples was checked at 570 nm using an ELX800 universal microplate reader (Biotek Instruments, Inc.). Experiments were replicated three times.

Annexin V and Propidium Iodide (PI) Staining

Apoptosis of nanoparticle-treated cells was assessed by flow cytometry by labeling the cells with FITC-Annexin V and PI assay. Cells were cultured at a density of 6×10^4 per 6 cm dish and grown overnight. Then, 100 μg/ml MSNs, MSNs@CADY, MSNs@CADY@miR-30-5p or MSNs@CADY@miR-30-5p inhibitor were added to the cells, and incubated for 48 h. Washing with PBS for three times, the cells were incubated at 25°C with Annexin V-FITC and PI stain in darkness for 10 min. Samples consisting of 10,000 stained cells were analyzed using flow cytometry.

Synthesis of 120 nm MSN Nanoparticles

The MSNs were synthesized as (Sha et al., 2018) reported with some modifications (Rosenholm et al., 2010; Wang et al., 2015).

The 120–150 nm MSNs were first synthesized using aminotrimethoxysilane (APS) as the amine provider, TMOS as the silica precursor, and cetyltriethylammnonium bromide (CTAB) as the structure-directing agent (Rosenholm et al., 2009). Two hundred milligrams of CTAB (Aldrich, St. Louis, MO, United States) was dissolved in 150 ml of 2M NaOH and 48 ml of water and heated to 80°C. Next, 1.2 ml of tetraethyl orthosilicate (Aldrich, 98%) was added. After incubation for 15 min at 80°C, 300 μl of 3-(trihydroxysilyl) propyl methylphosphonate (Aldrich, 42%) was added, then stirred for 2 h. The particles were collected after 12,000 rpm centrifugation and washed with methanol three times.

CADY Attachment

The self-assembled peptide CADY (GLWWKAWWKAWWK SLWWRKRKRKA) was purchased from Sangon Biotech Company. The CADY peptide was covalently conjugated to MSN-COOH using EDC and NHS. Two milligrams of MSN-COOH was dissolved in 1 ml of MES buffer (pH 6.0), and then, 4 mg of EDC and 4.2 mg of NHS were added. Then, the mixture was stirred for 4 h at 4°C. Subsequently, 100 μl of CADY antibody solution (10 mg/ml) was added and stirred for 4 h at 4°C. Then, it was washed three times with PBS to remove excess EDC. NHS, CADY and MSNs@CADY were suspended in 450 mM miR-30-5p inhibitor, after stirring for 48 h in the dark, MSNs@CADY@miR-30-5p inhibitor was collected by centrifugation, following PBS washing for three times, and vacuum dried overnight at room temperature.

Cellular Uptake and Internalization

A total of 2×10^4 HFLS cells were seeded in glass-bottom plates (35 mm, Corning Incorporated) in DMEM with 10% FBS and incubated at a final concentration of 50 μg/ml FITC-labeled MSNs and FITC-labeled MSNs@CADY for 24 h. The cells were incubated with 60 nM LysoTracker Red DND-99 (Beyotime Institute of Biotechnology, Haimen, China) for 1 h at 37°C. After washing with PBS, the cells were fixed with 4% paraformaldehyde and stained with 10 μg/ml DAPI (4′,6-diamidino-2-phenylindole, Sigma). The cells were washed three times with PBS and mounted. Micrographs were first observed under a Nikon fluorescence microscope (Nikon Eclipse Ti-S, CCD: Ri1) and then under a laser scanning confocal microscope (Leica TCS sp5, Germany) used for confocal luminescence imaging with a 63 × oil immersion objective lens.

Preparation of MSNs@PCM@TP

Since the melting point of PCM tetradecanol is 38–39°C, it is necessary to sufficiently mix ICG and PCM for loading into MSNs at a temperature higher than the melting point. First, 100 mg of tetradecanol was heated to 60°C to fully melt, and then, 10 mg of ICG and 15 mg of TP were added and thoroughly mixed by magnetic stirring for 2 h (Kalaria et al., 2009). Then, 100 mg MSNs were mixed with a large amount of chloroform, added to the PCM mixture solution, and stirred for 2 h at 60°C. During this mixing process, with the volatilization of trichloromethane, the PCM@TP-ICG mixture slowly infiltrates the mesopore cavities of MSNs through the mesopores. Finally, excessive hot water is added to the above preparation system to produce two phases that are obviously incompatible with each other: the MSNs water phase with PCM@TP-ICG and the chloroform phase with PCM@TP-ICG not encapsulated. The two phases were separated rapidly, and the water phase was immersed in an ice water solution for cooling for 1 min and then centrifuged at 1,1000 rpm for 5 min. The precipitates were washed with precooled deionized water 8 times and then freeze dried for 24 h at −50°C and 0.8 mbar in vacuum. The MSNs loaded with PCM@TP-ICG were recorded as MSNs@PCM@TP. In addition, with the same preparation method, the system constructed without TP is recorded as MSNs@PCM.

Testing of miR-30-5p and TP Loading Capacity of MSNs@CADY@miR-30-5p Inhibitor and MSNs@PCM@TP

MSNs@CADY was suspended in 450 mM miR-30-5p and miR-30-5p inhibitor. After stirring for 48 h in the dark, MSNs@CADY@miR-30-5p and MSNs@CADY@miR-30-5p inhibitor were collected by centrifugation, washed with PBS three times, and vacuum dried overnight at 25°C. The concentrations of miR-30-5p and miR-30-5p inhibitor were measured with a Nanodrop 3000 spectrophotometer (Thermo Fisher). The miR-30-5p loading capacity of the nanoparticles was calculated based on changes in miR-30-5p concentration before and after loading. The concentration of TP was measured by UV-Vis spectroscopy at 218 nm, and the TP-loading capacity of MSNs@PCM@TP was calculated according to the changes in TP concentration before and after loading by using UV-Vis spectroscopy at 218 nm.

For the miR-30-5p and TP drug release experiment, MSNs@CADY@miR-30-5p inhibitor and MSNs@PCM@TP were dispersed in 15 ml of PBS (pH 7.4) in semipermeable dialysis bags at 37°C with gentle shaking then take 4 ml of the released medium and add another 4 ml fresh medium. The amount of released TP was measured by UV-Vis spectroscopy at 218 nm. The amount of released miR-30-5p inhibitor was measured by a Nanodrop 3000 spectrophotometer.

Animals and Experimental Procedures and RA Evaluation

A collagen-induced RA rat model was generated according to a previous report (Wang et al., 2018). Female Sprague-Dawley rats (8 weeks old) were purchased from the Animal Center of Northeastern University. All animal experimental procedures were approved by the Laboratory of Animal Ethical Committee of Northeastern University. The rats were randomly allocated into eight groups ($n = 6$), and the rat grouping administration method and doses are shown in the **Table 1**.

In brief, except for rats in the control group, the rats in each group were intradermally injected with 600 μg of bovine type II collagen in 50% complete Freund's adjuvant, and a booster was administered with the same dose of CII in 50% incomplete Freund's adjuvant 14 days later. Starting 15 days after the first immunization, the rats in the respective groups were

TABLE 1 | The appropriate dose and method of administration in rats.

Group	Administration method	Drugs	Dose
Control group	I.P.	PBS (pH 7.5)	2 ml/time
RA model group	I.P.	PBS (pH 7.5)	2 ml/time
Methotrexate (MTX) group	I.P.	MTX	2.5 mg/kg
TP group	I.P.	TP	50 μg/kg
MSNs@PCM@TP group + 808 nm laser	I.P.	MSNs@PCM@TP	100 μg/ml
MSNs@PCM@TP group	I.P.	MSNs@PCM@TP	100 μg/ml
MSNs@CADY@miR-30-5p inhibitor group	I.C.	MSNs@CADY@miR-30-5p inhibitor	100 μg/ml
MSNs@CADY@miR-30-5p inhibitor + I.P. MSNs@PCM@TP + 808 nm laser group	I.C. (MSNs@CADY@miR-30-5p inhibitor), I.P. MSNs@PCM@TP + 808 nm laser	MSNs@CADY@miR-30-5p inhibitor + I.P. MSNs@PCM@TP + 808 nm laser	100 μg/ml MSNs@CADY@miR-30-5p inhibitor + 100 μg/ml I.P. MSNs@PCM@TP + 808 nm laser

administered different nanodrug treatments. The concentrations of the different nanoparticles were 100 mg/ml, the dose of I.C. MSNs@CADY and I.C. MSNs@CADY@miR-30-5p inhibitor was 30 ml/kg, and the dose of I.P. MSNs@PCM@TP was 55 ml/kg. The rats were given administered the drug every 7 days, while the control group and the RA model group received only saline injections.

The symptoms were classified as follows: none, weak, mild, moderate, and severe with scores from 0 to 4, respectively (Le Goff et al., 2009). The highest possible cumulative score of a single rat was 16.

Characterization

The morphology and structure of the products were characterized using a SEM (S-4800) and a TEM (JEOL JEM-2100F) at accelerating voltages of 5 kV and 200 kV, respectively. The pore-size distribution of the products was determined by dynamic light scattering (DLS) using a Malvern Zeta Seizer instrument. N_2 adsorption-desorption isotherms were measured using a Micromeritics ASAP 2020 M porosity analyzer. The samples were outgassed at 573 K for at least 2 h in a vacuum. The Brunauer-Emmett-Teller (BET) and Barrett-Joyner-Halenda (BJH) methods were used to determine pore volume, pore size and the surface areas of the samples.

Zeta Potential

Electrokinetic measurements were obtained at 25°C in a PBS (pH 7.2) between each functionalization step using a Zetasizer Nano apparatus (Malvern Instruments, United Kingdom). The zeta potential was calculated: on the basis of the Schmolukowski model.

Fourier Transform Infrared (FT-IR) Analysis

Chemical analyses of MSNs, FITC-labeled MSNs and CADY-coated FITC-labeled MSNs were carried out using an FT-IR spectrophotometer (Model 100 series, PerkinElmer, Inc.). The Spectra were recorded at ambient temperature over a wave number range of 4,000–400 cm^{-1} at a 2 cm^{-1} resolution based on an average of 64 scans.

Ultraviolet Visible (UV-Vis) Spectroscopy

UV-Vis spectroscopic analysis of TP was measured with an ABTRONICS Model No. LT2900 spectrophotometer in the range of 200–400 nm.

Statistical Analysis

The data are expressed as the mean ± SEM. All statistical analyses were performed using SPSS version 17.0. ANOVAs with *post hoc* LSD (SPSS, Chicago, IL, United States) were used to analyze data among groups, while Student's *t*-tests were used for all statistical analyses. A p-value of < 0.05 was considered statistically significant.

RESULTS

miR-30-5p Was Overexpressed in RA Clinical Tissues

To analyze the expression levels of miRNAs in RA patients, we screened tissues from 40 RA patients and 15 healthy volunteers, and we identified that miR-30-5p was overexpressed in 32 RASFs (32/40, 80%) compared with expression in the corresponding adjacent tissues (**Figure 1A**). Using TargetScan Human 7.2, we found that PIK3R2 was a putative target of miR-30-5p. Then, in the HFLS cells transfected with miR-30-5p, both the mRNA and protein level of PIK3R2 were decreased significantly, while transfection with the miR-30-5p inhibitor resulted in a significant increase in PIK3R2, suggesting that miR-30-5p targeted PIK3R2 (**Figures 1B,C** and **Supplementary Figure 1**).

Synthesis and Characterization of the MSNs and Surface Modifications

Nanoparticles with stable structures are the basis of drug carrier construction. In this study, MSNs were constructed as previously described with some modifications (Biswas, 2017), and their structure was characterized. The results of the TEM (**Figures 2A,B**), SEM (**Figure 2C**), and DLS (**Figure 2E**) analyses showed that the particle sizes of the MSNs were 120–150 nm. The N_2 adsorption-desorption isotherms showed that

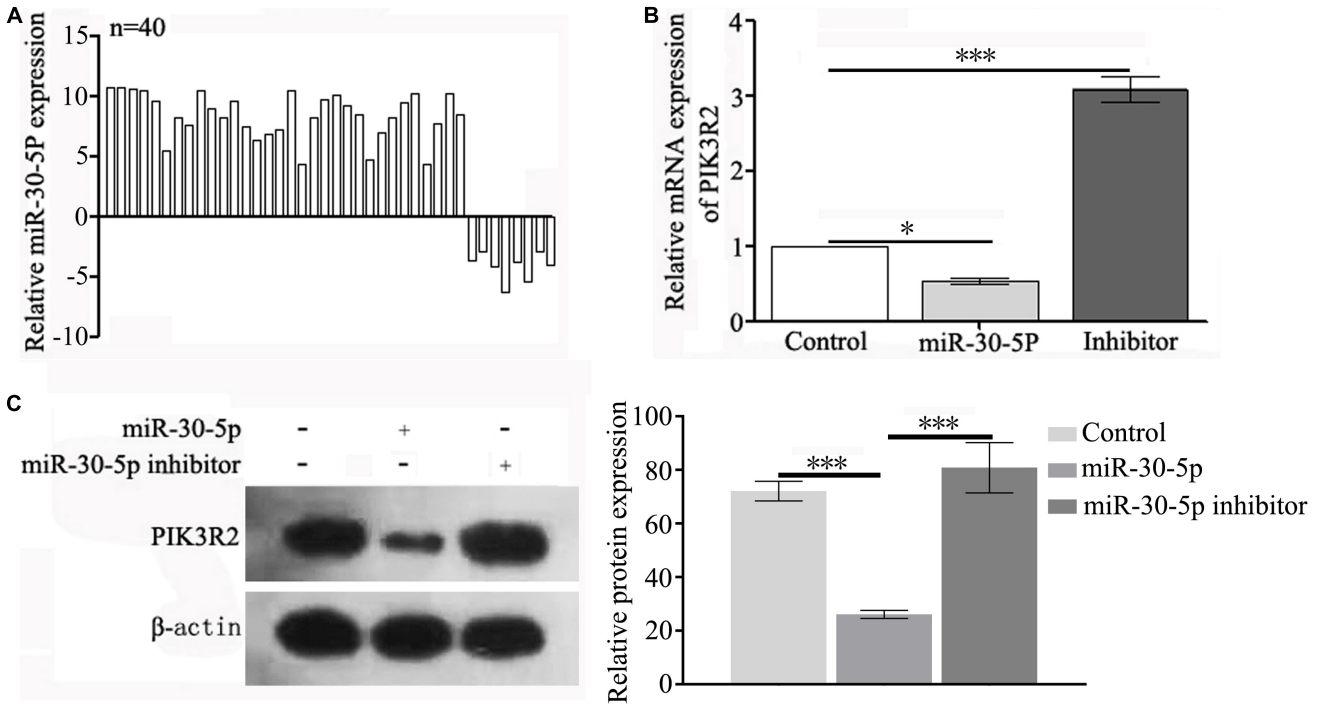

FIGURE 1 | miR-30-5p is overexpressed in RA clinical tissues and regulates the expression of PIK3R2 in the studied cell lines. **(A)** Relative mRNA expression of miR-30-5p in samples from 40 patients (28 males and 12 females) undergoing surgery was tested by qPCR. **(B)** Relative mRNA expression of PIK3R2 in HFLS cells transfected with miR-30-5p or miR-30-5p inhibitor, as determined by qPCR. **(C)** Protein expression of PIK3R2 in HFLS cells transfected with miR-30-5p or miR-30-5p inhibitor, as determined by Western blotting. Experiments in **(B,C)** were repeated three independent times (*$p < 0.05$, **$p < 0.01$, and ***$p < 0.001$).

the mesoporous distribution of the MSNs was approximately 3 nm (**Figure 2D**).

MSN Modifications and Drug Loading

Separate MSNs are easily aggregated in hydrophilic solvents, which affects MSN application. PEG-COOH modification on the surface of MSNs can resolve the nanoparticle aggregation issue. Similarly, polypeptides and fluorescent groups can be added to the surface of MSNs through carboxyl groups. In this study, we constructed MSNs@CADY for the smooth delivery of gene-targeting drugs into cells with FITC modification of the MSN surfaces to track the entry of nanodrug carriers into cells. **Figures 3A–E** shows the patterns and DLS test results for different nanoparticles (MSNs, MSNs-PEG-COOH, FITC-labeled MSNs-PEG, CADY-coated MSNs@miRNA, and MSNs@PCM@TP). Zeta potential was used to detect the surface modification effect of the nanoparticles. As shown in **Figure 3F**, FITC-labeled MSNs or CADY coated FITC-labeled MSNs emitted bright green fluorescence upon irradiation with an ultraviolet lamp, indicating that these modifications can be used to trace the nanodrug carriers. Compared with the zeta potential of the MSNs (8.54), the zeta potential of the MSNs@PEG-COOH, FITC-labeled MSNs and CADY-coated MSNs was 36.42, 9.07, and 8.96 fold, respectively (**Figure 3G**). The FT-IR spectra of the MSNs, FITC-labeled MSNs and CADY coated FITC-labeled MSNs are shown in **Figure 3H** and indicate that the surface of the MSNs was successfully modified by FITC and CADY.

Cytotoxicity Induced by MSNs@PEG-COOH in 293, HFLS and HL-7702 Cells

The cytotoxicity induced by the MSNs-PEG-COOH in the 293, HFLS and HL-7702 cells was tested using an MTT cell activity detection assay. The results showed that MSNs-PEG-COOH had no cytotoxicity at concentrations of 6.25–200 μg/ml after 24 and 48 h of incubation (**Figures 4A–C**).

Cellular Internalization of FITC-Labeled MSNs and FITC-Labeled MSNs@CADY

One of the key characteristics of nanodrug carriers is their ability to effectively deliver drugs into cells. Modification of membrane-penetrating peptides on the surface of drug carriers can effectively improve the efficiency of drug carriers against the cell membrane barrier. The secondary amphipathic peptide, CADY, has low cytotoxicity and no immunogenicity and has been verified to enhance the efficiency of drug uptake by cells (Rittner et al., 2002; Crombez et al., 2009; Konate et al., 2016).

In this study, to better introduce nanodrug carriers into HFLS cells, CADY modified MSNs (MSNs@CADY) were constructed, and FITC was used as a tracer for the MSNs. A total of 100 μg/ml FITC-labeled MSNs and FITC-labeled MSNs@CADY were separately incubated with HFLS cells for 12 h. As shown in **Figure 5**, compared with the amount of MSNs,

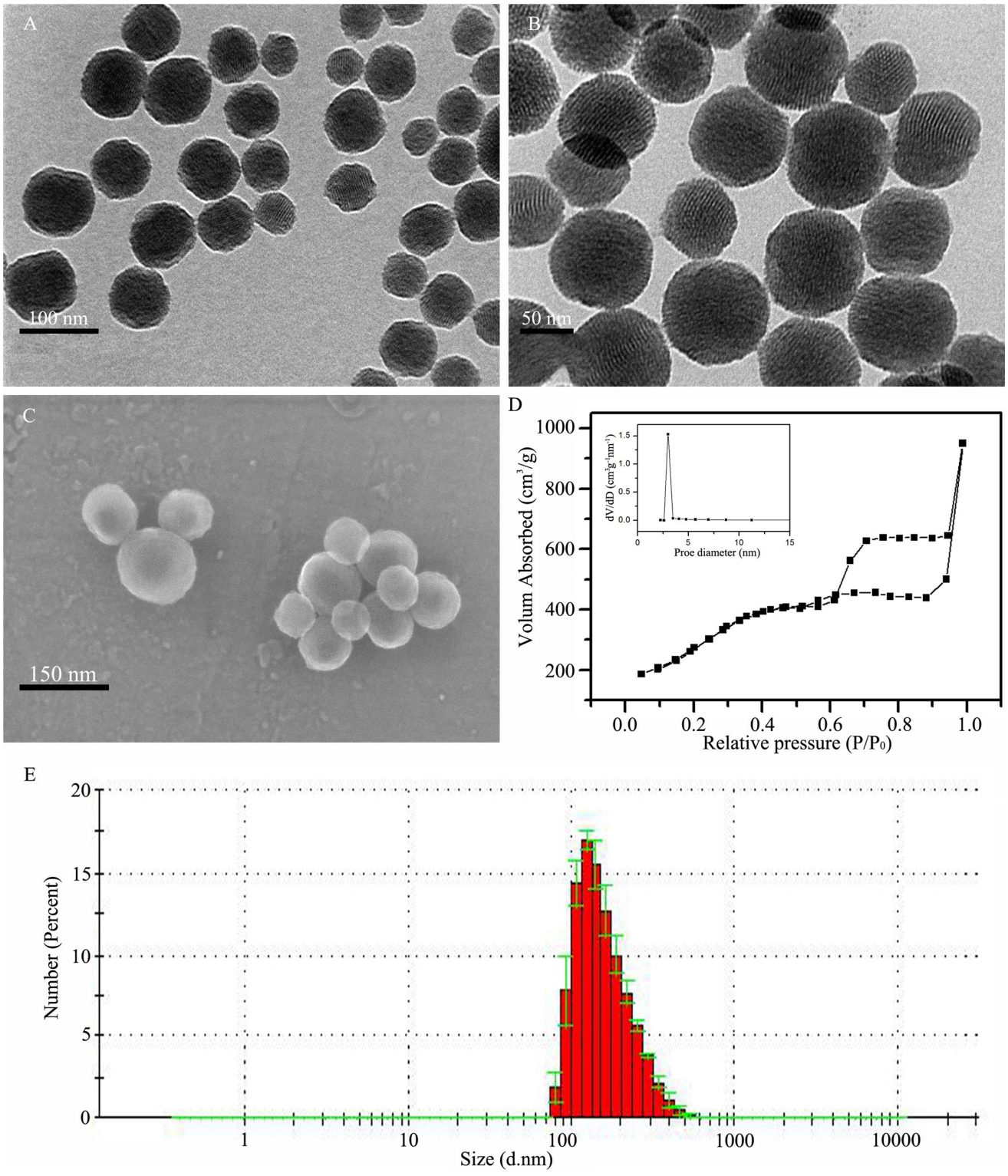

FIGURE 2 | Synthesis and characterization of MSNs. **(A,B)** TEM image of MSNs at different magnifications. **(C)** SEM image of MSNs. **(D)** The mesoporous morphology and mesoporous distribution (inset) of MSNs were determined by the N_2 adsorption-desorption isotherms. **(E)** Dynamic light scattering (DLS) determination of the particle diameter of MSNs.

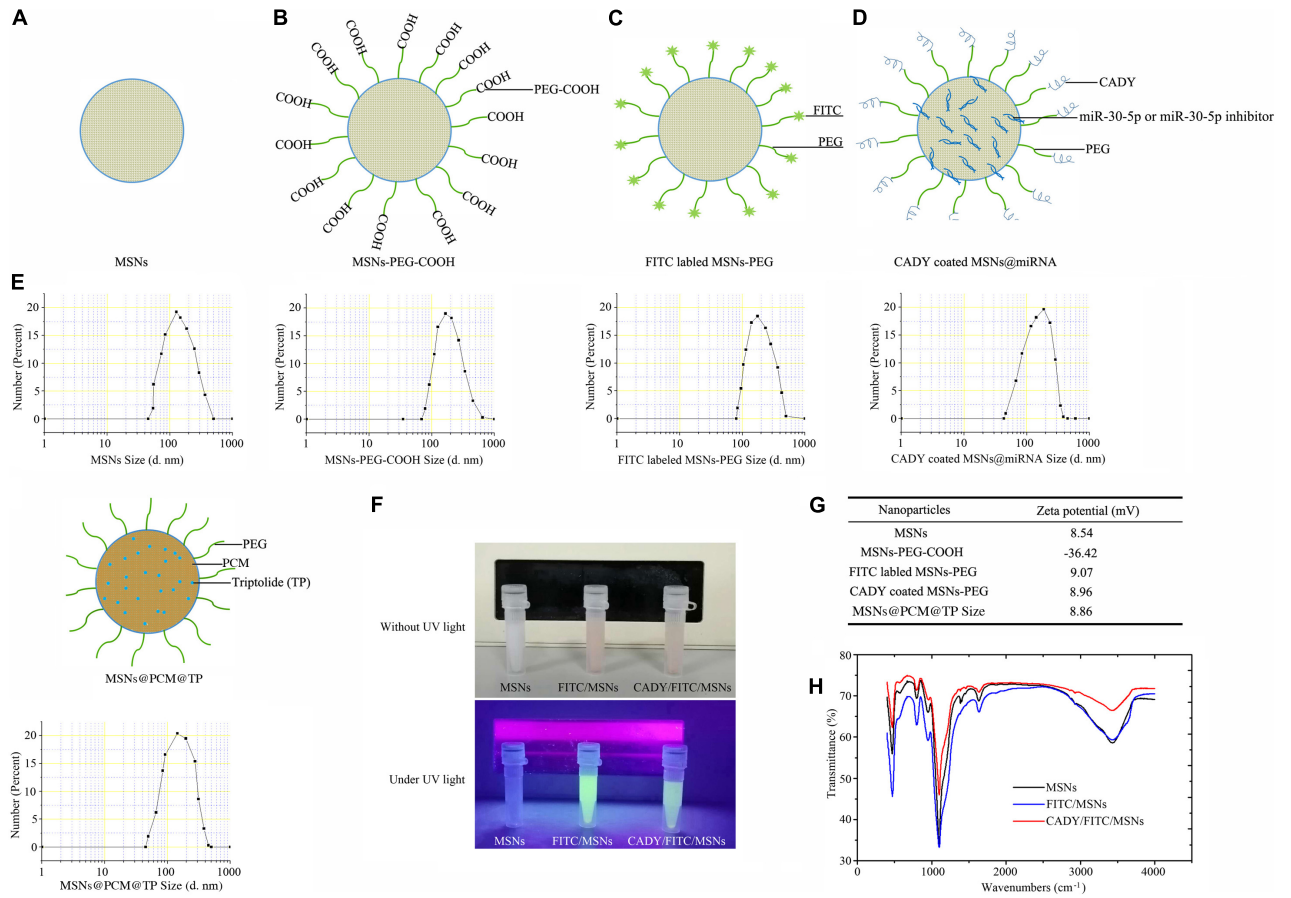

FIGURE 3 | Schematic of the procedures: DLS, zeta potential and FT-IR spectra of different nanoparticles. **(A–E)** Patterns of and DLS results of MSNs, MSNs-PEG-COOH, FITC-labeled MSNs-PEG, CADY-coated MSNs@miRNA, and MSNs@PCM@TP. **(F)** FITC-labeled MSNs and CADY-coated FITC-labeled MSNs were irradiated by an ultraviolet lamp. **(G)** Zeta potential of the MSNs, MSNs-PEG-COOH, FITC-labeled MSNs-PEG, CADY coated MSNs and TP-loaded MSNs-PEG. **(H)** FT-IR spectra of MSNs, FITC-labeled MSNs and CADY-coated FITC- labeled MSNs.

more MSNs@CADY (green fluorescence) was observed in and around the HFLS cells.

miR-30-5p Inhibitor-Loaded MSNs@CADY Can Inhibit Proliferation and Promote the Apoptosis of RASFs by Targeting PIK3R2

PI3K/AKT is a signaling pathway with high activity in SFs, and its abnormal activation can create an imbalance in SF proliferation and apoptosis. The miR-30-5p inhibitor loaded MSNs@CADY was constructed. According to the loading capacity results, 11.57 mg of miR-30-5p and 11.96 mg of miR-30-5p inhibitor were loaded in 1 mg of MSNs@CADY. The encapsulation efficiency of MSNs@CADY@miR-30-5p was similar to that of MSNs@CADY@miR-30-5p inhibitor, and both were able to stably release microRNA for at least 48 h (**Figure 6A**). RASFs were treated with 100 μg/ml MSNs, MSNs@CADY, MSNs@CADY@miR-30-5p or MSNs@CADY@miR-30-5p inhibitor for 24 h, and the expression of PIK3R2, PI3K, p-PI3K, AKT, and p-AKT was analyzed. As shown in **Figures 6B,C** and **Supplementary Figure 2**, the MSNs@CADY@miR-30-5p inhibitor upregulated the expression of PIK3R2 and downregulated the expression of p-PI3K and p-AKT. We also examined the proliferation and apoptosis of RASFs upon treatment them with nanodrug carriers and found that the MSNs@CADY@miR-30-5p inhibitor suppressed RASF proliferation (**Figure 6D**) and promoted RASF apoptosis (**Figure 6E**) in RASFs, suggesting that the MSNs@CADY@miR-30-5p inhibitor can suppress the growth of RASFs.

MSNs@PCM@TP Under 808 nm Laser Downregulated Activation of the Immune System in the RA Rat Model

Tripterygium wilfordii has been used clinically as an immunosuppressive agent in recent years. TP, an effective component in *Tripterygium wilfordii*, is one of the most important anti-inflammatory and immunosuppressive reagents that has been demonstrated in clinical trials (Ziaei and Halaby, 2016). However, a large amount of evidence has

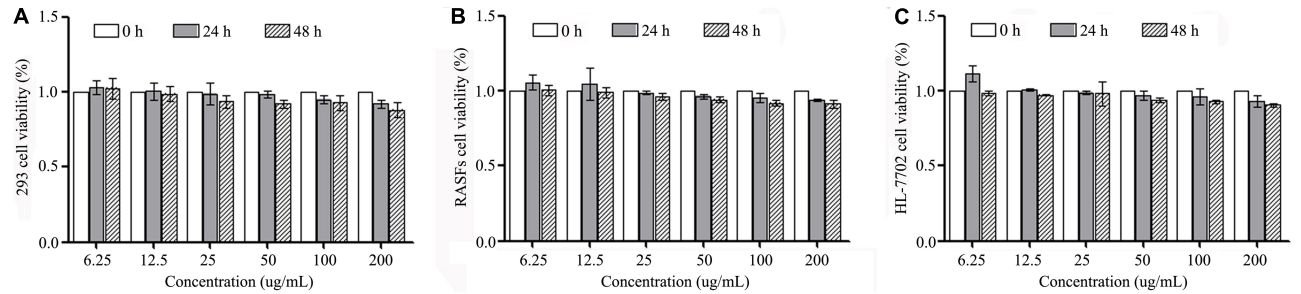

FIGURE 4 | Cytotoxicity induced by MSNs@PEG-COOH in **(A)** 293 cells, **(B)** HFLS cells, and **(C)** HL-7702 cells after treatment for 24 and 48 h. Experiments were repeated three independent times.

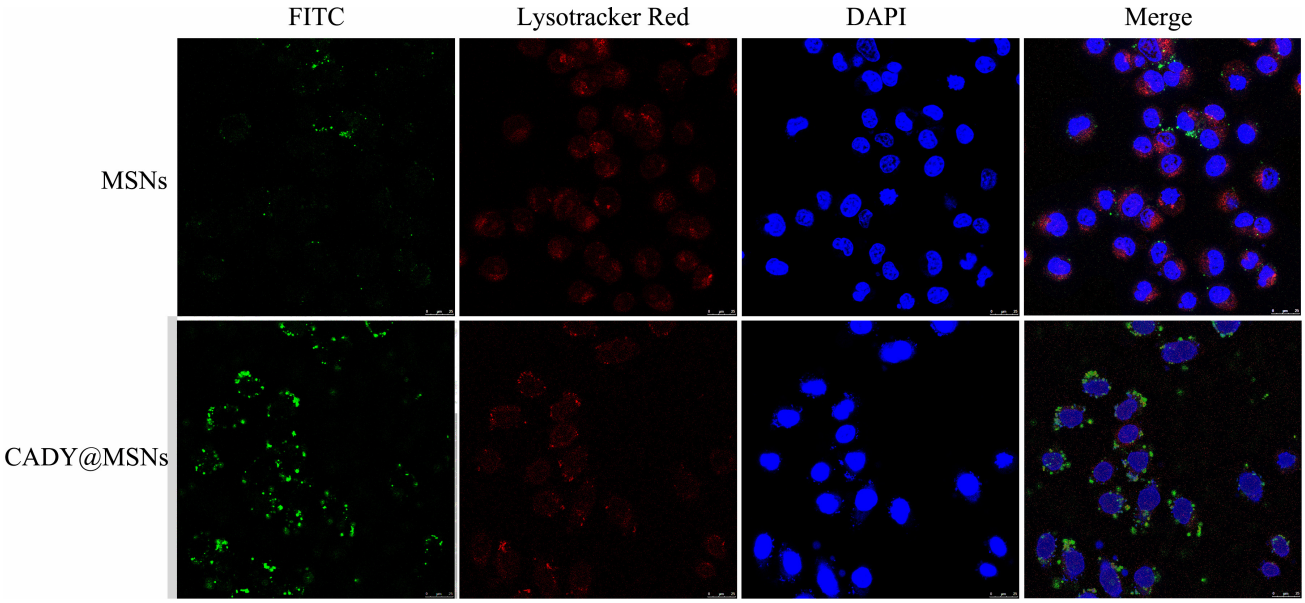

FIGURE 5 | Internalization characteristics of FITC-labeled MSNs and FITC-labeled MSNs@CADY by HFLS cells treated for 12 h, as observed by confocal laser scanning microscopy. Cells were stained with DAPI and LysoTracker Red DND-99.

shown that TP induces a certain degree of toxicity mainly in the heart, liver, bone marrow, chest, spleen, kidney, and reproductive system (Zhen et al., 1995; Shamon et al., 1997). Near infrared response nanodrug carriers have been used to improve many toxic drug formulations due to controlled release performance. Liu et al. (2005) constructed TP-PLA-NPs, which were found to enhance the antirheumatic inflammatory effect and decrease the toxicity of TP in the kidney, liver, and testis.

Here, we loaded TP together with PCM onto the MSNs and specifically tested the capacity of 230 nm MSNs to load TP (**Figure 7A**). The results showed that 1 mg of MSNs could load as much as 45.27 μg of TP. The temperature change of on MSNs@PCM under 808 nm laser was shown in **Figure 7B**, according to the results, under 808 nm laser, the temperature of MSNs@PCM increases rapidly, after 120s of irradiation, the temperature can rise to about 45°C, and finally to about 50°C. We then tested the encapsulation and release efficiency of the MSNs@PCM@TP in PBS at pH 7.4 with or without 808 nm laser. As shown in **Figure 7C**, under 808 nm laser, the cumulative drug release rate reached approximately 30% after 12 h, followed by a sustained slow release for a long period of time. However, without 808 nm laser irradiation, almost no TP is released from the MSNs@PCM@TP.

PTPN22 is a negative regulator of immune activation and plays an important role in RA (Clarke et al., 2017, 2018; Carmona and Martin, 2018). To detect the effect of the MSNs@PCM@TP + 808 nm laser on the expression of PTPN22 in RA rats, we compared the mRNA and protein levels of PTPN22 in the thymus and spleen of rats treated with 100 μg/ml of MSNs@PCM@TP + 808 nm laser for 1 week with those of the RA and RA + TP groups. Both the mRNA and protein levels of PTPN22 were found to increase significantly in the MSNs@PCM@TP + 808 nm laser group (**Figures 7D,E** and **Supplementary Figure 3**). The protein levels of IL-2, IL-6, and TNF-α in rat serum were also measured. According to the results,

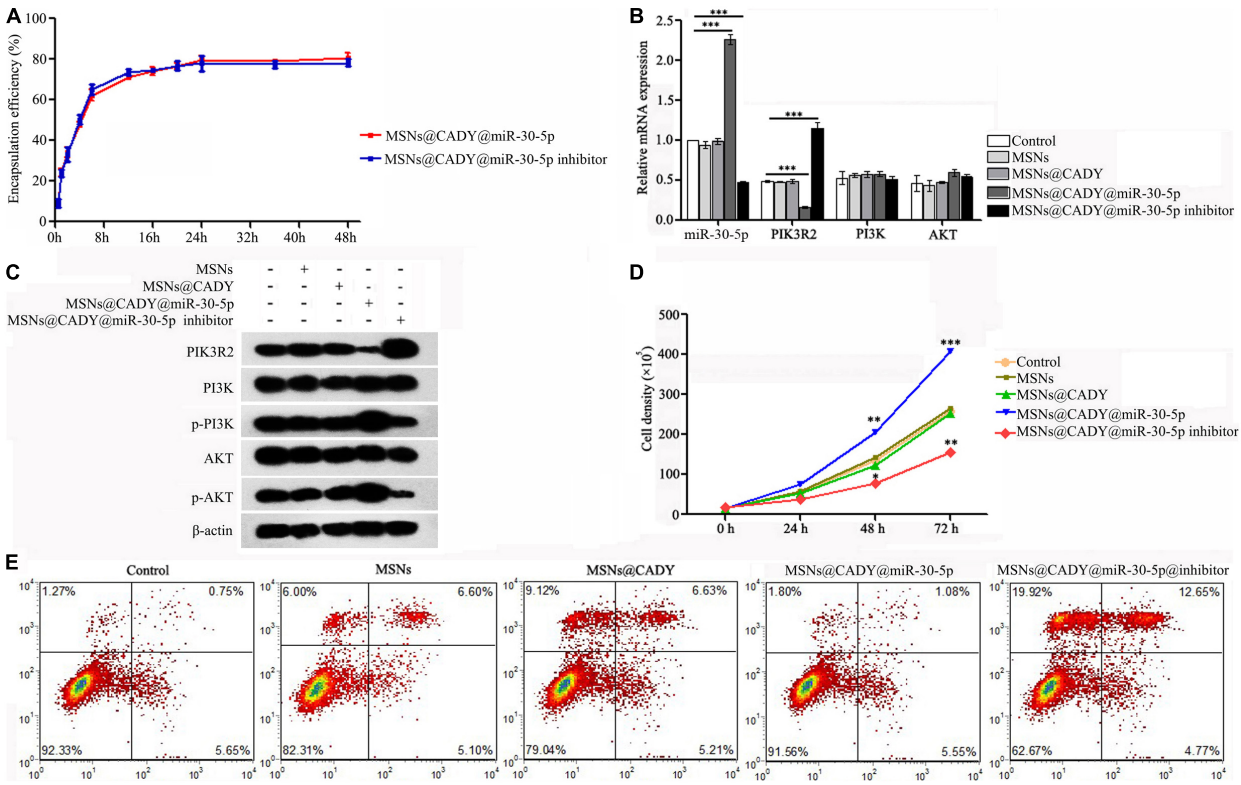

FIGURE 6 | miR-30-5p inhibitor-loaded MSNs@CADY inhibited the proliferation and promoted the apoptosis of RASF cells by targeting PIK3R2. **(A)** The encapsulation efficiency of MSNs@CADY@miR-30-5p and MSNs@CADY@miR-30-5p inhibitor for miR-30-5p and miR-30-5p inhibitor was determined using semipermeable dialysis bags in PBS (pH 7.4) at 37°C. RASFs were treated with 100 μg/ml MSNs, MSNs@CADY, MSNs@CADY@miR-30-5p and MSNs@CADY@miR-30-5p inhibitor for 24 h. **(B)** Relative mRNA expression of miR-30-5p, PIK3R2, PI3K, and AKT as determined by qPCR. **(C)** Relative protein expression of PIK3R2, PI3K, p-PI3K, AKT, and p-AKT as determined by Western blot. **(D)** The cell number was determined after treatment with different nanodrug carriers for 0, 24, 48, and 72 h. The graph represents the cell growth curve for each group. **(E)** The RASF apoptosis level in each group was measured by Annexin V/PI staining. Experiments were repeated three independent times (*$p < 0.05$, **$p < 0.01$, and ***$p < 0.001$).

MSNs@PCM@TP + 808 nm laser significantly decreased the protein levels of IL-2, IL-6, and TNF-α compared with the levels in the free TP group (**Figures 7F–H**).

The Combination of MSNs@CADY@miR-30-5p Inhibitor and MSNs@PCM@TP Has Great Potential for RA Treatment

Drugs are administered in different ways according to their mechanism of action and mode of absorption (Qian et al., 2019). Synergistic treatments with different drugs and different administration modes are widely used in clinical settings, and the therapeutic effects of combinations are often better than those of each individual drug alone. Therefore, we implemented a combination of I.C. MSNs@CADY@miR-30-5p inhibitor and I.P. MSNs@PCM@TP + 808 nm laser to treat RA rats.

Firstly, the biocompatibility of MSNs, MSNs@CADY and MSNs@PCM were tested in mice. According to the results, a final concentration of 500 μg/ml MSNs, MSNs@CADY and MSNs@PCM had caused no significant toxic reaction in the experimental group, and there was no significant difference in the weight change between the experimental group and the PBS control group (**Supplementary Figure 4**). For the animal experiments, we used the two most common drugs for RA, TP and MTX, as positive controls. Longitudinal measurements indicated that the joint diameter and arthritis scores of the rats treated with I.C. MSNs@CADY@miR-30-5p inhibitor alone and of the rats treated with I.P. MSNs@PCM@TP + 808 nm laser were significantly lower than those of the I.P. MTX and TP control group rats. Importantly, the effect of I.C. MSNs@CADY@miR-30-5p inhibitor + I.P. MSNs@PCM@TP + 808 nm laser was significantly greater than the effect of either I.C. MSNs@CADY@miR-30-5p inhibitor or I.P. MSNs@PCM@TP + 808 nm laser alone ($p < 0.001$, **Figures 8A,B**). F Results of histological examination showed severe articular cartilage destruction and inflammatory cell infiltration in the bone tissue in the RA groups. In contrast, a nearly healthy bone structure and articular cartilage surface were observed in the I.C. MSNs@CADY@miR-30-5p inhibitor + I.P. MSNs@PCM@TP + 808 nm laser group, and the therapeutic effect in the I.C. MSNs@CADY@miR-30-5p inhibitor + I.P. MSNs@PCM@TP + 808 nm laser group was also greater than that in the I.P. MTX and I.P. TP group (**Figure 8C**). These

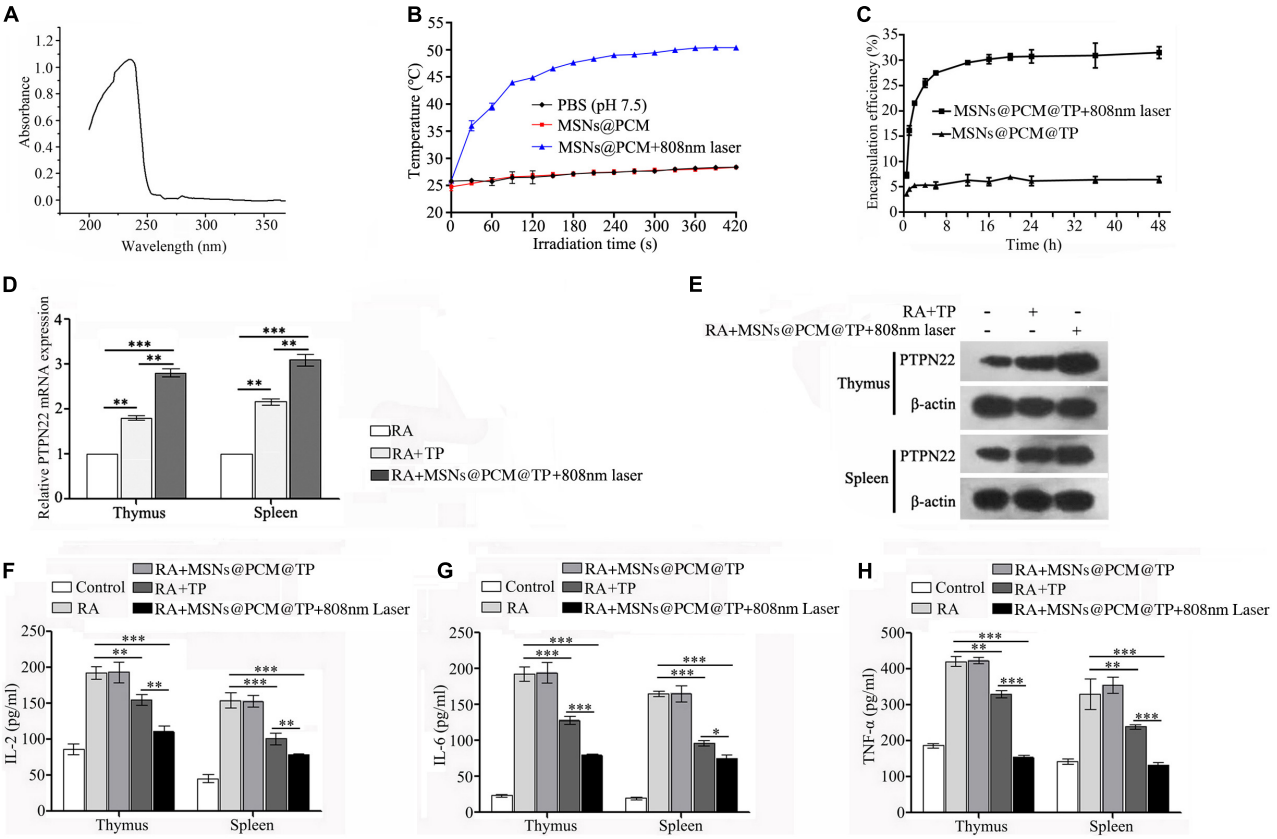

FIGURE 7 | MSNs@PCM@TP downregulated the activation of the immune system in the RA rat model. **(A)** The maximum absorption peak of TP in PBS (pH 7.4) was found by full wavelength scanning. **(B)** The temperature changing of MSNs@PCM under 808 nm laser. **(C)** Encapsulation efficiency profiles of the MSNs@PCM@TP for TP were determined by use of semipermeable dialysis bags in PBS (pH 7.4) at 37°C. **(D,E)** mRNA and protein expression of PTPN22 in the thymus and spleen of RA rat treated with 100 μg/ml MSNs@PCM@TP under 808 nm laser irradiation for 1 week as detected by qPCR and Western blot assay, respectively. **(F–H)** Serum levels of IL-2, IL-6, and TNF-α in rats treated with 100 μg/ml MSNs@PCM@TP under 808 nm laser irradiation for 1 week, as determined by ELISA. Experiments were repeated three independent times (*$p < 0.05$, **$p < 0.01$, and ***$p < 0.001$).

results indicate that the combination of MSNs@CADY@miR-30-5p inhibitor and MSNs@PCM@TP + 808 nm laser could be a potential treatment option for RA.

DISCUSSION

As a chronic autoimmune disease, rheumatoid arthritis mainly affects joint tissue and promotes osteopenia around the joint (Tanaka and Ohira, 2018). In this study, TP plus miR-30-5p inhibitor delivered via modified MSNs was evaluated for its therapeutic efficacy in RA.

Currently, RA treatment focuses on suppressing the overactive immune system and maintaining the balance between the proliferation and apoptosis of SFs. Given the rapid development of RA treatment drugs, most patients can control their RA symptoms. However, due to the reduced distribution of the RA drugs in diseased joints after administration, the curative effect is not ideal, and adverse reactions are severe. Furthermore, these drugs generally have poor bioavailability and must be administered frequently and in high doses (Xiao et al., 2009). Therefore, the adverse reactions of normal tissues to RA drugs limit the widespread clinical use of these drugs. Targeted therapy can deliver drugs to the lesion site, tissue or specific cells, providing a way to resolve the problems described above. As a targeted drug delivery system, nanopreparations have been widely studied and applied. At the cellular level, the PI3K/AKT signaling pathway phosphorylates and regulates many proteins related to cell metabolism, apoptosis, proliferation and differentiation, and inhibits cell apoptosis and promotes tumor growth. PIK3R2 is a negative regulator of the PI3K/AKT signaling pathway (Stanczyk et al., 2008; Song et al., 2016). PIK3R2 maintaining the balance between proliferation and apoptosis of SFs (Fan et al., 2018). Our results showed miR-30-5p overexpression and PIK3R2 downregulation in 32 of 40 clinical cases of RA. The expression of PIK3R2 decreased significantly in SFs transfected with miR-30-5p, which indicates that the inhibition of miR-30-5p can be used to maintain the balance between SF proliferation and apoptosis by increasing PIK3R2.

To improve the efficiency of miR-30-5p inhibitor in the RASFs, cell membrane penetrating peptide CADY-modified MSNs with good biocompatibility and release characteristics

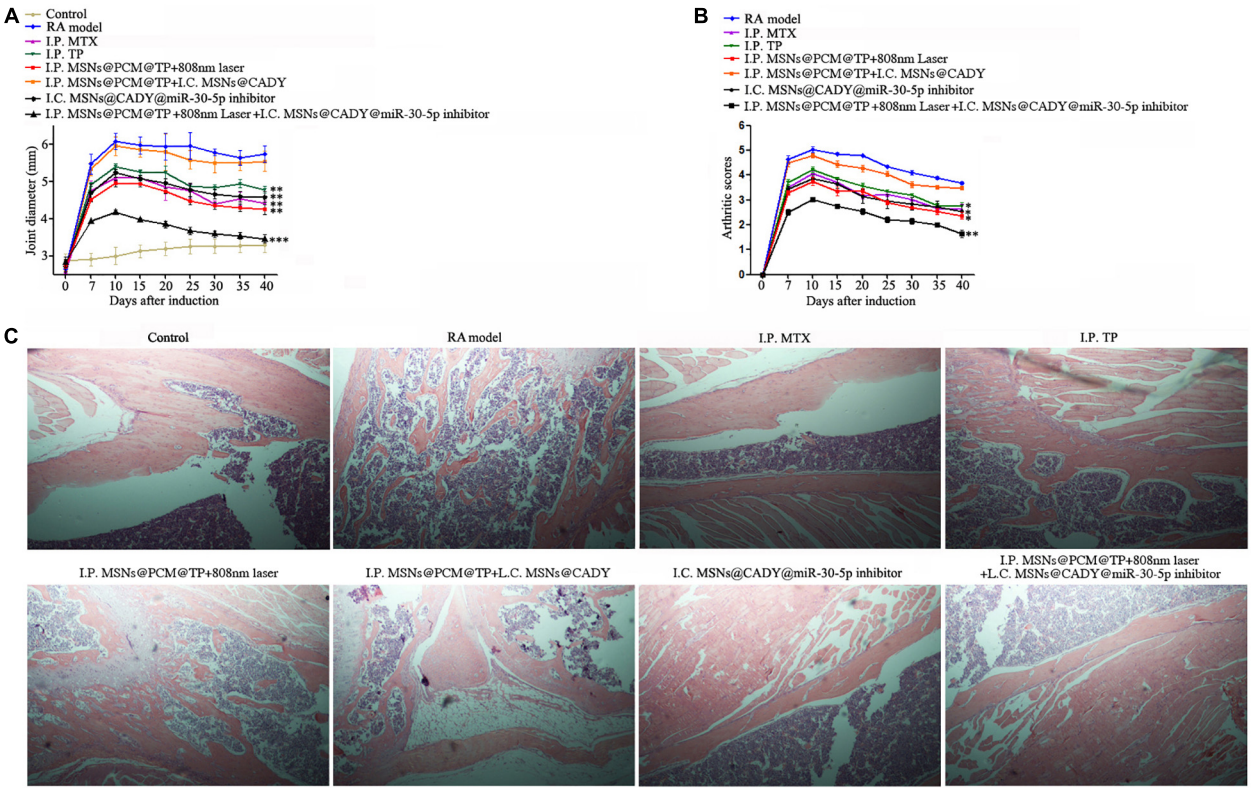

FIGURE 8 | Therapeutic potential of the combination of MSNs@CADY@miR-30-5p inhibitor and MSNs@PCM@TP + 808 nm laser in the treatment of RA. Rats treated with I.C. MSNs@CADY + I.P. MSNs@PCM@TP, I.C. MSNs@CADY@miR-30-5p inhibitor, I.P. MSNs@PCM@TP + 808 nm laser and I.C. MSNs@CADY@miR-30-5p inhibitor + I.P. MSNs@PCM@TP + 808 nm laser were examined for joint diameter, arthritis score, and joint histological damage. **(A)** Joint diameter of each group (n = 6). **(B)** Arthritis score of each group (n = 6). **(C)** Histological images of rat ankle joints.

were constructed. The results show that the cell entry efficiency of MSNs@CADY was significantly greater than that of MSNs. MSNs@CADY@miR-30-5p inhibitor effectively inhibited proliferation and promote apoptosis of the RASFs by targeting PIK3R2 to regulate the PI3K/AKT signaling pathway.

Tripterygium Wilfordii Hook F is a traditional Chinese herbal medicine used to treat RA. It has good efficacy and is also cost effective. TP is the main active ingredient in TWHF (Li et al., 2014). TP can inhibit the secretion of inflammatory cytokines and chemical factors by inhibiting the transcription activities of purine-box and NF-κB in epidermal cells, monocytes, human peripheral blood lymphocytes and T cells. Previous studies have shown that TP can also interfere with the expression of proinflammatory factors in LPS-stimulated mouse macrophages and can significantly inhibit their induction *in vivo* (Moore et al., 2001; Min et al., 2004). However, the use of TP is restricted because of the toxic side effects it induces in the heart, liver, bone marrow, chest, spleen, kidney, and reproductive system. Many studies have verified that loading TP into nanoparticles with good release properties is useful in reducing its cytotoxicity by reducing the local concentration of TP and prolonging the time of drug action (Mei et al., 2003; Liu et al., 2008). To ameliorate the side effects induced by TP, we loaded TP into near infrared response photothermal controlled-release MSNs, to control the release time of TP. According to the results, under 808 nm laser, the cumulative drug release rate reached approximately 30% after 12 h followed by a sustained slow release for a long period of time. However, without 808 nm laser irradiation, almost no TP was released from MSNs@PCM@TP. In subsequent animal experiments, MSNs@PCM@TP + 808 nm laser increased the mRNA and protein levels of PTPN22 in the thymus and spleen in the RA rats, while it decreased the protein levels of IL-2, IL-6 and TNF-α in RA rat serum, thereby achieving the objective of inhibiting the over activated immune system. Finally, I.C. MSNs@CADY@miR-30-5p inhibitor plus I.P. MSNs@PCM@TP + 808 nm laser were used in combination to treat RA rats, and the combination therapy significantly improved the therapeutic effect on RA by affecting different pathways of the overactive immune system and the imbalance of SFs.

In summary, this study demonstrated that the efficient delivery of triptolide plus miR-30-5p inhibitor using modified MSNs has therapeutic efficacy in RA treatment. The results of the pharmacodynamic study showed that the combination of MSNs@CADY@miR-30-5p inhibitor and MSNs@PCM@TP + 808 nm laser relieved joint swelling to some extent and inhibited articular cartilage destruction in the synovium. These findings suggest that the effective release of the

traditional Chinese medicine TP and the newly identified miR-30-5p inhibitor through the use of modified MSNs could lead to the development of innovative therapeutic approaches for RA.

DATA AVAILABILITY STATEMENT

Publicly available datasets were analyzed in this study. This data can be found here: http://www.targetscan.org/vert_72/.

ETHICS STATEMENT

The studies involving human participants were reviewed and approved by The Ethical Board of China-Japan Union Hospital of Jilin University. The patients/participants provided their written informed consent to participate in this study. The animal study was reviewed and approved by The Institutional Animal Care and Use Committee of Northeastern University.

AUTHOR CONTRIBUTIONS

XaZ performed the majority of the experiments, analyzed the data, wrote and edited the manuscript. YY analyzed the data and helped with revising the manuscript. XnZ collected and processed clinical samples. XW, TW, BB, NZ, and YZ advised on parts of the study. BW directed the study, analyzed and approved all of the data, wrote and edited the manuscript. All authors reviewed the manuscript.

FUNDING

This research was supported by the National Natural Science Foundation of China (31670770, 2016YFC1302402, and 31370784), LiaoNing Revitalization Talents Program (XLYC 1902063), and the Fundamental Research Funds for the Central Universities of China (N141008001, N162004006, and N172008008).

ACKNOWLEDGMENTS

We thank Dr. Andre Veillette at IRCM for help with useful ideas and experimental materials.

SUPPLEMENTARY MATERIAL

The Supplementary Material for this article can be found online at: https://www.frontiersin.org/articles/10.3389/fbioe.2020.00170/full#supplementary-material

REFERENCES

Altman, R., Asch, E., Bloch, D., Bole, G., Borenstein, D., Brandt, K., et al. (1986). Development of criteria for the classification and reporting of osteoarthritis. Classification of osteoarthritis of the knee. Diagnostic and therapeutic criteria committee of the American Rheumatism Association. *Arthritis Rheum.* 29, 1039–1049. doi: 10.1002/art.1780290816

Arnett, F. C., Edworthy, S. M., Bloch, D. A., McShane, D. J., Fries, J. F., Cooper, N. S., et al. (1988). The American Rheumatism Association 1987 revised criteria for the classification of rheumatoid arthritis. *Arthritis Rheum.* 31, 315–324. doi: 10.1002/art.1780310302

Biswas, N. (2017). Modified mesoporous silica nanoparticles for enhancing oral bioavailability and antihypertensive activity of poorly water soluble valsartan. *Eur. J. Pharm. Sci.* 99, 152–160. doi: 10.1016/j.ejps.2016.12.015

Cai, H., Liang, Z., Huang, W., Wen, L., and Chen, G. (2017). Engineering PLGA nano-based systems through understanding the influence of nanoparticle properties and cell-penetrating peptides for cochlear drug delivery. *Int. J. Pharm.* 532, 55–65. doi: 10.1016/j.ijpharm.2017.08.084

Carmona, F. D., and Martin, J. (2018). The potential of PTPN22 as a therapeutic target for rheumatoid arthritis. *Expert Opin. Ther. Targets* 22, 879–891. doi: 10.1080/14728222.2018.1526924

Choi, S. W., Zhang, Y., and Xia, Y. (2010). A temperature-sensitive drug release system based on phase-change materials. *Angew. Chem. Int. Ed. Engl.* 49, 7904–7908. doi: 10.1002/anie.201004057

Clarke, F., Jordan, C. K., Gutierrez-Martinez, E., Bibby, J. A., Sanchez-Blanco, C., Cornish, G. H., et al. (2017). Protein tyrosine phosphatase PTPN22 is dispensable for dendritic cell antigen processing and promotion of T-cell activation by dendritic cells. *PLoS One* 12:e0186625. doi: 10.1371/journal.pone.0186625

Clarke, F., Purvis, H. A., Sanchez-Blanco, C., Gutierrez-Martinez, E., Cornish, G. H., Zamoyska, R., et al. (2018). The protein tyrosine phosphatase PTPN22 negatively regulates presentation of immune complex derived antigens. *Sci. Rep.* 8:12692. doi: 10.1038/s41598-018-31179-x

Collison, J. (2016). Rheumatoid arthritis: tipping the balance towards resolution. *Nat. Rev. Rheumatol.* 12:622. doi: 10.1038/nrrheum.2016.159

Crombez, L., Aldrian-Herrada, G., Konate, K., Nguyen, Q. N., McMaster, G. K., Brasseur, R., et al. (2009). A new potent secondary amphipathic cell-penetrating peptide for siRNA delivery into mammalian cells. *Mol. Ther.* 17, 95–103. doi: 10.1038/mt.2008.215

Dowaidar, M., Abdelhamid, H. N., Hallbrink, M., Freimann, K., Kurrikoff, K., Zou, X., et al. (2017). Magnetic nanoparticle assisted self-assembly of cell penetrating peptides-oligonucleotides complexes for gene delivery. *Sci. Rep.* 7:9159. doi: 10.1038/s41598-017-09803-z

Fan, D., Guo, Q., Shen, J., Zheng, K., Lu, C., Zhang, G., et al. (2018). The effect of triptolide in rheumatoid arthritis: from basic research towards clinical translation. *Int. J. Mol. Sci.* 19:376. doi: 10.3390/ijms19020376

Fan, D., He, X., Bian, Y., Guo, Q., Zheng, K., Zhao, Y., et al. (2016). Triptolide modulates TREM-1 signal pathway to inhibit the inflammatory response in rheumatoid arthritis. *Int. J. Mol. Sci.* 17:498. doi: 10.3390/ijms17040498

Gao, J., Zhou, X. L., Kong, R. N., Ji, L. M., He, L. L., and Zhao, D. B. (2016). microRNA-126 targeting PIK3R2 promotes rheumatoid arthritis synovial fibroblasts proliferation and resistance to apoptosis by regulating PI3K/AKT pathway. *Exp. Mol. Pathol.* 100, 192–198. doi: 10.1016/j.yexmp.2015.12.015

Jeong, E. J., Choi, M., Lee, J., Rhim, T., and Lee, K. Y. (2015). The spacer arm length in cell-penetrating peptides influences chitosan/siRNA nanoparticle delivery for pulmonary inflammation treatment. *Nanoscale* 7, 20095–20104. doi: 10.1039/c5nr06903c

Kalaria, D. R., Sharma, G., Beniwal, V., and Ravi Kumar, M. N. (2009). Design of biodegradable nanoparticles for oral delivery of doxorubicin: in vivo pharmacokinetics and toxicity studies in rats. *Pharm. Res.* 26, 492–501. doi: 10.1007/s11095-008-9763-4

Konate, K., Lindberg, M. F., Vaissiere, A., Jourdan, C., Aldrian, G., Margeat, E., et al. (2016). Optimisation of vectorisation property: a comparative study for a secondary amphipathic peptide. *Int. J. Pharm.* 509, 71–84. doi: 10.1016/j.ijpharm.2016.05.030

Kong, X., Zhang, Y., Liu, C., Guo, W., Li, X., Su, X., et al. (2013). Anti-angiogenic effect of triptolide in rheumatoid arthritis by targeting angiogenic cascade. *PLoS One* 8:e77513. doi: 10.1371/journal.pone.0077513

Larsen, A., Dale, K., and Eek, M. (1977). Radiographic evaluation of rheumatoid arthritis and related conditions by standard reference films. *Acta Radiol. Diagn. (Stockh)* 18, 481–491. doi: 10.1177/028418517701800415

Le Goff, B., Soltner, E., Charrier, C., Maugars, Y., Redini, F., Heymann, D., et al. (2009). A combination of methotrexate and zoledronic acid prevents bone erosions and systemic bone mass loss in collagen induced arthritis. *Arthritis Res. Ther.* 11:R185. doi: 10.1186/ar2877

Li, X. J., Jiang, Z. Z., and Zhang, L. Y. (2014). Triptolide: progress on research in pharmacodynamics and toxicology. *J. Ethnopharmacol.* 155, 67–79. doi: 10.1016/j.jep.2014.06.006

Liu, M., Dong, J., Yang, Y., Yang, X., and Xu, H. (2005). Anti-inflammatory effects of triptolide loaded poly(D,L-lactic acid) nanoparticles on adjuvant-induced arthritis in rats. *J. Ethnopharmacol.* 97, 219–225. doi: 10.1016/j.jep.2004.10.031

Liu, M. X., Dong, J., Yang, Y. J., Yang, X. L., and Xu, H. B. (2008). Preliminary research on abating rat testicle toxicity due to triptolide after oral polymer nanoparticle delivery. *Drug Discov. Ther.* 2, 188–193.

Manchanda, R., Fernandez-Fernandez, A., Nagesetti, A., and McGoron, A. J. (2010). Preparation and characterization of a polymeric (PLGA) nanoparticulate drug delivery system with simultaneous incorporation of chemotherapeutic and thermo-optical agents. *Colloids Surf. B Biointerfaces* 75, 260–267. doi: 10.1016/j.colsurfb.2009.08.043

Mei, Z., Chen, H., Weng, T., Yang, Y., and Yang, X. (2003). Solid lipid nanoparticle and microemulsion for topical delivery of triptolide. *Eur. J. Pharm. Biopharm.* 56, 189–196. doi: 10.1016/s0939-6411(03)00067-5

Min, S. Y., Hwang, S. Y., Park, K. S., Lee, J. S., Lee, K. E., Kim, K. W., et al. (2004). Induction of IL-10-producing CD4+CD25+ T cells in animal model of collagen-induced arthritis by oral administration of type II collagen. *Arthritis Res. Ther.* 6, R213–R219. doi: 10.1186/ar1169

Moon, G. D., Choi, S. W., Cai, X., Li, W., Cho, E. C., Jeong, U., et al. (2011). A new theranostic system based on gold nanocages and phase-change materials with unique features for photoacoustic imaging and controlled release. *J. Am. Chem. Soc.* 133, 4762–4765. doi: 10.1021/ja200894u

Moore, K. W., de Waal Malefyt, R., Coffman, R. L., and O'Garra, A. (2001). Interleukin-10 and the interleukin-10 receptor. *Annu. Rev. Immunol.* 19, 683–765. doi: 10.1146/annurev.immunol.19.1.683

Mullen, M. B., and Saag, K. G. (2015). Evaluating and mitigating fracture risk in established rheumatoid arthritis. *Best Pract. Res. Clin. Rheum.* 29, 614–627. doi: 10.1016/j.berh.2015.09.005

Onozaki, K. (2009). Etiological and biological aspects of cigarette smoking in rheumatoid arthritis. *Inflamm. Allergy Drug Targets* 8, 364–368. doi: 10.2174/187152811090805036 4

Qian, K., Zhang, L., and Shi, K. (2019). Triptolide prevents osteoarthritis via inhibiting hsa-miR-20b. *Inflammopharmacology* 27, 109–119. doi: 10.1007/s10787-018-0509-6

Qu, Y., Zhang, Y. P., Wu, J., Jie, L. G., Deng, J. X., Zhao, D. B., et al. (2019). Downregulated microRNA-135a ameliorates rheumatoid arthritis by inactivation of the phosphatidylinositol 3-kinase/AKT signaling pathway via phosphatidylinositol 3-kinase regulatory subunit 2. *J. Cell. Physiol.* 234, 17663–17676. doi: 10.1002/jcp.28390

Rittner, K., Benavente, A., Bompard-Sorlet, A., Heitz, F., Divita, G., Brasseur, R., et al. (2002). New basic membrane-destabilizing peptides for plasmid-based gene delivery in vitro and in vivo. *Mol. Ther.* 5, 104–114. doi: 10.1006/mthe.2002.0523

Rosenholm, J. M., Meinander, A., Peuhu, E., Niemi, R., Eriksson, J. E., Sahlgren, C., et al. (2009). Targeting of porous hybrid silica nanoparticles to cancer cells. *ACS Nano* 3, 197–206. doi: 10.1021/nn800781r

Rosenholm, J. M., Peuhu, E., Bate-Eya, L. T., Eriksson, J. E., Sahlgren, C., and Linden, M. (2010). Cancer-cell-specific induction of apoptosis using mesoporous silica nanoparticles as drug-delivery vectors. *Small (Weinheim an der Bergstrasse, Germany)* 6, 1234–1241. doi: 10.1002/smll.200902355

Saxena, V., Sadoqi, M., and Shao, J. (2004). Indocyanine green-loaded biodegradable nanoparticles: preparation, physicochemical characterization and in vitro release. *Int. J. Pharm.* 278, 293–301. doi: 10.1016/j.ijpharm.2004.03.032

Sha, L., Wang, D., Mao, Y., Shi, W., Gao, T., Zhao, Q., et al. (2018). Hydrophobic interaction mediated coating of pluronics on mesoporous silica nanoparticle with stimuli responsiveness for cancer therapy. *Nanotechnology* 29:345101. doi: 10.1088/1361-6528/aac6b1

Shamon, L. A., Pezzuto, J. M., Graves, J. M., Mehta, R. R., Wangcharoentrakul, S., Sangsuwan, R., et al. (1997). Evaluation of the mutagenic, cytotoxic, and antitumor potential of triptolide, a highly oxygenated diterpene isolated from *Tripterygium wilfordii*. *Cancer Lett.* 112, 113–117. doi: 10.1016/s0304-3835(96)04554-5

Song, L., Li, D., Gu, Y., Wen, Z. M., Jie, J., Zhao, D., et al. (2016). MicroRNA-126 targeting PIK3R2 inhibits NSCLC A549 cell proliferation, migration, and invasion by regulation of PTEN/PI3K/AKT pathway. *Clin. Lung Cancer* 17, e65–e75. doi: 10.1016/j.cllc.2016.03.012

Stanczyk, J., Pedrioli, D. M., Brentano, F., Sanchez-Pernaute, O., Kolling, C., Gay, R. E., et al. (2008). Altered expression of MicroRNA in synovial fibroblasts and synovial tissue in rheumatoid arthritis. *Arthritis Rheum.* 58, 1001–1009. doi: 10.1002/art.23386

Tanaka, Y., and Ohira, T. (2018). Mechanisms and therapeutic targets for bone damage in rheumatoid arthritis, in particular the RANK-RANKL system. *Curr. Opin. Pharmacol.* 40, 110–119. doi: 10.1016/j.coph.2018.03.006

Tang, Q., Chang, S., Tian, Z., Sun, J., Hao, L., Wang, Z., et al. (2017). Efficacy of indocyanine green-mediated sonodynamic therapy on rheumatoid arthritis fibroblast-like synoviocytes. *Ultrasound Med. Biol.* 43, 2690–2698. doi: 10.1016/j.ultrasmedbio.2017.06.030

Wang, T., Jiang, H., Wan, L., Zhao, Q., Jiang, T., Wang, B., et al. (2015). Potential application of functional porous TiO2 nanoparticles in light-controlled drug release and targeted drug delivery. *Acta Biomater.* 13, 354–363. doi: 10.1016/j.actbio.2014.11.010

Wang, Y., Kou, J., Zhang, H., Wang, C., Li, H., Ren, Y., et al. (2018). The renin-angiotensin system in the synovium promotes periarticular osteopenia in a rat model of collagen-induced arthritis. *Int. Immunopharmacol.* 65, 550–558. doi: 10.1016/j.intimp.2018.11.001

Xiao, C., Zhou, J., He, Y., Jia, H., Zhao, L., Zhao, N., et al. (2009). Effects of triptolide from radix *Tripterygium wilfordii* (Leigongteng) on cartilage cytokines and transcription factor NF-kappaB: a study on induced arthritis in rats. *Chin. Med.* 4:13. doi: 10.1186/1749-8546-4-13

Xue, X., Gong, L., Qi, X., Wu, Y., Xing, G., Yao, J., et al. (2011). Knockout of hepatic P450 reductase aggravates triptolide-induced toxicity. *Toxicol. Lett.* 205, 47–54. doi: 10.1016/j.toxlet.2011.05.003

Zhang, J., Liu, L., Mu, X., Jiang, Z., and Zhang, L. (2012). Effect of triptolide on estradiol release from cultured rat granulosa cells. *Endocr. J.* 59, 473–481. doi: 10.1507/endocrj.ej11-0407

Zhen, Q. S., Ye, X., and Wei, Z. J. (1995). Recent progress in research on *Tripterygium*: a male antifertility plant. *Contraception* 51, 121–129. doi: 10.1016/0010-7824(94)00018-r

Ziaei, S., and Halaby, R. (2016). Immunosuppressive, anti-inflammatory and anti-cancer properties of triptolide: a mini review. *Avicenna J. Phytomed.* 6, 149–164.

Zwerina, J., Redlich, K., Schett, G., and Smolen, J. S. (2005). Pathogenesis of rheumatoid arthritis: targeting cytokines. *Ann. N. Y. Acad. Sci.* 1051, 716–729. doi: 10.1196/annals.1361.116

Conflict of Interest: The authors declare that the research was conducted in the absence of any commercial or financial relationships that could be construed as a potential conflict of interest.

frontiers in Bioengineering and Biotechnology

ORIGINAL RESEARCH
published: 24 June 2020
doi: 10.3389/fbioe.2020.00673

Antimony-Doped Tin Oxide Nanocrystals for Enhanced Photothermal Theragnosis Therapy of Cancers

Zhongjing Lv[1,2], Jiafeng Li[1], Feng Yang[1,2], Kun Cao[1], Qiang Bao[1], Yuhua Sun[1,2] and Jian Yuan[1]**

[1] Department of Stomatology, The Affiliated Hospital of Xuzhou Medical University, Xuzhou, China, [2] School of Stomatology, Xuzhou Medical University, Xuzhou, China

The doped semiconductor nanocrystal with free holes in valence band exhibits strong near-infrared (NIR) local surface plasmon resonance effects, which is essential for photothermal agents. Herein, the hydrophilic Sb doped SnO_2 nanocrystals were successfully prepared by a simple hydrothermal synthesis method. The doping makes the Sb doped SnO_2 nanocrystals possessing defect structures. Compared with the un-doped SnO_2 nanocrystals, Sb doped SnO_2 nanocrystals exhibit stronger absorption in the NIR region from 500 to 1,100 nm and higher photothermal conversion efficiency (up to 73.6%) which makes the synthesized Sb doped SnO_2 nanocrystals be used as excellent photothermal agents. Importantly, Sb doped SnO_2 nanocrystals can efficiently kill cancer cells both *in vitro* and *in vivo* under the irradiation of a 980 nm laser with a power density of 0.6 W cm^{-2}. In addition, Sb doped SnO_2 nanocrystals can also be served as efficient CT imaging agents owing to the large X-ray attenuation coefficient of tin.

Keywords: Sb doped SnO_2 nanocrystals, near-infrared absorption, photothermal agents, CT imaging, photothermal theragnosis therapy

OPEN ACCESS

Edited by:
Bo Li,
Shanghai Jiao Tong University, China

Reviewed by:
Xiaojuan Huang,
Shanghai Jiao Tong University, China
Zhiyin Xiao,
Jiaxing University, China

****Correspondence:***
Zhongjing Lv
zhongjing_lv2012@163.com
Jian Yuan
yuanjian2009_2010@163.com

Specialty section:
This article was submitted to Biomaterials, a section of the journal Frontiers in Bioengineering and Biotechnology

Received: *27 April 2020*
Accepted: *01 June 2020*
Published: *24 June 2020*

Citation:
Lv Z, Li J, Yang F, Cao K, Bao Q, Sun Y and Yuan J (2020) Antimony-Doped Tin Oxide Nanocrystals for Enhanced Photothermal Theragnosis Therapy of Cancers. Front. Bioeng. Biotechnol. 8:673. doi: 10.3389/fbioe.2020.00673

INTRODUCTION

Photothermal therapy (PTT) is a technique that uses light absorbers (i.e., photothermal agents) to absorb near-infrared (NIR) laser energy to generate excessive heat to "cook" cancer cells (Yang et al., 2010; Li et al., 2013). It is a potential and effective method to target cancer cells without damaging to surrounding healthy tissues. Nanomaterials currently reported with special optical properties are widely served as photothermal therapeutic agents, mainly including the following categories, namely, organic compound nanomaterials, carbon-based nanomaterials, precious metal nanostructures, and semiconductor nanomaterials (Zhang et al., 2012; Chen et al., 2013, 2014; Yang et al., 2013). Among these, the most widely studied photothermal agents are gold nanostructures which have excellent photothermal conversion effects, but their stability decreases after long-term laser irradiation (Zhang et al., 2012). Therefore, researchers have developed some novel photothermal therapy agents with good photostability. Improving the photothermal conversion efficiency of photothermal agents is essential for the practical application of photothermal therapy. For example, the photothermal conversion efficiency of polypyrrole material is 44.7% when excited

by 808 nm laser (Chen et al., 2012), the photothermal efficiency of $Cu_{7.2}S_4$ nanocrystal is 56.7% when excited by 980 nm laser (Li et al., 2014), and the photothermal efficiency of $Cu_{2-x}Se$ nanocrystal is 22.7% when excited by 808 nm laser (Hessel et al., 2011). Generally speaking, a photothermal agent which shows higher photothermal conversion efficiency could cause the same death rate of cancer cells with a shorter laser irradiation time, a lower laser irradiation density, or a lower dose of materials. In contrast, a photothermal agent which has lower photothermal conversion efficiency requires higher agent concentration, longer laser irradiation time, or higher laser power density. To give an example, because $Cu_{2-x}Se$ nanocrystals have low photothermal conversion efficiency, the 808 nm laser power density required for them as a photothermal agent is as high as 30 W cm^{-2} (Hessel et al., 2011), which is much higher than the laser power density limitation (0.33 W cm^{-2}) of the United States National Standard. In addition, in order to increase the *in vivo* circulation time of nanomaterials, the diameter of intravenously injected nanoparticles should generally be between 10 and 100 nm (Jiang et al., 2008; Choi et al., 2009). However, the diameters of some reported photothermal agents deviate from this size range. For example, CuS superstructure (Tian et al., 2011b), $W_{18}O_{49}$ nanowire (Chen et al., 2013), Au nanoshell (Liu et al., 2012), hollow CuS nanoparticle (Dong et al., 2013) and polyaniline (Yang et al., 2011) are all larger than 100 nm; Fe_3O_4 @ $Cu_{2-x}S$ (Tian et al., 2013) and Ge nanoparticles (Lambert et al., 2007) are smaller below 10 nm, thus limiting their bioapplications. It has been reported that large nanoparticles would be excluded through the reticuloendothelial tissue system (principally from the spleen and liver), small nanoparticles may be excluded through the kidney (Osaki et al., 2004; De Jong et al., 2008). In order to meet the extensive needs of PTT in the future, some novel photothermal therapeutic agents showing suitable size, good photostability, high photothermal performance, and low toxicity are necessary to be developed for effective photothermal therapy of cancer cells.

As a new type of photothermal conversion materials, semiconductor nanomaterials have many unique advantages. For example, semiconductor nanomaterials have the advantages of low cost, stable performance, easy functionalization, and facile preparation (Li et al., 2015). Two types of semiconductor photothermal nanomaterials, according to the causes of NIR absorption, have been reported. The first category is defect-structure semiconductor photothermal nanomaterials. The near-infrared absorption for this kind of materials is caused by the migration of carrier concentration caused by defects, and the absorption intensity and position vary with the degree of defects, including copper-based chalcogenides and transition metal oxides (Tian et al., 2011a; Chen et al., 2013). Copper-based chalcogenides are mainly p-type semiconductors with copper defects and many hole carriers whose migration could produce NIR absorption. The near-infrared absorption source of photothermal materials for transition metal oxides is resulted from oxygen deficiency. The second type is intrinsic semiconductors. The near-infrared absorption for this kind of nanomaterials is based on intrinsic band gap absorption (Song et al., 2015), including WS_2, MoS_2, Bi_2Se_3, etc. Compared with intrinsic semiconductor photothermal conversion materials, there are more types of defect-structured semiconductor photothermal agents. Plasma absorption peaks can also be tuned by defect adjustment to further improving its photothermal effect, but intrinsic semiconductors do not have this property.

The free holes in valence band of doped semiconductor nanocrystal make the nanocrystals strong and tunable near-infrared local surface plasmon resonance effects (LSPRs) (Luther et al., 2011). Furthermore, by doping and adjusting the plasmon resonance wavelength of the nanocrystal to be equal to or close to the wavelength of the driving laser, the photothermal performance of the nanocrystals can be great improved (Li et al., 2014). These properties have prompted us to develop new types of semiconductor nanocrystals with suitable sizes, high self-doping. To the best of our knowledge, this work is the first report on Sn doped SnO_2 nanocrystals as photothermal agents, with a diameter of approximately 18 nm, strong NIR absorption, 73.6% photothermal conversion efficiency. Most importantly, these nanoparticles can be suitably used as 980 nm laser-driven photothermal therapy agents, and can effectively kill cancer cells both *in vivo* and *in vitro* under the irradiation of a 980 nm laser with a prompt laser power density (0.6 W cm^{-2}). In addition, the Sn doped SnO_2 nanocrystals can also be used as CT imaging agents due to inherent properties, i.e., large X-ray attenuation coefficient of tin.

MATERIALS AND METHODS

Synthesis of Sb Doped SnO_2 Nanocrystals

For a typical preparation of 10% Sb-doping nanocrystals, $SnCl_4$ (0.9 mmol) and $SbCl_3$ (0.1 mmol) were dissolved in 5 mL DMF to prepare the precursor. After that, the precursor was added in a Teflon-lined autoclave in a mixed solvent (20 mL DMF and 20 mL ethanol), followed by 0.5 g PVP and 10 mL PEG. The reaction was kept at 160°C for 20 h. The green precipitate was centrifuged at 10,000 rpm for 10 min and washed twice with ethanol. For the synthesis of un-doped SnO_2 nanocrystals, no $SbCl_3$ was added during the process of preparation the precursor. $SnCl_4$ (1.0 mmol) was dissolved in 5 mL DMF to prepare the precursor. For the synthesis of varied molar percent Sb-doped SnO_2 nanocrystals, different molar ratios of $SnCl_4$ and $SbCl_3$ were added, making the total amount of metal precursors 1 mmol. The following reaction conditions remained unchanged.

Characterization

For the information of microstructure, morphology, and size of Sb-SnO_2 nanocrystals and the un-doped SnO_2 nanocrystals, can be obtained from TEM microscope (JEOL JEM-2010F). XPS was obtained by -ray photoelectron spectrometer (ESCA-Lab). The UV-vis absorption spectrum data is passed through Shimadzu's UV-1900 UV-vis-NIR spectrophotometer, using a quartz cuvette with a light path of 1 cm. The XRD patterns were achieved from a X-ray diffractometer (Bruker D4). The tin ions can be determined by Leeman laboratory inductively coupled plasma atomic emission spectrometer (ICP-AES).

In order to test the photothermal performance of Sb-SnO_2 nanocrystals and the un-doped SnO_2 nanocrystals, a 980 nm laser was used to irradiate through a quartz cuvette filled with nanocrystal dispersions (80 ppm). A 980 nm laser with adjustable external power (0–2 W) was used as the light source. After calibration, the power is ∼0.3 W and the spot size is ∼0.15 cm^2. Insert a thermocouple with an accuracy of ±0.1°C into the appropriate position in the above aqueous dispersion to avoid direct laser irradiation to the probes. The temperature changes were recorded every 5 s by a thermocouple thermometer.

CT Imaging With Sb-SnO_2 Nanocrystals

Sb-SnO_2 nanocrystals with different concentrations were scanned using a CT scanner. Before injection of Sb-SnO_2 nanocrystals, the mice were subjected to CT scanning as a control. Then the nanocrystals dispersion (5 mg/kg) was intratumorally injected into tumor model mice, and then the mice were subjected to CT scanning.

Photothermal Therapy of *in vitro* Cancer Cells With Sb-SnO_2 Nanocrystals

SCC15 cells were distributed in 96-well plates at a density of 100,000 cells per well, and cultured in RPMI-1640 medium at a temperature of 37°C and a CO_2 concentration of 5% for 24 h. Subsequently, the cell culture medium was removed, and the cells were washed three times with PBS buffer solution. 100 μL Sb-SnO_2 nanocrystal dispersed in PBS was added to different wells at a concentration gradient, and the culture was continued for 24 h. Using a 980 nm laser with a power of 0.6 W cm^{-2} (power ∼0.3 W, spot size ∼0.15 cm^2), the cells were irradiated for 0 min and 5 min, respectively, and then the cell survival rate was detected by CCK-8 essay. All tests are performed independently twice.

Quantitative Analysis of Extracellular Phagocytosis

The uptake of Sb-SnO_2 nanocrystals by SCC15 cells by was evaluated by ICP-AES. SCC15 cells were first seeded in 24 well plates, each with a density of 1×10^6 cells. After incubation with for 24 h, 200 μL of Sb-SnO_2 nanocrystals were then added to different wells (0, 20, 40, and 80 ppm). After incubation for 12 h, the cell culture fluid was removed. Prior to ablation with aqua regia, cells were carefully washed 5 times with PBS, and then diluted with ultrapure water for ICP-AES analysis to measure the amount of nanocrystals taken up by each cell.

Photothermal Therapy of *in vivo* Cancer Cells With Sb-SnO_2 Nanocrystals

All animal experiments are conducted according to the guidelines of the Animal Protection and Use Committee. Some immunodeficiency (SCID) nude mice were simultaneously inoculated with 1×10^6 SCC15 cells and the tumors were cultured for 28 days. SCID nude mice were randomly divided into four groups when the tumors grew to 5–8 mm in diameter, In Group 1, the mice were intratumorally injected only with PBS solution (PBS); In Group 2, the mice were only irradiated with 980 nm laser (NIR); In Group 3, the mice were intratumorally injected with un-doped SnO_2 nanocrystals (80 ppm) dispersed in PBS solution, and then irradiated with 980 nm laser (SnO_2 + NIR); In Group 4, the mice were intratumorally injected with Sb-SnO_2 nanocrystals (80 ppm) dispersed in PBS solution, and then irradiated with 980 nm laser (Sb-SnO_2 + NIR). The tumor mice in the Group 2 and Group 4 were simultaneously irradiated with a 980 nm laser (0.6 W cm^{-2}) for 5 min. During laser treatment, real-time infrared thermal imaging of the whole body of the mouse was recorded by using a photothermal analysis medical device attached to an infrared camera.

After the indicated treatments, the mice were sacrificed, and the tumor was removed and embedded in paraffin to make 4 μm slices. These slices were stained with H&E, inspected with the fluorescent lens of the Zeiss lens 40CFL, and the images were processed with the Zeiss image camera system.

Main Organ Analysis for Long-Term Toxicity

As for the main organ' histological examination analysis, a healthy mouse was intravenously injected with Sb-SnO_2 nanocrystals (10 mg/kg); as a control, another mouse was intravenously injected with PBS. After 15 days, the main organs (including heart, kidney, spleen, liver, and lung) from the sacrificed mice were harvested, and then sectioned into 4 μm slices, stained with H&E. The slices were examined via a microscope. To study the distribution of the Sb-SnO_2 nanocrystals, healthy mice were intravenously injected with Sb-SnO_2 nanocrystals (10 $mg{\cdot}kg^{-1}$). These mice were sacrificed to extract major organs at indicated time points (i.e., 1, 3, 7, and 14 days, n = 4 at each time point). These organs were then solubilized and then diluted using deionized water for ICP-MS analysis to determine tin content in each sample.

RESULTS AND DISCUSSION

In the presence of a surface ligand (PVP) and a mixed solvent (ethanol and DMF), hydrophilic nanocrystals coated with PVP (determined by FTIR in **Supplementary Figure S1**) can be prepared by a simple hydrothermal synthesis method. In order to determine the structural crystal phase of the synthesized nanocrystals, we used X-ray diffractometer to characterize the samples, as shown in **Figure 1a**. All the X-ray diffraction peaks of the as-prepared products can be well matched with the cassiterite phase SnO_2 without any other phases (such as Sb_2O_5 and SnO), indicating that the doped Sb occurs by replacing Sn atoms in the SnO_2 structure. In addition, the lattice constants are very close to those in the JCPDS file (No. 14-1445), which proved that the Sb doped SnO_2 nanocrystals were formed. Transmission electron microscopy (TEM) images show that the Sb-SnO_2 nanocrystals are well dispersed (**Figure 1b**), with an average diameter of ∼18 nm. Further microstructural information of the synthesized Sb-SnO_2 nanocrystals can be obtained from high resolution transmission electron microscopy (HRTEM, **Supplementary Figure S2**). The HRTEM image shows that the sample is single crystal with a lattice spacing of 0.334 nm,

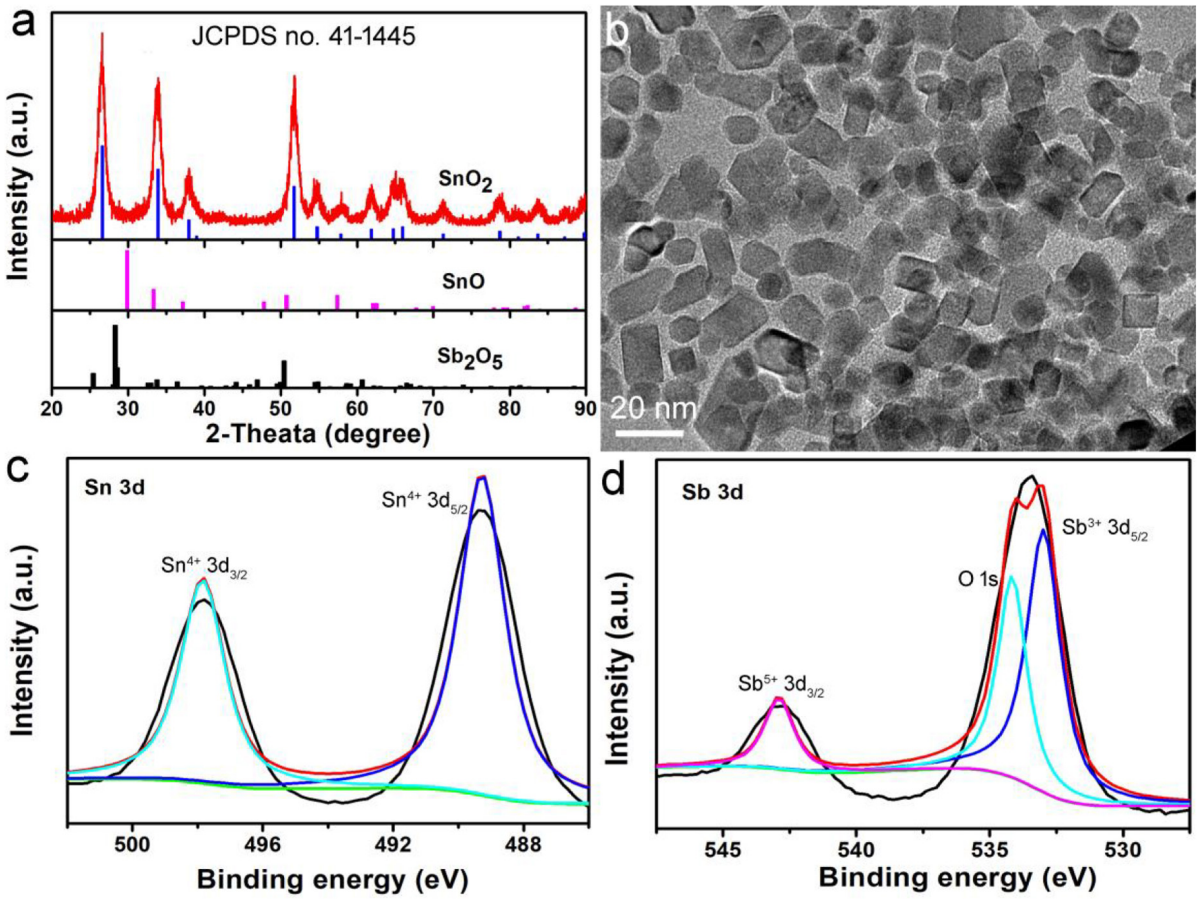

FIGURE 1 | (a) XRD patterns and **(b)** TEM image of Sb-SnO_2 nanocrystals. High resolution XPS spectra of **(c)** Sn 3d and **(d)** Sb 3d in Sb-SnO_2 nanocrystals.

which can be indexed to the (110) crystal plane of the Sb-SnO_2 crystal. In addition, the obtained fast Fourier transform (FFT) (**Supplementary Figure S3**) can belonged to the [110] crystal band axis of Sb-SnO_2 crystals. To further confirming the oxidation states of Sb and Sn atoms, XPS analysis was performed. From the XPS results, one can see that there was only Sb, Sn, and O in the Sb doped SnO_2 (Sb-SnO_2) without other impurities (**Supplementary Figure S4**). The high resolution XPS spectra of Sn 3d in Sb-SnO_2 were given in **Figure 1c**. The peaks at 487.4 and 495.8 eV were assigned to Sn $3d_{5/2}$ and Sn $3d_{3/2}$ of Sn (IV) in Sb-SnO_2 crystals, respectively (Xu et al., 2013). The binding energies at 533.4 and 542.8 eV can be, respectively, attributed to Sn^{3+} $3d_{5/2}$ and Sn^{5+} $3d_{3/2}$ in Sb-SnO_2 crystals (**Figure 1d**). The mixed valence of Sn in Sb-SnO_2 nanocrystals indicated the defect structures of the nanocrystals, which is essential for the optical properties of semiconductor photothermal agents. The actual doping contents can be obtained from the XPS analysis. It was found to be about 9.2%, which are slightly lower than the target content. Based the results above, it can be proved that we have successfully synthesized Sb-SnO_2 nanocrystals.

The most notable feature of the obtained Sb-SnO_2 nanocrystals is that they have strong absorption in the near infrared region due to the defect structure. PVP-coated Sb-SnO_2 nanocrystals are well dispersed in water even for a month, still showing strong NIR absorption, indicating that the nanocrystals have good stability and good dispersion. **Figure 2A** shows the UV-vis-NIR absorption spectra of Sb-SnO_2 nanocrystals at a concentration of 80 ppm. As demonstrated in **Figure 1d**, there was defect structure in the Sb-SnO_2 nanocrystals, which made the nanocrystals showing strong NIR absorption. There was an enhanced absorption from 500 to 1,100 nm. The strong absorption strength is mainly attributed to many defects and high monodispersion. However, the un-doped SnO_2 nanocrystals showed little NIR absorption (resulted from the band gap absorption) as they have no defect structures (**Figure 2B**). Due to the near-infrared absorption characteristics of Sb-SnO_2 nanocrystals and the strong absorption wavelength at 980 nm, these nanocrystals can be better used as photothermal agents for cancer treatment driven by 980 nm laser. We then measured the photothermal performance of Sb-SnO_2 nanocrystals (80 ppm) under the continuous irradiation of a 980 nm laser with a power of 0.3 W. The nanocrystals' temperature increased from room temperature (26.7°C) to 57.2°C (**Figure 2C**). As an alternative, pure water was also irradiated by 980 nm laser for 5 min and only increased from room temperature to 30.2°C, and the temperature rise was less than 4°C. To better illustrate the

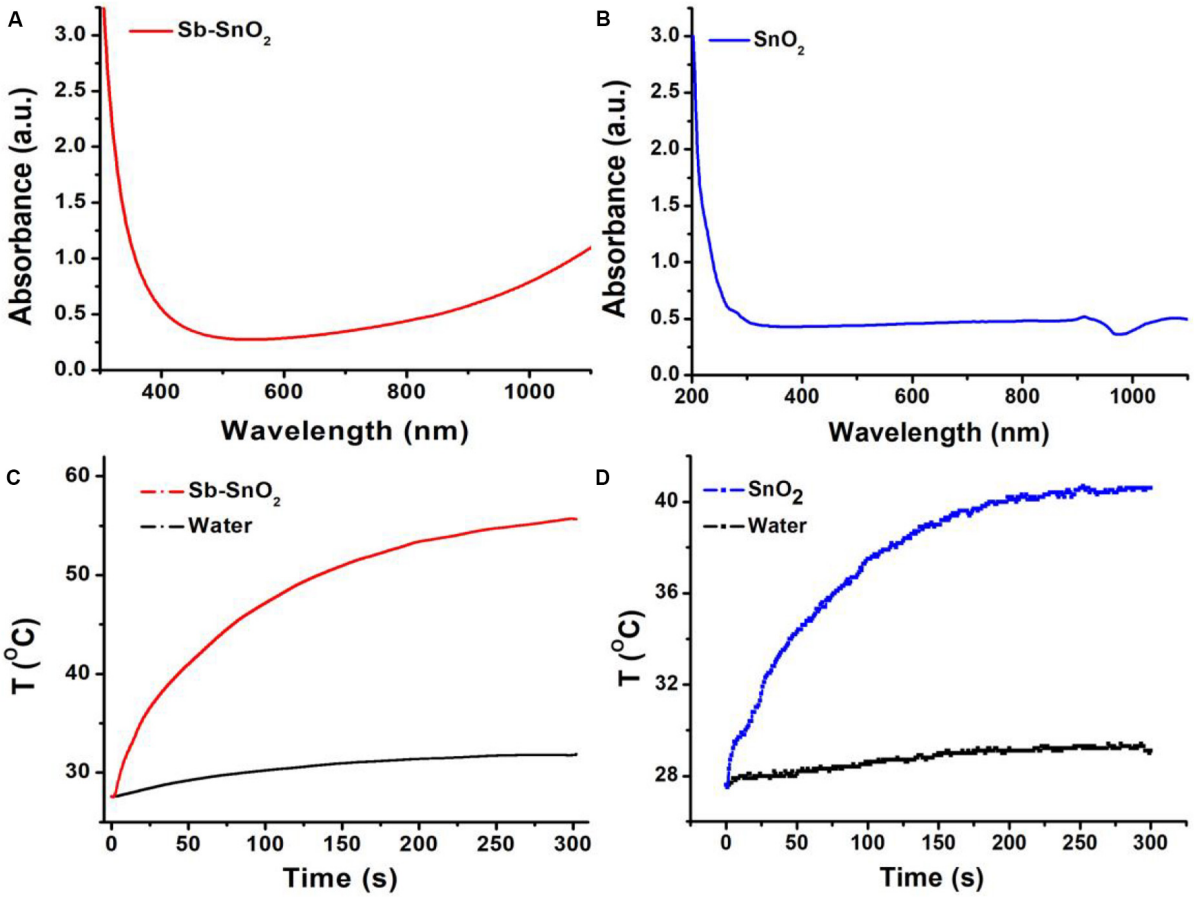

FIGURE 2 | (A) UV-vis spectra and **(B)** photothermal effect of Sb-SnO_2 nanocrystals. **(C)** UV-vis spectra and **(D)** photothermal effect of SnO_2 nanocrystals.

photothermal effect of Sb-SnO_2 nanocrystals, the photothermal conversion of un-doped SnO_2 nanocrystals was also measured. As shown in **Figure 2D**, the temperature of un-doped SnO_2 nanocrystals at the same condition only increased from room temperature to 41.8°C which is much lower than that of Sb-SnO_2 nanocrystals. Therefore, the doping in SnO_2 nanocrystals made Sb-SnO_2 nanocrystals possess defect, strong NIR absorption, and excellent photothermal effect.

The photothermal conversion efficiency is an important index for evaluating the photothermal performance of photothermal agents. Generally speaking, photothermal reagents with high photothermal conversion efficiency cause the same death rate of cancer cells only with lower agent concentration, shorter illumination time, or lower laser irradiation power density, which is a healthy biological tissue advantageous. In order to further study the advantages of the photothermal properties of our synthesized Sb-SnO_2 nanocrystals, we tested the photothermal conversion efficiency of Sb-SnO_2 nanocrystals.

According to the report of Roper et al. (2007), we tested the photothermal conversion efficiency of Sb-SnO_2 nanocrystals. The nano-particles are dispersed in the medium (such as water). After laser irradiation with a certain power, the light energy is converted into thermal energy. The heat transferred by the nano-particles to the medium is a fixed value per unit time. When the heat transfer from the nanoparticles to the medium reaches a balance with the heat transfer from the medium to the surrounding environment, the temperature will not change. Based on this, Roper derives the calculation formula (1) of the photothermal conversion efficiency as following:

$$\eta_T = \frac{hA(T_{max} - T_{amb}) - Q_0}{I(1 - 10^{-A_\lambda})} \quad (1)$$

In which h is the heat transfer coefficient and A is the surface area of the container. T_{max} is the highest temperature of the system, and T_{amb} is the ambient temperature. I is the laser power (mW), and A_λ is the absorption of the medium at the excitation wavelength. Q_0, heat input rate (mW) of the system, can be independently calculated due to the light absorption of the solution. hA can be obtained by measuring the rate of cooling temperature after light source shut off. The value of hA is obtained by the following formula (2):

$$\tau_s = \frac{m_D C_D}{hA} \quad (2)$$

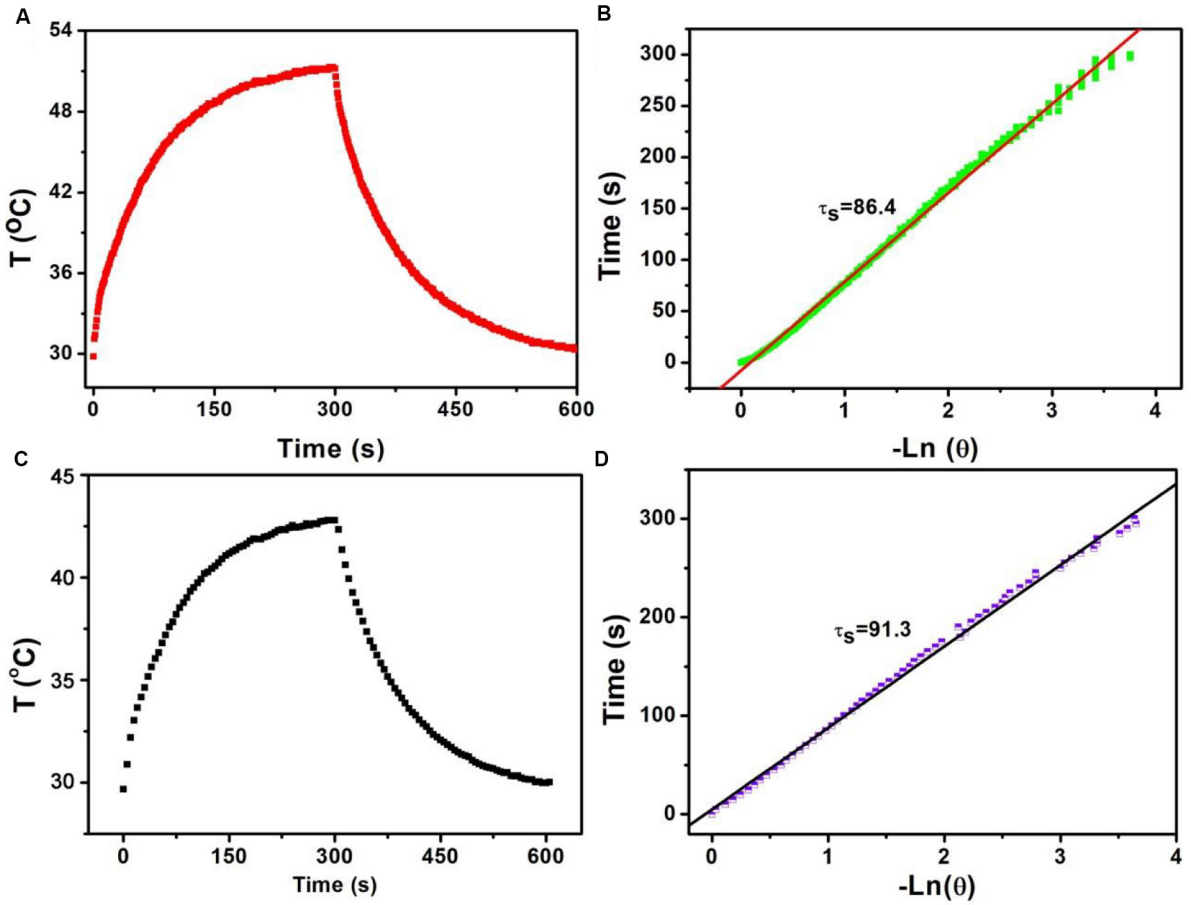

FIGURE 3 | (A) Temperature change of Sb-SnO_2 nanocrystals irradiated by a 980 laser for 300 s, then shut off the laser for 300 s. **(B)** Time constant of Sb-SnO_2 nanocrystals. **(C)** Temperature change of un-doped SnO_2 nanocrystals irradiated by a 980 laser for 300 s, then shut off the laser for 300 s. **(D)** Time constant of un-doped SnO_2 nanocrystals.

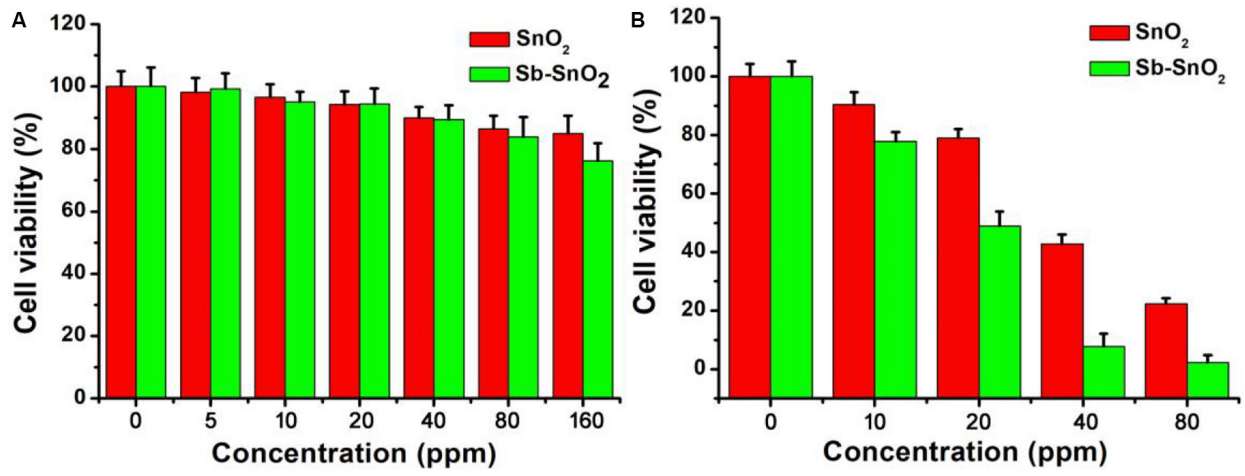

FIGURE 4 | (A) CCK-8 essay for Sb-SnO_2 nanocrystals and SnO_2 nanocrystals incubated with cells for 24 h, respectively. **(B)** Photothermal therapy of cancer cells *in vitro* with Sb-SnO_2 nanocrystals and SnO_2 nanocrystals, respectively.

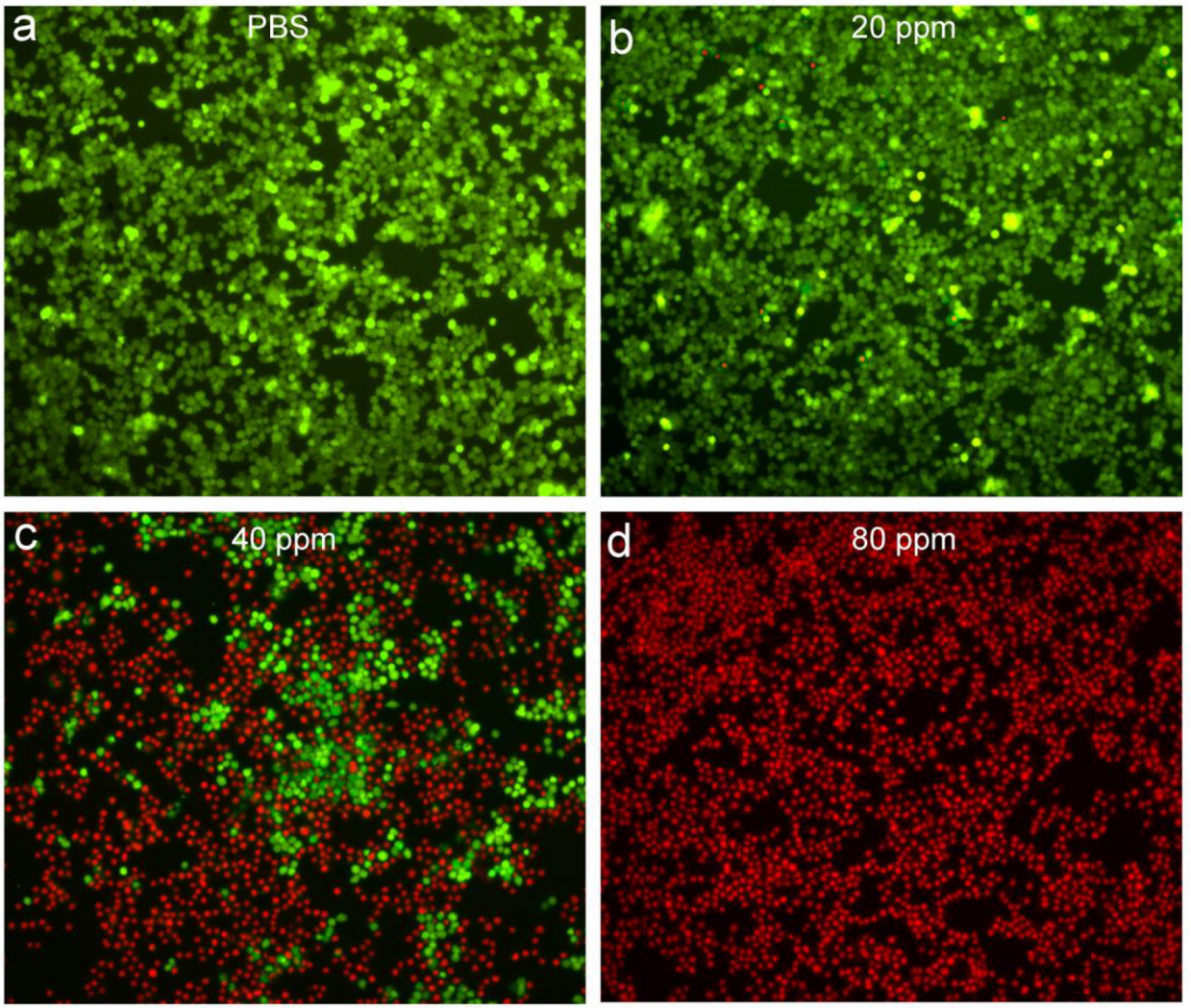

FIGURE 5 | Confocal micrographs of the cells after different treatments: **(a)** PBS, **(b)** 20 ppm nanocrystals, **(c)** 40 ppm nanocrystals, **(d)** 80 ppm nanocrystals. The cells were irradiated by a 980 nm laser with a power density of 0.6 W cm^{-2}. Magnification: 100 times.

Where τ_s is the time constant of the cooling system after the laser shut off, and m_D and C_D are the mass and specific heat capacity of the dispersed nanoparticle medium, respectively.

Based on the above formula, we can calculate the photothermal conversion efficiency of Sb-SnO_2 nanocrystals. We used a 980 nm laser with a power density of 0.3 W to irradiate the Sb-SnO_2 nanocrystal water dispersion (80 ppm), and then the laser was turned off to allow it to cool naturally. The temperature change during the entire process was recorded, as shown in **Figure 3A**. According to the cooling process after the laser turned off, the negative natural logarithm curve of cooling time and temperature driving force is obtained (**Figure 3B**). According to **Figure 3A**, $(T_{max} - T_{amb})$ is 21.4°C. According to **Figure 2A**, the value of A_{980} is 0.75. Q_0 was measure to be 130.4 mW by independent measurement of pure water without nanocrystals. The mass of water is 0.3 g and the specific heat capacity is 4.2 J g^{-1}. In **Figure 3B**, the slope of the curve is the time constant of heat transfer in the system, τ_s is 86.4 s. Therefore, the heat conversion efficiency of Sb-SnO_2 nanocrystals under the 980 nm laser irradiation can be calculated to be 73.6%. This value (73.6%) is much higher than those of other semiconductor photothermal agents. To better understanding the effect Sb-doping on photothermal conversion efficiency of Sb- SnO_2 nanocrystals, we have calculated the photothermal conversion efficiencies of varied Sb-doping. The results were shown in **Supplementary Table S1**. It was found that photothermal conversion efficiency increased with the increase of Sb doping, but the increasing trend slowed down when the doping content reached to 8%. As a control, the photothermal conversion efficiency of un-doped SnO_2 nanocrystals under the same conditions was calculated to be 52.4% (**Figures 3C,D**), much lower than that of Sb-SnO_2 nanocrystals due to the fact that no defects existed in un-doped SnO_2 nanocrystals. In general, the photothermal conversion efficiency is higher with higher NIR absorption. In addition, due

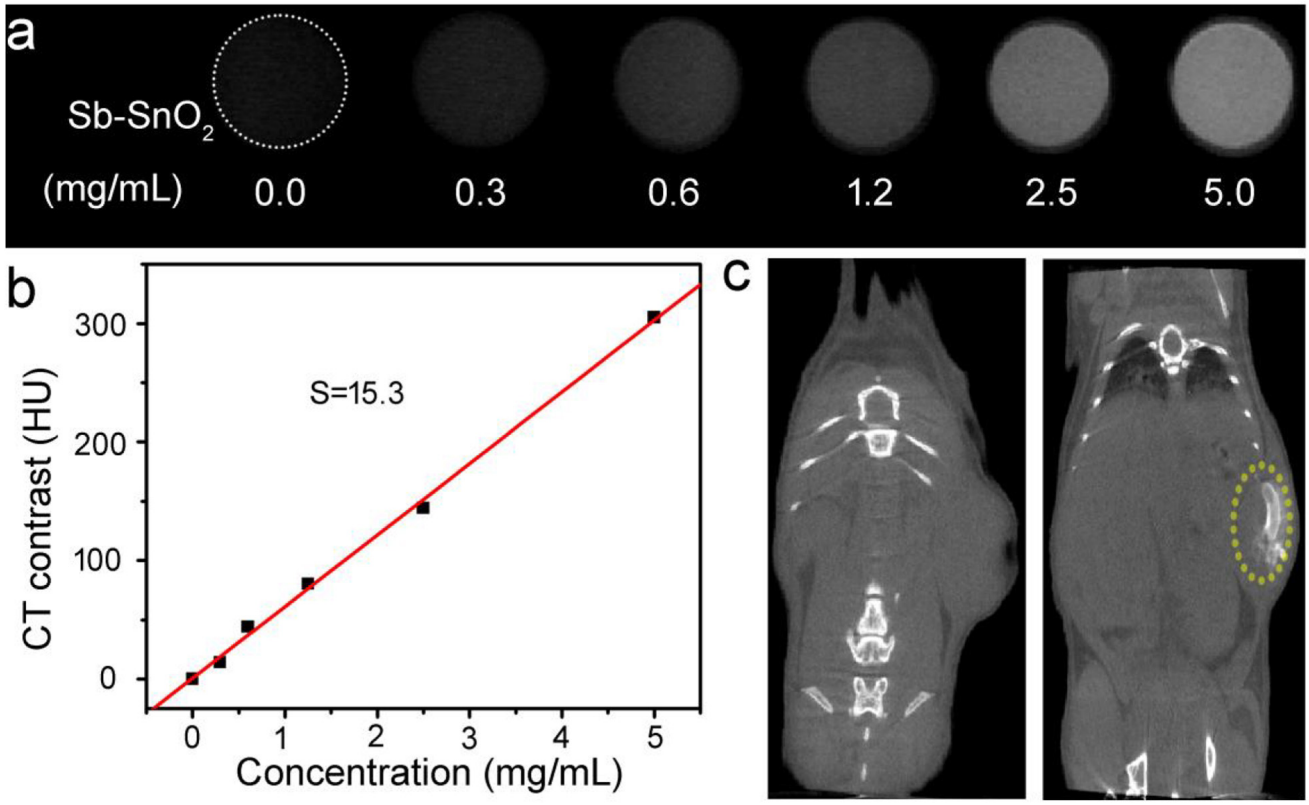

FIGURE 6 | (a) CT signals of Sb-SnO_2 nanocrystals with varied concentrations. **(b)** CT contrast value vs. the concentration of nanocrystals. **(c)** CT image of a mouse before (left) and after (right) the injection of nanocrystals.

to the size-dependent light absorption and scattering effects, the photothermal conversion efficiency of Sb-SnO_2 nanocrystals is higher than those of the previously reported nanoparticles with lager size.

As the synthesized Sb-SnO_2 nanocrystals have high photothermal conversion efficiency, we therefore believe that these synthesized nanocrystals can be used as an excellent photothermal therapeutic agent. To confirm our conjecture, we first used the CCK-8 essay with SCC15 cells to evaluate the photothermal toxicity of Sb-SnO_2 nanocrystals *in vitro*. Therefore, we cultured different concentrations of Sb-SnO_2 nanocrystal dispersion in PBS (0, 5, 10, 20, 40, 80, and 160 ppm) with SCC15 cells for 24 h, and then tested the cell viability by CCK-8 essay. We first studied the destruction of cells with Sb-SnO_2 nanocrystalline PBS dispersion in the absence of laser irradiation, as shown in **Figure 4A**. The results showed that at a material concentration of 40 ppm, the cell survival rate is about 90% (**Figure 4A**). When the concentration increased to 80 ppm, the cell viability was still above 80%, indicating the good biocompatibility. Compared with the un-doped the SnO_2 (green histogram), the biocompatibility showed little difference. The good biocompatibility provides an effective reference to evaluate the damage of Sb-SnO_2 nanocrystals to cells under the laser irradiation. It can be seen from **Figure 4B** (red histogram) that in the presence of Sb-SnO_2 nanocrystals (80 ppm), only ∼2% of the cells were survived when irradiated by a 980 nm laser (output power 0.6 W cm^{-2}) for 5 min. As a control, ∼98% of the cells without laser irradiation were survived (red histogram), which demonstrated that Sb-SnO_2 nanocrystals can be of promising photothermal agents. We also evaluated the photothermal toxicity of un-doped SnO_2 to cancer cells (green histogram). We can directly see that the cell viability is much lower using un-doped SnO_2 nanocrystals. ∼22% of the cells treated with un-doped SnO_2 were survived, while only ∼2% of cells survived treated with Sb-SnO_2 nanocrystals. In order to better evaluate the efficiency of Sb-SnO_2 nanocrystals as a photothermal agent *in vitro*, it is very necessary to study the uptake effect of nanocrystals by cancer cells. We used ICP-AES to detect the amount of nanocrystals taken by each cell after co-incubation of Sb-SnO_2 nanocrystals and SCC15 cells for 12 h. As shown in **Supplementary Figure S5**, with the increase of the concentration of nanocrystals (i.e., 0–80 ppm), the uptake of nanocrystals per cell after 12 h of culture increased (0.080–5.35 pg/cell). This indicated that Sb-SnO_2 nanocrystals can be engulfed by cells through endocytosis.

In order to more intuitively observe the effect of the photothermal effect of Sb-SnO_2 nanocrystals on the SCC15 cells, we stained the live and dead cells with calcein-AM and propidium iodide. **Figures 5a–d** shows the confocal micrographs of the cells after different treatments. It indicated that the

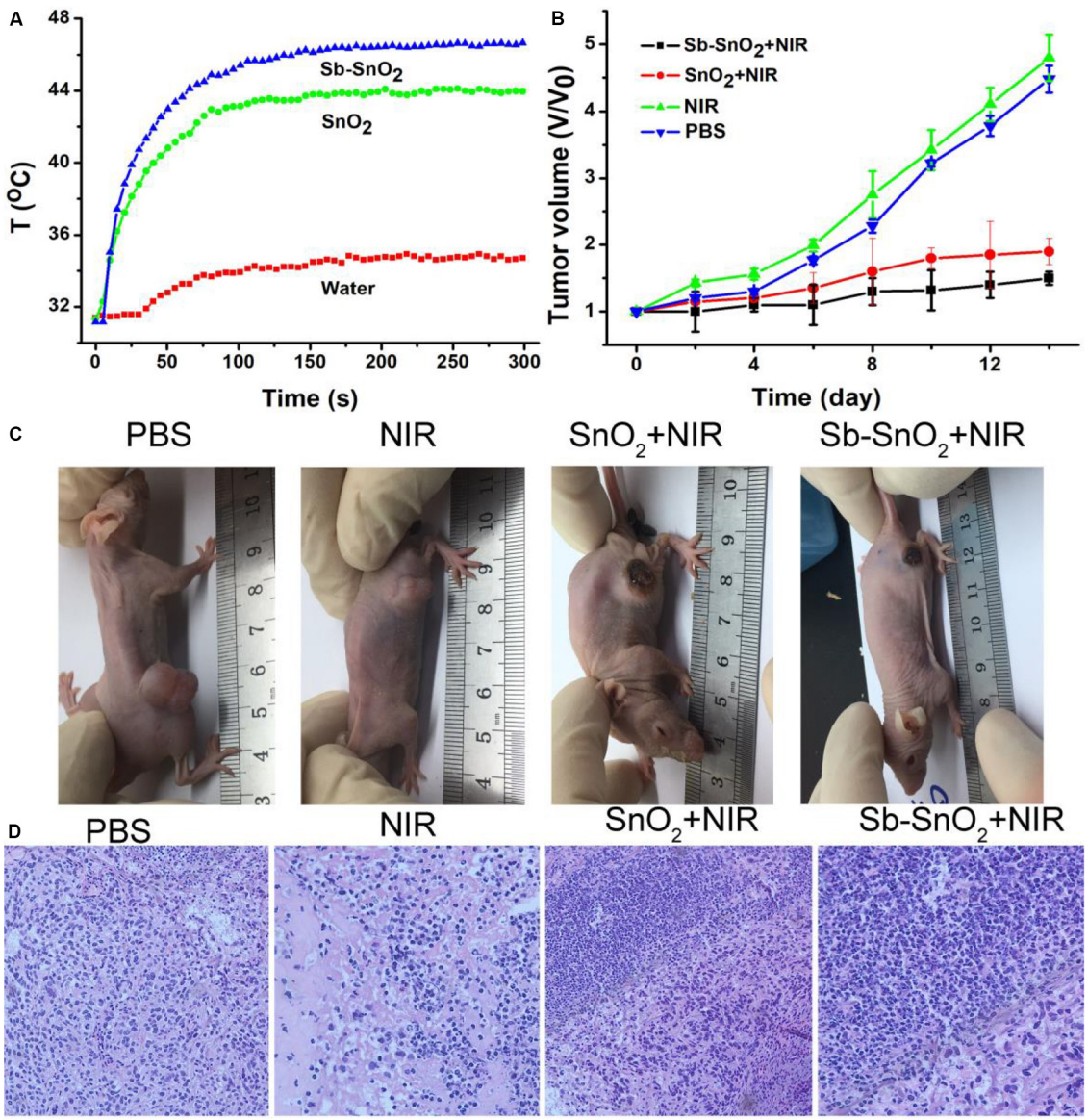

FIGURE 7 | (A) Photothermal effect after injection of PBS, SnO_2, and Sb-SnO_2, respectively. **(B)** Tumor volume changes in different groups. **(C)** Mice picture after indicated treatments for 14 days. **(D)** H&E images of *ex vivo* tumor sections in different groups.

dead cells increased more with the increase of concentration of nanocrystals. When the concentration of nanocrystals was 80 ppm, all the cells are almost dead. The results of live/dead cell staining analysis were matched well with CCK8 assay. Both the live/dead cell staining analysis and the CCK8 assay confirmed that Sb-SnO_2 nanocrystals combined with NIR laser irradiation showed a good inhibitory effect on SCC15 cell proliferation.

Sb-SnO_2 nanocrystals not only have a good photothermal effect, but also have great potential in CT imaging diagnosis. Since Sn has a large atomic number, it can have a large X-ray attenuation coefficient like Au, Bi, and I (Liu et al., 2016; Zhou et al., 2016). Thus Sb-SnO_2 nanocrystals can be used as CT contrast agents. To test the hypothesis, we measured the Sb-SnO_2 nanocrystals with different concentrations for CT imaging scanning experiments. It showed that the CT signal increased with the increase of the concentration of nanocrystals (**Figure 6a**). At the same time, it can be seen in **Figure 6b** that as the HU value of nanocrystals increased linearly with concentration, which illustrated the water dispersion of nanocrystals showing good dispersibility. The slope of the HU value of this nanocrystals is about 15.3 HU L/g (**Figure 6b**), which is high enough for CT imaging. Next, we evaluated the *in vivo* CT imaging performance of Sb-SnO_2 nanocrystals. Before injection of Sb-SnO_2 nanocrystals, the mice were subjected to CT scanning as a control. Then the nanocrystals dispersion was injected into tumor model mice by intratumoral injection. **Figure 6c** reveals

the CT view of the mouse tumor site before and after the injection of nanocrystals (100 μL, 5 mg mL^{-1}). As shown in the figure, the tumor area has a clear signal after injection compared with before injection, and the corresponding tumor injection site also shows a bright contrast with other soft tissues. At the same time, the CT average of the tumor area is much higher than other soft tissues. These results indicated that Sb-SnO_2 nanocrystals can be used as an efficiency CT imaging agents.

In vitro cell experiments show that Sb-SnO_2 nanocrystals can effectively kill cancer cells under the drive of 980 nm laser. In order to make an overall assessment of the photothermal effect of Sb-SnO_2 nanocrystals, we also explored the photothermal treatment effect of Sb-SnO_2 nanocrystals on tumor model mice driven by 980 nm laser (**Supplementary Figure S6**). During the laser treatment, an infrared camera can be used to monitor the temperature change the tumor. As shown in **Figure 7A**, there was a significant heating effect under laser irradiation in Group 4; for comparison, there was a lower temperature increase in Group 3. This happened because Sb-SnO_2 nanocrystals had better photothermal effect than SnO_2 nanocrystals. For mice in Group 2, NIR laser alone cannot make the temperature of the tumor obvious increase.

After treatments, tumor volume changes are recorded every 2 days. As shown in **Figure 7B**, Tumor were significantly suppressed in group 4; the tumor suppression of the third group is lower than that of the fourth group. As comparison, the tumor in Groups 1and 2 grew rapidly and there was no obvious difference between the two groups. We can also see the difference in tumor changes from the pictures of the mice 14 days after treatments (**Figure 7C**), which was consistent with the tumor growth curves in **Figure 7B**. These results indicated that Sb-SnO_2 nanocrystals still showed excellent photothermal performance *in vivo*. It can be concluded that Sb-SnO_2 nanocrystals combined with NIR laser irradiation can successfully inhibited tumor growth due to the excellent the photothermal effect resulted from Sb-SnO_2 nanocrystals.

For further evaluation the photothermal ablation effect of tumor cells *in vivo*, we stained the tumor tissue with H&E. The micrograph after staining is shown in **Figure 7D**. As we expected, a large number of death of cancer cells treated by injection with Sb-SnO_2 nanocrystals and then laser irradiation were observed, but less cell death in SnO_2 nanocrystals and laser irradiation. For the control groups, the shape and size of cancer cells were almost unchanged. These results indicated that cancer cells *in vivo* can also be effectively destroyed by the high temperature generated by the photothermal effect of Sb-SnO_2 nanocrystals. Taken together, these results undoubtedly confirm that the synthesized Sb-SnO_2 can be used as excellent photothermal theranostics agents due to their excellent photothermal effect and CT imaging performance, and have great potential for photothermal treatment of cancers.

To evaluate the *in vivo* biosafety of Sb-SnO_2 nanocrystals, further bio-safety experiment on histological examination analysis with H&E staining for the main organs was conducted to observe the size, shape and number of cells after the intravenous injection of Sb-SnO_2 nanocrystals. From the H&E staining of the major organs including heart, kidney, spleen, liver, and lung, no inflammation or damage is observed (**Supplementary Figure S7**). To study the distribution of the Sb-SnO_2 nanocrystals, the contents of nanocrystals accumulated in main organs were also evaluated. It showed (**Supplementary Figure S8**) that the Sb-SnO_2 nanocrystals mainly accumulate at liver and spleen, which indicates that this material was mainly degraded in these two organs.

CONCLUSION

In conclusion, the hydrophilic Sb doped SnO_2 nanocrystals with a size of 18 nm were successfully prepared by a facile hydrothermal synthesis method. The doping makes the Sb-SnO_2 nanocrystals possessing defect structures, which contributes to the enhanced absorption in the NIR region. Thus the Sb-SnO_2 nanocrystals show excellent photothermal effect, with photothermal conversion efficiency up to 73.6%. Compared with un-doped SnO_2 nanocrystals, experiments on cancer cells both *in vitro* and *in vivo* proved that the photothermal effect from Sb-SnO_2 nanocrystals can more effectively kill cancer cells. In addition, Sb-SnO_2 nanocrystals can also be used as efficient CT imaging agents owing to the large X-ray attenuation coefficient of tin. Therefore, the synthesized Sb-SnO_2 nanocrystals can be used as excellent photothermal theragnosis agents.

DATA AVAILABILITY STATEMENT

All datasets generated for this study are included in the article/**Supplementary Material**.

ETHICS STATEMENT

The animal study was reviewed and approved by Affiliated Hospital of Xuzhou Medical University.

AUTHOR CONTRIBUTIONS

ZL and JY designed the project. ZL, JL, FY, and KC carried out the experiments. ZL, QB, and YS performed the experimental data analysis. ZL and JY wrote the manuscript. All authors contributed to discussion of the results.

FUNDING

This study was supported by the Natural Science Foundation of Jiangsu Province (BK20160225).

SUPPLEMENTARY MATERIAL

The Supplementary Material for this article can be found online at: https://www.frontiersin.org/articles/10.3389/fbioe.2020.00673/full#supplementary-material

REFERENCES

Chen, M., Fang, X., Tang, S., and Zheng, N. (2012). Polypyrrole nanoparticles for high-performance in vivo near-infrared photothermal cancer therapy. *Chem. Commun.* 48, 8934–8936.

Chen, Q., Wang, C., Zhan, Z., He, W., Cheng, Z., Li, Y., et al. (2014). Near-infrared dye bound albumin with separated imaging and therapy wavelength channels for imaging-guided photothermal therapy. *Biomaterials* 35, 8206–8214. doi: 10.1016/j.biomaterials.2014.06.013

Chen, Z., Wang, Q., Wang, H., Zhang, L., Song, G., Song, L., et al. (2013). Ultrathin PEGylated W18O49 nanowires as a new 980 nm-laser-driven photothermal agent for efficient ablation of cancer cells in vivo. *Adv. Mater.* 25, 2095–2100. doi: 10.1002/adma.201204616

Choi, H. S., Ipe, B. I., Misra, P., Lee, J. H., Bawendi, M. G., and Frangioni, J. V. (2009). Tissue- and organ-selective biodistribution of NIR fluorescent quantum dots. *Nano Lett.* 9, 2354–2359. doi: 10.1021/nl900872r

De Jong, W. H., Hagens, W. I., Krystek, P., Burger, M. C., Sips, A. J., and Geertsma, R. E. (2008). Particle size-dependent organ distribution of gold nanoparticles after intravenous administration. *Biomaterials* 29, 1912–1919. doi: 10.1016/j.biomaterials.2007.12.037

Dong, K., Liu, Z., Li, Z., Ren, J., and Qu, X. (2013). Hydrophobic anticancer drug delivery by a 980 nm laser-driven photothermal vehicle for efficient synergistic therapy of cancer cells in vivo. *Adv. Mater.* 25, 4452–4458. doi: 10.1002/adma.201301232

Hessel, C. M., Pattani, V. P., Rasch, M., Panthani, M. G., Koo, B., Tunnell, J. W., et al. (2011). Copper selenide nanocrystals for photothermal therapy. *Nano Lett.* 11, 2560–2566. doi: 10.1021/nl201400z

Jiang, W., Kim, B. Y., Rutka, J. T., and Chan, W. C. (2008). Nanoparticle-mediated cellular response is size-dependent. *Nat. Nanotechnol.* 3, 145–150. doi: 10.1038/nnano.2008.30

Lambert, T. N., Andrews, N. L., Gerung, H., Boyle, T. J., Oliver, J. M., Wilson, B. S., et al. (2007). Water-soluble germanium(0) nanocrystals: cell recognition and near-infrared photothermal conversion properties. *Small* 3, 691–699. doi: 10.1002/smll.200600529

Li, B., Wang, Q., Zou, R., Liu, X., Xu, K., Li, W., et al. (2014). Cu7.2S4 nanocrystals: a novel photothermal agent with a 56.7% photothermal conversion efficiency for photothermal therapy of cancer cells. *Nanoscale* 6, 3274–3282.

Li, B., Ye, K., Zhang, Y., Qin, J., Zou, R., Xu, K., et al. (2015). Photothermal theragnosis synergistic therapy based on bimetal sulphide nanocrystals rather than nanocomposites. *Adv. Mater.* 27, 1339–1345. doi: 10.1002/adma.201404257

Li, W., Zamani, R., Rivera Gil, P., Pelaz, B., Ibanez, M., Cadavid, D., et al. (2013). CuTe nanocrystals: shape and size control, plasmonic properties, and use as SERS probes and photothermal agents. *J. Am. Chem. Soc.* 135, 7098–7101. doi: 10.1021/ja401428e

Liu, H., Liu, T., Wu, X., Li, L., Tan, L., Chen, D., et al. (2012). Targeting gold nanoshells on silica nanorattles: a drug cocktail to fight breast tumors via a single irradiation with near-infrared laser light. *Adv. Mater.* 24, 755–761. doi: 10.1002/adma.201103343

Liu, J., Wang, P., Zhang, X., Wang, L., Wang, D., Gu, Z., et al. (2016). Rapid degradation and high renal clearance of Cu3BiS3 nanodots for efficient cancer diagnosis and photothermal therapy in vivo. *ACS Nano* 10, 4587–4598.

Luther, J. M., Jain, P. K., Ewers, T., and Alivisatos, A. P. (2011). Localized surface plasmon resonances arising from free carriers in doped quantum dots. *Nat. Mater.* 10, 361–366. doi: 10.1038/nmat3004

Osaki, F., Kanamori, T., Sando, S., Sera, T., and Aoyama, Y. (2004). A quantum dot conjugated sugar ball and its cellular uptake. On the size effects of endocytosis in the subviral region. *J. Am. Chem. Soc.* 126, 6520–6521. doi: 10.1021/ja048792a

Roper, D. K., Ahn, W., and Hoepfner, M. (2007). Microscale heat transfer transduced by surface plasmon resonant gold nanoparticles. *J. Phys. Chem. C Nanomater. Interfaces* 111, 3636–3641. doi: 10.1021/jp064341w

Song, G., Liang, C., Gong, H., Li, M., Zheng, X., Cheng, L., et al. (2015). Core-shell MnSe@Bi2Se3 fabricated via a cation exchange method as novel nanotheranostics for multimodal imaging and synergistic thermoradiotherapy. *Adv. Mater.* 27, 6110–6117. doi: 10.1002/adma.201503006

Tian, Q., Hu, J., Zhu, Y., Zou, R., Chen, Z., Yang, S., et al. (2013). Sub-10 nm Fe3O4@Cu2-xS core-shell nanoparticles for dual-modal imaging and photothermal therapy. *J. Am. Chem. Soc.* 135, 8571–8577. doi: 10.1021/ja4013497

Tian, Q., Jiang, F., Zou, R., Liu, Q., Chen, Z., Zhu, M., et al. (2011a). Hydrophilic Cu9S5 nanocrystals: a photothermal agent with a 25.7% heat conversion efficiency for photothermal ablation of cancer cells in vivo. *ACS Nano* 5, 9761–9771. doi: 10.1021/nn203293t

Tian, Q., Tang, M., Sun, Y., Zou, R., Chen, Z., Zhu, M., et al. (2011b). Hydrophilic flower-like CuS superstructures as an efficient 980 nm laser-driven photothermal agent for ablation of cancer cells. *Adv. Mater.* 23, 3542–3547. doi: 10.1002/adma.201101295

Xu, J. M., Li, L., Wang, S., Ding, H. L., Zhang, Y. X., and Li, G. H. (2013). Influence of Sb doping on the structural and optical properties of tin oxide nanocrystals. *Cryst Eng. Comm.* 15:3296. doi: 10.1039/c3ce40241j

Yang, J., Choi, J., Bang, D., Kim, E., Lim, E. K., Park, H., et al. (2011). Convertible organic nanoparticles for near-infrared photothermal ablation of cancer cells. *Angew. Chem. Int. Ed. Engl.* 50, 441–444. doi: 10.1002/anie.201005075

Yang, K., Feng, L., Shi, X., and Liu, Z. (2013). Nano-graphene in biomedicine: theranostic applications. *Chem. Soc. Rev.* 42, 530–547. doi: 10.1039/c2cs35342c

Yang, K., Zhang, S., Zhang, G., Sun, X., Lee, S. T., and Liu, Z. (2010). Graphene in mice: ultrahigh in vivo tumor uptake and efficient photothermal therapy. *Nano Lett.* 10, 3318–3323. doi: 10.1021/nl100996u

Zhang, Z., Wang, L., Wang, J., Jiang, X., Li, X., Hu, Z., et al. (2012). Mesoporous silica-coated gold nanorods as a light-mediated multifunctional theranostic platform for cancer treatment. *Adv. Mater.* 24, 1418–1423. doi: 10.1002/adma.201104714

Zhou, S. M., Ma, D. K., Zhang, S. H., Wang, W., Chen, W., Huang, S. M., et al. (2016). PEGylated Cu3BiS3 hollow nanospheres as a new photothermal agent for 980 nm-laser-driven photothermochemotherapy and a contrast agent for X-ray computed tomography imaging. *Nanoscale* 8, 1374–1382. doi: 10.1039/c5nr06041a

Conflict of Interest: The authors declare that the research was conducted in the absence of any commercial or financial relationships that could be construed as a potential conflict of interest.

frontiers in Bioengineering and Biotechnology

ORIGINAL RESEARCH
published: 14 August 2020
doi: 10.3389/fbioe.2020.00981

Cu_3BiS_3 Nanocrystals as Efficient Nanoplatforms for CT Imaging Guided Photothermal Therapy of Arterial Inflammation

Ran Lu[1†], Jingyi Zhu[2†], Chaowen Yu[1], Zhonglin Nie[1] and Yong Gao[1]*

[1] Department of Vascular Surgery, The First Affiliated Hospital of Bengbu Medical College, Bengbu, China, [2] School of Pharmaceutical Sciences, Nanjing Tech University, Nanjing, China

OPEN ACCESS

Edited by:
Bo Li,
Shanghai Ninth People's Hospital, Shanghai Jiao Tong University School of Medicine, China

Reviewed by:
Xing Zhang,
Shanghai Jiao Tong University, China
Xijian Liu,
Shanghai University of Engineering Sciences, China

***Correspondence:**
Yong Gao
drgao2406@163.com

[†] These authors have contributed equally to this work

Specialty section:
This article was submitted to Biomaterials, a section of the journal Frontiers in Bioengineering and Biotechnology

Received: 24 June 2020
Accepted: 28 July 2020
Published: 14 August 2020

Citation:
Lu R, Zhu J, Yu C, Nie Z and Gao Y (2020) Cu_3BiS_3 Nanocrystals as Efficient Nanoplatforms for CT Imaging Guided Photothermal Therapy of Arterial Inflammation. Front. Bioeng. Biotechnol. 8:981. doi: 10.3389/fbioe.2020.00981

Cardio-cerebrovascular diseases caused by chronic inflammatory atherosclerosis seriously damage human health. Nano-photothermal technology has been proven to inhibit the development of vascular inflammation, but the currently reported photothermal agents cannot efficient monitor it during the development of the disease. Herein, we designed and prepared an efficient bifunctional nanoplatform for CT imaging guided photothermal therapy of arterial inflammation. Cu_3BiS_3 nanocrystals with a size of about 12 nm were synthesized by a simple hydrothermal method. The as-prepared Cu_3BiS_3 nanocrystals showed intense absorption in the NIR region, thus exhibited amazing photothermal effect. The photothermal conversion efficiency of Cu_3BiS_3 nanocrystals was reach up to 58.6% under the excitation of an 808 nm laser with a power density of 0.4 W cm^{-2}. Cu_3BiS_3 nanocrystals can efficiently kill the macrophages both *in vitro* and *in vivo*, which plays an important role in the development of atherosclerosis, thus can be used as an effective way to inhibit the occurrence of hypertension. Importantly, Cu_3BiS_3 nanocrystals can be used as an efficient CT contrast agent to monitor carotid inflammation. Our work provides an insight for imaging guided photothermal therapy of arterial inflammation.

Keywords: Cu_3BiS_3 nanocrystals, atherosclerosis, arterial inflammation, photothermal therapy, CT imaging

INTRODUCTION

Atherosclerosis (AS) is one of the cardiovascular diseases which are the leading cause of human death (Libby et al., 2011; Tzoulaki et al., 2016). Macrophages are the key cells that play an important role in AS formation. Nanoparticle based photothermal therapy (PTT) exhibits a very promising potential due to its less side effects which can kill macrophages resulted from the photothermal effect of nanoparticles, comparing to the traditional whole body chemotherapy, and stent implant surgery having in-stent restenosis risks (Tabas, 2010; Wang et al., 2019). With the development of nanotechnology, PTT technology as an emerging minimally invasive technology shows great potential for the diagnosis and treatment of atherosclerosis (Qin et al., 2015). Photothermal therapy technology is to use photothermal materials with good optical property of near-infrared (NIR) absorption under laser irradiation to achieve local high temperature, thereby effectively killing

cells at the lesion site with no surgery (Li et al., 2013, 2017; Song et al., 2017). The NIR (700–1400 nm) laser is an important NIR light source widely used in phototherapy which has very strong penetration ability to biological tissues (Liu et al., 2016). During the progression of atherosclerosis, massive infiltration of monocytes/macrophages and other inflammatory cells and the pathological proliferation of vascular smooth muscle cells promotes plaque formation, secondary stenosis and even occlusion, leading to the occurrence of ischemic diseases (Wang et al., 2019; Zhang et al., 2019). Similar to cancer cells, hyperthermia can also be used to inhibit or kill the aforementioned pathologically expanded cells. Although this minimally invasive technique is widely used in the treatment of cancer, there are few reports on its application to atherosclerosis, and the application of photothermal therapy technology to atherosclerosis has important research significance.

Nano-photothermal technology, especially NIR-laser-driven photothermal therapy technology, has been rapidly developed in recent years. If photothermal treatment technology is to be applied to the treatment of atherosclerosis, the main issue is to explore photothermal agents with low toxicity, multi-function and high photothermal effect (Chen et al., 2013; Li et al., 2014; Shao et al., 2016; Jin et al., 2018). This is consistent with the application of photothermal therapy technology in cancer treatment. Photothermal agents reported to date mainly include carbon materials, organic materials, metal materials and semiconductor materials (Chen et al., 2013). Gold nanostructures are the most extensively and thoroughly studied photothermal agents, but the morphology of noble metal nanostructures will obviously change under the continuous irradiation by lasers which ultimately affect their photothermal properties (Tian et al., 2013). Also, precious metals' price is also one of the issues to restrict the development of such photothermal agents. Organic compounds mainly include nanoparticles of dyes, polyaniline and polypyrrole (Li et al., 2018; Li and Pu, 2019). This type of photothermal conversion material is biodegradable, but easily photodegradable or photobleached. Carbon photothermal materials, including graphene and carbon nanotubes, have stable performance, but low light absorption coefficient (Robinson et al., 2010, 2011). Semiconductor photothermal nanomaterials show several advantages, such as low price, simple synthesis, high absorption coefficient, stable photothermal performance, and easy functionalization (Meng et al., 2016; Ni et al., 2017; Tan et al., 2017).

Ternary semiconductor nanomaterials can inherit the properties of the corresponding binary semiconductors and produce new characteristics (Liu et al., 2016; Zhou et al., 2016; Li et al., 2017). In particular, copper-based bimetallic sulfides containing elements with imaging properties (such as copper iron sulfur, copper cobalt sulfur, copper manganese sulfur, and copper bismuth sulfur) can theoretically be used as both photothermal agents and imaging contrast agents. Moreover, since the valence of copper in the bimetallic copper-based sulfide is mainly monovalent, it is easily oxidized to divalent and thus degraded in the body (Liu et al., 2016). Therefore, the bimetallic copper-based sulfide is expected to be an ideal photothermal diagnostic agent. However, the previously reported bimetallic sulfides do not have plasmon resonance near-infrared absorption properties. The main reason is that these compounds do not have defective structures. The Cu_3BiS_3 nanocrystals designed and synthesized by Hu et al. used these materials for the first time in the diagnosis and treatment of cancer (Ai et al., 2011). By adjusting the copper defects of Cu_3BiS_3 nanocrystals, the as-prepared Cu_3BiS_3 nanocrystals can simultaneously exhibit intense NIR absorption properties like $Cu_{2-x}S$ nanocrystals due to copper defects, and also possess CT imaging capability due to the inherently high X-ray attenuation coefficient of bismuth. However, the size of Cu_3BiS_3 nanocrystals is difficult to adjust. The resulting nanocrystals are large in size and have poor photothermal effects (Hessel et al., 2011; Li et al., 2017). Thus the nanocrystals are easily restricted to the kidneys after being injected into the mice via the tail vein. Reducing its size can effectively improve its photothermal performance, and shorten the time in the body (Liu et al., 2016). It has been reported that adjusting the morphological structure or size of materials can improve the MRI/CT imaging performance (Ai et al., 2011; Lee et al., 2012). Therefore, the key to solving the unsatisfactory photothermal/imaging performance of bimetallic sulfide lies in the fine-tuning synthesis of the defect degree, morphology and particle size of bimetallic copper-based sulfide nanomaterials.

In this work, we designed and prepared Cu_3BiS_3 nanocrystals with a size of about 12 nm by a modified hydrothermal method in the presence of ethylenediamine. Cu_3BiS_3 nanocrystals showed intense absorption in the NIR region, thus exhibited excellent photothermal performance. The photothermal conversion efficiency of Cu_3BiS_3 nanocrystals reached up to 58.6% under the irradiation of an 808 nm laser at a power density of 0.4 W cm^{-2}. What's more, Cu_3BiS_3 nanocrystals can efficiently kill the macrophages both *in vitro* and *in vivo*, which plays an important role in the development of atherosclerosis, thus can be used as an effective way to inhibit the occurrence of hypertension. In addition, Cu_3BiS_3 nanocrystals can be used as an efficient CT contrast agent for carotid inflammation. As far as we know, this is first work on Cu_3BiS_3 nanocrystals for CT imaging guided photothermal therapy of arterial inflammation.

MATERIALS AND METHODS

Synthesis of Cu_3BiS_3 Nanocrystals

$Cu(NO_3)_2$ (1 mmol), $Bi(NO_3)_3$ (1 mmol), and Sodium dimethyldithiocarbamate (3 mmol) and polyvinylpyrrolidone (PVP, 100 mg) were fully dissolved in deionized (DI, 40 mL) water under stirring, ethylenediamine (100 μL) was then added. The precursor solution was then transferred to a PTFE hydrothermal reactor, and kept at 200°C for 24 h. Black products could be obtained by centrifuge. The products were washed with ethanol and deionized water three times.

Characterization

Transmission electron microscope was used to detect the shape and size of Cu_3BiS_3 nanocrystals. UV-vis spectrophotometer was used to detect the absorption spectrum of Cu_3BiS_3 nanocrystals. X-ray photoelectron spectrometer was used to

analyze the electronic spectrum of Cu_3BiS_3 nanocrystals. X-ray diffractometer was used to detect the phase of Cu_3BiS_3 nanocrystals. Inductively coupled plasma emission spectrometer was used to test the concentration of released ions. 808 nm lasers were used as the light source.

Cell Culture

Raw264.7 macrophage cells was routinely digested and centrifuged. After removing the supernatant, DMEM high glucose complete medium was added to resuspend the cells. The resuspended cells were incubated in a petri dish at a density of $1 \times 10^5/cm^2$ and continue culturing in an incubator (37°C, 5% CO_2). The cells were digested with trypsin, and continued to expand when the degree of cell fusion reaches 80%.

CCK-8 Cell Viability Test

Raw264.7 cells were incubated in a 96-well plate. After the cell fusion reached 80%, cells were incubated for 12 h with Cu_3BiS_3 nanocrystals with different concentrations (0, 10, 20, 40, 80, 160, 320 ppm). Then the Raw264.7 cells were excited by an 808nm laser (0.3 W/cm^2, 5 min). Then the medium was removed and the cells were washed with PBS three times to prepare CCK-8 working solution (the ratio of CCK-8 reagent to medium is 1:10). After that, CCK-8 working solution (100 μL) was added to each well. After 1 h, a multi-functional microplate reader was used to detect the absorbance at 450nm wavelength, and the analysis data was collected.

Live/Dead Cell Staining

The cultured Raw264.7 cells were collected and inoculated in a 96-well plate and in an incubator (37°C, 5% CO_2). When the degree of cell fusion reached 80%, the cells were incubated with or without Cu_3BiS_3 nanocrystals in high glucose medium for 12 h. The cells were divided into different groups: blank control group (Control); Cu_3BiS_3 nanocrystals combined with 808 nm laser at different power density (0.1, 0.2, 0.4 W/cm^2). After the treatments, the culture supernatant was removed, washed with PBS for three times. CalceinAM and PI were then added, and incubated in a 37°C incubator for 20 min. Then the cells were observed under an inverted fluorescence microscope.

Animal Model Construction

All animal experiments were approved by the Animal Ethics Committee of The First Affiliated Hospital of Bengbu Medical

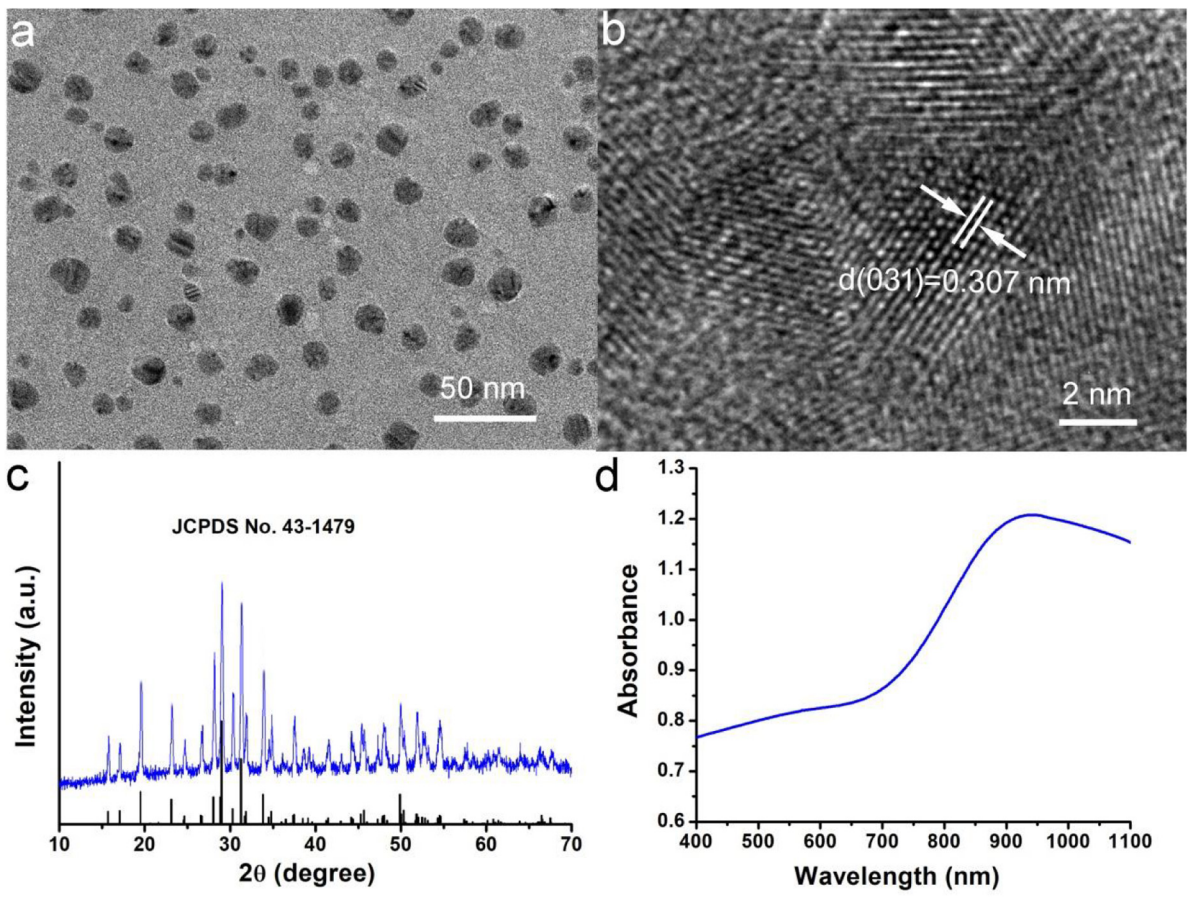

FIGURE 1 | (a) Typical TEM image of Cu_3BiS_3 nanocrystals. **(b)** High resolution TEM image of Cu_3BiS_3 nanocrystals. **(c)** XRD pattern of Cu_3BiS_3 nanocrystals. **(d)** UV-vis-NIR spectra of Cu_3BiS_3 nanocrystals at room temperature.

College. 28 of 8-week-old ApoE-/- mice were selected and fixed on the rat board after anesthetized with chloral hydrate. The left carotid artery was exposed under the microscope via making a longitudinal incision in the left neck. A 5 mm length silicone tube was placed around the left carotid artery to wrap it around the left carotid artery. The silk thread was ligated and fixed, and the skin and subcutaneous layers were sutured layer by layer, placed in a 35°C incubator to wake up, and then put back into the cage.

Infrared Thermal Imaging and Photothermal Therapy *in vivo*

Two weeks after the surgery, ApoE-/- mice were divided into two groups: control group and experiment group. The mice were locally injected with PBS or Cu_3BiS_3 nanocrystals. The mice were simultaneously irradiated to the 808 nm lasers (0.4 W/cm^2, 5 min). An infrared thermal imaging camera was used to detect the temperature change of the mice during the treatment.

Histological Analysis

The overall status of the mice in each group was observed after surgery. The mice were sacrificed by spinal dislocation on 14 days of photothermal treatment. The left carotid artery and main organs of each group were surgically obtained and dehydrated with 10% sucrose for 1.5–2 h. After that, they are transferred to 30% sucrose for soaking overnight, and then embed frozen sections with OCT to make continuous sections with a thickness of 6–8 μm. The slices were dried overnight in a dark and ventilated place. The next day, the slices were loaded into a slice box and sealed and stored in a −20° refrigerator; or after dehydration, they were embedded into paraffin blocks to make continuous slices with a thickness of 6–8 μm. When necessary, the sections were stained for immunofluorescence or immunohistochemical, observed under a fluorescence microscope.

Carotid Tissue Immunofluorescence Staining

Carotid artery slices were soaked in PBS for three times (5 min each time) to remove OCT embedding agent. The membrane was perforated with 0.1% Triton-X for 10 min, rinsed with PBS for three times. 5% goat serum was blocked at room temperature for 30 min. Diluted anti-mouse CD68 and CD31 antibodies were added, respectively. The slides were removed

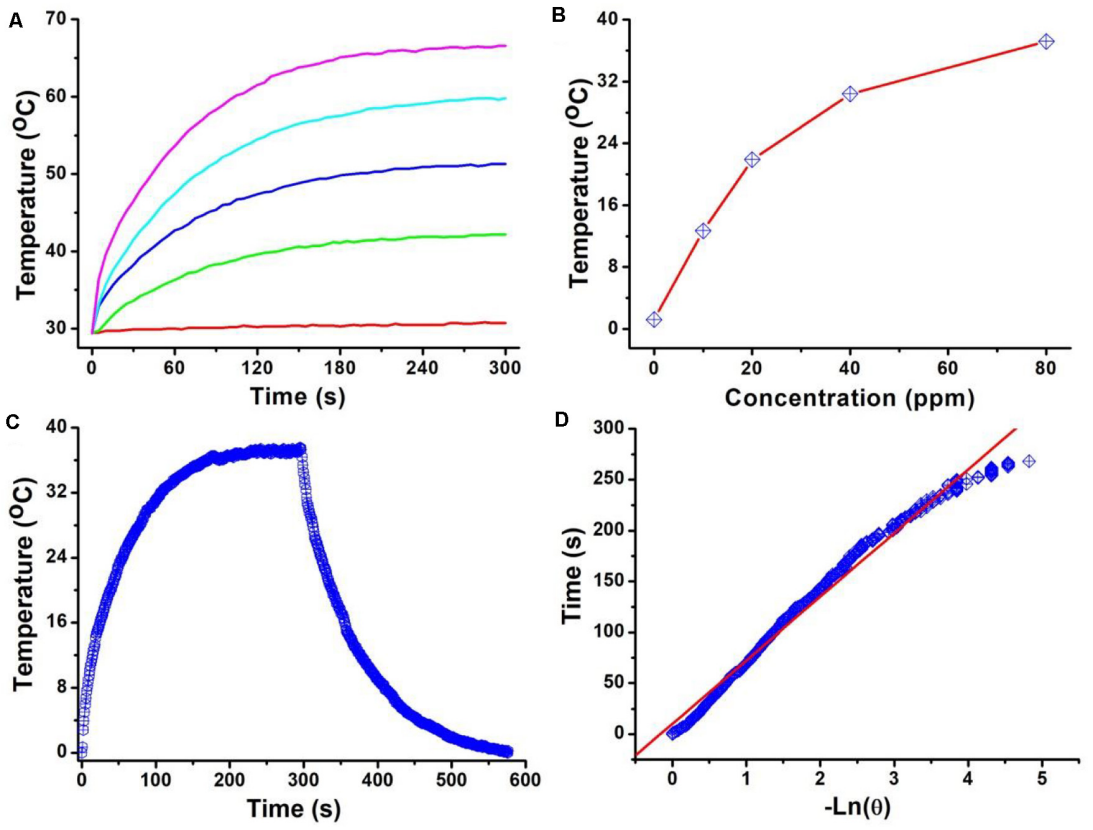

FIGURE 2 | (A) Temperature of Cu_3BiS_3 nanocrystals with different concentrations (0, 20, 40, 60, 80 ppm) under the excitation of an 808 nm laser (0.4 W cm^{-2}, 300 s). **(B)** Temperature change as a function of the concentration of Cu_3BiS_3 nanocrystals. **(C)** Temperature change of Cu_3BiS_3 nanocrystals (80 ppm) under the irradiation of the 808 nm laser (0.4 W cm^{-2}, 300 s) and shutting off the laser to cool to the room temperature. **(D)** Time constant of Cu_3BiS_3 nanocrystals from the cooling process.

the next day and rinsed with PBS for three times. DAPI (1:500) was added dropwise to stain nuclei for 30 s, rinsed twice with PBS for 5 min each time. After anti-fluorescence quenching, the tablet was sealed, observed and photographed under a fluorescence microscope.

Carotid Artery Hematoxylin-Eosin Staining

The slices of carotid artery and main organ tissues were rinsed with distilled water for three times, 5 min each time. Then the slices were stained with hematoxylin and eosin (HE) dye for 2 min, rinsed with distilled water. The slices were gradually dehydrated with 70, 85, 95, and 100% alcohol in sequence. Finally, The slices were observed under microscope after sealing with neutral gum.

CT Imaging

Cu_3BiS_3 nanocrystals with varied concentrations (0, 0.5, 1.0, 2.0, 4.0 mg/mL) were placed in PE tubes and then scanned by CT imaging system. CT imaging *in vivo* was performed using Cu_3BiS_3 nanocrystals as CT contrast agents. ApoE-/- mice with carotid inflammation model were locally injected with Cu_3BiS_3 nanocrystals dispersed in PBS in surgical site. Pre- and post-injection, the mice were scanned by the same CT imaging system.

Long-Term Toxicity *in vivo*

The long-term toxicity *in vivo* of Cu_3BiS_3 nanocrystals was evaluated by H&E analysis of major organs and the biodistribution of Cu_3BiS_3 nanocrystals in main organs. For H&E analysis of major organs (lung, liver, spleen, kidney, and heart), healthy mice were intravenously injected with Cu_3BiS_3 nanocrystals (10 $mg{\cdot}kg^{-1}$, treatment group) or PBS solution (control group), major organs were collected for H&E analysis. The biodistribution of the Cu_3BiS_3 nanocrystals was evaluated by intravenous injection with Cu_3BiS_3 nanocrystals (10 $mg{\cdot}kg^{-1}$). Major organs were achieved at different time points (i.e., 1, 3, 6, 9 days) for H&E analysis.

RESULTS AND DISCUSSION

Hydrophilic Cu_3BiS_3 nanocrystals were synthesized by hydrothermal method. In **Figure 1a**, transmission electron microscopy (TEM) image presented that the synthesized Cu_3BiS_3 nanocrystals showed good dispersion. The size of nanocrystals was about 12 nm (**Supplementary Figure S1**)

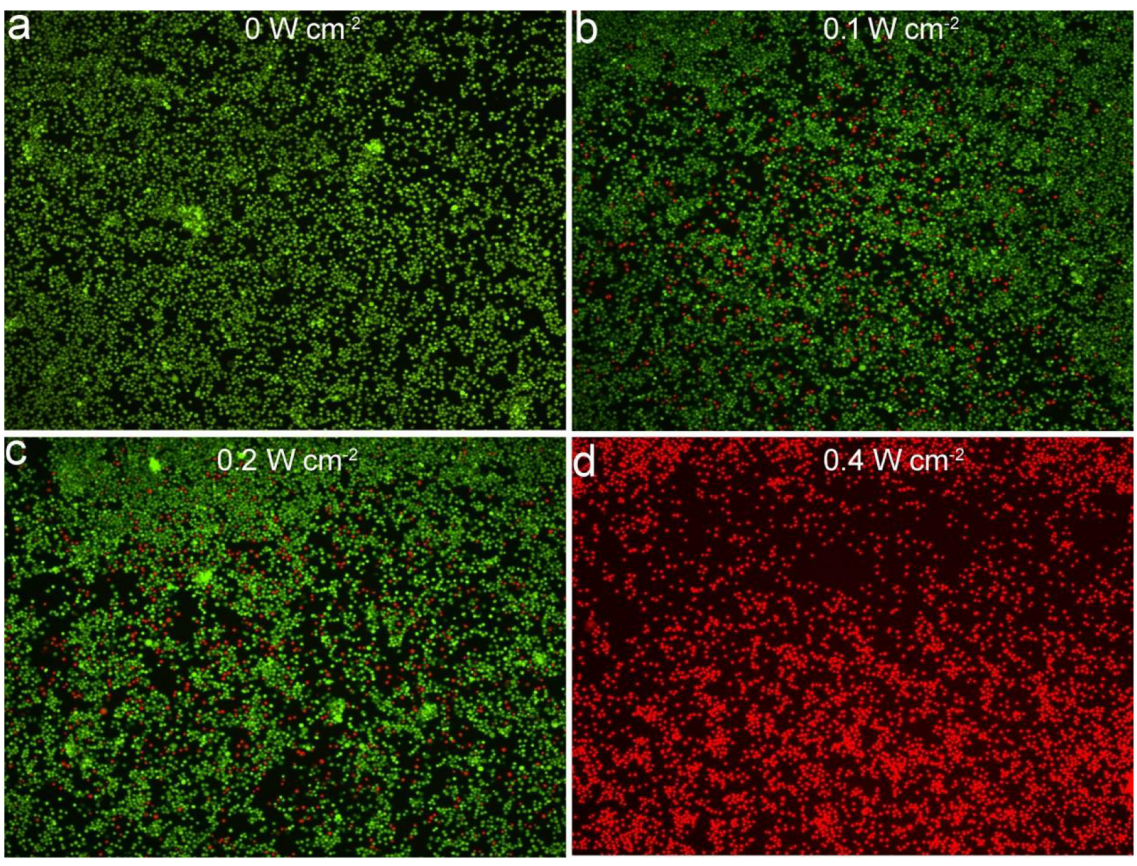

FIGURE 3 | Confocal images of fluorescence staining live/dead cells incubated with Cu_3BiS_3 nanocrystals then excited by an 808 nm laser with varied power densities: **(a)** 0 W cm^{-2}, **(b)** 0.1 W cm^{-2}, **(c)** 0.2 W cm^{-2}, **(d)** 0.4 W cm^{-2}. Magnification: 200 times.

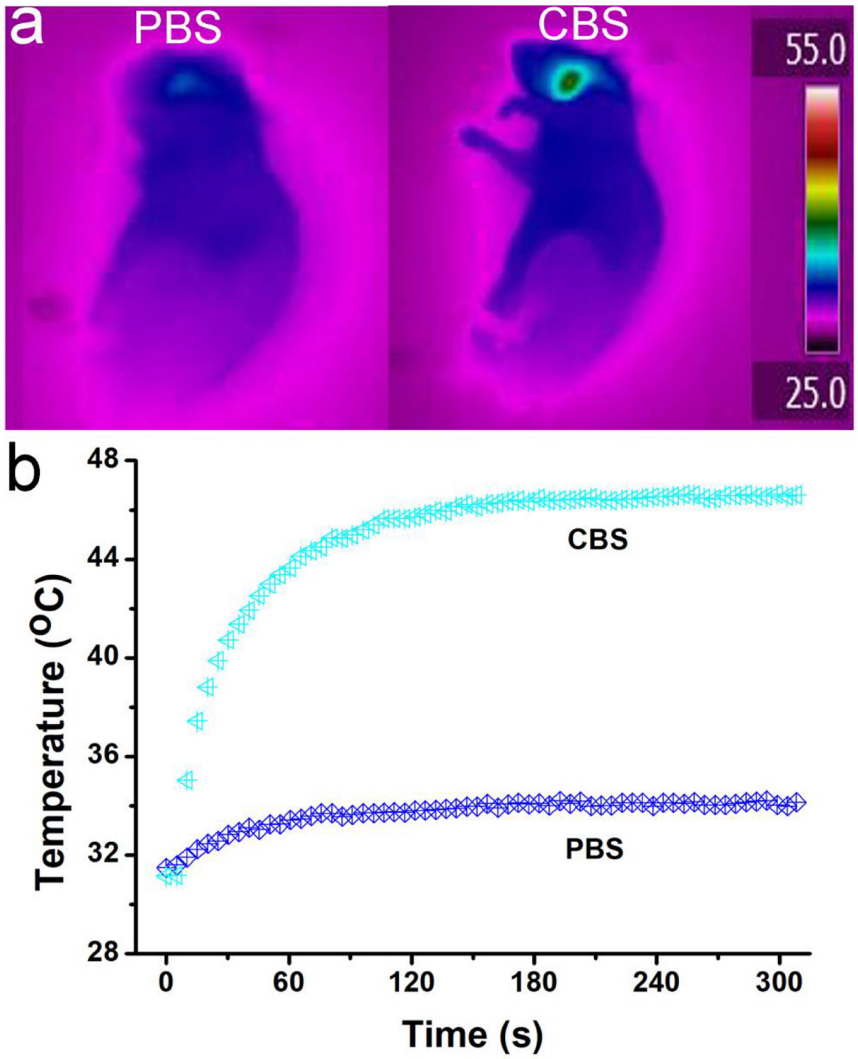

FIGURE 4 | (a) Infrared thermography of ApoE-/- mice treated by injection of PBS (left)/Cu_3BiS_3 (CBS, right) nanocrystals (right) and the 808 nm laser irradiation (0.4 W cm^{-2}) for 300 s. **(b)** Temperature change during the photothermal therapy.

which was much smaller than that of previously reported Cu_3BiS_3 nanocrystals (Li et al., 2017), indicating that the synthesized nanocrystals were more suitable for bioapplication. This reduction in particle size may be related to the presence of ethylenediamine. As an ion complexing agent, ethylenediamine can control the release rate of iron ions in the reaction, and the size of nanocrystals can be reduced (Liu et al., 2020). We further studied the microstructure of Cu_3BiS_3 nanocrystals with high-resolution transmission electron microscopy (HRTEM). As shown in **Figure 1b**, the single crystal plane spacing was 0.307 nm, which corresponded to the crystal plane spacing of the (031) plane of Cu_3BiS_3 nanocrystals. Additionally, all the X-ray diffraction patterns (XRD, **Figure 1c**) of Cu_3BiS_3 nanocrystals can be well indexed as Cu_3BiS_3 nanocrystals. The lattice parameters were consistent with those on the JCPDS file (No. 16-0713). The perfect match indicated that the synthesized Cu_3BiS_3 nanocrystals with high crystallinity and high purity. We then measured the optical property. As expected, the Cu_3BiS_3 nanocrystals showed strong absorption in NIR region centered at 905 nm (**Figure 1D**), indicating that Cu_3BiS_3 nanocrystals showed great potential as photothermal agents.

The intense NIR absorption of Cu_3BiS_3 nanocrystals motivated us to evaluate the photothermal performance of Cu_3BiS_3 nanocrystals. The aqueous dispersions of nanocrystals with varied concentrations were placed in the PE tubes, and excited by an 808 nm laser. The temperature change was recorded by infrared thermal imager. As shown in **Figure 2A**, the temperature of aqueous dispersions of nanocrystals increased dramatically under the irradiation of the 808 nm laser, while the temperature of pure water showed little change, indicating that Cu_3BiS_3 nanocrystals exhibited excellent photothermal effect. As the concentration increased, the elevated temperature increased. Obviously, Cu_3BiS_3 nanocrystals showed concentration-dependent photothermal effect. **Figure 2B** provides the direct

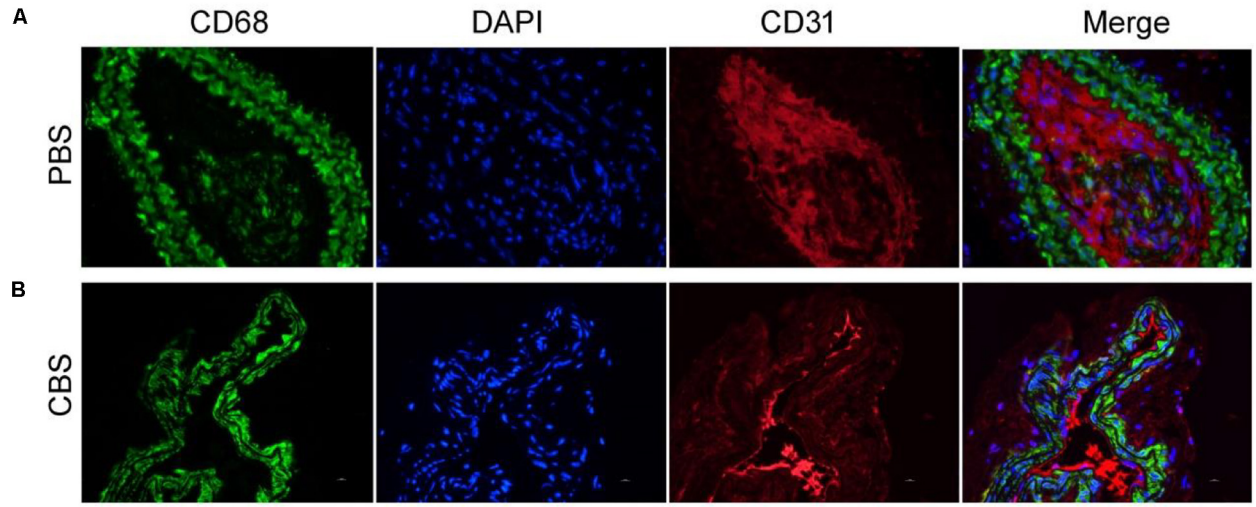

FIGURE 5 | Immunofluorescence staining of macrophages, endothelial cells, and merge pictures in the **(A)** control group (PBS) and **(B)** experimental group (CBS). Magnification: 200 times.

relationship between the concentration of Cu_3BiS_3 nanocrystals and the temperature. When the concentration was 80 ppm, the temperature of the aqueous dispersion was increased by 37.2°C, while the temperature of pure water was increased by less than 2°C, demonstrating the excellent photothermal performance of Cu_3BiS_3 nanocrystals. To further evaluate the photothermal performance of Cu_3BiS_3 nanocrystals, the photothermal conversion efficiency of Cu_3BiS_3 nanocrystals was measured according to previously reported methods. As shown in **Figure 2C**, 80 ppm of Cu_3BiS_3 nanocrystals was excited by the 808 nm laser (0.3 W) until the temperature reached equilibrium and no longer changed. Then the laser was removed away, and the cooling temperature during the cooling process was recorded (**Figure 2D**). The time constant can be calculated to be 98.3 s. Thus, the photothermal conversion efficiency of Cu_3BiS_3 was calculated to be 58.6% which is high enough for photothermal therapy.

In order to detect the cytotoxicity of Cu_3BiS_3 nanocrystals, we used different concentrations of Cu_3BiS_3 nanocrystals (0∼320 ppm) to co-culture with macrophages for 12 h, and then tested the cell activity of each group by CCK-8 experiment. The results showed that the concentration was below 160 ppm, Cu_3BiS_3 nanocrystals had no significant effect on the activity of macrophages (Raw264.7); when the concentration reached 320 ppm, Raw264.7 activity decreased significantly (see **Supplementary Figure S2A**). Based on the photothermal curves of Cu_3BiS_3 nanocrystals under the action of near-infrared light, Cu_3BiS_3 nanocrystals showed a good heating effect at a concentration of 40 ppm; the temperature was increase by 20°C. We thus chose 40 ppm as the concentration used in subsequent experiments.

Macrophage infiltration is one of the main causes of arterial inflammation and arterial stenosis, so we examined the effect of thermal effects based on Cu_3BiS_3 nanocrystals on macrophage activity. Cell phagocytosis experiments without using an additional target or selective groups have been studied by many groups (Van Furth et al., 1979; Han et al., 2016; Wang et al., 2019). Nanoparticles were mostly aggregated in lysosomes, and macrophages have much larger amounts of lysosomes than endothelial cells (Van Furth et al., 1979; Han et al., 2016; Wang et al., 2019). In that case, macrophages, as a kind immunocyte, phagocytized a higher proportion of nanoparticles than other cells. As shown in **Supplementary Figure S2B**, the CCK-8 test found that most cells under the co-action of Cu_3BiS_3 nanocrystals and 808 nm laser irradiation (0.4 W cm^{-2}), and the cell activity was significantly higher than those of cells treated with NIR laser at lower power density. As expected, the cell activity of the control group (no NIR laser irradiation) did not change significantly. Meanwhile, NIR Laser alone had almost no effect on the cell activity (**Supplementary Figure S3**). In addition, we also stained the living/dead cells of each treatment group to further clarify the status of the cells in each treatment group. As shown in **Figures 3a–d**, no significant cell death was observed in the control group, while nearly 40% of the cells treated with the 808 nm laser (0.1 W cm^{-2}) were killed, 55% of the cells treated with the 808 nm laser with a higher power density of 0.2 W cm^{-2} were killed, and more than 90% of the cells treated with the 808 nm laser were killed when the laser power density was 0.4 W cm^{-2}, which was consistent with the CCK-8 results.

After verifying that Cu_3BiS_3 nanocrystals can effectively kill macrophages *in vitro*, we further used ApoE-/- mice to make arterial inflammation and stenosis models for photothermal therapy *in vivo*. ApoE-/- mice were divided into two groups: control group and experiment group. The mice were locally injected with PBS or Cu_3BiS_3 nanocrystals. The mice were simultaneously excited by the 808 nm lasers (0.4 W/cm^2, 5 min). An infrared thermal imaging camera was used to detect the surface temperature change of the mice during the treatment. The infrared thermal imager dynamically recorded the local temperature changes of the left neck of the mouse. As shown

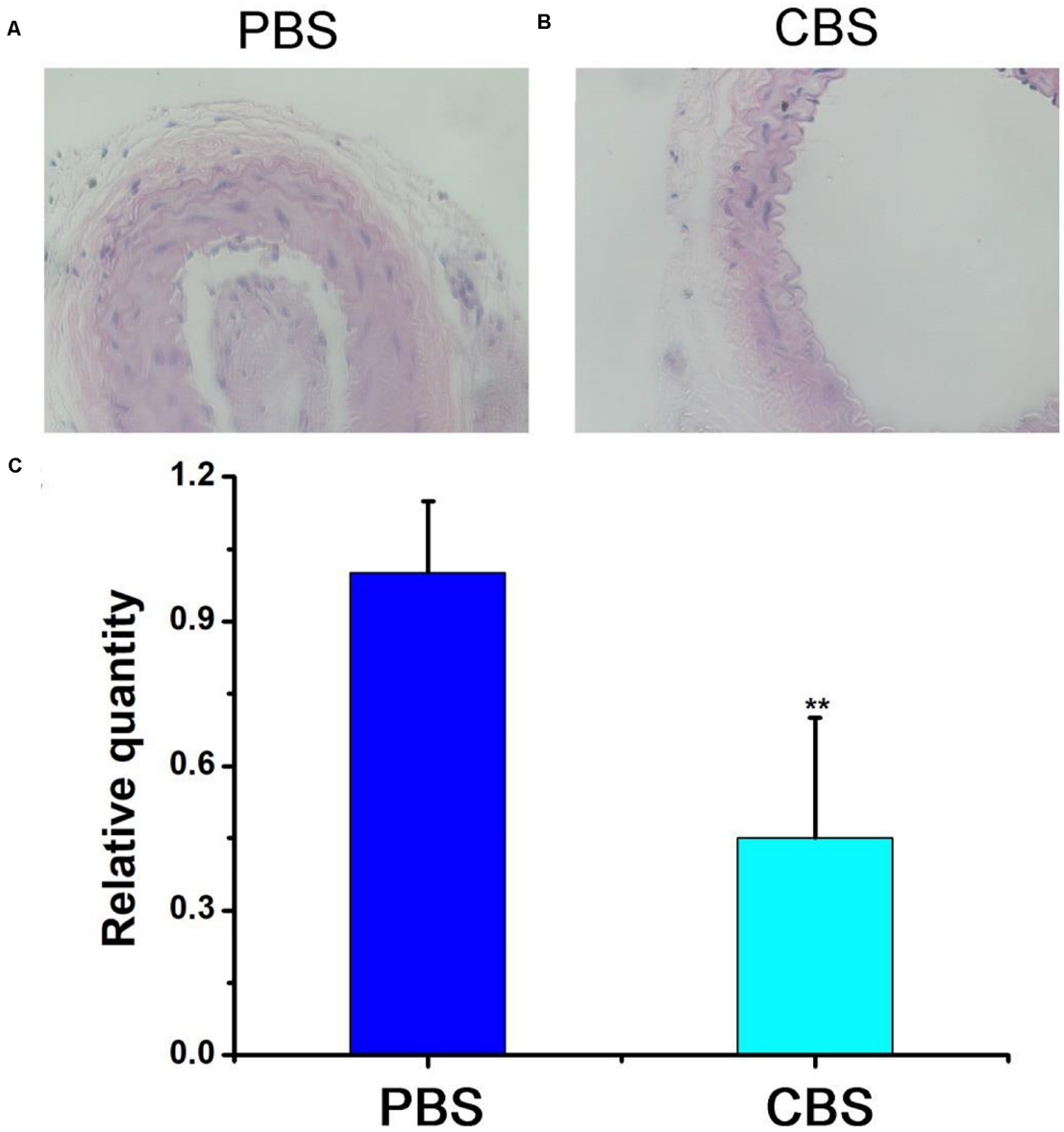

FIGURE 6 | HE staining of the carotid artery in the **(A)** control group (PBS) and **(B)** experimental group (CBS). **(C)** Statistics. Magnification: 200 times.

in **Figures 4a,b**, the local temperature of the Cu_3BiS_3 + PTT group can rapidly increase to 46.6°C within 300 s, while the local temperature of the PBS + PTT group still kept below 35°C during the whole process, showing an obvious contrast in infrared thermography. Therefore, Cu_3BiS_3 nanocrystals still showed excellent photothermal effect *in vivo* driven by the 808 nm laser.

Two weeks after photothermal therapy *in vivo*, the left carotid artery of each group of mice was removed for immunofluorescence staining. In immunofluorescence, we used CD68 as a marker for macrophages and CD31 as a marker for vascular smooth muscle cells. The results showed that the number of infiltrated $CD68^+$ macrophages in the middle artery wall of the control group (PBS + NIR, **Figure 5A**) was much higher than that of experiment (Cu_3BiS_3 + PTT, **Figure 5B**) group. This indicates that the photothermal therapy based on Cu_3BiS_3 nanocrystals can effectively inhibit the infiltration of macrophages in the inflammatory arterial wall in a short period of time, which may reduce the adverse results caused by the infiltration of a large number of inflammatory macrophages.

In order to further evaluate the effect of ablation of arterial wall macrophages on reducing the thickness of the arterial wall and inhibiting the progress of arterial stenosis, we tested the thickness of the carotid artery wall of mice by HE staining. The results showed that the thickness of the intima/media in the experimental (CBS + NIR) group was much lower than that in the control (PBS + NIR) group (**Figures 6A,B**). Effectively inhibit the thickening of the intima/media of the arterial wall, thereby reducing the occurrence of arterial stenosis. In addition,

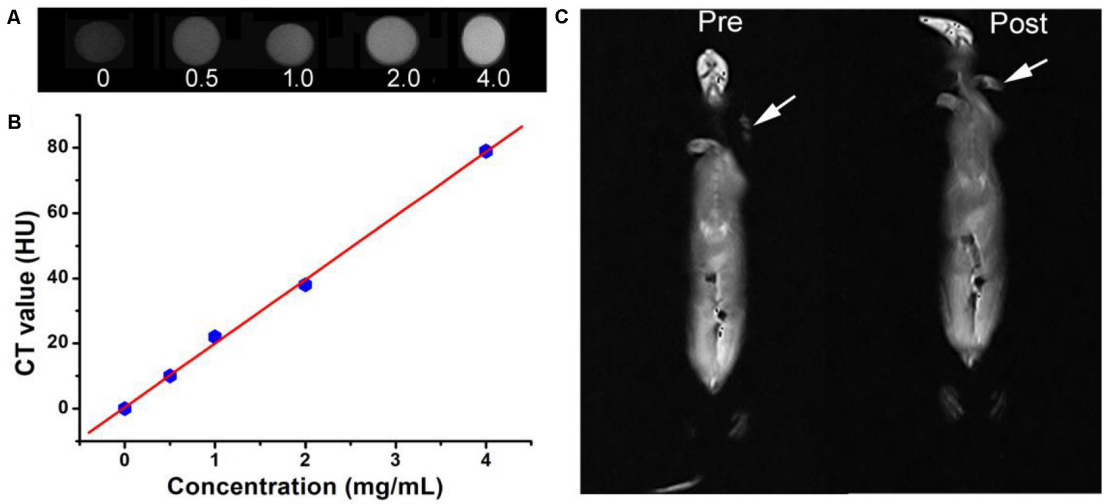

FIGURE 7 | (A) CT image *in vitro* of Cu_3BiS_3 nanocrystals with varied concentrations (0, 0.5, 1.0, 2.0, 4.0 mg/mL). **(B)** CT value as a function of the concentration of Cu_3BiS_3 nanocrystals. **(C)** CT images *in vivo* of the ApoE-/- mice pre- and post-injected with Cu_3BiS_3 nanocrystals (4 mg/mL).

this result was consistent with the arterial wall inflammatory macrophage infiltration results (**Figure 6C**). The relative quantity of macrophages in the experimental group was much lower than that in the control group. The arterial intima/media thickness was positively correlated with the amount of arterial wall macrophage infiltration to a certain extent, further indicating that inflammatory macrophage infiltration in the artery, the key role in wall hyperplasia. The most sensitive part in a carotid artery should be the thin layer of endothelial cells, however, in the previous study, it has found macrophages are even more vulnerable than endothelial cells (Peng et al., 2015, 2020; Wang et al., 2019). And because the highest temperature in this photothermal proves is lower than 50°C (**Figure 4b**), it would not cause much damage to the carotid artery. According to previous studies, photothermal process can cause some inflammation response, while there is also reports indicate that the laser irradiation can inhibited excessive inflammation, facilitated angiogenesis, as well as improving revascularization (Dong et al., 2018; Ma et al., 2018). As for the material itself, previous work has been proofed that they have little inflammation response (Peng et al., 2020). And nti-CD68 receptor-targeted Fe-doped hollow silica nanoparticles were used as dual-modal US/MRI contrast agent for identifying macrophages of aorta ventralis atherosclerotic plaques in ApoE-/- mice (Ji et al., 2018). To sum up, we can think that photothermal therapy based on Cu_3BiS_3 nanocrystals can effectively suppress the thickening of the arterial wall by ablating inflammatory macrophages in the arterial wall in the short term, thereby effectively inhibiting the occurrence of arterial stenosis.

In addition to the excellent photothermal effect, Cu_3BiS_3 nanocrystals also exhibited excellent CT imaging performance because of the high attenuation coefficient of bismuth. Cu_3BiS_3 nanocrystals with varied concentrations (0, 0.5, 1.0, 2.0, 4.0 mg/mL) were placed in PE tubes and then scanned by CT imaging system. As shown in **Figure 7A**, CT signal was increased with the increase of the concentration of Cu_3BiS_3 nanocrystals; the CT signal of Cu_3BiS_3 nanocrystals with a concentration of 4 mg/mL was higher than that of pure water, indicating the excellent CT imaging performance. In addition, CT values increased linearly with the concentration of Cu_3BiS_3 nanocrystals. The slope was calculated to be 19.55 HU L/g, higher than some of previously reported CT contrast agents (**Figure 7B**). We then studied the CT imaging *in vivo* using Cu_3BiS_3 nanocrystals as CT contrast agents. ApoE-/- mice with carotid inflammation model were locally injected with Cu_3BiS_3 nanocrystals dispersed in PBS in surgical site. Pre- and post-injection, the mice were scanned by a CT imaging system. As shown in **Figure 7C**, there was a significant difference in CT signal pre- and post- injection of Cu_3BiS_3 nanocrystals in the artery of ApoE-/- mice. Therefore, Cu_3BiS_3 nanocrystals can be an efficient CT contrast agent for CT imaging of carotid inflammation.

The long-term toxicity *in vivo* of Cu_3BiS_3 nanocrystals was evaluated by H&E analysis of major organs and the biodistribution of Cu_3BiS_3 nanocrystals in main organs. For H&E analysis of major organs (lung, liver, spleen, kidney, and heart), healthy mice were intravenously injected with Cu_3BiS_3 nanocrystals (10 $mg{\cdot}kg^{-1}$, treatment group) or PBS solution (control group), major organs were collected for H&E analysis. It was found that the shape and size of the cells both in the treatment group and in the control group almost showed no change (**Supplementary Figure S4**), indicating the low toxicity *in vivo* of Cu_3BiS_3 nanocrystals. The biodistribution of the Cu_3BiS_3 nanocrystals was evaluated by intravenous injection with Cu_3BiS_3 nanocrystals (10 mg kg^{-1}). Major organs were achieved at different time points (i.e., 1, 3, 6, 9 days). It showed (**Supplementary Figure S5**) that the Cu_3BiS_3 nanocrystals mainly accumulate in the kidney and spleen after the intravenous administration. The content in these two organs gradually

decreased over time, indicating that Cu_3BiS_3 nanocrystals were mainly degraded through these two organs.

CONCLUSION

In conclusion, Cu_3BiS_3 nanocrystals with a size of about 12 nm were successfully designed and prepared by a simple hydrothermal method. Cu_3BiS_3 nanocrystals showed excellent photothermal effect when driven by an 808 nm laser. The photothermal conversion efficiency of Cu_3BiS_3 nanocrystals was calculated to be 58.6% due to the strong NIR absorption. Under the irradiation of an 808 nm laser, Cu_3BiS_3 nanocrystals can efficiently kill the macrophages both *in vitro* and *in vivo*, which plays an important role in the development of atherosclerosis, thus can be used as an effective way to inhibit the occurrence of hypertension. In addition, Cu_3BiS_3 nanocrystals can be used as an efficient CT contrast agent for carotid inflammation. Therefore, Cu_3BiS_3 nanocrystals show great potential for CT imaging guided photothermal therapy of arterial inflammation.

DATA AVAILABILITY STATEMENT

All datasets generated for this study are included in the article/**Supplementary Material**.

ETHICS STATEMENT

The animal study was reviewed and approved by the First Affiliated Hospital of Bengbu Medical College.

AUTHOR CONTRIBUTIONS

RL, JZ, and YG designed the project and performed the experimental data analysis. RL, JZ, CY, and ZN carried out the experiment. RL and YG wrote the manuscript. All the authors contributed to discussion of the results.

FUNDING

This study was supported by the Natural Science Research Projects Fund in Colleges and Universities of Anhui Province (KJ2019A0327).

SUPPLEMENTARY MATERIAL

The Supplementary Material for this article can be found online at: https://www.frontiersin.org/articles/10.3389/fbioe.2020.00981/full#supplementary-material

REFERENCES

Ai, K., Liu, Y., Liu, J., Yuan, Q., He, Y., and Lu, L. (2011). Large-scale synthesis of bi2s3nanodots as a contrast agent for in Vivo X-ray computed tomography imaging. *Adv. Mater.* 23, 4886–4891. doi: 10.1002/adma.201103289

Chen, Z., Wang, Q., Wang, H., Zhang, L., Song, G., Song, L., et al. (2013). Ultrathin PEGylated W18O49Nanowires as a New 980 nm-laser-driven photothermal agent for efficient ablation of cancer cells in vivo. *Adv. Mater.* 25, 2095–2100. doi: 10.1021/acsami.9b12258

Dong, Q., Wang, X. W., Hu, X. X., Xiao, L. Q., Zhang, L., Song, L. J., et al. (2018). Simultaneous application of photothermal therapy and an anti-inflammatory prodrug using pyrene-aspirin-loaded gold nanorod graphitic nanocapsules. *Angew. Chem. Intern. Edn.* 57, 177–181. doi: 10.1002/anie.201709648

Han, C. Z., Juncadella, I. J., Kinchen, J. M., Buckley, M. W., Klibanov, A. L., Dryden, K., et al. (2016). Macrophages redirect phagocytosis by non-professional phagocytes and influence inflammation. *Nature* 539, 570–574. doi: 10.1038/nature20141

Hessel, C. M., Pattani, V. P., Rasch, M., Panthani, M. G., Koo, B., Tunnell, J. W., et al. (2011). Copper selenide nanocrystals for photothermal therapy. *Nano Lett* .11, 2560–2566. doi: 10.1021/nl201400z

Ji, R., Li, X. Y., Zhou, C., Tian, Q. W., Li, C., Xia, S. J., et al. (2018). Identifying macrophage enrichment in atherosclerotic plaques by targeting dual-modal US imaging/MRI based on biodegradable Fe-doped hollow silica nanospheres conjugated with anti-CD68 antibody. *Nanoscale* 10, 20246–20255. doi: 10.1039/c8nr04703k

Jin, Q., Liu, J., Zhu, W., Dong, Z., Liu, Z., and Cheng, L. (2018). Albumin-assisted synthesis of ultrasmall FeS2 nanodots for imaging-guided photothermal enhanced photodynamic therapy. *ACS Appl. Mater. Interf.* 10, 332–340. doi: 10.1021/acsami.7b16890

Lee, D.-E., Koo, H., Sun, I.-C., Ryu, J. H., Kim, K., and Kwon, I. C. (2012). Multifunctional nanoparticles for multimodal imaging and theragnosis. *Chem. Soc. Rev.* 41, 2656–2672. doi: 10.1039/c2cs15261d

Li, B., Wang, Q., Zou, R., Liu, X., Xu, K., Li, W., et al. (2014). Cu7.2S4 nanocrystals: a novel photothermal agent with a 56.7% photothermal conversion efficiency for photothermal therapy of cancer cells. *Nanoscale* 6, 3274–3282. doi: 10.1039/c3nr06242b

Li, B., Yuan, F., He, G., Han, X., Wang, X., Qin, J., et al. (2017). Ultrasmall CuCo2S4Nanocrystals: all-in-one theragnosis nanoplatform with magnetic resonance/near-infrared imaging for efficiently photothermal therapy of tumors. *Adv. Funct. Mater.* 27:1606218. doi: 10.1002/adfm.201606218

Li, J., and Pu, K. (2019). Development of organic semiconducting materials for deep-tissue optical imaging, phototherapy and photoactivation. *Chem. Soc. Rev.* 48, 38–71. doi: 10.1039/c8cs00001h

Li, J. C., Rao, J. H., and Pu, K. Y. (2018). Recent progress on semiconducting polymer nanoparticles for molecular imaging and cancer phototherapy. *Biomaterials* 155, 217–235. doi: 10.1016/j.biomaterials.2017.11.025

Li, W., Zamani, R., Rivera Gil, P., Pelaz, B., Ibanez, M., Cadavid, D., et al. (2013). CuTe nanocrystals: shape and size control, plasmonic properties, and use as SERS probes and photothermal agents. *J. Am. Chem. Soc.* 135, 7098–7101. doi: 10.1021/ja401428e

Libby, P., Ridker, P. M., and Hansson, G. K. (2011). Progress and challenges in translating the biology of atherosclerosis. *Nature* 473, 317–325. doi: 10.1038/nature10146

Liu, J., Guo, X., Zhao, Z., Li, B., Qin, J., Peng, Z., et al. (2020). Fe3S4 nanoparticles for arterial inflammation therapy: integration of magnetic hyperthermia and photothermal treatment. *Appl. Mater. Today* 18:100457. doi: 10.1016/j.apmt.2019.100457

Liu, J., Wang, P., Zhang, X., Wang, L., Wang, D., Gu, Z., et al. (2016). Rapid degradation and high renal clearance of Cu3BiS3 nanodots for efficient cancer diagnosis and photothermal therapy in vivo. *ACS Nano* 10, 4587–4598. doi: 10.1021/acsnano.6b00745

Ma, J. X., Yang, Q. M., Xia, Y. C., Zhang, W. G., and Nie, F. F. (2018). Effect of 810nm near-infrared laser on revascularization of ischemic flaps in rats. *Photomed. Laser Surg.* 36, 290–297. doi: 10.1089/pho.2017.4360

Meng, Z., Wei, F., Ma, W., Yu, N., Wei, P., Wang, Z., et al. (2016). Design and synthesis of "All-in-One" multifunctional FeS2 nanoparticles for magnetic resonance and near-infrared imaging guided photothermal therapy of tumors. *Adv. Funct. Mater.* 26, 8231–8242. doi: 10.1002/adfm.201603776

Ni, D., Zhang, J., Wang, J., Hu, P., Jin, Y., Tang, Z., et al. (2017). Oxygen vacancy enables markedly enhanced magnetic resonance imaging-guided photothermal therapy of a Gd(3+)-doped contrast agent. *ACS Nano* 11, 4256–4264. doi: 10.1021/acsnano.7b01297

Peng, X., Liu, J. C., Ming, C., Li, B., Zhao, Z., Ye, K. C., et al. (2020). AgFeS2 nanoparticles as a novel photothermal platform for effective artery stenosis therapy. *Nanoscale* 12, 11288–11296. doi: 10.1039/d0nr01587c

Peng, Z., Qin, J., Li, B., Ye, K., Zhang, Y., Yang, X., et al. (2015). An effective approach to reduce inflammation and stenosis in carotid artery: polypyrrole nanoparticle-based photothermal therapy. *Nanoscale* 7, 7682–7691. doi: 10.1039/c5nr00542f

Qin, J., Peng, Z., Li, B., Ye, K., Zhang, Y., Yuan, F., et al. (2015). Gold nanorods as a theranostic platform for in vitro and in vivo imaging and photothermal therapy of inflammatory macrophages. *Nanoscale* 7, 13991–14001. doi: 10.1039/c5nr02521d

Robinson, J. T., Tabakman, S. M., Liang, Y., Wang, H., Casalongue, H. S., Vinh, D., et al. (2011). Ultrasmall reduced graphene oxide with high near-infrared absorbance for photothermal therapy. *J. Am. Chem. Soc.* 133, 6825–6831. doi: 10.1021/ja2010175

Robinson, J. T., Welsher, K., Tabakman, S. M., Sherlock, S. P., Wang, H., Luong, R., et al. (2010). High performance in vivo near-IR (>1 mum) imaging and photothermal cancer therapy with carbon nanotubes. *Nano Res.* 3, 779–793. doi: 10.1007/s12274-010-0045-1

Shao, J., Xie, H., Huang, H., Li, Z., Sun, Z., Xu, Y., et al. (2016). Biodegradable black phosphorus-based nanospheres for in vivo photothermal cancer therapy. *Nat. Commun.* 7:12967. doi: 10.1038/ncomms12967

Song, G. S., Ji, C. H., Liang, C., Song, X. J., Yi, X., Dong, Z. L., et al. (2017). TaOx decorated perfluorocarbon nanodroplets as oxygen reservoirs to overcome tumor hypoxia and enhance cancer radiotherapy. *Biomaterials* 112, 257–263. doi: 10.1016/j.biomaterials.2016.10.020

Tabas, I. (2010). Macrophage death and defective inflammation resolution in atherosclerosis. *Nat. Rev. Immunol.* 10, 36–46. doi: 10.1038/nri2675

Tan, C., Cao, X., Wu, X. J., He, Q., Yang, J., Zhang, X., et al. (2017). Recent advances in ultrathin two-dimensional nanomaterials. *Chem. Rev.* 117:6225. doi: 10.1021/acs.chemrev.6b00558

Tian, Q., Hu, J., Zhu, Y., Zou, R., Chen, Z., Yang, S., et al. (2013). Sub-10 nm Fe3O4@Cu2-xS core-shell nanoparticles for dual-modal imaging and photothermal therapy. *J. Am. Chem. Soc.* 135, 8571–8577. doi: 10.1021/ja4013497

Tzoulaki, I., Elliott, P., Kontis, V., and Ezzati, M. (2016). Worldwide exposures to cardiovascular risk factors and associated health effects: current knowledge and data Gaps. *Circulation* 133, 2314–2333. doi: 10.1161/CIRCULATIONAHA.115.008718

Van Furth, R., Raeburn, J. A., and Van Zwet, T. L. (1979). Characteristics of human mononuclear phagocytes. *Blood* 54, 485–500. doi: 10.1182/blood.V54.2.485.485

Wang, X., Wu, X., Qin, J., Ye, K., Lai, F., Li, B., et al. (2019). Differential phagocytosis-based photothermal ablation of inflammatory macrophages in atherosclerotic disease. *ACS Appl. Mater. Interf.* 11, 41009–41018.

Zhang, X., Liu, J. C., Yang, X. R., He, G. J., Li, B., Qin, J. B., et al. (2019). CuCo2S4 nanocrystals as a nanoplatform for photothermal therapy of arterial inflammation. *Nanoscale* 11, 9733–9742.

Zhou, M., Tian, M., and Li, C. (2016). Copper-based nanomaterials for cancer imaging and therapy. *Bioconjug. Chem.* 27, 1188–1199. doi: 10.1021/acs.bioconjchem.6b00156

Conflict of Interest: The authors declare that the research was conducted in the absence of any commercial or financial relationships that could be construed as a potential conflict of interest.

frontiers in Materials

ORIGINAL RESEARCH
published: 25 August 2020
doi: 10.3389/fmats.2020.00234

Bismuth Sulfide Nanorods as Efficient Photothermal Theragnosis Agents for Cancer Treatment

*Jing Jiang†, Xin Che†, Yiwen Qian, Luoziyi Wang, Yu Zhang and Zhiliang Wang**

Department of Ophthalmology, Huashan Hospital, Fudan University, Shanghai, China

Bi_2S_3 nanostructures can theoretically have photothermal properties. However, there are few reports on the application of bismuth sulfide in photothermal therapy due to the poor photothermal effect. To address this problem, herein we obtained Bi_2S_3 nanorods with defect structures via a facile method. Due to the special shape and defects, the Bi_2S_3 nanorods exhibited a strong absorption band in the NIR region, thus showed excellent photothermal effect. The photothermal conversion efficiency of Bi_2S_3 nanorods was calculated to be as high as 78.1% due to the strong NIR absorption. Importantly, the photothermal ablation experiments both *in vitro* and *in vivo* proved that the Bi_2S_3 nanorods can effectively kill cancer cells under the irradiation of an 808 nm laser. In addition, Bi_2S_3 nanorods can be used as effective CT imaging agents due to inherently high X-ray attenuation coefficient of bismuth. Our work demonstrated that the Bi_2S_3 nanorods were very promising photothermal nanoplatforms for photothermal therapy of cancers, guided by CT imaging.

Keywords: Bi_2S_3 nanorods, photothermal agents, CT imaging, photothermal therapy, photothermal conversion efficiency

OPEN ACCESS

Edited by:
Guanjie He,
University of Lincoln, United Kingdom

Reviewed by:
Nuo Yu,
Donghua University, China
Jichun Liu,
908th Hospital of the PLA, China

***Correspondence:**
Zhiliang Wang
ophwzl@163.com

†These authors have contributed equally to this work

Specialty section:
This article was submitted to Biomaterials, a section of the journal Frontiers in Materials

Received: *20 May 2020*
Accepted: *25 June 2020*
Published: *25 August 2020*

Citation:
Jiang J, Che X, Qian Y, Wang L, Zhang Y and Wang Z (2020) Bismuth Sulfide Nanorods as Efficient Photothermal Theragnosis Agents for Cancer Treatment. Front. Mater. 7:234. doi: 10.3389/fmats.2020.00234

INTRODUCTION

Photothermal therapy (PTT), which utilizes photothermal agents to convert near-infrared (NIR, 700–1400 nm) light energy into heat energy to "cook" cancer cells, has attracted increasing attention in recent years (Li et al., 2018). Some progresses have been achieved in the research of photothermal agents, but the application of photothermal therapy still faces considerable challenges (Yang et al., 2019). What's more, only a few of the nanostructured materials obtained by chemical synthesis that have been reported so far exhibit the absorption properties necessary for near-infrared light-to-heat conversion materials. Gold nanostructures have been extensively studied at the initial development stage of photothermal agents (Poper et al., 2007; Wang et al., 2009; Liu et al., 2012). Due to their adjustable absorption bands from the visible region to the near-infrared region, the gold nanostructures possess attracting photothermal performances. However, these gold nanostructures, especially gold nanorods, irreversibly transform into nanoparticles under the irradiation of NIR lasers (Tian et al., 2013). Therefore, several kinds of photothermal agents (including graphene oxides, semiconductors, and organic materials) were developed as alternatives to gold nanostructures (Chen et al., 2013). However, most of reported photothermal agents are hydrophobic, so complex hydrophilic modification processes are needed to make them meet the requirements of photothermal therapy applications (Hessel et al., 2011; Tian et al., 2011; Li et al., 2014). Since the hydrophilic modification will change the dielectric constant of the nanostructure,

the optical absorption properties of the nano-agents would be affected (Hessel et al., 2011). In addition, the 808 nm wavelength is widely used to study the photothermal effect of photothermal agents. The safely limit power density of the 808 nm laser on the skin is too low (∼0.33 W cm^{-2}) (Robinson et al., 2010). At this power density, the photothermal effects produced by photothermal agents are mostly difficult to kill cancer cells due to the poor photothermal performance of photothermal nano-agents (Liu et al., 2016; Zhang et al., 2016). Most of the photothermal agents reported so far have a single function and do not have imaging capabilities (Chang et al., 2013; Li et al., 2014). In this way, the early development of cancer cannot be monitored, which delays the timing of cancer treatment. There are also some reported photothermal agents that can simultaneously perform photothermal treatment and imaging diagnosis of tumors, but there are also certain problems. For example, Cu_3BiS_3 has photothermal effect and CT imaging capability, but the photothermal efficiency is low (Li et al., 2015). Therefore, in order to meet the severe requirements of photothermal therapy in the future, it is of great necessity to explore novel photothermal agents with excellent photothermal effect and multifunction.

It has been reported that Bi_2S_3 nanostructures with a direct band gap structure can exhibit a local plasma resonance effect (LSPR) in NIR region (Song et al., 2015). Moreover, due to its excellent biocompatibility and properties with photothermal effect resulted from intrinsic band gap absorption; Bi_2S_3 nanostructures have proved to be a promising photothermal agent (Xie et al., 2017). Additionally, bismuth is a high atomic number element with a relatively high X-ray attenuation coefficient, which can be used for CT imaging detection to observe the development of early tumors in cancer (Ai et al., 2011). However, because the absorption of bismuth sulfide is derived from the intrinsic band gap, it is difficult to adjust its optical properties, and it also makes its absorption coefficient and photothermal efficiency low. Therefore, there are few reports on the application of bismuth sulfide in photothermal therapy. Previous studies have confirmed that nano-agents can have absorption bands in the near infrared region due to their special morphology (Chen et al., 2010; Xu et al., 2012; Li W. et al., 2013). For example, gold nanorods may have long-axis absorption peaks in the near infrared region compared to gold nanoparticles (Chen et al., 2010). Thus bismuth sulfide with special morphology may have an absorption peak in the near infrared region. In general, Bi_2S_3 nanostructures can theoretically have excellent photothermal properties and CT imaging capabilities.

In this work, Bi_2S_3 nanorods served as photothermal theragnosis agents were prepared via a facile method. Due to the special shape and defects, the Bi_2S_3 nanorods exhibited a strong absorption band in the NIR region, thus showed excellent photothermal effect with a photothermal conversion efficiency up to 78.1%. Importantly, Bi_2S_3 nanorods can effectively kill cancer cells both *in vitro* and *in vivo* under the irradiation of an 808 nm laser. In addition, Bi_2S_3 nanorods can be used as effective CT imaging agents due to inherently high X-ray attenuation coefficient of bismuth. Our work demonstrated that the Bi_2S_3 nanorods are promising photothermal nanoplatforms for photothermal therapy of cancers, guided by CT imaging.

MATERIALS AND METHODS

Synthesis of Bi_2S_3 Nanorods

Bi_2S_3 nanorods were synthesized by a modified solvothermal method. Under magnetic stirring, 1 mmol of $Bi(NO_3)_3$ and 1.5 mmol of sodium diethyldithiocarbamate were fully dissolved in ethylene glycol (EG, 25 mL) and polyethylene glycol (PEG, M_W = 400 Da, 15 mL). The solution was then transferred to a 50 mL stainless steel reactor and kept at 180°C for 24 h. The black products can be obtained by ethanol washing and centrifugation.

Characterization

The morphology, microstructure, and size of the Bi_2S_3 nanorods can be determined by TEM. The XRD test was performed using a Bruker D4 X-ray diffractometer using Cu Ka radiation (λ = 0.15418 nm). The XPS test was performed on X-ray photoelectron spectrometer. The UV-vis-NIR absorption spectrum data was obtained from Shimadzu's UV-vis spectrophotometer. The released ions can be determined by Leeman laboratory inductively coupled plasma atomic emission spectrometer.

In order to measure the photothermal conversion performance of Bi_2S_3 nanorods, the light source was an 808 nm wavelength semiconductor laser with adjustable external power (0–1 W). 0.1 mL of nanorod dispersion with different concentrations was irradiated by an 808 nm laser. The output power was independently calibrated by a portable optical power meter and is ∼0.2 W, with a spot size of ∼0.66 cm^2. The temperature was recorded every 5 s by a thermal imaging camera.

To further evaluate the photothermal performance of Bi_2S_3 nanorods, we tested the photothermal efficiency of 40 ppm nanorods using a previous reported method (Roper et al., 2007). The Bi_2S_3 nanorods were dispersed in deionized water and continuously irradiated by an 808 nm laser (0.3 W cm^{-2}). The radiation source was immediately turned off when a steady-state temperature rise was achieved, and the temperature decrease was recorded to test the heat transfer rate of the system. The calculation formula (1) of the photothermal conversion efficiency (η_T) is as follows:

$$\eta_T = \frac{hA(T_{max} - T_{amb}) - Q_0}{I(1 - 10^{-A_\lambda})} \quad (1)$$

In which I is the laser power, A_λ is the absorption at the excitation wavelength. A is the surface area of the container. h is the heat transfer coefficient. T_{max} is the highest temperature of the system, and T_{amb} is the room temperature. Q_0 is the heat input rate (mW). The value of hA is obtained by the following formula (2):

$$\tau_s = \frac{m_D C_D}{hA} \quad (2)$$

Among them, τ_s is the time constant of sampling system. m_D and C_D are the mass (0.1 g) and specific heat capacity (4.2 J/g) of the

dispersed nanoparticle media, respectively. The value of τ_s can be obtained by formula (3):

$$t = -\tau_s \ln\theta = -\tau_s \ln\left(\frac{T - T_{amb}}{T_{\max} - T_{amb}}\right) \quad (3)$$

Therefore, the time constant of the system heat transfer can be obtained by the linear relationship between the cooling time and the negative natural logarithm of the temperature driving force.

CT Imaging

Bi_2S_3 nanorods aqueous dispersion (100 μL) with varied concentrations was placed in PE tubes; these PE tubes were fixed with a self-made device, and directly used a micro-CT imaging system.

EL-4 tumor (∼5 × 8 mm) model mice were first anesthetized with 100 μL 10% trichloroacetaldehyde, intratumoral injection of nanostructured PBS dispersion (100 μL, 5 mg mL-1), and the mice were scanned via micro-CT imaging system before and after the injection of nanorods. Scanning parameters are consistent with those of *in vitro* experiments. CT images were reconstructed on the same workstation using software provided by the supplier. The CT value was obtained by the software of CT imaging workstation. All animal experiments are conducted according to the guidelines of the Institutional Animal Care and Use Committee of the Huashan Hospital affiliated to Fudan University.

Photothermal Treatment of Cancer Cells *in vitro*

EL-4 cells are distributed in 96-well plates at a density of 10,000 per well. The cells were incubated in an RPMI-1640 medium at a temperature of 37°C and a CO_2 concentration of 5%. Subsequently, the cells were washed with PBS three times. 100 μL of Bi_2S_3 nanorods dispersed in PBS at different concentrations was then added to the wells, and the incubation was continued for 24 h. An 808 nm laser with a power density of 0.3 W cm^{-2} (power: ∼0.2 W, spot size: ∼0.66 cm^2) was used to irradiate the cells for 5 min. Cell survival rate can be determined by CCK-8 essay. In order to optimize the effect of laser power density on cell viability, 100 μL of Bi_2S_3 nanorod dispersion with a concentration of 40 ppm was added to the wells, and the incubation was continued for 24 h. An 808 nm laser with varied power density was used to irradiate the cells for 5 min. Then CCK-8 evaluation was used to measure the cell viability. All tests are performed independently three times.

Photothermal Therapy of Cancer Cells *in vivo*

The mice were inoculated with 1.5 × 10^6 EL-4 cells. When the tumor diameter of the mice grew to 5–8 mm for 3 weeks, the mice were divided into four groups (5 mice in each group) randomly. Group 1: intratumoral injection of Bi_2S_3 nanorods (i.e., NRs); Group 2: intratumoral injection of normal saline and irradiation with 808 nm laser (i.e., NIR); Group 3: intratumoral injection of Bi_2S_3 nanorods and irradiation with 808 nm laser with a power density of 0.3 W cm^{-2} (i.e., 0.3Treatment); Group 4: intratumoral injection of Bi_2S_3 nanorods and irradiation with 808 nm laser with a power density of 0.5 W cm^{-2} (i.e., 0.5Treatment). For Group 1 and 2, the potential *in vivo* toxicity of Bi_2S_3 nanorods or NIR laser alone was mainly investigated. For group 3 and 4, the two groups were examined for the effect of power density on cancer cells under the combined action of Bi_2S_3 nanorods and 808 nm lasers. For groups 2 and 4, they were investigated to evaluate the photothermal effect *in vivo* of Bi_2S_3 nanorods. After different treatments, tumor volume and body weight of the mice are measured every 2 days. Then the mice were sacrificed and the tumors were removed from the mice and embedded in paraffin to make 4 μm slices. These slices were stained with H&E, then inspected with the fluorescent lens of the Zeiss lens, and the image was processed with the Zeiss image camera system.

Biocompatibility Evaluation *in vivo*

Healthy mice were intravenously injected with 10 mg·kg^{-1} of the Bi_2S_3 nanorods. Major organs, including lung, liver, spleen, kidney and heart, were achieved at different time points (i.e., 1, 7, 14, 21 days, n = 3). These organs were then solubilized, and determined by ICP-AES analysis to confirm the content of bismuth. Blood samples from the Bi_2S_3 nanorod group and PBS group were collected at the different time points (i.e., 0, 1, 7, 14, 21 days) to evaluate the aspartate aminotransferase (AST) and alanine aminotransferase (ALT). In addition, the major organs were collected for histological analysis pre- and post-injection of Bi_2S_3 nanorods at varied time points (i.e., 7, 14, 21 days).

RESULTS AND DISCUSSION

In order to prepare Bi_2S_3 nanorods (NRs), $Bi(NO_3)_3$, Sodium diethyldithiocarbamate and polyethylene glycol (PEG) were fully dissolved in ethylene glycol (EG) to form a uniform solution, which was then transferred to a reaction kettle and reacted at 180^{o}C for 24 h. Black products can be obtained after centrifuge and washing with water for three times. In order to clarify the crystal phase of the synthesized products, we characterized the sample with an X-ray diffractometer. All the main peaks of X-ray diffraction patterns (**Figure 1a**) of the products can be well matched with the peaks of orthorhombic structured Bi_2S_3 (JCPDS No. 17-0325). From **Figure 1a**, the very narrow and intense peak of (130) indicated that the nanostructure grew along the (130) direction. Subsequently, we analyzed the elemental composition and oxidation states of the products, as shown in **Figure 1b**. The X-ray photoelectron spectrum (XPS) revealed that the sample contained five elements, i.e., Bi, S, O, N, and C. The elements O, N, and C were from the reaction precursors, indicating that the sample contained only Bi and S. The high resolution XPS of Bi and S indicated that the valence of bismuth was trivalent, and the valence of sulfur was a mixture of monovalent and divalent, meaning that there existed defect structure in Bi_2S_3 (**Supplementary Figure S1**). The TEM image (**Figure 1c**) revealed that the Bi_2S_3 nanostructures were monodispersed nanorods with sizes ranging from 50 to 300 nm. From the

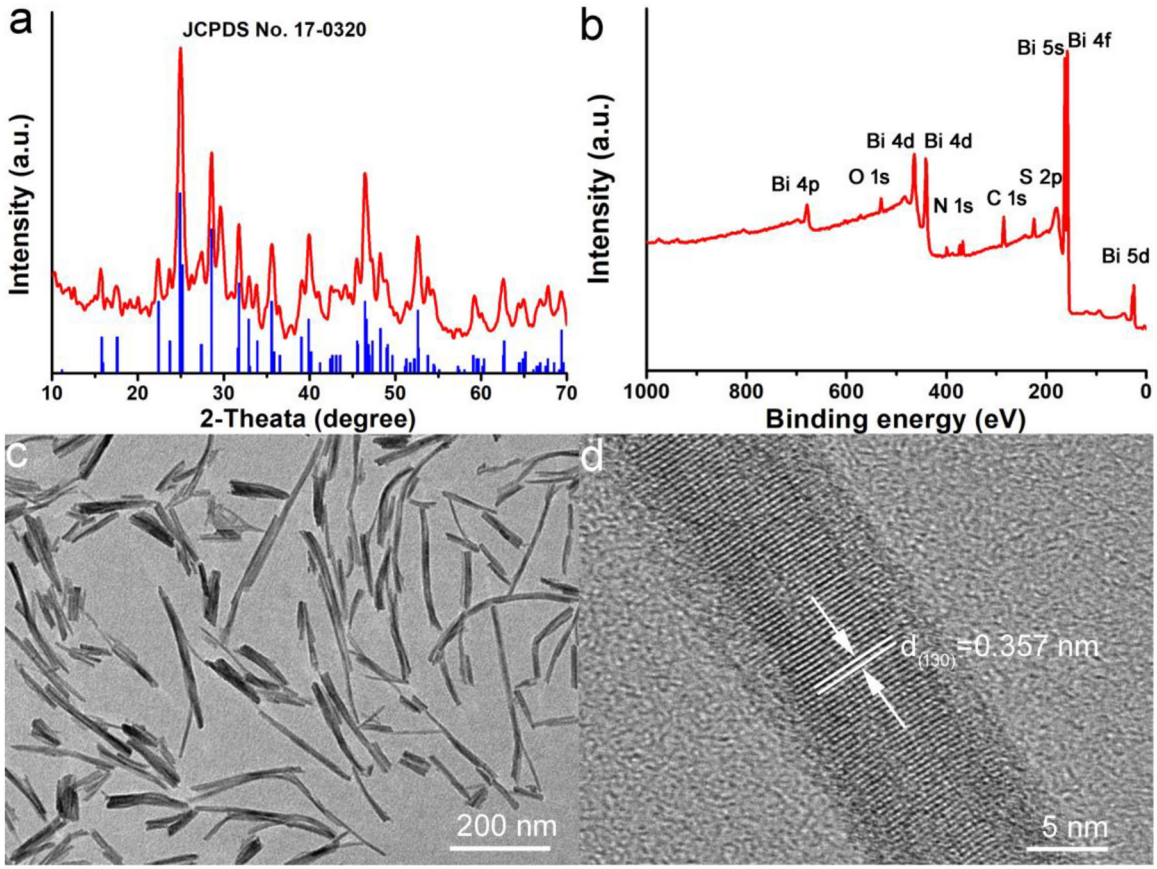

FIGURE 1 | (a) XRD pattern of Bi_2S_3 nanorods. **(b)** XPS spectra of Bi_2S_3 nanorods. **(c)** TEM and **(d)** high resolution TEM of Bi_2S_3 nanorods.

high resolution TEM image (**Figure 1d**), it can be seen that these nanorods were formed by the directional arrangement of bundled 5–22 nm nanorods. The microstructure information of nanorods can be further obtained from high-resolution TEM. The interplanar spacing was 0.357 nm, corresponding to the spacing of the (310) plane of the orthorhombic structured Bi_2S_3. Therefore, it can be concluded that Bi_2S_3 nanorods were successfully prepared.

Since the surface ligand of Bi_2S_3 nanorods was PEG, the nanorods were hydrophilic and can be directly dispersed in water without complicated surface modification. The absorption property of Bi_2S_3 nanorods in the NIR region has an important influence on its photothermal effect. **Figure 2A** shows the UV-vis absorption spectrum of Bi_2S_3 nanorod aqueous dispersions. Surprisingly, there was a broad and strong absorption band in the NIR region which was very different from those of Bi_2S_3 nanomaterials. After the concentration of the nanorod aqueous dispersion was determined by inductively coupled plasma atomic emission spectrometer (ICP-AES), the excitation coefficient of Bi_2S_3 nanorods can be calculated to be 12.3 L g^{-1} cm^{-1} which was higher than those of previously reported Bi_2S_3 nanomaterials (Song et al., 2015; Xie et al., 2017). The strong NIR absorption motivated us to evaluate their photothermal effect of Bi_2S_3 nanorods. Although the maximum absorption wavelength of Bi_2S_3 nanorods was centered at 550 nm (**Figure 2A**), 550 nm is located in the visible light region which exhibits weak penetration and strong scattering in biological tissue. The wavelength of the light source that excites the photothermal agent is in the range of 600–1400 nm. According to the optical properties of Bi_2S_3 nanorods, 808 nm lasers were chosen to study the photothermal effect. We measured the temperature change of the nanorods with a concentration gradient under the irradiation of an 808 nm laser. As shown in **Figure 2B**, the temperature of Bi_2S_3 nanorod dispersion at a concentration of 40 ppm increased by 22^{o}C under an 808 nm laser irradiation at a power density of 0.3 W cm^{-2}, while the temperature of pure water only increased by less than 2^{o}C at the same conditions. It can be concluded that Bi_2S_3 nanorods can quickly and efficiently convert 808 nm laser energy into heat energy. Thus the Bi_2S_3 nanorods showed excellent photothermal effect. Photothermal stability is an important indicator for evaluating photothermal agents. As shown in **Figure 2C**, the maximum temperature rise showed almost no changes after five circles of laser on/off, indicating the excellent photothermal stability of Bi_2S_3 nanorods. We also measured the optical properties of Bi_2S_3 nanorods after the four circles of laser ON/OFF. The absorption intensity showed little

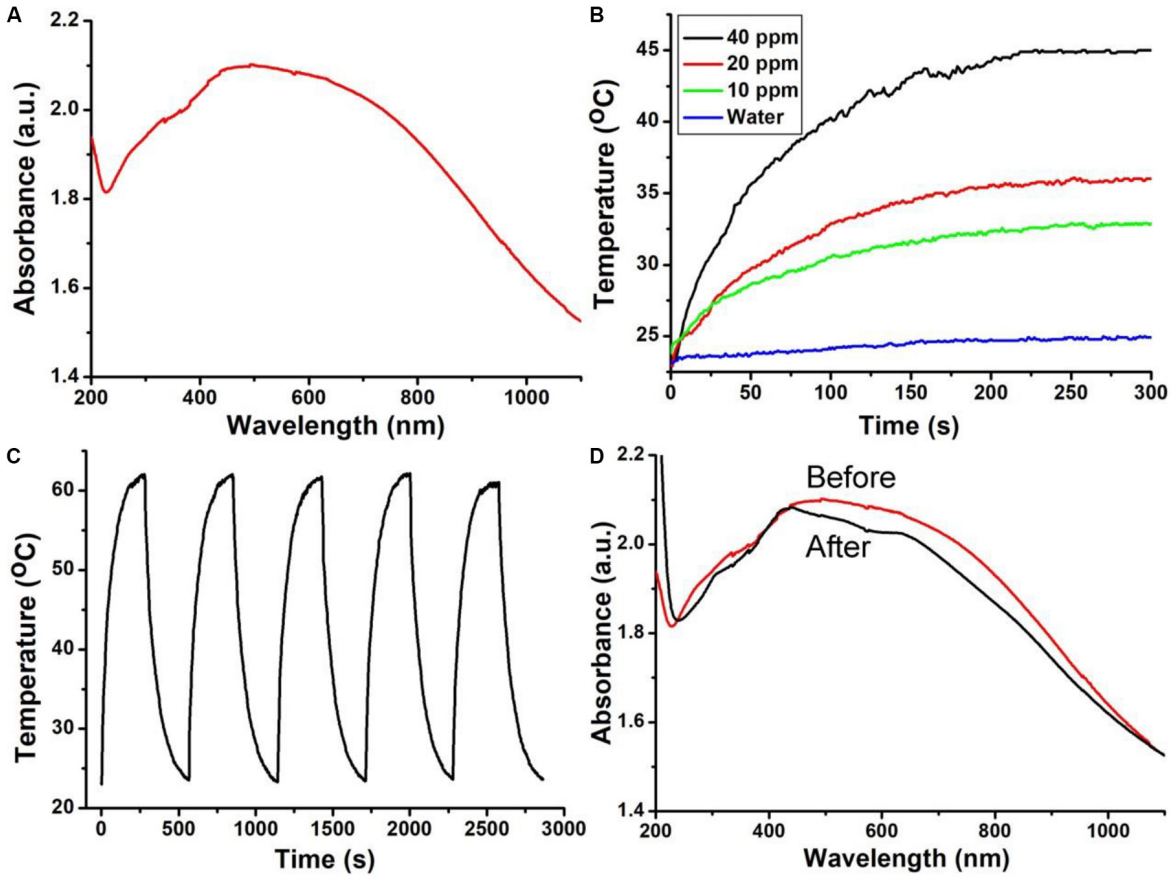

FIGURE 2 | (A) UV-vis spectra and **(B)** photothermal effect of Bi_2S_3 nanorods. **(C)** Temperature change of Bi_2S_3 nanorods during the five circles of laser ON/OFF. **(D)** UV-vis spectra of Bi_2S_3 nanorods before (red line) and after photothermal stability measurement.

decrease (**Figure 2D**), further confirming the good photothermal stability. Therefore, Bi_2S_3 nanorods can be very promising photothermal agents due to the excellent photothermal effect and photothermal stability.

In order to further study the photothermal properties of Bi_2S_3 nanorods, we calculated the photothermal conversion efficiency of the Bi_2S_3 nanorods using a method similar to the previous report (Roper et al., 2007). We recorded the temperature change of the nanorod solution (40 ppm) under the irradiation of an 808 nm laser (0.25 W) with time until an equilibrium temperature was reached (**Figure 3A**). The time constant (τ_s) of the system heat transfer can be obtained from **Figure 3B**, and was calculated to be 63.9 s. Based on the data in **Figures 2A**, **3**, we calculated the photothermal conversion efficiency of the Bi_2S_3 nanorods driven at 808 nm to be 78.1% which was much higher than some previously reported semiconductor pohotothermal agents (Song et al., 2015). The as-prepared Bi_2S_3 nanomaterials exhibited higher excitation coefficient (12.3 L g^{-1} cm^{-1}) than those of previously reported Bi_2S_3 nanomaterials (Song et al., 2015; Xie et al., 2017). Usually, the NIR absorption of Bi_2S_3 nanomaterials is derived from intrinsic band gap which resulted in low excitation coefficient. In our work, the Bi_2S_3 nanomaterials possessed defect structure and special shape. The defect structure made the Bi_2S_3 nanomaterials have metal-like absorption properties. Meanwhile, the special shape made its absorption peak blue shift (Chen et al., 2010). Therefore, the as-prepared Bi_2S_3 nanomaterials showed higher excitation coefficient due to the defect structure and special shape, contributing to the high photothermal conversion efficiency. Similar to the $Cu_{2-x}Te$ nanocrystals, the optical property of these Bi_2S_3 nanorods can be adjusted through the shape and defects (Li W. et al., 2013). Therefore, the Bi_2S_3 nanorods can be expected to be used as photothermal agents for cancer treatment by 808 nm laser-driven photothermal therapy.

The excellent photothermal properties of Bi_2S_3 nanorods inspired us to study the therapeutic effects of the nanorods on tumor cells. Prior to this, we evaluated the toxicity of the Bi_2S_3 nanorods. Bi_2S_3 nanorods incubated with EL-4 cancer cells for 24 h, and then a standard CCK-8 essay was used to evaluate the cell survival rate. It was found that the cell viability was 92% when the concentration was 40 ppm (**Supplementary Figure S2A**) at which the temperature of Bi_2S_3 nanorods dispersion could reach 22°C and was enough to kill cancer cells. When the concentration reached up to 160 ppm, the cell survival rate was still as high as 85%, indicating that Bi_2S_3 nanorods showed low toxicity. Previously reported photothermal agents used a larger laser power for photothermal treatment due to the low photothermal

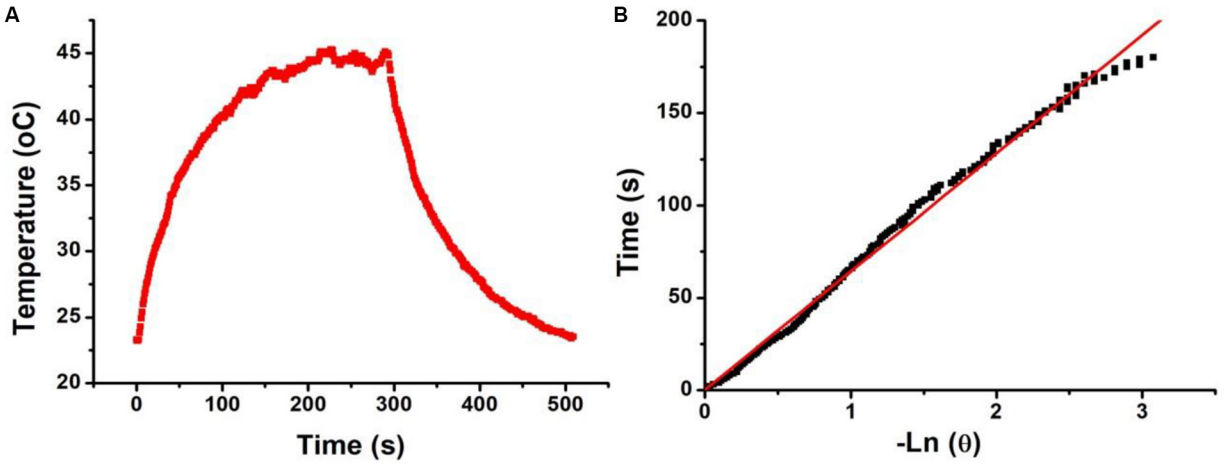

FIGURE 3 | (A) Temperature change of Bi_2S_3 nanorods (40 ppm) irradiated by an 808 laser for 300s, then shut off the laser for 300 s. **(B)** Time constant of Bi_2S_3 nanorods, τ_s = 63.9.

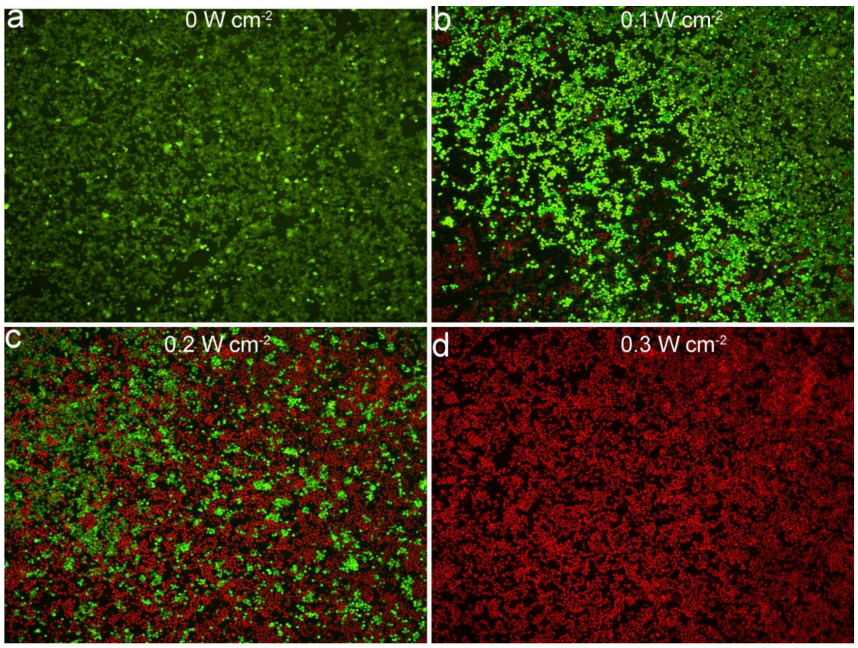

FIGURE 4 | Images of staining live/dead cells treated with an 808 nm laser at different power density. **(a)** 0 W cm^{-2}. **(b)** 0.1 W cm^{-2}. **(c)** 0.2 W cm^{-2}. **(d)** 0.3 W cm^{-2}. Magnification: 100 times.

efficiency of photothermal agents. We then studied the effect of photothermal treatment of the nanorods (40 ppm) on cancer cells under different laser power density conditions. As shown in **Supplementary Figure S2B**, cell viability decreased as the laser power density increased. When the laser power density was 0.3 W cm^{-2}, the cell viability is less than 2%, indicating an excellent phototherapy of cancer cells *in vitro*. In order to observe vividly the effect of the photothermal effect of Bi_2S_3 nanorods on the El-4 cells, we stained the live and dead cells with calcein-AM and propidium iodide. **Figure 4** shows the confocal micrographs of the cells after photothermal treatment under an 808 nm laser with indicated power density. It indicated that the dead cells increased more with the increase of power density, and the results of live/dead cell staining analysis were matched well with CCK-8 assay in **Supplementary Figure S2B**. Both the CCK8 assay and the live/dead cell staining analysis confirmed that Bi_2S_3 nanorods combined with NIR laser irradiation showed a good phototherapy effect on El-4 cell proliferation.

CT imaging is an effective detection tool which is widely used in clinical diagnosis and medical research. Many elements with high X-ray attenuation coefficients have been developed to be used as CT imaging diagnostic agents, including bismuth,

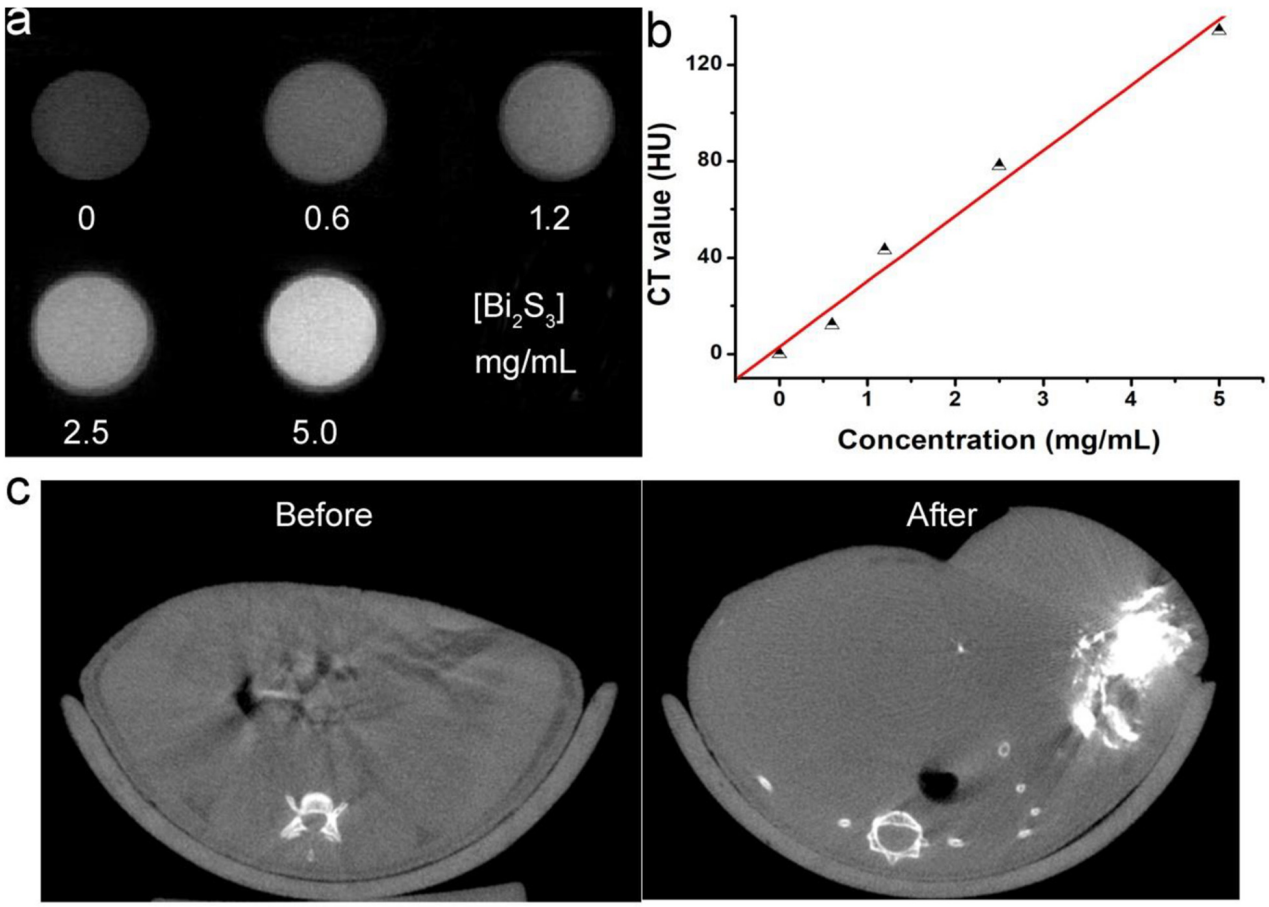

FIGURE 5 | (a) CT signals of Bi_2S_3 nanorods. **(b)** CT value as a function of the concentration of Bi_2S_3 nanorods. **(c)** CT image of a mouse before (left) and after (right) the injection of Bi_2S_3 nanorods.

iodine, gold, lanthanides, etc. Thus Bi_2S_3 nanorods can be used for CT imaging detection. We placed Bi_2S_3 nanorods aqueous dispersions with different concentrations in test tubes for CT imaging experiments. **Figure 5a** shows CT images of Bi_2S_3 nanorods aqueous dispersions with different concentrations. It was obviously observed that the CT signal intensity gradually increased as the concentration increased. At the same time, it can be seen in **Figure 5b** that the HU value of the Bi_2S_3 nanorods increased linearly with the concentration, and the slope (**Figure 5b**) of the HU value of the Bi_2S_3 nanorods was about 27.1 HU L/g, which was higher than those of some other nanomaterial (Li J. et al., 2013; Li et al., 2015). Subsequently, we used EL-4 tumor model mice to evaluate the *in vivo* CT imaging effect of Bi_2S_3 nanorods. Before the injection of Bi_2S_3 nanorods, the tumor model mice were scanned by CT as a control. After that, the nanostructure dispersion was injected into the tumor model mice by intratumoral injection. **Figure 5c** reveals the CT coronal view of the mouse tumor site before and after intratumoral injection of Bi_2S_3 nanorods (100 μL, 5 mg mL^{-1}). As shown in the **Figure 5c**, the tumor area showed a clear signal after injection compared with that before injection. The tumor site injected with Bi_2S_3 nanorods also showed a brighter contrast then other soft tissues. Additionally, the average CT value of the tumor area increased from 17 to 125. Therefore, Bi_2S_3 nanorods were expected to be used as diagnostic reagents for CT imaging.

As Bi_2S_3 nanorods had excellent photothermal properties, we believed that these nanorods can be used as photothermal therapeutic agents *in vivo*. We explored the photothermal treatment effect of Bi_2S_3 nanorods on tumor model mice driven by 808 nm laser. EL-4 cell tumor model mice were randomly divided into four groups (see experimental section) and received different treatments. During the 808 nm laser treatment, an infrared camera can be used to obtain an infrared thermal image of the whole body of the mouse. After 100 s, the surface temperature of the Group 4 (injected Bi_2S_3 nanorods and then irradiated with an 808 nm laser at 0.5 W cm^{-2}) increased to ∼55°C, while the temperature change of Group 1 (only 808 nm laser irradiation) didn't not increase significantly as the irradiation time was extended (**Figure 6A**). These results indicated that the Bi_2S_3 nanorods still had a good photothermal effect *in vivo*. After the corresponding treatment, we recorded the change in tumor volume 2 days using vernier calipers. As shown in **Figure 6B**, the tumor disappears without recurrence only for the mice in Group 4. The tumor volume of mice in Group 3was

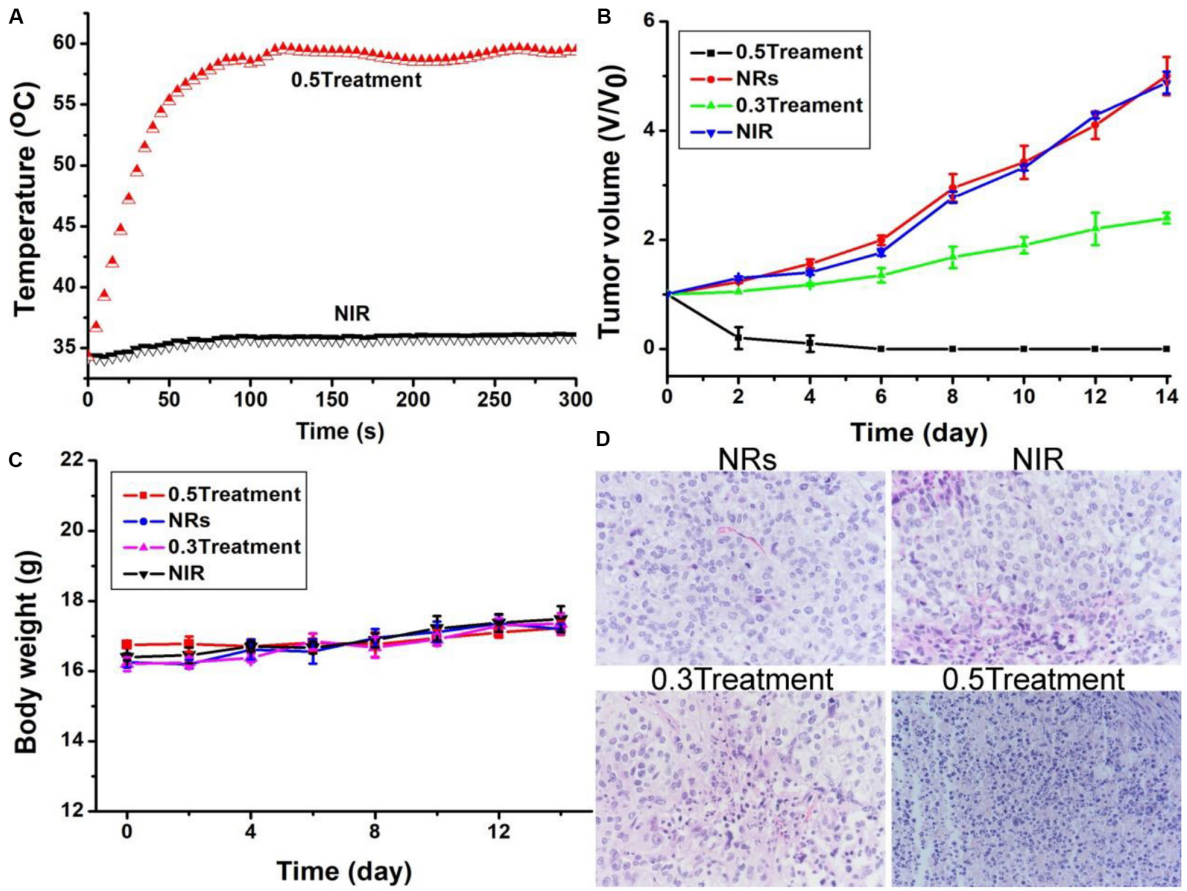

FIGURE 6 | (A) Photothermal effect after injection of PBS, and Bi_2S_3 nanorods under the irradiation of the 808 nm laser with a power density of 0.5 W cm^{-2}, respectively. **(B)** Tumor volume and **(C)** Body weight changes in different groups. **(D)** H&E images of *ex vivo* tumor sections in different groups. Magnification: 200 times.

significantly inhibited but the tumor was still growing because the laser power density in Group 3 was lower. Although the photothermal effect from the nanorods (40 ppm) could efficiently kill cancer cells *in vitro* under the irradiation of the 808 nm laser (0.3 W cm^{-2}), the power density of the lasers will be attenuated when the laser passes through the skin of the mice, making the inhibition of tumor growth rather than complete elimination in Group 3. The tumors of the mice in the other two control groups were not suppressed, and the tumor growth curves between the two groups were almost indistinguishable. We also tested the weight changes of each group of mice after the indicated treatment. There was no significant difference between the four groups of mice (**Figure 6C**), indicating that the treatment conditions we gave showed no side effects.

After treatment, all tumors were taken out and made into 4 μm slices. The slices were stained with H&E. The micrographs after staining are shown in **Figure 6D**. As expected, compared with Group 3 and 4, the changes in size, morphology and cell nuclear were not clearly observed in the Groups 1 and 2 injected with nanorods alone or only irradiated with laser. Cell necrosis in Groups 1 and 2 was only ∼5.3 and 8.7%, respectively (**Supplementary Figure S3**). However, cancer cells injected with nanorods showed severe cell destruction after laser irradiation. After co-treatment with nanorods and lasers, cell necrosis such as nuclear shrinkage, nuclear rupture, and nuclear dissolution occurred. In addition, as the laser power density was increased from 0.3 W cm^{-2} to 0.3 W cm^{-2}, more cell necrosis was observed. It can be observed that the interstitial structure around the cells is more severely damaged, and some cells are completely detached from the cells in Group 4. The tumor cell necrosis rate in Groups 3 and 4 was 55.2 and 90.8%, respectively. These results indicated that cancer cells *in vivo* can be effectively killed by the photothermal effect of Bi_2S_3 nanorods. Therefore, the combination of Bi_2S_3 nanorods and 808 nm laser is very feasible for photothermal therapy of cancer cells.

Photothermal agents should have excellent biocompatibility. We first studied the biodistribution of the Bi_2S_3 nanorods. Healthy mice were intravenously injected with 10 mg·kg^{-1} of the Bi_2S_3 nanorods. Major organs, including lung, liver, spleen, kidney and heart, were achieved at different time points (i.e., 1, 7, 14, 21 days, n = 3). These organs were then solubilized, and determined by ICP-AES analysis to confirm the content of bismuth. It showed (**Supplementary Figure S4**) that the Bi_2S_3 nanorods mainly accumulate in

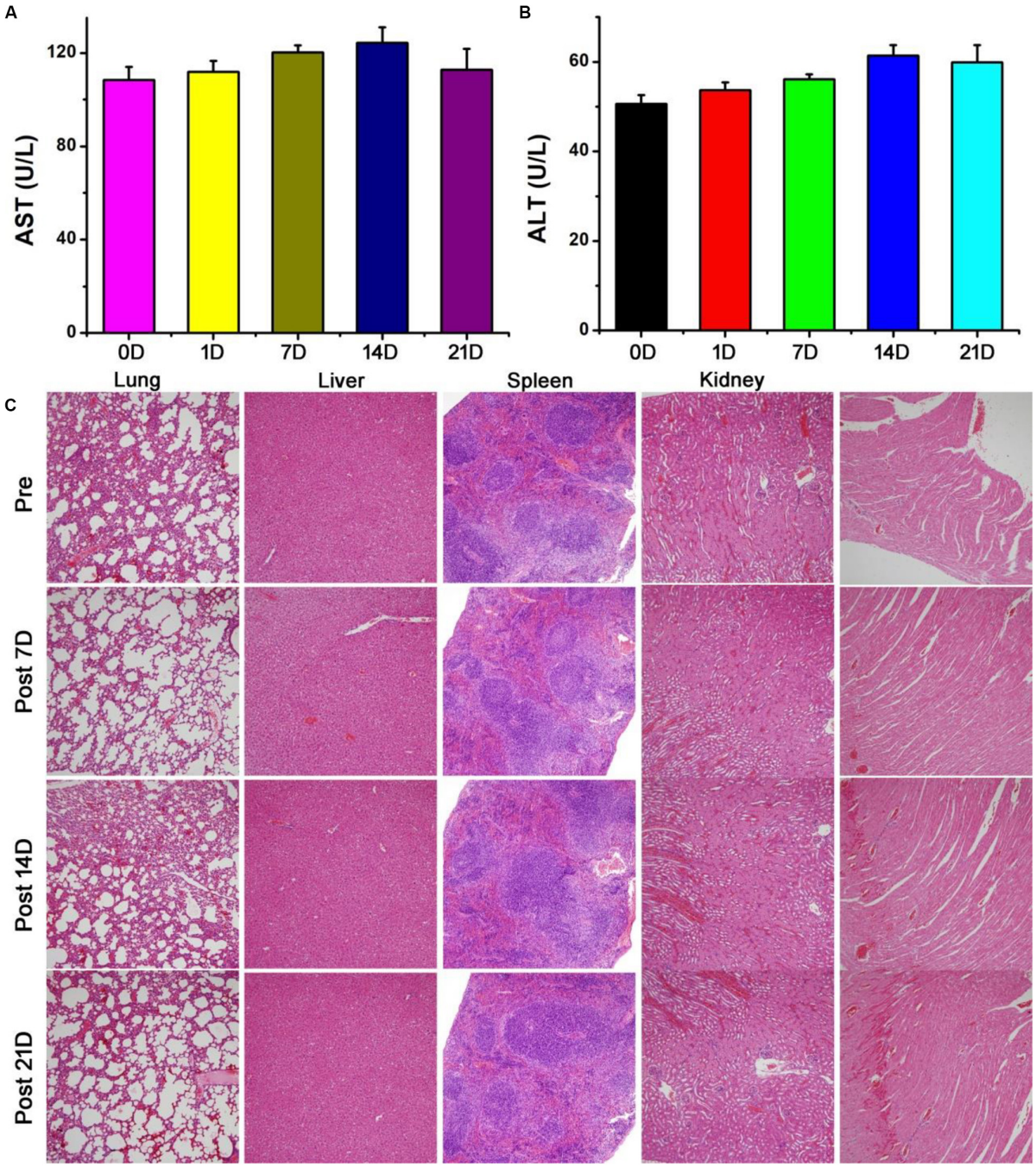

FIGURE 7 | Blood biochemical results of control group and Bi_2S_3 nanorod at different time points (1, 7, 14, 21 days) after injection: **(A)** aspartate aminotransferase (AST), **(B)** alanine aminotransferase (ALT). **(C)** HE analysis of main organs at different time points (0, 7, 14, 21 days) after injection, including lung, liver, spleen, kidney and heart. Magnification: 100 times.

the liver and spleen after the intravenous administration, indicating that Bi_2S_3 nanorods were mainly degraded through these two organs. Furthermore, blood samples from the Bi_2S_3 nanorod group and PBS group were collected at the different time points (i.e., 0, 1, 7, 14, 21 days). No obvious difference was observed in the aspartate aminotransferase (AST, **Figure 7A**) and alanine aminotransferase (ALT, **Figure 7B**), indicating that Bi_2S_3 nanorods showed little influence on liver and kidney at the given dose. In addition, the major organs were collected for histological analysis pre- and post-injection of Bi_2S_3 nanorods at varied time points (i.e., 7, 14, 21 days). No obvious organ damage, such as the change of the

shape and size of the cells, were noted compared with the control group (**Figure 7C**). The results suggested that the Bi_2S_3 nanorods showed good biocompatibility.

CONCLUSION

In conclusion, the Bi_2S_3 nanorods were successfully prepared by a facile solvothermal synthesis method to be served as a promising photothermal theragnosis agent. The Bi_2S_3 nanorods exhibited a strong NIR absorption band due to the special shape and defects, thus showed amazing photothermal effect with a photothermal conversion efficiency as high as 78.1%. The photothermal ablation experiment of cells both *in vitro* and *in vivo* prove that the Bi_2S_3 nanorods have a good photothermal effect under the irradiation of an 808 nm laser and can effectively kill cancer cells. *In vivo* and *in vitro* CT imaging experiments demonstrate that Bi_2S_3 nanorods are expected to be effective CT imaging agents. Therefore, the Bi_2S_3 nanorods can be used as promising photothermal theragnosis agents due to the excellent photothermal effect, CT imaging capability and low toxicity.

DATA AVAILABILITY STATEMENT

All datasets presented in this study are included in the article/**Supplementary Material**.

ETHICS STATEMENT

The animal study was reviewed and approved by Huashan Hospital, Fudan University.

AUTHOR CONTRIBUTIONS

JJ and ZW designed the project. JJ, XC, YQ, and LW carried out the experiment. JJ, YZ, and ZW performed the experimental data analysis. JJ and ZW wrote the manuscript. All authors contributed to discussion of the results.

FUNDING

This study was supported by the National Natural Science Foundation of China (81670868).

SUPPLEMENTARY MATERIAL

The Supplementary Material for this article can be found online at: https://www.frontiersin.org/articles/10.3389/fmats.2020.00234/full#supplementary-material

REFERENCES

Ai, K., Liu, Y., Liu, J., Yuan, Q., He, Y., and Lu, L. (2011). Large-scale synthesis of Bi2S3Nanodots as a contrast agent for in vivo X-ray computed tomography imaging. *Adv. Mater.* 23, 4886–4891. doi: 10.1002/adma.201103289

Chang, J.-Y., Lin, J.-M., Su, L.-F., and Chang, C.-F. (2013). Improved performance of $cuins_2$ quantum dot-sensitized solar cells based on a multilayered architecture. *ACS Appl. Mater. Interf.* 5, 8740–8752.

Chen, H., Shao, L., Ming, T., Sun, Z., Zhao, C., Yang, B., et al. (2010). Understanding the photothermal conversion efficiency of gold nanocrystals. *Small* 6, 2272–2280. doi: 10.1002/smll.201001109

Chen, Z., Wang, Q., Wang, H., Zhang, L., Song, G., Song, L., et al. (2013). Ultrathin PEGylated $W_{18}O_{49}$ nanowires as a new 980 nm-laser-driven photothermal agent for efficient ablation of cancer cells in vivo. *Adv. Mater.* 25, 2095–2100. doi: 10.1002/adma.201204616

Hessel, C. M., Pattani, V. P., Rasch, M., Panthani, M. G., Koo, B., Tunnell, J. W., et al. (2011). Copper selenide nanocrystals for photothermal therapy. *Nano Lett.* 11, 2560–2566. doi: 10.1021/nl201400z

Li, B., Wang, Q., Zou, R., Liu, X., Xu, K., Li, W., et al. (2014). $Cu_{7.2}S_4$ nanocrystals: a novel photothermal agent with a 56.7% photothermal conversion efficiency for photothermal therapy of cancer cells. *Nanoscale* 6, 3274–3282.

Li, B., Ye, K., Zhang, Y., Qin, J., Zou, R., Xu, K., et al. (2015). Photothermal theragnosis synergistic therapy based on bimetal sulphide nanocrystals rather than nanocomposites. *Adv. Mater.* 27, 1339–1345. doi: 10.1002/adma.201404257

Li, J., Jiang, F., Yang, B., Song, X. R., Liu, Y., Yang, H. H., et al. (2013). Topological insulator bismuth selenide as a theranostic platform for simultaneous cancer imaging and therapy. *Sci. Rep.* 3:1998.

Li, J. C., Rao, J. H., and Pu, K. Y. (2018). Recent progress on semiconducting polymer nanoparticles for molecular imaging and cancer phototherapy. *Biomaterials* 155, 217–235. doi: 10.1016/j.biomaterials.2017.11.025

Li, W., Zamani, R., Rivera Gil, P., Pelaz, B., Ibanez, M., Cadavid, D., et al. (2013). CuTe nanocrystals: shape and size control, plasmonic properties, and use as SERS probes and photothermal agents. *J. Am. Chem. Soc.* 135, 7098–7101. doi: 10.1021/ja401428e

Liu, H., Liu, T., Wu, X., Li, L., Tan, L., Chen, D., et al. (2012). Targeting gold nanoshells on silica nanorattles: a drug cocktail to fight breast tumors via a single irradiation with near-infrared laser light. *Adv. Mater.* 24, 755–761. doi: 10.1002/adma.201103343

Liu, J., Yang, Y., Zhu, W., Yi, X., Dong, Z., Xu, X., et al. (2016). Nanoscale metal-organic frameworks for combined photodynamic & radiation therapy in cancer treatment. *Biomaterials* 97, 1–9.

Poper, D. K., Ahn, W., and Hoepfner, M. (2007). Microscale heat transfer transduced by surface plasmon resonant gold nanoparticles. *J. Phys. Chem. C* 111, 3636–3641. doi: 10.1021/jp064341w

Robinson, J. T., Welsher, K., Tabakman, S. M., Sherlock, S. P., Wang, H., Luong, R., et al. (2010). High performance in vivo near-IR (>1 mum) imaging and photothermal cancer therapy with carbon nanotubes. *Nano Res.* 3, 779–793. doi: 10.1007/s12274-010-0045-1

Roper, D. K., Ahn, W., and Hoepfner, M. (2007). Microscale heat transfer transduced by surface plasmon resonant gold nanoparticles. *J. Phys. Chem. C* 111, 3636–3641. doi: 10.1021/jp064341w

Song, G., Liang, C., Gong, H., Li, M., Zheng, X., Cheng, L., et al. (2015). Core-shell MnSe@Bi_2Se_3fabricated via a cation exchange method as novel nanotheranostics for multimodal imaging and synergistic thermoradiotherapy. *Adv. Mater.* 27, 6110–6117. doi: 10.1002/adma.201503006

Tian, Q., Hu, J., Zhu, Y., Zou, R., Chen, Z., Yang, S., et al. (2013). Sub-10 nm Fe_3O_4@$Cu_{2-x}S$ core-shell nanoparticles for dual-modal imaging and photothermal therapy. *J. Am. Chem. Soc.* 135, 8571–8577. doi: 10.1021/ja4013497

Tian, Q., Jiang, F., Zou, R., Liu, Q., Chen, Z., Zhu, M., et al. (2011). Hydrophilic Cu_9S_5 nanocrystals: a photothermal agent with a 25.7% heat conversion efficiency for photothermal ablation of cancer cells in vivo. *ACS Nano* 5, 9761–9771. doi: 10.1021/nn203293t

Wang, C., Chen, J., Talavage, T., and Irudayaraj, J. (2009). Gold nanorod/Fe_3O_4 nanoparticle "nano-pearl-necklaces" for simultaneous targeting, dual-mode

imaging, and photothermal ablation of cancer cells. *Angew. Chem. Int. Ed. Engl.* 48, 2759–2763. doi: 10.1002/anie.200805282

Xie, H., Shao, J., Wang, J., Sun, Z., Yu, X.-F., and Wang, Q.-Q. (2017). Near-infrared optical performances of two Bi_2Se_3 nanosheets. *RSC Adv.* 7, 50234–50238. doi: 10.1039/c7ra09872c

Xu, G., Yamada, T., Otsubo, K., Sakaida, S., and Kitagawa, H. (2012). Facile "modular assembly" for fast construction of a highly oriented crystalline MOF nanofilm. *J. Am. Chem. Soc.* 134, 16524–16527. doi: 10.1021/ja307953m

Yang, G., Phua, S. Z. F., Bindra, A. K., and Zhao, Y. (2019). Degradability and clearance of inorganic nanoparticles for biomedical applications. *Adv. Mater.* 31:e1805730.

Zhang, S., Sun, C., Zeng, J., Sun, Q., Wang, G., Wang, Y., et al. (2016). Ultrasmall PEGylated $Cu_{2-x}Se$ nanoparticles as a multifunctional theranostic agent for multimodal imaging guided photothermal therapy of cancer. *Adv. Mater.* 28, 8927–8936. doi: 10.1002/adma.201602193

Conflict of Interest: The authors declare that the research was conducted in the absence of any commercial or financial relationships that could be construed as a potential conflict of interest.

frontiers in Bioengineering and Biotechnology

ORIGINAL RESEARCH
published: 15 September 2020
doi: 10.3389/fbioe.2020.579439

Constructing Cu_7S_4@SiO_2/DOX Multifunctional Nanoplatforms for Synergistic Photothermal–Chemotherapy on Melanoma Tumors

*Leilei Zhang[1,2], Hui Pan[1,2], Yongyun Li[1,2], Fang Li[1,2] and Xiaolin Huang[1,2]**

[1] Department of Ophthalmology, Ninth People's Hospital, Shanghai Jiao Tong University School of Medicine, Shanghai, China, [2] Shanghai Key Laboratory of Orbital Diseases and Ocular Oncology, Shanghai, China

The integration of photothermal therapy and chemotherapy has been recognized to be an efficient strategy through the instant thermally ablation and long-term chemical inhibition, thus achieving high therapeutical effect. In the present work, we designed and prepared Cu_7S_4@SiO_2/DOX nanocomposites and used them as efficient nanoplatforms for synergistic photothermal-chemo therapy on melanoma tumors. The Cu_7S_4@SiO_2/DOX was constructed by firstly synthesizing Cu_7S_4 nanocrystals, then *in situ* growing SiO_2 shell on the surface of Cu_7S_4 nanocrystals, and finally loading DOX within SiO_2 shell. The Cu_7S_4@SiO_2/DOX was composed of Cu_7S_4 core as the photothermal transducer, SiO_2 shell as DOX carrier and DOX as the model of anticancer drug. Once exposed to a 1064 nm laser, the Cu_7S_4@SiO_2/DOX could simultaneous generate heat for photothermal therapy and accelerate the DOX release. When the Cu_7S_4@SiO_2/DOX was injected into the center of tumor, the tumor exhibit rapid temperature elevation once exposed to the NIR laser and the tumor growth is significantly inhibited through the synergistic photothermal-chemo therapy, in comparison to the limited therapeutical effect of photothermal therapy or chemotherapy alone. Therefore, the Cu_7S_4@SiO_2/DOX with photothermal-chemo function can be used as excellent nanoplatforms for treating solid tumor with high theoretical effect.

Keywords: $Cu_{2-x}S$ nanocrystals, mesoporous SiO_2, photothermal therapy, chemotherapy, melanoma

OPEN ACCESS

Edited by:
Guanjie He,
University of Lincoln, United Kingdom

Reviewed by:
Xiaojuan Huang,
Shanghai Jiao Tong University, China
Kaibing Xu,
Donghua University, China
Jichun Liu,
Jianghuai Military Region Rear Hospital, China

****Correspondence:***
Xiaolin Huang
drmaureenhuang@163.com

Specialty section:
This article was submitted to Biomaterials, a section of the journal Frontiers in Bioengineering and Biotechnology

Received: *02 July 2020*
Accepted: *24 August 2020*
Published: *15 September 2020*

Citation:
Zhang L, Pan H, Li Y, Li F and Huang X (2020) Constructing Cu_7S_4@SiO_2/DOX Multifunctional Nanoplatforms for Synergistic Photothermal– Chemotherapy on Melanoma Tumors. Front. Bioeng. Biotechnol. 8:579439. doi: 10.3389/fbioe.2020.579439

INTRODUCTION

The near infrared (NIR) light-driven cancer treatments have caught a numerous attention for years due to the NIR light with higher tissue-penetration depth than visible light and the better safety than ultraviolet light (Cheng et al., 2014; Vankayala and Hwang, 2018). Among these NIR-induced therapy modalities, the photothermal therapy is an emerging one that utilizes NIR absorbents as energy transducers to convert NIR laser energy into heat (>42°C), so that thermally ablate cancer cells (Zou et al., 2016; Yu et al., 2018b). For the development of photothermal therapy, the photothermal nanoagents are the key point and they should be capable of strong and broad NIR photoabsorption and high photothermal conversion efficiency. Apart from the noble metal nanostructures (Dreaden et al., 2011; Huang et al., 2011) and the organic-based nanoparticles (Liu et al., 2013; Zha et al., 2013), the recent progress of photothermal nanoagents focus on

semiconductor nanomaterials because of their abundant types, tunable composites, photostability as well as efficient photothermal effect (Huang et al., 2017). The semiconductor-based photothermal nanomaterials mainly include the metal oxides such as the doped TiO_{2-x} nanocrystals (Ren et al., 2015; Ou et al., 2016; Yu et al., 2017) and oxygen-deficient WO_{3-x} nanocrystals (Xu et al., 2015; Wen et al., 2016), and the metal sulfides including $Cu_{2-x}S$ nanostructures (Tian et al., 2011a,b) and Bi_2S_3 nanodots (Li et al., 2016). For example, $Cu_{7.2}S_4$ nanoparticles were prepared by the thermolysis of $Cu(DEDTC)_2$ precursors and they exhibited strong NIR absorption, photostability and photothermal conversion efficiency up to 56.7%, which were used as a photothermal nanoagent for the photothermal ablation of cancer cells (Li et al., 2014). However, the therapeutical effect of photothermal therapy is executed only under the illumination of laser and it would disappear instantly when laser is switched off. Thus, to achieve the long-term therapeutical effect for photothermal nanoagents, it is quite necessary to combine with other therapeutical modalities.

The integration of photothermal therapy and chemotherapy has been recognized to be an efficient strategy through the instant thermally ablation and long-term chemical inhibition (You et al., 2012; Yu et al., 2018a; Zhang et al., 2020). Importantly, the photothermal effect can accelerate the drug releasing rate and induce the chemo-sensitization effect, thus achieving the synergistic effect with higher therapeutical results than photothermal therapy or chemotherapy alone. Up to data, there are a number of nanoagents with the photothermal effect and drug loading capacity, which can be allocated into two types. The first type consists the photothermal nanomaterials with a large volume of inner cavity or high specific surface area, such as CuS hollow nanospheres (Wang et al., 2018), two-dimensional MoS_2 nanosheets (Liu et al., 2014) and metal-organic frameworks (Zhang et al., 2018). For instance, CuS hollow nanospheres with 87.7% of high doxorubicin (DOX) content were prepared while the DOX release rate at pH 7.4 was only 4.6% and at pH 5.0 was 10.3% within 10 h (Wang et al., 2018). The second type is the combination of photothermal nanoagent and drug carrier, which includes Cu_9S_5@mSiO_2-PEG core-shell structures (Song et al., 2013), Au@copolymer-liposome nanostructures (Zheng et al., 2016) and CuS@gel nanocomposites (Meng et al., 2016). For example, a thermosensitive MEO_2MA@MEO_2MA-co-OEGMA nanogels were firstly prepared and then CuS nanoagents were *in situ* deposited within nanogels, whereas the DOX loading content was less than 10%, (Meng et al., 2016). Therefore, it is of great importance to design and synthesis of photothermal-chemo nanoagents with the high photothermal conversion efficiency and high drug loading capacity.

In order to integrate synergistic photothermal-chemo functions, we prepared a Cu_7S_4@SiO_2/DOX. The Cu_7S_4@SiO_2/DOX was constructed by firstly synthesizing Cu_7S_4 nanocrystals, then *in situ* growing SiO_2 shell on the surface of Cu_7S_4 nanocrystals, and finally loading DOX within SiO_2 shell. The Cu_7S_4@SiO_2 nanoplatforms exhibited the strong and broad NIR absorption and could rapidly convert 1064 nm laser energy into heat with the efficiency of 48.2%, and they also demonstrated large specific surface area and pores with high DOX loading content of 59.8%. Importantly, After the irradiation cycles, 90.1% of DOX was released from Cu_7S_4@SiO_2/DOX with the help of 1064 nm NIR laser at pH 5.4 in comparison to 61.5% of the released DOX without irradiation, indicating photothermal effect accelerated the DOX release. More importantly, when Cu_7S_4@SiO_2/DOX was intratumorally injected into tumor-bearing mice, the tumor growth was heavily inhibited through the synergistic photothermal-chemo therapy compared with the limited therapeutical effect of photothermal therapy or chemotherapy alone. Therefore, the Cu_7S_4@SiO_2/DOX with high photothermal conversion efficiency and drug loading capacity can be used for treating solid tumor with high therapeutical effect.

MATERIALS AND METHODS

Materials

Sodium diethyldithiocarbamate (SDEDTC), $CuCl_2{\cdot}2H_2O$ (AR), oleic acid (AR), oleylamine (80–90%), cetyltrimethylammonium bromide (CTAB), sodium hydroxide (NaOH, AR), doxorubicin hydrochloride (DOX) and tetraethylorthosilicate (TEOS, GR) were brought from Sigma Aldrich.

Preparation of Cu_7S_4 Nanocrystals

The Cu_7S_4 nanocrystals were prepared by a typical thermolysis method (Li et al., 2014). Firstly, $CuCl_2{\cdot}2H_2O$ (20 mmol) was dissolved into 10 mL deionized water, which was then dropwise added into aqueous solution of SDEDTC (90 mL, 50 mmol) under magnetically stirring. After stirring for 2 h, the above solution was centrifuged (5000 rpm, 5 min) and washed with deionized water. The precipitate [$Cu(DEDTC)_2$ precursor] was dried in vacuum at 50°C for further use. Secondly, oleic acid (15 mL) and oleylamine (10 mL) were added into three-neck bottle and heated to 280°C within 30 min under the continuous nitrogen flow to remove any moisture and oxygen. The $Cu(DEDTC)_2$ precursor (1 mmol) dissolved in 2 mL oleic acid was injected to the three-neck bottle and heated at 280°C for 10 min. The dark green mixture was quickly cooled to 60°C by air flow and then 20 mL ethanol was introduced to precipitate Cu_7S_4 nanocrystals. Finally, the Cu_7S_4 nanocrystals were dispersed in ethanol followed by centrifuging and washed with ethanol for three times.

Preparation of Cu_7S_4@SiO_2 Nanoplatforms

The Cu_7S_4@SiO_2 nanoplatforms were prepared by *in situ* growing SiO_2 shell on the surface of Cu_7S_4 nanocrystals. Firstly, the hydrophobic Cu_7S_4 nanocrystals were converted into hydrophilic Cu_7S_4 through the surface-modification with CTAB. The Cu_7S_4 nanocrystals in chloroform solution (5 mL, 10 mg/mL) were added into aqueous solution of CTAB (20 mL, 100 mg/mL), which was stirred vigorously at 40°C for 24 h and then centrifuged to collect hydrophilic Cu_7S_4 nanocrystals. Secondly, the hydrophilic Cu_7S_4 nanocrystals were dispersed

into 50 mL deionized water, followed by the introduction of NaOH solution (0.1 mL, 10 mg/mL) and TEOS (0.1 mL) under sonication. After 1 h of sonication, then 100 μL of PEG-silane was added and the mixture was maintained at 40°C for another 8 h. The products were centrifuged and washed with deionized water for three times for collecting Cu_7S_4@SiO_2 nanoplatforms.

Characterizations

The size, morphology, phase of Cu_7S_4@SiO_2 nanoplatforms were characterized by using JEOL 2100F transmission electron microscopy (TEM). The photoabsorption of Cu_7S_4@SiO_2 nanoplatforms was studied on a Shimadzu UV-1900 spectrophotometer. The concentration of copper irons released from the Cu_7S_4@SiO_2 nanoplatforms was determined by an inductively coupled plasma atomic emission spectroscopy (ICP-AES). The specific surface area and pore diameter of Cu_7S_4@SiO_2 powder were investigated on the Autosorb-iQ/Autosorb-iQ Brunauer-Emmett-Teller (BET).

Photothermal Conversion Efficiency

The photothermal performance of Cu_7S_4@SiO_2 nanoplatforms was investigated by illuminating their aqueous dispersion at a series of concentrations under a 1064 nm laser with the output power density of 0.6 Wcm^{-2}. The temperature change was recorded by using a thermal imaging camera. The photothermal conversion efficiency of Cu_7S_4@SiO_2 was calculated according to the previous report (Li et al., 2014) by applying the below equations:

$$\eta = \frac{hA(\Delta T_{max,dis} - \Delta T_{max,H_2O}}{I(1 - 10^{-A_{1064}})} \quad (1)$$

$$\tau_s = \frac{m_D C_D}{hA} \quad (2)$$

Where I and A_{1064}, respectively, stand for the NIR laser intensity and the absorbance at 1064 nm. $\Delta T_{max,dis}$ and $\Delta T_{max,H_2O}$ are the temperature change of deionized water and the solution containing Cu_7S_4@SiO_2 nanoplatforms. The h and A are the heat transfer coefficient and the surface area, and the value of hA is determined from Eq. 2 by using the system time constant τ_s with the help of the mass (m_D) and the heat capacity (C_D) of deionized water.

Dox Loading and Releasing

For loading DOX, Cu_7S_4@SiO_2 (2.5 mL, 10 mg/mL) and DOX (10 mg) were dispersed into PBS solution, which was magnetically stirred in the dark. After 24 h of stir, the mixture was centrifuged (12,000 rpm, 30 min) and the supernatant was collected. The DOX loading content was calculated based on (load weight of DOX/Cu_7S_4@SiO_2/DOX) × 100%, in which the load weight of DOX was determined by (10 mg – DOX in the supernatant). For DOX releasing, Cu_7S_4@SiO_2/DOX was dispersed into PBS at pH 7.4 or pH 5.4 and divided into two groups. One group was used as control and 0.5 mL solution were taken out which was centrifuged (12,000 rpm, 15 min) at each time point. Another group was irradiated by a 1064 nm NIR laser (0.6 Wcm^{-2}) at a specific time. The DOX releasing rate was calculated by using (the release weight of DOX/the load weight of DOX) × 100%.

Photothermal-Chemo Therapy *in vitro*

Melanoma cells were seeded into a 96-well plate (1.2×10^4 cells per well) at 37°C in the presence of 5% CO_2 for 24 h. After incubation, the cell medium was removed, the cells were divided into four groups: (1) control, (2) DOX, (3) Cu_7S_4@SiO_2/DOX+NIR, (4) Cu_7S_4@SiO_2+NIR. Hundred microliter of the dispersion at varied concentrations was then added into the wells. After incubation for another 24 h, the cells were washed with PBS buffer solution for three times. Then the cells were irradiated with/without a 1064 nm laser. Cell viability was measured using the CCK-8 assay.

To visually compare the viability difference in cellular level among four groups, cells were seeded into a 24-well plate at a density of 1.2×10^5 cells per well. After the cells in the four groups were treated, the cells were stained with calcein AM (live cells) and propidium iodide (dead cells) to distinguish live cells with green fluorescence and dead cells with red fluorescence.

Photothermal-Chemo Therapy *in vivo* and Histological Examination

The BALB/c mice (∼16 g, male) with 4T1 tumors (the surface diameter of 0.3∼0.5 cm) on the back were divided into four groups (n = 3): (1) The control group; (2) DOX group; (3) Cu_7S_4@SiO_2+NIR group; (4) Cu_7S_4@SiO_2/DOX+NIR group. The mice in (2) group were intratumorally injected with DOX PBS solution (50 μL, 80 μg), and mice in (3 and 4) group were, respectively, injected with Cu_7S_4@SiO_2 (50 μL, 0.1 mg mL^{-1}) or Cu_7S_4@SiO_2/DOX PBS solution (50 μL, 0.1 mg mL^{-1}). The tumors on mice in (3, 4) group were exposed to a 1064 nm NIR laser (0.6 Wcm^{-2}) at the 0.5 h post-injection and mice body. After treatments, mice in all groups were observed regarding their body weight and tumor sizes. When a tumor size was beyond 1.0 cm, mice in all groups were sacrificed and tumors were extracted for histological examination.

RESULTS AND DISCUSSION

The Cu_7S_4@SiO_2 nanoplatforms were prepared by *in situ* growing SiO_2 shell on the surface of Cu_7S_4 nanocrystals. Firstly, Cu_7S_4 nanocrystals were synthesized through a typical thermolysis method, where the $Cu(DEDTC)_2$ precursor with Cu source and S source was heated to 280°C for 10 min to produce uniform Cu_7S_4 nanocrystals. Secondly, the Cu_7S_4 nanocrystals were served as the core to allow the coating of SiO_2 shell through the hydrolysis of TEOS. During the SiO_2 coating, CTAB were used as a soft template. SiO_2 grew around the template due to electrostatic interactions. **Supplementary Figure S1** shows the size and zeta potential of nanoparticles during the process of synthesis. FTIR spectra in **Supplementary Figure S2** demonstrated that PEG was coated on the surface of Cu7S4@SiO_2 nanoplatforms, thus the nanoplatforms could be realized the bioapplication directly. The as-obtained Cu_7S_4@SiO_2 nanoplatforms have a uniform morphology and the average size

of 100 nm, as shown in the TEM image (**Figure 1a**). Obviously, the Cu_7S_4@SiO_2 nanoplatforms consist of Cu_7S_4 as the core and SiO_2 as the shell, and the Cu_7S_4 nanocrystals have the average diameter of 50 nm and the SiO_2 shells have the average thickness of 25 nm. The nanoplatforms showed good dispersion as the size in water showed little change over time demonstrated by dynamic light scattering (DLS, **Supplementary Figure S3**). Furthermore, the high-resolution (HR-TEM) image in **Figure 1b** demonstrates the apparent lattice with an interplane *d* spacing of ∼0.277 nm, which can be indexed to the (110) plane of the orthorhombic Cu_7S_4 (JCPDS card no. 22-0250), which verifies the core is Cu_7S_4 nanocrystals. Subsequently, the phase of Cu_7S_4@SiO_2 powders was characterized by using XRD. The XRD pattern (**Figure 1c**) reveals that there are four prominent peaks centered at 27.87°, 32.30°, 46.40°, and 54.70°, which can be respectively, corresponded to the (202), (220), (224), and (422) planes for the orthorhombic Cu_7S_4 (JCPDS card no. 22-0250). It should be noted that there is a broad peak between 10° and 40°, which should be attributed to the characteristic peak originating from the amorphous SiO_2 shell. **Supplementary Figure S4** shows the XPS spectra of Cu 2p in the Cu_7S_4@SiO_2 nanoparticles. The binding energy peaks at 932.8 and 954.6 eV can be assigned to Cu^+ coordinated to Cu in Cu_7S_4@SiO_2 nanoparticles, whereas the binding energy peak at 943.2 eV is formally described as Cu^{2+}. The coexistence of Cu^+ and Cu^{2+} indicated the Cu vacancies on the surface of Cu_7S_4 nanocrystals (Li et al., 2015). Thus, the above results confirmed the successful preparation of Cu_7S_4@SiO_2 nanoplatforms with Cu_7S_4 core and SiO_2 shell.

Subsequently, the photoabsorption of Cu_7S_4@SiO_2 nanoplatforms was studied by using UV-vis-NIR spectrometer. The Cu_7S_4@SiO_2 nanoplatforms can be well dispersed into deionized water and their aqueous solution shows the dark green. As demonstrated in UV-vis-NIR photoabsorption spectra (**Figure 1d**), the aqueous solution containing Cu_7S_4@SiO_2 nanoplatforms exhibits the strong absorption in the UV-vis region with the edge at ∼590 nm, which can be ascribed to the bandgap absorption of Cu_7S_4 as a typical semiconductor. Importantly, the aqueous solution of Cu_7S_4@SiO_2 demonstrates a strong and broad NIR absorption (>650 nm) and the absorption intensity goes up with the increase of wavelength

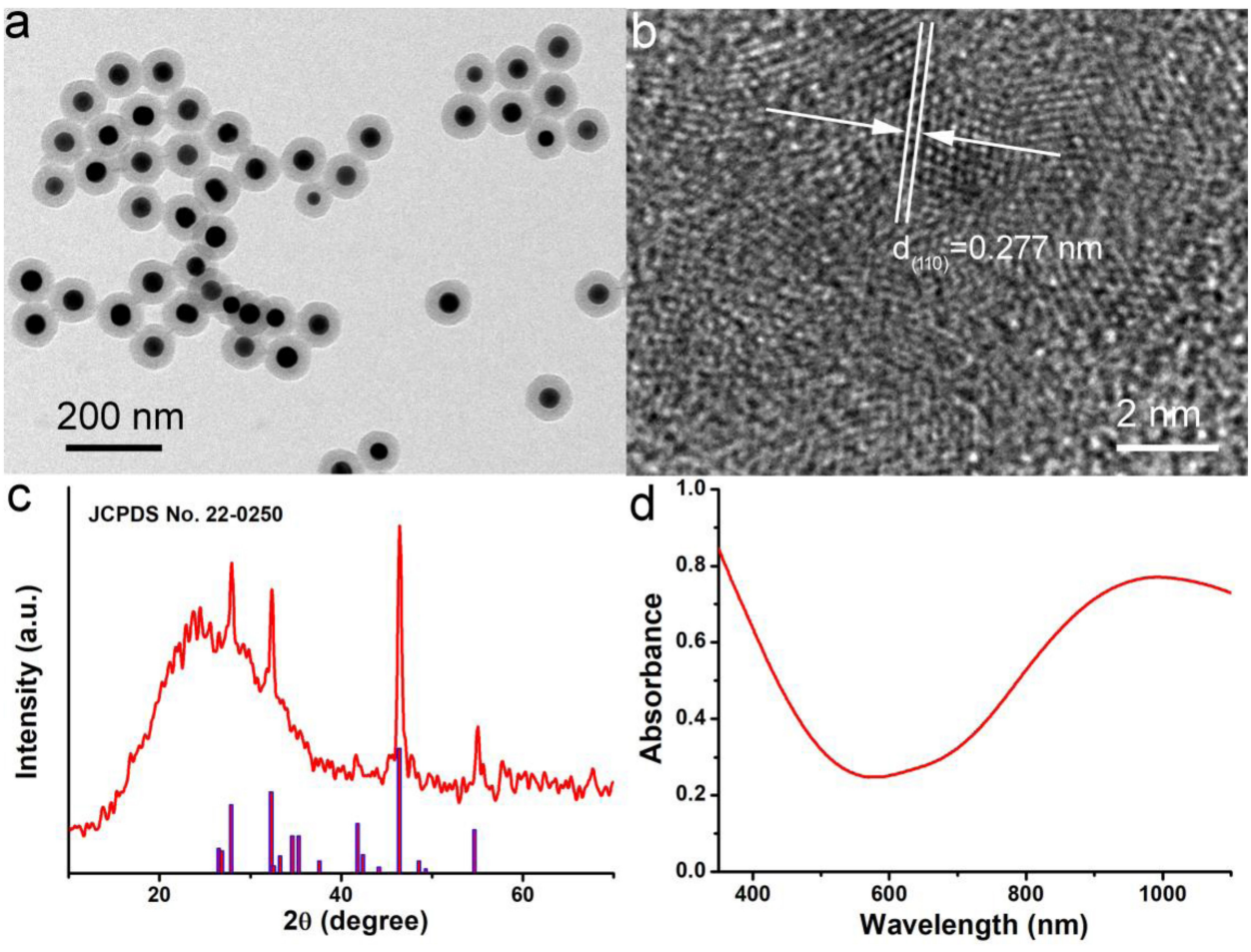

FIGURE 1 | (a) TEM image of Cu_7S_4@SiO_2 nanoplatforms showing the Cu_7S_4 core and mesoporous SiO_2 shell. **(b)** HR-TEM image of Cu_7S_4 core with the clear lattice. **(c)** XRD pattern of Cu_7S_4@SiO_2 nanoparticles. **(d)** The typical UV-vis-NIR photoabsorption spectrum of Cu_7S_4@SiO_2 dispersed in deionized water.

up to 1100 nm. Compared to the bandgap-induced UV-vis absorption, this kind of NIR absorption should be attributed to the localized surface plasmon resonances (LSPR) effect because of Cu vacancies on the surface of Cu_7S_4 nanocrystals, which has been reported for other $Cu_{2-x}S$ nanocrystals (Zhao et al., 2009; Luther et al., 2011). By determining the Cu_7S_4@SiO_2 nanoparticle concentration via ICP-AES, the extinction coefficient of the nanoparticles at 1064 nm was measured to be 13.9 L g^{-1} cm^{-1}, which was higher than the that of cobalt/manganese oxide (CMO) nanocrystals (Liu et al., 2019). Thus, Cu_7S_4@SiO_2 nanoplatforms are capable of strong and broad NIR photoabsorption because of Cu_7S_4 core.

Owing to the strong NIR absorption, we further explored the photothermal performance of Cu_7S_4@SiO_2 nanoparticles. The wavelength of NIR laser is quite important for photothermal therapy, and two biological transparency windows are reported as NIR-I (650–950 nm) and NIR-II (1000–1350 nm). Compared to the commonly used 808 nm, 915 m and 980 nm NIR laser, 1064 nm NIR laser can offer more efficient tissue penetration depth by considering absorption and scattering effects (Tsai et al., 2013). Therefore, we selected 1064 nm NIR laser to study the photothermal effect of Cu_7S_4@SiO_2 nanoparticles. When exposed to a 1064 nm NIR laser at the intensity of 0.6 W cm^{-2}, the temperature of deionized water increases slightly (∼1.3°C) within 5 min of irradiation, which confirmed the negligible photothermal effect from deionized water (**Figure 2A**). In contrast, once exposed to laser, the aqueous solutions containing Cu_7S_4@SiO_2 nanoparticles exhibit rapid temperature elevation within 120 s and then show a slow temperature elevation due to the balance between heat production and loss. **Figure 2B** summarizes the temperature elevation versus to the concentration, and they are determined to be 14.2, 21.8, 31.5, and 39.4°C for the concentration of 10, 20, 30, and 40 ppm, respectively. To further clarify the photothermal performance of Cu_7S_4@SiO_2 nanoparticles, we carried out an experiment to calculate its photothermal conversion efficiency. The aqueous solution of Cu_7S_4@SiO_2 nanoparticles were subjected to a 1064 nm NIR laser on/off, and

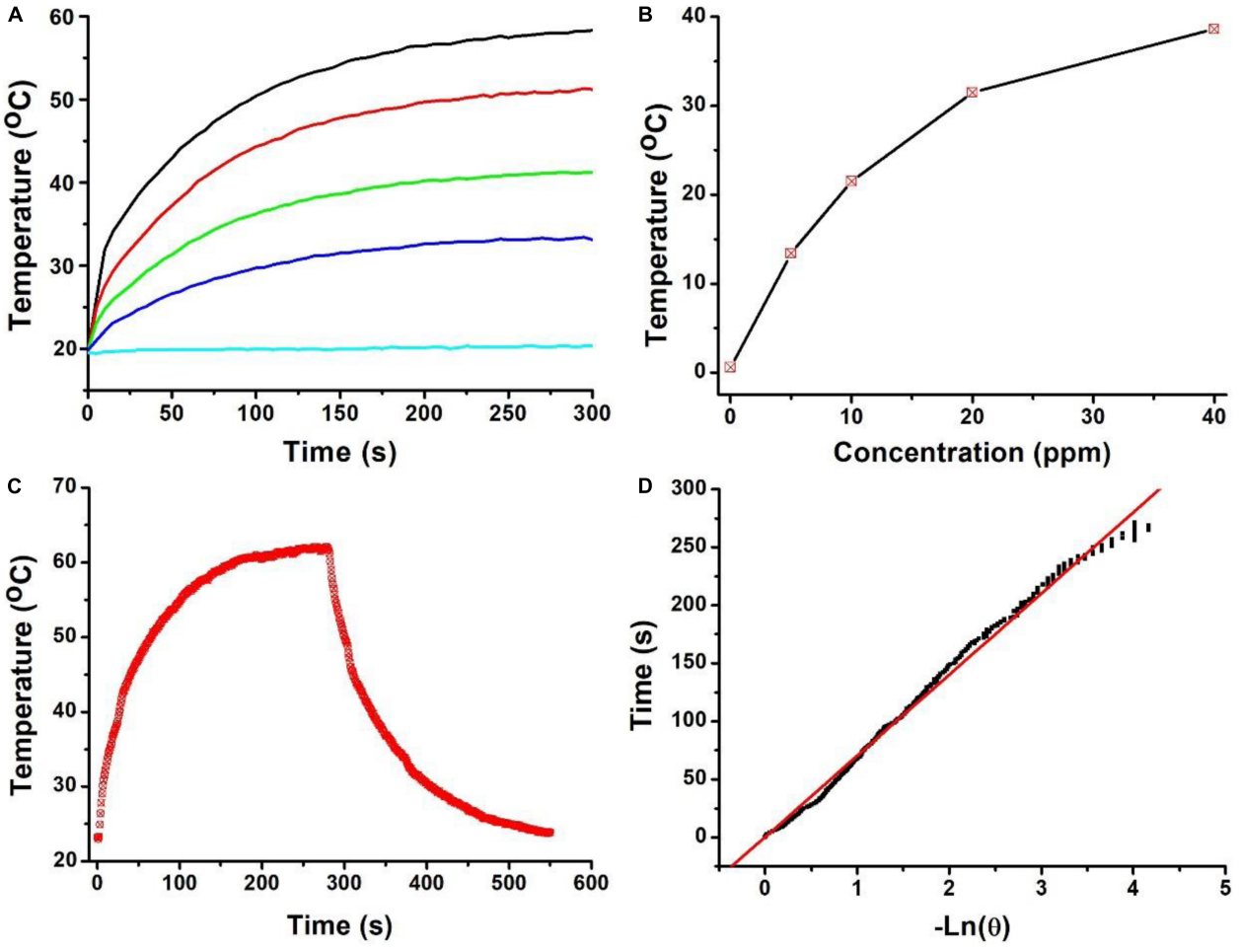

FIGURE 2 | (A) Temperature curves of solution containing the Cu_7S_4@SiO_2 nanoparticles with the Cu concentration of 0–40 ppm. **(B)** The Temperature elevation versus the concentrations of Cu_7S_4@SiO_2 nanoparticles. **(C)** Temperature curve of a solution containing the Cu_7S_4@SiO_2 nanoparticles with 1064 nm NIR laser on/off. **(D)** The linear fit of time data with ln(θ) to obtain system time constant τ_s.

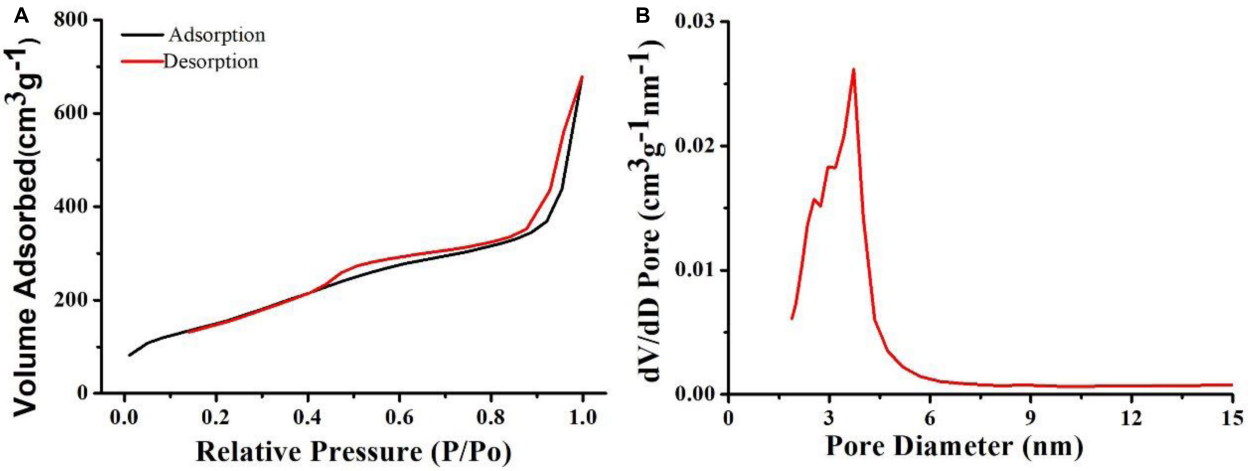

FIGURE 3 | (A) The nitrogen adsorption-desorption curve of Cu_7S_4@SiO_2 nanoparticles. **(B)** The pore diameter of Cu_7S_4@SiO_2 nanoparticles.

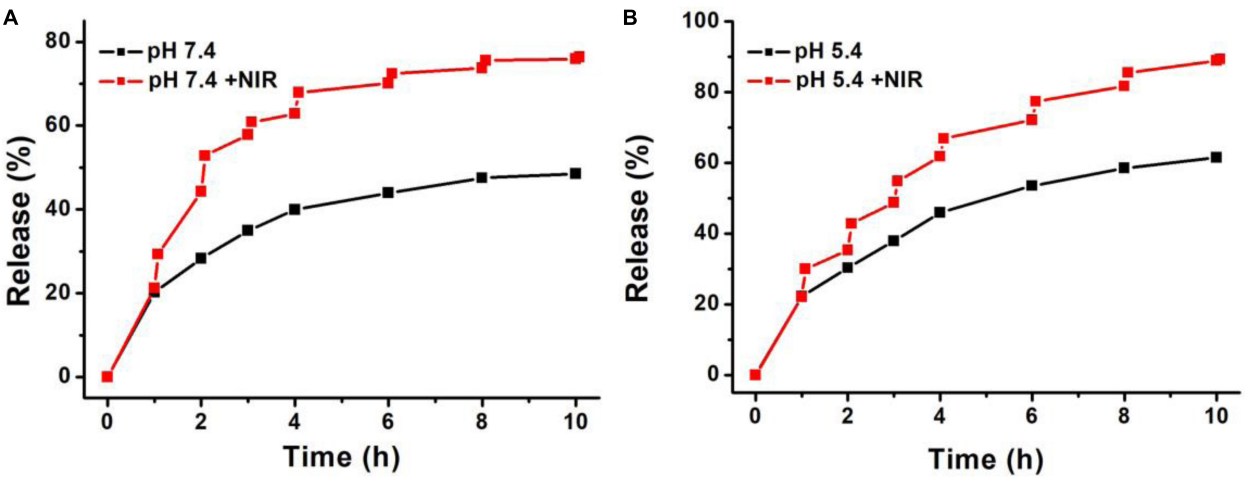

FIGURE 4 | The DOX-releasing profile of Cu_7S_4@SiO_2/DOX in **(A)** PBS solution (pH = 7.4) and **(B)** acetate buffer (pH 5.4) in the absence or presence of 1064 nm NIR laser.

the whole temperature change was recorded in **Figure 2C**. The system time constant τ_s can be obtained by linearly plotting the time data with ln(θ), as shown in **Figure 2D**. By referencing to the previous reports, the photothermal conversion efficiency of Cu_7S_4@SiO_2 nanoparticles is 48.2% which is comparable to the reported CuS nanomaterials (Li et al., 2014). Therefore, the Cu_7S_4@SiO_2 nanoparticles can rapidly and efficiently convert 1064 nm NIR laser energy into heat with the concentration-relied photothermal performance.

After demonstrating the photothermal performance of Cu_7S_4@SiO_2 nanoparticles, we evaluated their DOX loading capacity due to the SiO_2 shell. Prior to loading DOX, the Brunauer-Emmett-Teller (BET) surface area and pore size were investigated by using nitrogen adsorption-desorption curves. The nitrogen adsorption/desorption isotherms (**Figure 3A**) illustrate that the Cu_7S_4@SiO_2 nanoparticles have a specific surface area of 125.9 m^2/g, showing the high surface area. In addition, the pore diameter of Cu_7S_4@SiO_2 nanoparticles was also recorded and the average pore diameter was determined to be ∼4.5 nm (**Figure 3B**). Therefore, the mesoporous SiO_2 shell confers high specific surface area and pores, which will facilitate the following DOX loading.

The release ability of DOX from Cu_7S_4@SiO_2/DOX (the DOX loading content is 29.8%) was studied by dispersing Cu_7S_4@SiO_2/DOX into PBS solution. At the time point of 1, 2, 3, 4, 6, 8, and 10 h, part of solution was taken out from the original 10 mL dispersion and centrifuged for collecting the released DOX in the supernatant, and the amount of DOX in the supernatant was calculated by applying absorption-concentration curve. **Figure 4A** shows the DOX releasing profile at pH 7.4, and it is clear that, with the prolong of time, the DOX releasing rate unceasingly goes up which can be determined to be 19.5% at 1 h, 28.4% at 2 h, and 39.4% at 4 h. After 4 h, the DOX releasing rate becomes

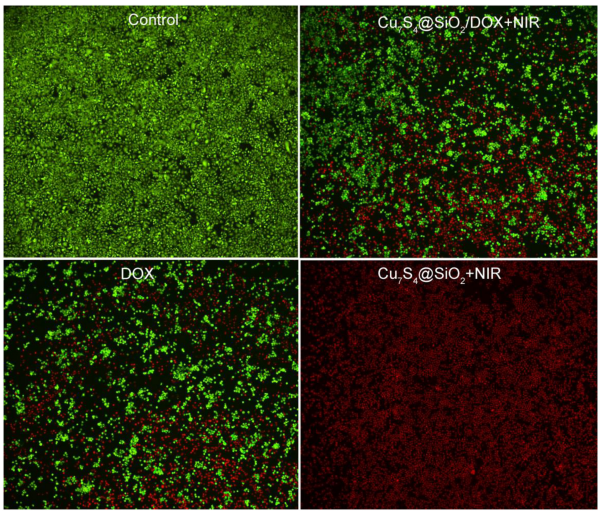

FIGURE 5 | Confocal images of calcein AM (green, live cells) and propidium iodide (red, dead cells) co-stained cells after incubation with Cu_7S_4@SiO_2/DOX for different treatments. Magnification: 100 times.

very slow. In order to study the effect of NIR laser-induced photothermal effect on the DOX releasing rate, we irradiated the Cu_7S_4@SiO_2/DOX dispersion at the time point of 1, 2, 3, 4, 6, 8, and 10 h by using a 1064 nm NIR laser (5 min, 0.6 W cm^{-2}). For instance, after the firstly irradiation, the DOX releasing rate is calculated to be 45.8% which is much higher than that (28.4%) at the 2 h, indicating NIR laser-induced photothermal effect can significantly enhance the DOX releasing rate. After the irradiation cycles, 75.6% of DOX is released from Cu_7S_4@SiO_2/DOX with the help of 1064 nm NIR laser in comparison to 47.4% of the released DOX without irradiation, within 10 h. Thereby, it is concluded that the Cu_7S_4 nanocrystals within Cu_7S_4@SiO_2/DOX can produce heat to accelerate the DOX release. To study the DOX release behavior from Cu_7S_4@SiO_2/DOX at the simulating tumor microenvironment, the release of the DOX against buffer solution at pH 5.4 was measured. It was found that the drug release rate became much faster at pH 5.4 (**Figure 4B**) due to the increase in the solubility of the DOX under acidic conditions, which is beneficial for cancer therapy since the microenvironments of extracellular tissues of tumors and intracellular lysosomes and endosomes are acidic.

Giving the efficient photothermal conversion effect, the high DOX loading capacity and the NIR-enhanced DOX releasing, Cu_7S_4@SiO_2/DOX can be used as excellent nanoagents for photothermal-chemo therapy. To demonstrate the synergy effect of photothermal-chemo therapy, the combination index of Cu_7S_4@SiO_2/DOX nanoparticles was measured according to previous work (Wang et al., 2013). The half-maximal inhibitory concentration (IC50) of cancer cells incubated with Cu_7S_4@SiO_2/DOX nanoparticles for combination photothermal-chemo therapy is 0.52 mg mL^{-1}, while the IC50 for the sole photothermal therapy and chemotherapy is 0.67 and 1.35 mg mL^{-1}, respectively. The combination index was calculated to evaluate the combination effect of different therapies and found to be 0.823, which demonstrated the synergistic effect of Cu_7S_4@SiO_2/DOX nanoparticles for photothermal-chemo therapy. Additionally, to visualize the efficiency of photothermal-chemo therapy, cells after the indicated treatments were co-stained with calcein-AM and propidium iodide (PI, **Figure 5**). The results further demonstrated the synergetic effect.

Before realizing bioapplication, the Cu^{2+} release of Cu_7S_4@SiO_2 nanoparticles in PBS was evaluated because of Cu^{2+} being toxic. It was revealed that the concentration of the released Cu^{2+} from Cu_7S_4@SiO_2 nanoparticles was very low (**Supplementary Figure S5**), which caused almost no toxicity. We then evaluated the toxicity *in vivo* of Cu_7S_4@SiO_2. In the experimental group, the material was injected intravenously into mice, while mice in the control group were injected with PBS.

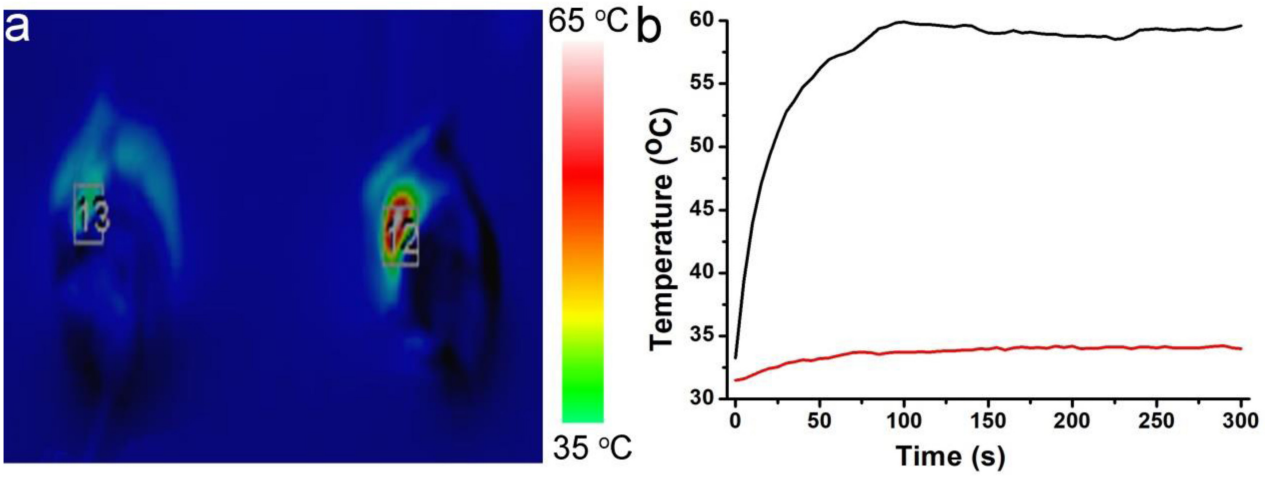

FIGURE 6 | (a) The thermal image of mice after intratumorally injecting with Cu_7S_4@SiO_2/DOX PBS solution (right) or PBS solution (left) under the irradiation of 1064 nm NIR laser at the power density of 0.6 Wcm^{-2}. **(b)** The temperature curves showing the temperature change in tumor area.

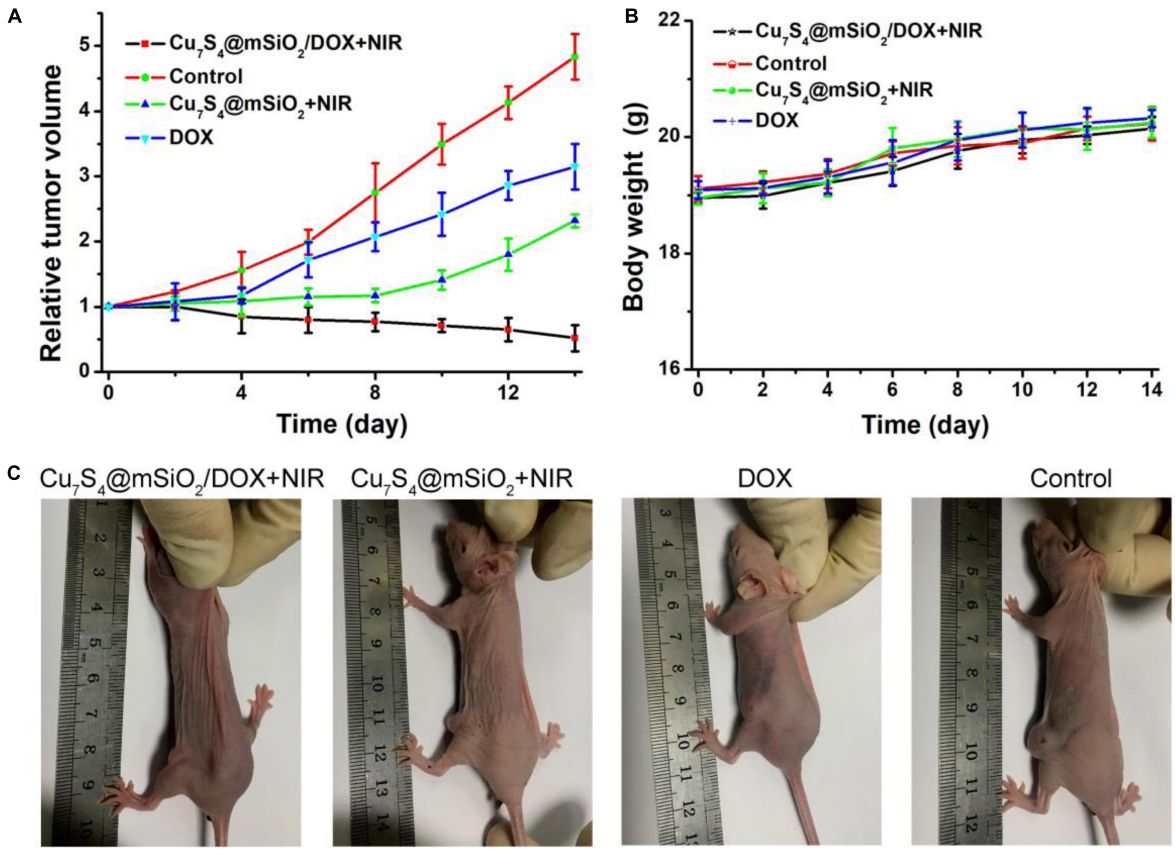

FIGURE 7 | (A) The relative tumor volumes of mice after different treatments over a period of 14 days. **(B)** The body weight of mice in these groups. **(C)** The typical photographs of mice at the 14th day.

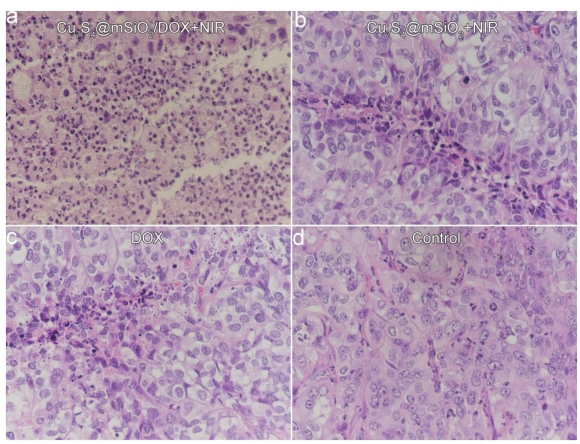

FIGURE 8 | The typical images of tumor slices stained with H&E assay for **(a)** Cu_7S_4@SiO_2/DOX+NIR group, **(b)** Cu_7S_4@SiO_2+NIR group, **(c)** DOX group, and **(d)** Control group.

After a month, HE analysis of the main organs of mice in the two groups showed no significant difference (**Supplementary Figure S6**). To perform photothermal-chemo therapy of tumors, mice bearing with melanoma tumor were randomly allocated into four groups as follow: (1) The control group; (2) DOX group; (3) Cu_7S_4@SiO_2+NIR group; (4) Cu_7S_4@SiO_2/DOX+NIR group. The mice in (2) group were intratumorally injected with DOX PBS solution (50 μL, 80 μg), and mice in (3 and 4) group were intratumorally injected with Cu_7S_4@SiO_2 (50 μL, 0.1 mg mL^{-1}) and Cu_7S_4@SiO_2/DOX PBS solution (50 μL, 0.1 mg mL^{-1}). **Figure 6a** shows the typical thermal image of mice with the tumor area exposed to a 1064 nm NIR laser (0.6 Wcm^{-2}), in which the tumor treated with Cu_7S_4@SiO_2/DOX shows the bright red while the tumor received PBS exhibits the normal color. The surface temperature of tumor treated with Cu_7S_4@SiO_2/DOX increases from ∼34.2°C to the balanced ∼57.9 °C at 300 s, resulting in temperature elevation of 23.7°C which was much higher than that (3.5°C) for the tumor received PBS (**Figure 6b**). Thus, the Cu_7S_4@SiO_2/DOX within tumor remain high photothermal conversion effect, which can convert 1064 nm NIR laser energy into enough heat to thermally ablate cancer cells.

After different treatments, mice in all groups were raised under the standard condition for the long-term observation of cancer treatment efficacy. The tumor sizes and body weights were recorded. The change of relative tumor volumes is demonstrated in **Figure 7A**. Obviously, the tumor volume in the control

group increases greatly which was five times the initial volume. For the tumors in the DOX group and Cu_7S_4@SiO_2+NIR group, their growth has been inhibited, due to the cytotoxicity of DOX for DOX group and the photothermal therapy for Cu_7S_4@SiO_2+NIR group. Interestingly, in the case of the tumors in the Cu_7S_4@SiO_2/DOX+NIR group, their volume goes down continuously with the significant inhibition efficiency compared to the other three groups. The high inhibition efficiency should be due to the synergistic photothermal-chemo effect from the combination of Cu_7S_4@SiO_2/DOX and NIR laser irradiation. On the one side, the photothermal therapy can instantly kill part of cancer cells through high temperature, and on the other side, the load DOX within Cu_7S_4@SiO_2/DOX can continuous release to kill the remaining cancer cells, thus achieving the synergistic effect on melanoma tumors. In addition, there was no any sign of loss in body weight for all groups (**Figure 7B**). Therefore, the satisfactory inhibition efficiency can be realized from the synergistic photothermal-chemo therapy by the combination of Cu_7S_4@SiO_2/DOX and 1064 nm NIR laser, while no obvious side effect for mice.

Furthermore, mice in all groups were sacrificed when a tumor size was beyond 1.0 cm (**Figure 7C**). The tumors were extracted for the sacrificed mice, which were embedded in paraffin and crysectioned into slices. After stained with H&E assay, the tumor slices were imaged for histological examination. **Figure 8** manifests the typical morphology of tumor cells, and the cancer cells shows the normal and complete morphology in regard to the cell size, shape and nuclear. The significant cell damage is noticed for Cu_7S_4@SiO_2/DOX+NIR group (**Figure 8a**), including the destroyed cell membranes and the condensed nucleus. For the tumor cells in the Cu7S4@SiO_2+NIR group (**Figure 8b**) and DOX group (**Figure 8c**), there are some cells showing the destroyed morphology, indicating the limited therapeutical effect through photothermal therapy or chemotherapy. On the contrary, the cell size and shape showed no difference in the control group (**Figure 8d**). The above histological examination solidly verifies the higher therapeutical effect of photothermal-chemo therapy than photothermal therapy or chemotherapy.

CONCLUSION

In summary, we prepared the Cu_7S_4@SiO_2/DOX and used them as efficient nanoplatforms for synergistic photothermal-chemo therapy on melanoma tumors. The Cu_7S_4@SiO_2/DOX was prepared by firstly synthesizing Cu_7S_4 nanocrystals, then *in situ* growing SiO_2 shell on the surface of Cu_7S_4 nanocrystals, and finally loading DOX. The Cu_7S_4@SiO_2 consisted of Cu_7S_4 core with the average diameter of 50 nm and SiO_2 shell with the average thickness of 25 nm. The Cu_7S_4@SiO_2 nanoplatforms exhibited the strong and broad NIR absorption and rapidly converted 1064 nm laser energy into heat, and they also demonstrated high specific surface area and a large amount of pores with high DOX-loading content of 59.8%. Importantly, under the irradiation of 1064 nm laser, Cu_7S_4@SiO_2/DOX simultaneous generated heat and accelerated the DOX release. Give these advantages, mice were intratumorally injected with Cu_7S_4@SiO_2/DOX and irradiated with1064 nm laser, which achieved the highest therapeutical effect through synergistic photothermal-chemo therapy compared to photothermal therapy or chemotherapy alone. Therefore, the Cu_7S_4@SiO_2/DOX can be served as novel and efficient photothermal-chemo nanoagents for efficient tumor therapy.

DATA AVAILABILITY STATEMENT

All datasets presented in this study are included in the article/**Supplementary Material.**

ETHICS STATEMENT

The animal study was reviewed and approved by the Ninth People's Hospital, Shanghai Jiao Tong University School of Medicine.

AUTHOR CONTRIBUTIONS

LZ and HP contributed equally to this work. LZ, HP, and XH designed the project and wrote the manuscript. LZ, HP, and YL carried out the experiment. LZ and FL performed the experimental data analysis. All the authors contributed to discussion of the results.

FUNDING

This work was supported by grants from the National Natural Science Foundation of China (81402258, 81702781, 81972524, and 81602366) and the Science and Technology Commission of Shanghai (17DZ2260100).

SUPPLEMENTARY MATERIAL

The Supplementary Material for this article can be found online at: https://www.frontiersin.org/articles/10.3389/fbioe.2020.579439/full#supplementary-material

REFERENCES

Cheng, L., Wang, C., Feng, L., Yang, K., and Liu, Z. (2014). Functional nanomaterials for phototherapies of cancer. *Chem. Rev.* 114, 10869–10939. doi: 10.1021/cr400532z

Dreaden, E. C., Mackey, M. A., Huang, X. H., Kang, B., and El-Sayed, M. A. (2011). Beating cancer in multiple ways using nanogold. *Chem. Soc. Rev.* 40, 3391–3404. doi: 10.1039/c0cs00180e

Huang, X., Zhang, W., Guan, G., Song, G., Zou, R., and Hu, J. (2017). Design and functionalization of the nir-responsive photothermal semiconductor

nanomaterials for cancer theranostics. *Acc. Chem. Res.* 50, 2529–2538. doi: 10.1021/acs.accounts.7b00294

Huang, X. Q., Tang, S. H., Mu, X. L., Dai, Y., Chen, G. X., Zhou, Z. Y., et al. (2011). Freestanding palladium nanosheets with plasmonic and catalytic properties. *Nat. Nanotechnol.* 6, 28–32. doi: 10.1038/nnano.2010.235

Li, B., Wang, Q., Zou, R., Liu, X., Xu, K., Li, W., et al. (2014). Cu7.2S4 nanocrystals: a novel photothermal agent with a 56.7% photothermal conversion efficiency for photothermal therapy of cancer cells. *Nanoscale* 6, 3274–3282. doi: 10.1039/c3nr06242b

Li, B., Ye, K., Zhang, Y., Qin, J., Zou, R., Xu, K., et al. (2015). Photothermal theragnosis synergistic therapy based on bimetal sulphide nanocrystals rather than nanocomposites. *Adv. Mater.* 27, 1339–1345. doi: 10.1002/adma.201404257

Li, Z. L., Hu, Y., Chan, M. L., Howard, K. A., Fan, X. L., Sun, Y., et al. (2016). Highly porous PEGylated Bi2S3 nano-urchins as a versatile platform for in vivo triple-modal imaging, photothermal therapy and drug delivery. *Nanoscale* 8, 16005–16016. doi: 10.1039/c6nr03398a

Liu, J. C., Wu, G. F., Tang, Z. Y., Sun, Q., Wu, J. X., and Lv, R. F. (2019). Cobalt/manganese oxides as theragnosis nanoplatforms with magnetic resonance/Near-infrared imaging for efficient photothermal therapy of tumors. *Front. Mater.* 6:286. doi: 10.3389/Fmats.2019.00286

Liu, T., Wang, C., Gu, X., Gong, H., Cheng, L., Shi, X. Z., et al. (2014). Drug delivery with PEGylated MoS2 nano-sheets for combined photothermal and chemotherapy of cancer. *Adv. Mater.* 26, 3433–3440. doi: 10.1002/adma.201305256

Liu, Y. L., Ai, K. L., Liu, J. H., Deng, M., He, Y. Y., and Lu, L. H. (2013). Dopamine-melanin colloidal nanospheres: an efficient near-infrared photothermal therapeutic agent for in vivo cancer therapy. *Adv. Mater.* 25, 1353–1359. doi: 10.1002/adma.201204683

Luther, J. M., Jain, P. K., Ewers, T., and Alivisatos, A. P. (2011). Localized surface plasmon resonances arising from free carriers in doped quantum dots. *Nat. Mater.* 10, 361–366. doi: 10.1038/nmat3004

Meng, Z., Wei, F., Wang, R., Xia, M., Chen, Z., Wang, H., et al. (2016). NIR-laser-switched in vivo smart nanocapsules for synergic photothermal and chemotherapy of tumors. *Adv. Mater.* 28, 245–253. doi: 10.1002/adma.201502669

Ou, G., Li, Z., Li, D., Cheng, L., Liu, Z., and Wu, H. (2016). Photothermal therapy by using titanium oxide nanoparticles. *Nano. Res.* 9, 1236–1243. doi: 10.1007/s12274-016-1019-8

Ren, W. Z., Yan, Y., Zeng, L. Y., Shi, Z. Z., Gong, A., Schaaf, P., et al. (2015). A near infrared light triggered hydrogenated black TiO2 for cancer photothermal therapy. *Adv. Healthc. Mater.* 4, 1526–1536. doi: 10.1002/adhm.201500273

Song, G., Wang, Q., Wang, Y., Lv, G., Li, C., Zou, R., et al. (2013). A low-toxic multifunctional nanoplatform based on Cu9S5@mSiO2 core-shell nanocomposites: combining photothermal- and chemotherapies with infrared thermal imaging for cancer treatment. *Adv. Funct. Mater.* 23, 4281–4292. doi: 10.1002/adfm.201370178

Tian, Q. W., Jiang, F. R., Zou, R. J., Liu, Q., Chen, Z. G., Zhu, M. F., et al. (2011a). Hydrophilic Cu9S5 nanocrystals: a photothermal agent with a 25.7% heat conversion efficiency for photothermal ablation of cancer cells in vivo. *ACS Nano* 5, 9761–9771. doi: 10.1021/nn203293t

Tian, Q. W., Tang, M. H., Sun, Y. G., Zou, R. J., Chen, Z. G., Zhu, M. F., et al. (2011b). Hydrophilic flower-like CuS superstructures as an efficient 980 nm laser-driven photothermal agent for ablation of cancer cells. *Adv. Mater.* 23, 3542–3547. doi: 10.1002/adma.201101295

Tsai, M. F., Chang, S. H. G., Cheng, F. Y., Shanmugam, V., Cheng, Y. S., Su, C. H., et al. (2013). Au nanorod design as light-absorber in the first and second biological near-infrared windows for in vivo photothermal therapy. *ACS Nano* 7, 5330–5342. doi: 10.1021/nn401187c

Vankayala, R., and Hwang, K. C. (2018). Near-Infrared-light-activatable nanomaterial-mediated phototheranostic nanomedicines: an emerging paradigm for cancer treatment. *Adv. Mater.* 30:1706320. doi: 10.1002/adma.201706320

Wang, D., Dong, H., Li, M., Cao, Y., Yang, F., Zhang, K., et al. (2018). Erythrocyte-cancer hybrid membrane camouflaged hollow copper sulfide nanoparticles for prolonged circulation life and homotypic-targeting photothermal/chemotherapy of melanoma. *ACS Nano* 12, 5241–5252. doi: 10.1021/acsnano.7b08355

Wang, Y., Wang, K. Y., Zhao, J. F., Liu, X. G., Bu, J., Yan, X. Y., et al. (2013). Multifunctional mesoporous silica-coated graphene nanosheet used for chemo-photothermal synergistic targeted therapy of glioma. *J. Am. Chem. Soc.* 135, 4799–4804. doi: 10.1021/ja312221g

Wen, L., Chen, L., Zheng, S., Zeng, J., Duan, G., Wang, Y., et al. (2016). Ultrasmall biocompatible WO3-x nanodots for multi-modality imaging and combined therapy of cancers. *Adv. Mater.* 28, 5072–5079. doi: 10.1002/adma.201506428

Xu, W., Meng, Z., Yu, N., Chen, Z., Sun, B., Jiang, X., et al. (2015). PEGylated CsxWO3 nanorods as an efficient and stable 915 nm-laser-driven photothermal agent against cancer cells. *RSC Adv.* 5, 7074–7082. doi: 10.1039/C4RA15524F

You, J., Zhang, R., Zhang, G. D., Zhong, M., Liu, Y., Van Pelt, C. S., et al. (2012). Photothermal-chemotherapy with doxorubicin-loaded hollow gold nanospheres: a platform for near-infrared light-trigged drug release. *J. Controll. Release* 158, 319–328. doi: 10.1016/j.jconrel.2011.10.028

Yu, N., Hu, Y., Wang, X., Liu, G., Wang, Z., Liu, Z., et al. (2017). Dynamically tuning near-infrared-induced photothermal performances of TiO2 nanocrystals by Nb doping for imaging-guided photothermal therapy of tumors. *Nanoscale* 9, 9148–9159. doi: 10.1039/c7nr02180a

Yu, N., Li, J., Wang, Z., Yang, S., Liu, Z., Wang, Y., et al. (2018a). Blue Te nanoneedles with strong nir photothermal and laser-enhanced anticancer effects as "all-in-one" nanoagents for synergistic thermo-chemotherapy of tumors. *Adv. Healthc. Mater.* 7:1800643. doi: 10.1002/adhm.201800643

Yu, N., Wang, Z., Zhang, J., Liu, Z., Zhu, B., Yu, J., et al. (2018b). Thiol-capped Bi nanoparticles as stable and all-in-one type theranostic nanoagents for tumor imaging and thermoradiotherapy. *Biomaterials* 161, 279–291. doi: 10.1016/j.biomaterials.2018.01.047

Zha, Z., Yue, X., Ren, Q., and Dai, Z. (2013). Uniform polypyrrole nanoparticles with high photothermal conversion efficiency for photothermal ablation of cancer cells. *Adv. Mater.* 25, 777–782. doi: 10.1002/adma.201202211

Zhang, K., Meng, X., Cao, Y., Yang, Z., Dong, H., Zhang, Y., et al. (2018). Metal-organic framework nanoshuttle for synergistic photodynamic and low-temperature photothermal therapy. *Adv. Funct. Mater.* 28:1804634. doi: 10.1002/adfm.201804634

Zhang, M. Y., Liu, X. J., Luo, Q., Wang, Q., Zhao, L. J., Deng, G. Y., et al. (2020). Tumor environment responsive degradable CuS@mSiO2@MnO2/DOX for MRI guided synergistic chemo-photothermal therapy and chemodynamic therapy. *Chem. Eng. J.* 389:124450. doi: 10.1016/J.Cej.2020.124450

Zhao, Y., Pan, H., Lou, Y., Qiu, X., Zhu, J., and Burda, C. (2009). Plasmonic Cu2-xS nanocrystals: optical and structural properties of copper-deficient copper(I) sulfides. *J. Am. Chem. Soc.* 131, 4253–4261. doi: 10.1021/ja805655b

Zheng, T. T., Li, G. G., Zhou, F., Wu, R., Zhu, J. J., and Wang, H. (2016). Gold-nanosponge-based multistimuli-responsive drug vehicles for targeted chemo-photothermal therapy. *Adv. Mater.* 28, 8218–8226. doi: 10.1002/adma.201602486

Zou, L., Wang, H., He, B., Zeng, L., Tan, T., Cao, H., et al. (2016). Current approaches of photothermal therapy in treating cancer metastasis with nanotherapeutics. *Theranostics* 6, 762–772. doi: 10.7150/thno.14988

Conflict of Interest: The authors declare that the research was conducted in the absence of any commercial or financial relationships that could be construed as a potential conflict of interest.

The reviewer XH declared a shared affiliation, with no collaboration, with the authors to the handling editor.

frontiers in Materials

ORIGINAL RESEARCH
published: 25 September 2020
doi: 10.3389/fmats.2020.00289

$CuFeS_2$ Nanoassemblies With Intense Near-Infrared Absorbance for Photothermal Therapy of Tumors

Shan Huang[1], Gang Li[2], Zhengyuan Yang[1], Min Hua[3], Zhe Yuan[4] and Xin Jin[5]**

[1] College of Engineering, Zhejiang Normal University, Jinhua, China, [2] School of Mechanical Engineering, Hubei University of Arts and Science, Xiangyang, China, [3] USC-SJTU Institute of Cultural and Creative Industry, Shanghai Jiao Tong University, Shanghai, China, [4] Xingzhi College, Zhejiang Normal University, Jinhua, China, [5] Department of Orthopedics, Shengli Oilfield Central Hospital, Dongying, China

Photothermal therapy is an efficient cancer treatment method. The development of nanoagents with high biocompatibility and a near-infrared (NIR) photoabsorption band is a prerequisite to the success of this method. However, the therapeutic efficiency of photothermal therapy is rather limited because most nanoagents have a low photothermal conversion efficiency. In this study, we aimed to develop $CuFeS_2$ nanoassemblies with an excellent photothermal effect using the liquid-solid-solution method. The $CuFeS_2$ nanoassemblies we developed are composed of ultrasmall $CuFeS_2$ nanoparticles with an average size of 5 nm, which have strong NIR photoabsorption. Under NIR laser illumination at 808 nm at the output power intensity of 1.0 W cm^{-2}, the $CuFeS_2$ nanoassemblies could rapidly convert NIR light into heat, achieving a high photothermal conversion efficiency of 46.8%. When K7M2 cells were incubated with the $CuFeS_2$ nanoassemblies and then exposed to irradiation, their viability decreased progressively as the concentration of the $CuFeS_2$ nanoassemblies increased. Furthermore, a concentration of 40 ppm of $CuFeS_2$ nanoassemblies was lethal to the cells. Importantly, after an intratumoral injection of 40 ppm of $CuFeS_2$ nanoassemblies, the tumor showed a high contrast in the thermal image after laser irradiation, and tumor cells with condensed nuclei and a loss of cell morphology could be thermally ablated. Therefore, the $CuFeS_2$ nanoassemblies we synthesized have a high biocompatibility and robust photothermal effect and can, thus, be utilized as a novel and efficient photothermal agent for tumor therapy.

Keywords: near infrared light, bioimaging, photothermal conversion, $CuFeS_2$ nanoassemblies, cancer therapy

OPEN ACCESS

Edited by:
Ming Ma,
Shanghai Institute of Ceramics (CAS), China

Reviewed by:
Wenlong Zhang,
Xinxiang Medical University, China
Guoying Deng,
Shanghai General Hospital, China

****Correspondence:***
Gang Li
ligang@zjnu.cn
Xin Jin
slytjx@163.com

Specialty section:
This article was submitted to Biomaterials, a section of the journal Frontiers in Materials

Received: *11 June 2020*
Accepted: *30 July 2020*
Published: *25 September 2020*

Citation:
Huang S, Li G, Yang Z, Hua M, Yuan Z and Jin X (2020) $CuFeS_2$ Nanoassemblies With Intense Near-Infrared Absorbance for Photothermal Therapy of Tumors. Front. Mater. 7:289. doi: 10.3389/fmats.2020.00289

INTRODUCTION

Photothermal therapy, which utilizes *ex vivo* near-infrared (NIR) lasers to irradiate photothermal materials within a tumor to generate heat (>45°C) so that tumor cells can be thermally ablated, is an emerging treatment modality for killing cancer cells with high therapeutic efficiency (Zou et al., 2016; Vankayala and Hwang, 2018). The use of photothermal materials with broad and strong photoabsorption in the NIR region (650–1100 nm) is essential for successful photothermal therapy. Photothermal therapy using NIR lasers attracts increasing attention from researchers all over the world due to its safety and high tissue-penetration capacity compared to visible and ultraviolet light.

Up to date, several kinds of photothermal materials have been investigated and used for treating malignant tumors, including organic nanoparticles, such as polypyrrole nanoparticles (Zha et al., 2013) and melanin nanoparticles (Liu et al., 2013), reduced graphene oxide nanosheets (Yang et al., 2010; Robinson et al., 2011) and carbon dots (Ge et al., 2015), metal nanostructures (Au nanorods (Dreaden et al., 2011), Pd nanosheets (Huang et al., 2011), and Bi nanoparticles (Yu et al., 2018b), and semiconductor nanomaterials, such as mental sulfides and oxide-based nanocrystals (Tian et al., 2011b; Huang et al., 2017; Yu et al., 2017, 2018a). In particular, a number of semiconductor nanomaterials have received tremendous attention due to their tunable composites, easy synthesis, and strong and stable photothermal effect. For example, CuS-based photothermal nanomaterials have been reported with varied ratios of Cu/S and different morphologies, such as CuS nanodots (Li et al., 2010), flower-like CuS superstructures (Tian et al., 2011b), Cu_9S_5 nanocrystals (Tian et al., 2011a), and $Cu_{7.2}S_4$ nanocrystals (Ling et al., 2014). These photothermal nanomaterials have exhibited strong photothermal effects under the irradiation of NIR lasers at different wavelengths (808, 915, 980, and 1064 nm). However, the application of semiconductor nanomaterials is rather hindered because of their unsatisfactory biocompatibility and hydrophobic surface. Thus, it is still necessary to develop semiconductor nanomaterials with high photothermal conversion efficiency and biocompatibility for photothermal therapy of malignant tumors.

Most recent research has increasingly focused on ternary nanostructures instead of metal mono- and dichalcogenides. Ternary nanostructures are capable of strong photoabsorption and also have a tunable feature for adjusting their intrinsic photoabsorption band and adding imaging properties, which can be employed for multimodal imaging and enhanced therapies (Jiang et al., 2017). For example, ternary Cu_5FeS_4 cubes with an average size of 5 nm and a strong NIR photoabsorption and magnetic resonance imaging (MRI) ability, which enables them to be used as T_1-weighted MRI contrast and photothermal nanoagents, have been developed by using the pyrolysis route (Wang et al., 2018). The Cu-Fe-S and Cu-Fe-Se nanostructures, with different compositions, such as Cu_5FeS_4 particles, Cu_5FeS_4 nanocrystals, $Cu_{1.1}Fe_{1.1}S_2$ nanocrystals, and $CuFeS_2$ nanocrystals, are one of the most interesting ternary systems (Pei et al., 2011; Gabka et al., 2016; Zhao et al., 2016; Wang et al., 2018). Among these Cu-Fe-S nanostructures, $CuFeS_2$ nanocrystals are antiferromagnetic semiconductors, showing an excellent photoabsorption band ranging from the ultraviolet region to the NIR region. Currently, there are only a few available methods for preparing $CuFeS_2$ nanocrystals. For example, one method involves the injection of sodium diethyldithiocarbamate to a mixture of $CuCl_2$, $FeCl_3$, and oleic acid in 1-dodecanethiol. The $CuFeS_2$ nanocrystals obtained by using this method have an average size of ∼6 nm and an optical band gap of 1.2 eV, which is much higher than that (0.6–0.7 eV) of bulk $CuFeS_2$ (Wang et al., 2010; Kumar et al., 2013). However, these synthesis methods require a complex operation and usually lead to water solubility problems, which limits their bio-applications. It has been revealed that nanoassemblies, similar to self-assembled WO_{3-x} hierarchical nanostructures (Li et al., 2014) and CuS superstructures (Tian et al., 2011b) could serve as excellent laser-cavity mirrors which could make near-infrared light reflect multiple times on the surface of nanoassemblies, and thus can be used to promote the photothermal conversion efficiency. Therefore, it is vital to develop a simple method for synthesizing $CuFeS_2$ nanocrystals with strong NIR photoabsorption, a high photothermal conversion efficiency, and hydrophilicity.

The aim of this study was to synthesize $CuFeS_2$ nanoassemblies to be used as efficient photothermal nanoagents for photothermal therapy of cancer cells both *in vitro* and *in vivo*. The $CuFeS_2$ nanoassemblies are prepared by using the liquid-solid-solution method, in which the metal ions of Cu^{2+} and Fe^{3+} react with the S precursor in the mixed solution containing deionized water, ethanol, oleic acid, sodium oleate, and poly(N-vinyl-2-pyrrolidone) at 180°C for 48 h. The obtained $CuFeS_2$ nanoassemblies are composed of ultrasmall $CuFeS_2$ nanoparticles, and they exhibit a strong and broad NIR photoabsorption. Under laser irradiation at 808 nm, the aqueous solution containing the $CuFeS_2$ nanoassemblies can rapidly convert laser energy into heat, achieving a high photothermal conversion efficiency of 46.8%. Importantly, after incubation with $CuFeS_2$ nanoassemblies, cancer cells show high activity without laser irradiation, indicating that the $CuFeS_2$ nanoassemblies are highly biocompatible. Moreover, when the $CuFeS_2$ nanoassemblies are injected into tumors, the tumors show high contrast in thermal images and can be thermally ablated using laser irradiation at 808 nm. Therefore, the $CuFeS_2$ nanoassemblies can be utilized as novel and efficient photothermal nanoagents for tumor therapy.

MATERIALS AND METHODS

Synthesis of $CuFeS_2$ Nanoassemblies

$CuCl_2{\cdot}2H_2O$, $FeCl_3{\cdot}6H_2O$, 1-dodecanethiol, oleic acid, sodium oleate, poly(N-vinyl-2-pyrrolidone) (PVP, K30), and anhydro ethanol were purchased from Sigma and were used without further purification. The $CuFeS_2$ nanoassemblies were prepared by using the liquid-solid-solution method. In a typical synthesis route, $CuCl_2{\cdot}2H_2O$ (0.5 mmol) and $FeCl_3{\cdot}6H_2O$ (0.5 mmol) were introduced to a mixed solution containing deionized water (5 mL), ethanol (10 mL), oleic acid (10 mL), sodium oleate (5 mmol), and PVP (0.5 mg), and the mixture was stirred for 30 min at room temperature (∼23°C). Then, 10 mmol of 1-dodecanethiol was introduced into the above solution, which was stirred again for 60 min. The solution was sealed and treated in an autoclave at 180°C for 48 h. Then, the black precipitates were washed three times with a solution of ethanol/water (8/2 vol.). One part of the black precipitates was dispersed into the deionized water while another part was vacuum dried at 60°C.

Characterization of the $CuFeS_2$ Nanoassemblies

The morphology of the $CuFeS_2$ nanoassemblies was studied by using transmission electron microscopy (TEM, JEOL2100F). The composites and phase of the $CuFeS_2$ powder were measured by using x-ray photoelectron spectroscopy (XPS, EscaLab) and an

x-ray diffractometer (XRD, Bruker D4). The photoabsorption of the $CuFeS_2$ nanoassemblies in deionized water was tested by using a spectrophotometer (Shimadzu, UV-1900). The photothermal performance was investigated using a laser at 808 nm to illuminate the $CuFeS_2$ nanoassemblies in deionized water, and their temperature change was recorded using a thermal imaging camera (FLIR A300).

Cytotoxicity Test

Cytotoxicity testing of the $CuFeS_2$ nanoassemblies was carried out by using the methyl thiazolyl tetrazolium (MTT) assay. In a typical procedure, K7M2 cells were seeded into 96-well culture plates at a density of 1×10^4/well under standard conditions for 12 h. Then, the medium was replaced with a new medium that contained $CuFeS_2$ nanoassemblies at the final concentrations of 0, 2.5, 5, 10, 20, 40, 80, and 160 ppm, followed by incubation for 24 h. Subsequently, the cells were washed with PBS, and fresh medium containing MTT (5 mg mL^{-1}) was introduced to each well. After incubation for 2 h, the old medium was discarded, followed by the addition of 100 μL of dimethyl sulfoxide solution, and the absorption intensity at 570 nm was measured.

Photothermal Cell Therapy

To measure the efficiency of photothermal therapy *in vitro*, K7M2 cells were cultured into 96-well plates (1×10^4 cells/well) under standard conditions. After 12 h, the cell medium was replaced with fresh medium containing the $CuFeS_2$ nanoassemblies at the final concentrations of 0, 10, 20, and 40 ppm. A total 1 h later, the K7M2 cells were exposed to laser illumination at 808 nm (1.0 W cm^{-2}, 5 min). Subsequently, the cells were washed with PBS for the MTT test. In the meantime, after photothermal therapy, cells in the parallel group were stained with Calcein AM and Propidium iodide (PI) using the Calcein AM/PI assay for 1 h and imaged by using a microscope (Leica).

Photothermal Therapy of Solid Tumors

Mice bearing K7M2 tumors with a surface diameter of ∼0.5 cm were divided into two groups (n = 3/group) and they were anesthetized with pentobarbital (50 mg kg^{-1}) before laser irradiation. The mice in the first group (PBS + Laser) were intratumorally injected with a PBS solution (50 μL) and irradiated at 808 nm with a laser (1.0 W cm^{-2}, 5 min). The mice in the second group ($CuFeS_2$ + Laser) were intratumorally injected with $CuFeS_2$ nanoassemblies in PBS solution (50 μL, 40 ppm) and then irradiated at 808 nm with a laser (1.0 W cm^{-2} for 5 min). During the irradiation, the thermal image of the mouse body was monitored, and the surface temperature of the tumor was recorded.

Histological Examination

After photothermal therapy for 1 day, mice in all groups were sacrificed to harvest the tumors and main organs which were subsequently fixed in paraffin and then cryosectioned. The tissue slices were subsequently stained with hematoxylin and eosin (H&E), and examined using a digital microscope (Zeiss AxioCam MRc5).

Biocompatibility *in vivo*

The biodistribution of the $CuFeS_2$ nanoassemblies was evaluated using healthy mice intravenously injected with 12 mg·kg^{-1} of the $CuFeS_2$ nanoassemblies. Major organs, such as kidney, liver, spleen, heart, and lungs were achieved at different time points (i.e., 1, 7, 14, 20 days) after administration. Copper content in these organs were determined by ICP-AES analysis. Meanwhile, blood samples were collected at different time points (i.e., 0, 1, 7, 14, 20 days) after the intravenous injection of the $CuFeS_2$ nanoassemblies (12 mg·kg^{-1}) or PBS solution.

RESULTS AND DISCUSSION

The $CuFeS_2$ nanoassemblies were prepared by using the liquid-solid-solution method, in which the metal ions of Cu^{2+} and Fe^{3+} reacted with the S precursor in a mixed solution containing deionized water, ethanol, oleic acid, sodium oleate, and PVP at 180°C for 48 h. After the end of the reaction, black precipitates were obtained, and their morphology and size were first characterized by using TEM. The TEM image in **Figure 1a** reveals that the black precipitates are composed of nanoparticles with a size of 200–500 nm and do not have a clear morphology. The size of as-prepared products in water measured by dynamic light scattering (DLS) were around 400 nm (**Supplementary Figure S1A**), indicating that those products were mostly individually dispersed. Moreover, the size of the products in PBS determined by DLS showed very little change over time (**Supplementary Figure S1B**), also indicating a good dispersion. It should be noted that the term nanoassemblies is used to describe the sample as it is composed of a number of ultrasmall particles, which have an average size of ∼5 nm. The high resolution TEM image in **Figure 1b** exhibits a clear lattice with an interplane spacing of ∼0.3 nm, which corresponds to the (112) plane of the tetragonal $CuFeS_2$ (JCPDS card no. 81–1959), indicating that the ultrasmall particles are $CuFeS_2$. Furthermore, the phase of $CuFeS_2$ nanoassemblies was also studied by using the XRD pattern (**Figure 1c**); there were three prominent diffraction peaks at 27.9°, 46.4°, and 55.0° which can be well indexed to (112), (220), and (312) of the tetragonal $CuFeS_2$ (JCPDS no. 81–1959), respectively. Therefore, the above TEM and XRD analyses, demonstrate the successful synthesis of $CuFeS_2$ nanoassemblies.

Subsequently, the elements of $CuFeS_2$ nanoassemblies were investigated using XPS. The XPS survey spectrum (**Figure 1d**) confirmed the obvious signals of Cu 2p, Fe 2p, and S 2p, which suggested that the nanoassemblies are made of Cu/Fe/S elements. In addition, the average Cu:Fe:S composition of the $CuFeS_2$ nanoassemblies was determined to be 1.00:0.97:2.12, which is quite close to the ideal ratio of 1:1:2. From the Cu 2p core-level spectrum (**Supplementary Figure S2A**), we could observe Cu^{1+} $2p_{3/2}$ at 932.6 eV and Cu^{1+} $2p_{2/2}$ at 952.5 eV while there was no trace of a satellite peak for Cu^{2+} $2p_{3/2}$ at around 942 eV, verifying that the Cu element in the $CuFeS_2$ nanoassemblies is Cu^{1+}. For the Fe2p core-level spectrum (**Supplementary Figure S2B**), Fe $2p_{3/2}$ and $2p_{1/2}$ are, respectively, centered at 710.6 eV and 723.6 eV which are in good agreement with Fe^{3+}, indicating that the Fe element in the $CuFeS_2$ nanoassemblies is at the state of + 3.

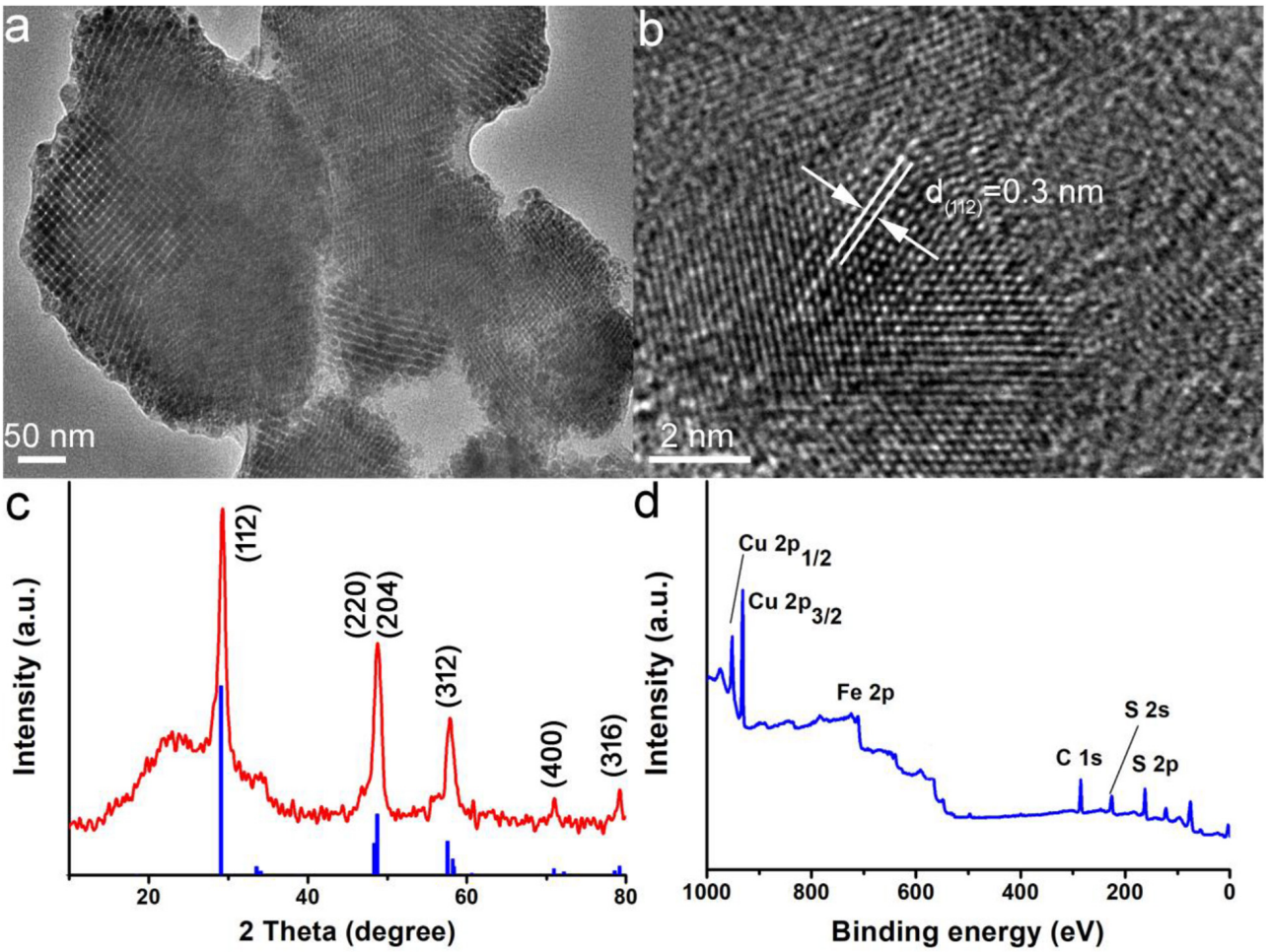

FIGURE 1 | Characterization of $CuFeS_2$ nanoassemblies using transmission electron microscopy (TEM) **(a)** TEM image, **(b)** High resolution (HR)-TEM image, **(c)** X-ray diffraction (XRD) pattern, and **(d)** X-ray photoelectron spectroscopy (XPS) survey spectrum of $CuFeS_2$ nanoassemblies.

Thus, XPS analysis confirmed the presence of Cu^{1+} and Fe^{3+} in the $CuFeS_2$ nanoassemblies.

It has been reported that $CuFeS_2$ nanomaterials are capable of NIR absorbance. To study the photoabsorption performance, $CuFeS_2$ nanoassemblies were dispersed into deionized water and tested by using a UV-vis-NIR spectrophotometer. The solution of $CuFeS_2$ nanoassemblies is dark yellow, and it shows a strong and broad absorbance ranging from 300 to 1100 nm with the peak centered at 500 nm (**Figure 2A**). Subsequently, we investigated the NIR-laser-induced photothermal effect by using an 808 nm laser to illuminate the $CuFeS_2$ nanoassemblies in deionized water. Under the illumination of the laser at 1.0 cm^{-2}, the temperature of deionized water goes up by less than 1.8°C after irradiation for 5 min, indicating no obvious photothermal effect for deionized water (**Figure 2B**). With the addition of the $CuFeS_2$ nanoassemblies, the temperature goes up quickly and the temperature elevation is determined to be 10.8, 20.4, or 29.7°C for the concentrations of 10, 20, or 40 ppm, respectively, indicating a rapid laser response and a high photothermal conversion. The above results confirm the strong and concentration-related performance of the $CuFeS_2$ nanoassemblies when illuminated by a NIR laser at 808 nm.

In order to calculate the photothermal conversion efficiency (η) of the $CuFeS_2$ nanoassemblies, we dispersed them into deionized water, which was then exposed to 808 nm NIR laser (1.0 cm^{-2}, 5 min) irradiation. The temperature curve during the laser's on and off periods was recorded, as demonstrated in **Figure 3A**. The temperature quickly increased once the nanoassemblies were exposed to 808 nm irradiation and then it decreased when the laser was turned off. **Figure 3B** shows the system time constant τ_s which was obtained from the cooling period when the laser was switched off, and was determined to be 168.4 s. The photothermal conversion efficiency was calculated by using the following equations:

$$\eta = \frac{hA\left(\triangle T_{\max,\mathrm{dis}} - \triangle T_{\max,\mathrm{H2O}}\right)}{I(1-10^{-A_{808}})}$$

$$\tau_s = \frac{m_D C_D}{hA}$$

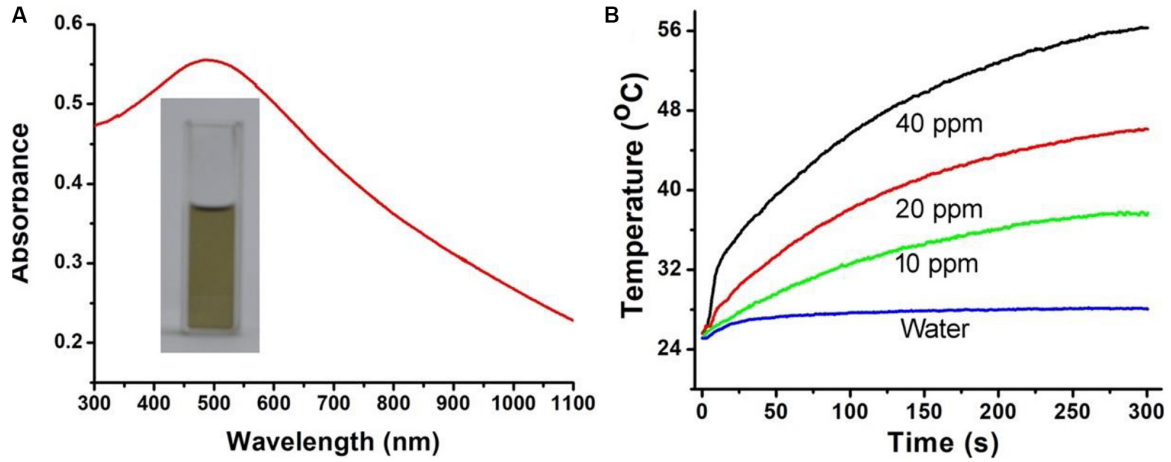

FIGURE 2 | (A) A representative photograph and photoabsorption spectrum of the $CuFeS_2$ nanoassemblies dispersed in water. **(B)** Temperature elevation curves of the solution containing $CuFeS_2$ nanoassemblies at a concentration of 0–40 ppm.

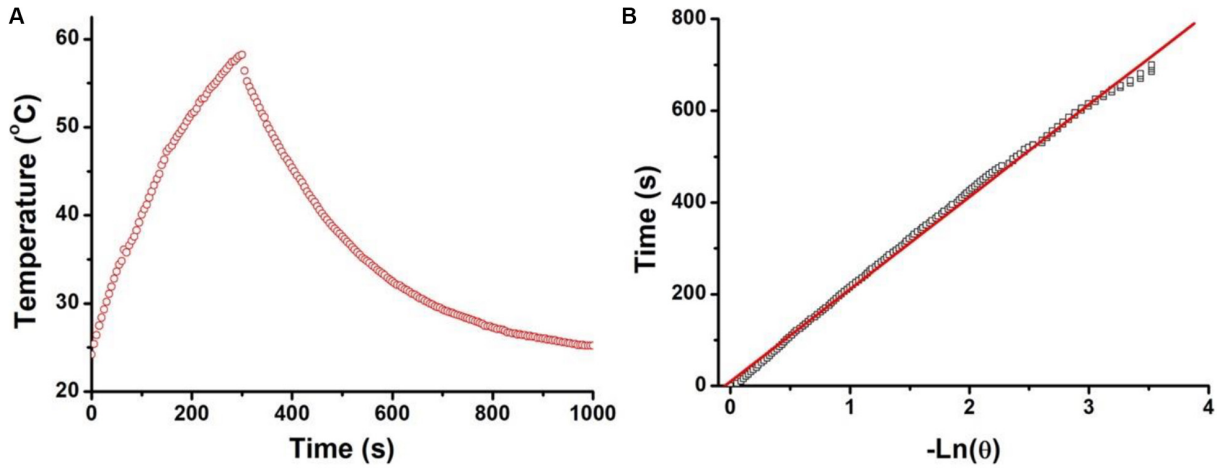

FIGURE 3 | (A) Temperature curve of a solution containing the $CuFeS_2$ nanoassemblies during the periods the 808 nm laser was switched on and off. **(B)** The system time constant τ_s by linear fitting time data with ln(θ).

where I and A_{808} stand for the NIR laser power and the absorbance of dispersion at 808 nm, respectively. The value of hA can be calculated from the equation used to calculate the system time constant τ_s with the help of the mass (m_D, 0.2 g) and the heat capacity (C_D, 4.2 J g^{-1}) of deionized water. $\Delta T_{max,dis}$ and $\Delta T_{max,H2O}$ are the temperature changes of the $CuFeS_2$ nanoassemblies and of deionized water, respectively. The photothermal conversion efficiency of the $CuFeS_2$ nanoassemblies was calculated to be 46.8%. Therefore, the $CuFeS_2$ nanoassemblies have a high photothermal conversion efficiency, indicating a great potential to be utilized as an efficient photothermal nanoagent for treating cancer cells.

Next, we investigated the effects of these $CuFeS_2$ nanoassemblies on the viability of K7M2 cells *in vitro* through the MTT method. After incubation with the $CuFeS_2$ nanoassemblies at the concentrations of 0, 2.5, 5, 10, 20, 40, 80, and 160 ppm for 24 h (**Figure 4A**), K7M2 cells retained high viability. Their viability at 160 ppm was determined to be as high as >85%, indicating the low cytotoxicity of the $CuFeS_2$ nanoassemblies. Moreover, we have investigated the photothermal therapeutic ability of the $CuFeS_2$ nanoassemblies by incubating them with cells and then irradiating them with a laser at 808 nm (1.0 cm^{-2}, 5 min). Compared to the cells that were not incubated with $CuFeS_2$ nanoassemblies, the viability of the cells treated with $CuFeS_2$ nanoassemblies decreased as the concentration of the added $CuFeS_2$ nanoassemblies increased. The average viability of the K7M2 cells was 78, 36.5, and 8.6% at the $CuFeS_2$ nanoassemblies concentrations of 10, 20, and 40 ppm (**Figure 4B**), respectively. In the meantime, the treated cells were treated with a Calcine AM/PI assay to clarify the therapeutic photothermal effects of the $CuFeS_2$ nanoassemblies. Laser-irradiated cells treated with PBS showed green fluorescence (**Figure 5a**), which indicated that the laser had no effect on the activity of these cells. In contrast, laser-irradiated cells incubated

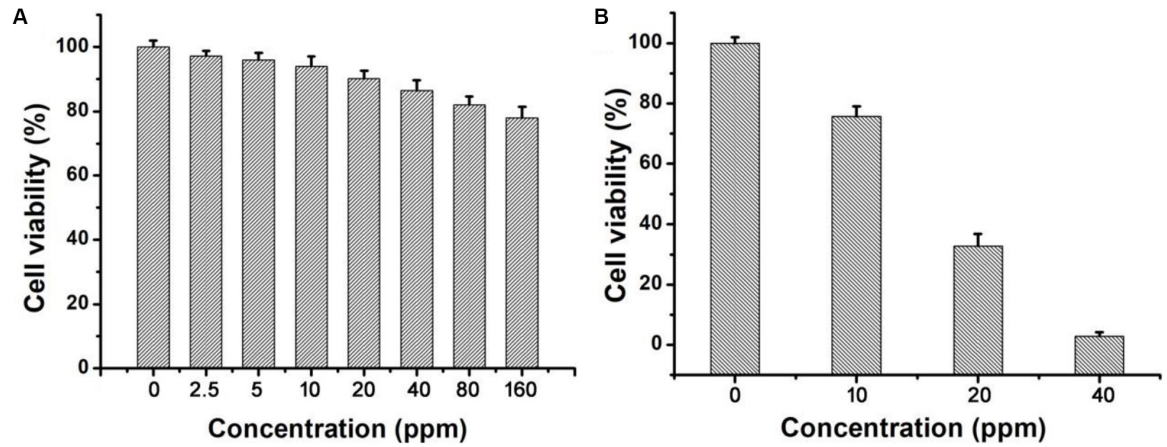

FIGURE 4 | (A) The relative viability of K7M2 cells after incubation with the $CuFeS_2$ nanoassemblies at a series of concentrations (0, 2.5, 5, 10, 20, 40, 80, and 160 ppm). **(B)** The relative viability of K7M2 cells after incubation with the $CuFeS_2$ nanoassemblies (0, 10, 20, and 40 ppm) followed by laser irradiation at 808 nm.

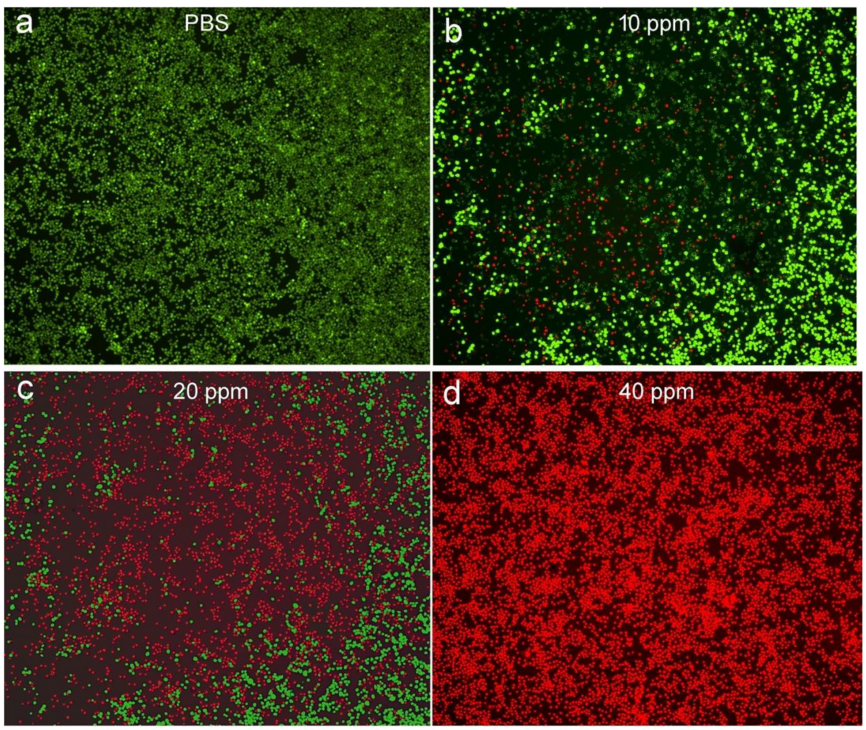

FIGURE 5 | Fluorescence images of Calcein AM/Propidium iodine-stained K7M2 cells after incubation with **(a)** PBS solution and **(b–d)** the $CuFeS_2$ nanoassemblies at different concentrations (10, 20, and 40 ppm) followed by laser irradiation at 808 nm.

with the $CuFeS_2$ nanoassemblies simultaneously showed green and red fluorescence at the concentration of 10 ppm, whereas only red fluorescence appeared at the concentration of 40 ppm, indicating all cells were killed (**Figures 5b–d**). Thus, we can confirm that, when exposed to the 808 nm NIR laser, the high photothermal effect of the $CuFeS_2$ nanoassemblies has a high therapeutic efficiency in K7M2 cells.

After establishing the high photothermal ablation efficiency *in vitro*, we further examined the photothermal therapy *in vivo*. Mice bearing K7M2 tumors with a surface diameter of ~0.5 cm were divided into two groups: (1) PBS + Laser, (2) $CuFeS_2$ + Laser. The center of the tumors of mice in group (1) was injected with PBS solution (50 μL), while the tumor center of mice in group (2) was injected with a $CuFeS_2$ PBS solution (50 μL, 40 ppm). The tumors in groups (1) and (2) were then laser-illuminated at 808 nm with an output power intensity of 1.0 cm^{-2} for 5 min, and the thermal image of the mouse body was captured. **Figure 6a** demonstrates the thermal

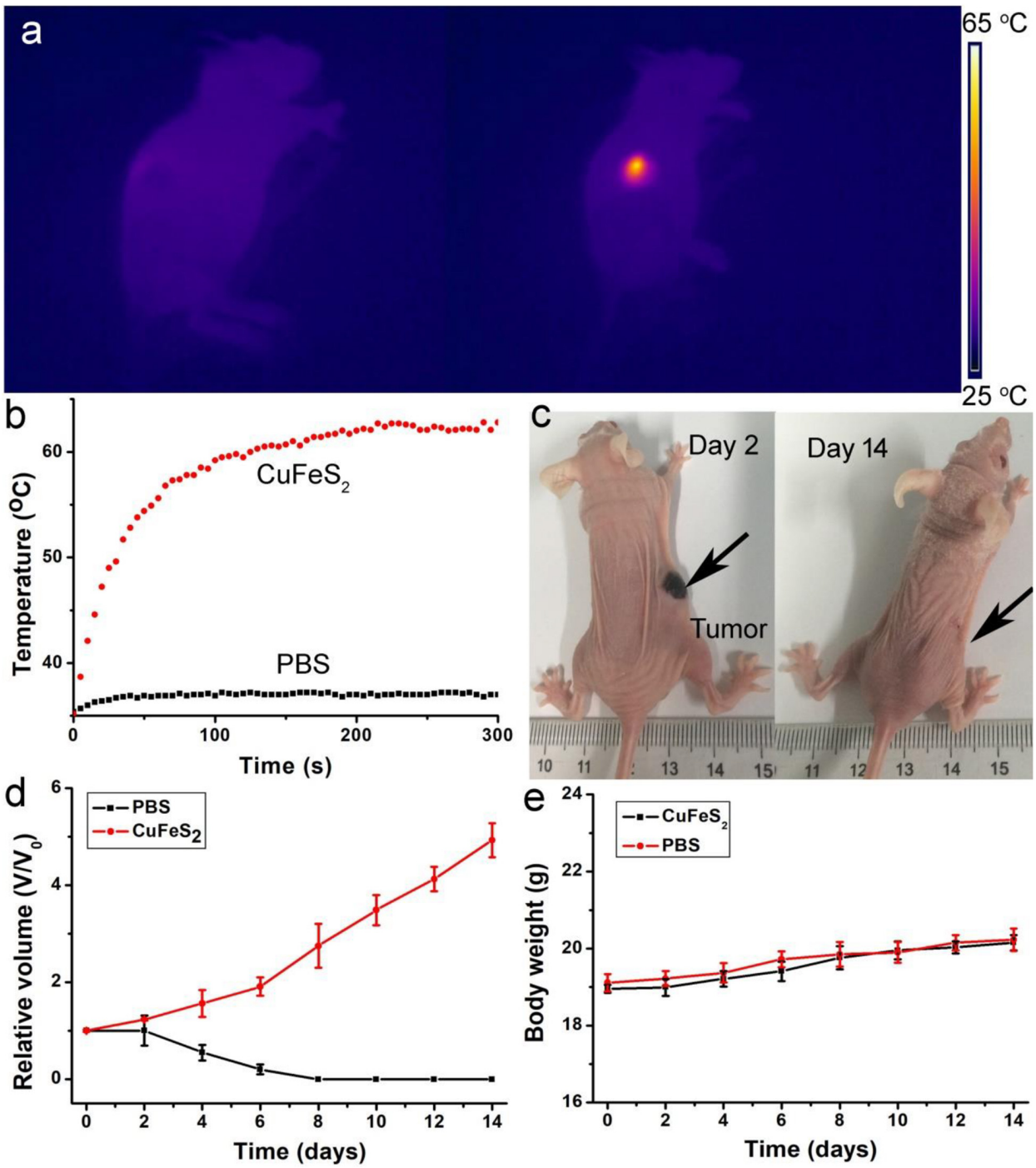

FIGURE 6 | (a) Thermal image of a mouse body showing the tumor area injected with PBS (left) and $CuFeS_2$ nanoassemblies (right) and exposed to 808 nm NIR laser irradiation. **(b)** Typical temperature elevation curves of the treated tumors. **(c)** Photographs of mice after photothermal therapy. **(d)** Growth curves of tumors over time in the two groups after the treatments. **(e)** Body weight curves over time in the two groups after the treatments.

image of mice in groups (1) and (2), demonstrating that the tumor treated with the $CuFeS_2$ PBS solution showed a much brighter red fluorescence than that of the tumor treated with the PBS solution. The temperature profile of tumors in groups (1) and (2) is shown in **Figure 6b**. The tumor treated with the $CuFeS_2$ PBS solution showed a high max temperature of 63°C whereas the PBS-treated tumor exhibited a max temperature of 38°C. The high temperature in the tumor area is attributed to the high photothermal conversion efficiency of the $CuFeS_2$ nanoassemblies, which can result in a high therapeutic effect.

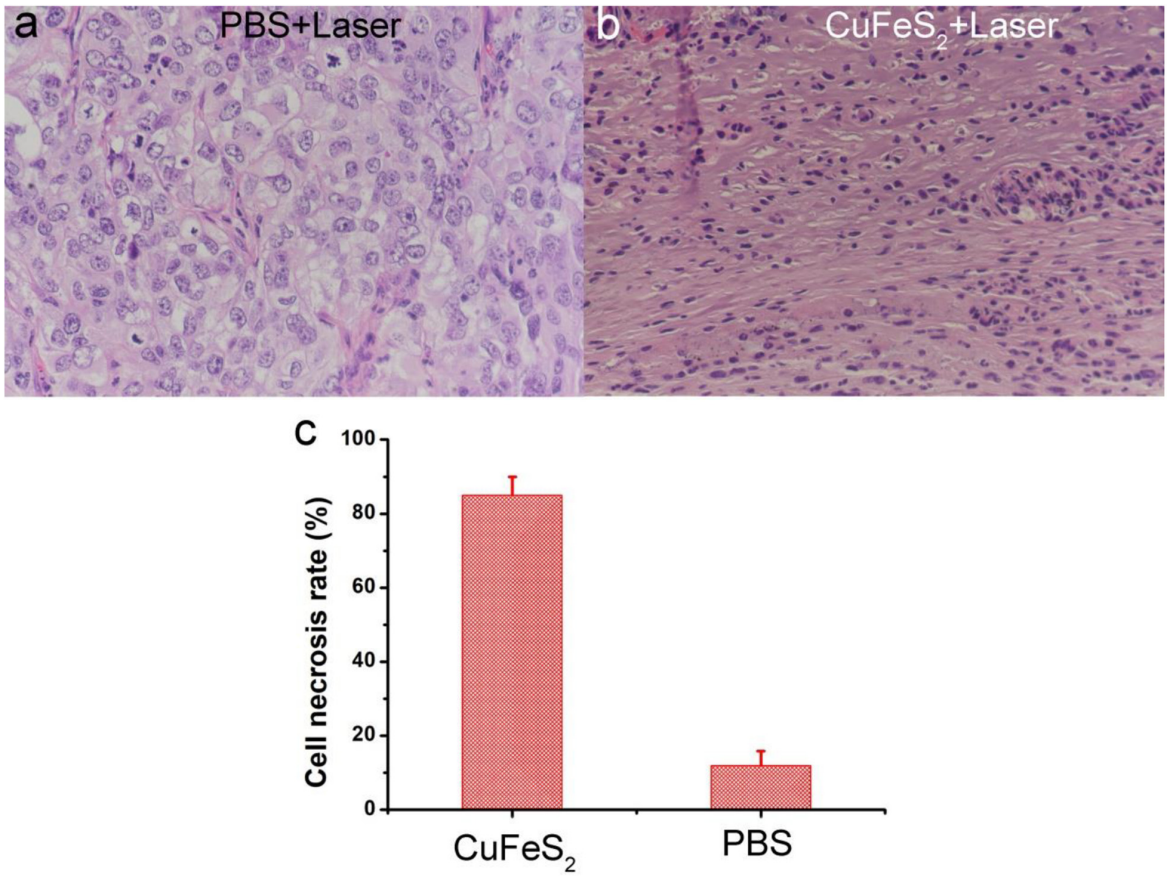

FIGURE 7 | Photographs of hematoxylin and eosin (H&E)-stained tumor slices **(a)** Tumor treated with PBS and laser irradiation and **(b)** Tumor treated with $CuFeS_2$ nanoassemblies and laser irradiation. **(c)** The cell necrosis rate of the treated tumors.

After the photothermal therapy, a scar could be found at the site of the $CuFeS_2$-treated tumor at day 2, while the original tumor and scar disappeared at day 14 (**Figure 6c**). Additionally, the tumors of mice in group (2) were disappeared and there was no reoccurrence observed (**Figure 6d**), while the tumors gradually increased in group (1). What's more, there was almost no difference in body weight among the two groups of mice (**Figure 6e**), indicating the low toxicity of $CuFeS_2$ nanoassemblies at the given conditions.

After photothermal therapy, the mice in the two groups were sacrificed, and tumors were extracted and sectioned for H&E staining. The typical images of H&E-stained tumor slices are shown in **Figures 7a,b**. The cells of the tumor which were injected with PBS and irradiated have a normal morphology, indicating the laser had no effect on tumor cells at the given intensity. On the contrary, the cells of the tumor which were injected with the $CuFeS_2$ nanoassemblies and irradiated by 808 nm lasers had condensed nuclei. In addition, the loss of normal cell morphology can be observed. Furthermore, the average cell necrosis rate was 88.4% in tumors treated with $CuFeS_2$ and laser irradiation which was significantly higher than that (11.8%) of tumors treated with PBS and laser irradiation (**Figure 7c**). Therefore, the $CuFeS_2$ nanoassemblies developed in this study have been demonstrated to have excellent photothermal performance *in vivo*, and can, thus, be employed as an efficient nanomaterials for photothermal therapy of solid tumors.

The ideal photothermal agents should have excellent biocompatibility for biological applications. The biodistribution of the $CuFeS_2$ nanoassemblies was evaluated using healthy mice intravenously injected with 12 $mg{\cdot}kg^{-1}$ of the $CuFeS_2$ nanoassemblies. Major organs, such as the kidney, liver, spleen, heart, and lungs were achieved at different time points (i.e., 1, 7, 14, 20 days) after administration. Copper content in these organs were determined by ICP-AES analysis. It showed (**Supplementary Figure S3**) that the $CuFeS_2$ nanoassemblies mainly accumulated in the liver and spleen after the intravenous administration. The content in these two organs gradually decreased over time, indicating that $CuFeS_2$ nanoassemblies were mainly degraded through these two organs. The cytotoxicity of $CuFeS_2$ nanoassemblies on major organs was evaluated via H&E analysis. A total 20 days of the intravenous injection of the $CuFeS_2$ nanoassemblies (12 $mg{\cdot}kg^{-1}$) or PBS solution, major organs were collected for H&E analysis. The shape and size of the organs in the two groups almost showed no change (**Supplementary Figure S4**). Meanwhile, blood samples were collected at the different time points (i.e., 0, 1,

7, 14, 20 days) after the intravenous injection of the $CuFeS_2$ nanoassemblies (12 $mg{\cdot}kg^{-1}$) or PBS solution. There was no obvious difference in the alanine aminotransferase (ALT, **Supplementary Figure S5A**) and aspartate aminotransferase (AST, **Supplementary Figure S5B**), which indicated that $CuFeS_2$ nanoassemblies at the given dose showed almost no effect on the liver and kidney. Therefore, the $CuFeS_2$ nanoassemblies showed excellent biocompatibility.

CONCLUSION

In summary, the $CuFeS_2$ nanoassemblies we synthesized in this study are efficient photothermal nanoagents for photothermal therapy of cancer cells *in vitro* and *in vivo*. The $CuFeS_2$ nanoassemblies are synthesized by using the liquid-solid-solution method, and are composed of ultrasmall $CuFeS_2$ nanoparticles with an average size of 5 nm. Furthermore, the $CuFeS_2$ nanoassemblies exhibit strong NIR photoabsorption and can rapidly convert laser energy into heat, achieving a high photothermal conversion efficiency of 46.8%. Following incubation with $CuFeS_2$ nanoassemblies without laser irradiation, cancer cells retain high activity indicating the $CuFeS_2$ nanoassemblies have high biocompatibility. However, under laser irradiation at 808 nm the cells can be thermally ablated due to the high photothermal effect of the $CuFeS_2$ nanoassemblies. Furthermore, when the $CuFeS_2$ nanoassemblies are injected into tumors, the tumors show a high contrast in thermal images when laser-irradiated, and the tumor cells are then thermally ablated. Therefore, the $CuFeS_2$ nanoassemblies can be utilized as novel and efficient photothermal nanoagents for tumor therapy and inspire the development of other novel nanoagents using an assembly strategy.

DATA AVAILABILITY STATEMENT

All datasets presented in this study are included in the article/**Supplementary Material**.

ETHICS STATEMENT

The animal study was reviewed and approved by Shengli Oilfield Central Hospital.

AUTHOR CONTRIBUTIONS

SH and GL designed the project. SH, ZYa, MH, ZYu, and XJ carried out the experiment. SH, MH, and GL performed the experimental data analysis. SH, GL, and XJ wrote the manuscript. All the authors contributed to the discussion of the results.

FUNDING

This study was supported by the Zhejiang Province Public Welfare Technology Application Research Project of China (No. LGF19G010005) and the Zhejiang Provincial Natural Science Foundation of China (No. LQ19E050011).

SUPPLEMENTARY MATERIAL

The Supplementary Material for this article can be found online at: https://www.frontiersin.org/articles/10.3389/fmats.2020.00289/full#supplementary-material

REFERENCES

Dreaden, E. C., Mackey, M. A., Huang, X. H., Kang, B., and El-Sayed, M. A. (2011). Beating cancer in multiple ways using nanogold. *Chem. Soc. Rev.* 40, 3391–3404. doi: 10.1039/c0cs00180e

Gabka, G., Bujak, P., Zukrowski, J., Zabost, D., Kotwica, K., Malinowska, K., et al. (2016). Non-injection synthesis of monodisperse Cu-Fe-S nanocrystals and their size dependent properties. *Phys. Chem. Chem. Phys.* 18, 15091–15101. doi: 10.1039/C6CP01887D

Ge, J. C., Jia, Q. Y., Liu, W. M., Guo, L., Liu, Q. Y., Lan, M. H., et al. (2015). Red-emissive carbon dots for fluorescent, photoacoustic, and thermal theranostics in living mice. *Adv. Mater.* 27, 4169–4177. doi: 10.1002/adma.201500323

Huang, X., Zhang, W., Guan, G., Song, G., Zou, R., and Hu, J. (2017). Design and functionalization of the nir-responsive photothermal semiconductor nanomaterials for cancer theranostics. *Acc. Chem. Res.* 50, 2529–2538. doi: 10.1021/acs.accounts.7b00294

Huang, X. Q., Tang, S. H., Mu, X. L., Dai, Y., Chen, G. X., Zhou, Z. Y., et al. (2011). Freestanding palladium nanosheets with plasmonic and catalytic properties. *Nature Nanotechnol.* 6, 28–32. doi: 10.1038/nnano.2010.235

Jiang, X., Zhang, S., Feng, R., Lei, C., Zeng, J., Mo, Z., et al. (2017). Ultra-small magnetic CuFeSe2 ternary nanocrystals for multimodal imaging guided photothermal therapy of cancer. *Acs Nano* 11, 5633–5645. doi: 10.1021/acsnano.7b01032

Kumar, P., Uma, S., and Nagarajan, R. (2013). Precursor driven one pot synthesis of wurtzite and chalcopyrite CuFeS2. *Chem. Commun.* 49, 7316–7318. doi: 10.1039/c3cc43456g

Li, B., Zhang, Y., Zou, R., Wang, Q., Zhang, B., An, L., et al. (2014). Self-assembled WO3-x hierarchical nanostructures for photothermal therapy with a 915 nm laser rather than the common 980 nm laser. *Dalton Trans.* 43, 6244–6250. doi: 10.1039/c3dt53396d

Li, Y. B., Lu, W., Huang, Q. A., Huang, M. A., Li, C., and Chen, W. (2010). Copper sulfide nanoparticles for photothermal ablation of tumor cells. *Nanomedicine* 5, 1161–1171. doi: 10.2217/nnm.10.85

Ling, C., Zhou, L. Q., and Jia, H. (2014). First-principles study of crystalline CoWO4 as oxygen evolution reaction catalyst. *RSC Adv.* 4, 24692–24697. doi: 10.1039/c4ra03893b

Liu, Y. L., Ai, K. L., Liu, J. H., Deng, M., He, Y. Y., and Lu, L. H. (2013). Dopamine-melanin colloidal nanospheres: An efficient near-infrared photothermal therapeutic agent for in vivo cancer therapy. *Adv. Mater.* 25, 1353–1359. doi: 10.1002/adma.201204683

Pei, L. Z., Wang, J. F., Tao, X. X., Wang, S. B., Dong, Y. P., Fan, C. G., et al. (2011). Synthesis of CuS and Cu1.1Fe1.1S2 crystals and their electrochemical properties. *Mater. Charact.* 62, 354–359. doi: 10.1016/j.matchar.2011.01.001

Robinson, J. T., Tabakman, S. M., Liang, Y. Y., Wang, H. L., Casalongue, H. S., Vinh, D., et al. (2011). Ultrasmall reduced graphene oxide with high near-infrared absorbance for photothermal therapy. *J. Am. Chem. Soc.* 133, 6825–6831. doi: 10.1021/ja2010175

Tian, Q. W., Jiang, F. R., Zou, R. J., Liu, Q., Chen, Z. G., Zhu, M. F., et al. (2011a). Hydrophilic Cu9S5 nanocrystals: A photothermal agent with a 25.7% heat conversion efficiency for photothermal ablation of cancer cells in vivo. *ACS Nano* 5, 9761–9771. doi: 10.1021/nn203293t

Tian, Q. W., Tang, M. H., Sun, Y. G., Zou, R. J., Chen, Z. G., Zhu, M. F., et al. (2011b). Hydrophilic flower-like CuS superstructures as an efficient 980 nm laser-driven photothermal agent for ablation of cancer cells. *Adv. Mater.* 23, 3542–3547. doi: 10.1002/adma.201101295

Vankayala, R., and Hwang, K. C. (2018). Near-Infrared-light-activatable nanomaterial-mediated phototheranostic nanomedicines: An emerging paradigm for cancer treatment. *Adv. Mater.* 30:e1706320. doi: 10.1002/adma.201706320

Wang, D., Zhang, Y. W., and Guo, Q. (2018). Sub-10 nm Cu5FeS4 cube for magnetic resonance imaging-guided photothermal therapy of cancer. *Int. J. Nanomed.* 13, 7987–7996. doi: 10.2147/IJN.S181056

Wang, Y.-H. A., Bao, N., and Gupta, A. (2010). Shape-controlled synthesis of semiconducting CuFeS2 nanocrystals. *Solid State Sci.* 12, 387–390. doi: 10.1016/j.solidstatesciences.2009.11.019

Yang, K., Zhang, S., Zhang, G. X., Sun, X. M., Lee, S. T., and Liu, Z. (2010). Graphene in mice: Ultrahigh in vivo tumor uptake and efficient photothermal therapy. *Nano Lett.* 10, 3318–3323. doi: 10.1021/nl100996u

Yu, N., Hu, Y., Wang, X., Liu, G., Wang, Z., Liu, Z., et al. (2017). Dynamically tuning near-infrared-induced photothermal performances of TiO2 nanocrystals by Nb doping for imaging-guided photothermal therapy of tumors. *Nanoscale* 9, 9148–9159. doi: 10.1039/C7NR02180A

Yu, N., Peng, C., Wang, Z., Liu, Z., Zhu, B., Yi, Z., et al. (2018a). Dopant-dependent crystallization and photothermal effect of Sb-doped SnO2 nanoparticles as stable theranostic nanoagents for tumor ablation. *Nanoscale* 10, 2542–2554. doi: 10.1039/C7NR08811F

Yu, N., Wang, Z., Zhang, J., Liu, Z., Zhu, B., Yu, J., et al. (2018b). Thiol-capped Bi nanoparticles as stable and all-in-one type theranostic nanoagents for tumor imaging and thermoradiotherapy. *Biomaterials* 161, 279–291. doi: 10.1016/j.biomaterials.2018.01.047

Zha, Z., Yue, X., Ren, Q., and Dai, Z. (2013). Uniform polypyrrole nanoparticles with high photothermal conversion efficiency for photothermal ablation of cancer cells. *Adv. Mater.* 25, 777–782. doi: 10.1002/adma.201202211

Zhao, Q., Yi, X., Li, M., Zhong, X., Shi, Q., and Yang, K. (2016). High near-infrared absorbing Cu5FeS4 nanoparticles for dual-modal imaging and photothermal therapy. *Nanoscale* 8, 13368–13376. doi: 10.1039/C6NR04444A

Zou, L., Wang, H., He, B., Zeng, L., Tan, T., Cao, H., et al. (2016). Current approaches of photothermal therapy in treating cancer metastasis with nanotherapeutics. *Theranostics* 6, 762–772. doi: 10.7150/thno.14988

Conflict of Interest: The authors declare that the research was conducted in the absence of any commercial or financial relationships that could be construed as a potential conflict of interest.

frontiers in Bioengineering and Biotechnology

ORIGINAL RESEARCH
published: 21 October 2020
doi: 10.3389/fbioe.2020.585631

Multifunctional $CuBiS_2$ Nanoparticles for Computed Tomography Guided Photothermal Therapy in Preventing Arterial Restenosis After Endovascular Treatment

Xiaoyu Wu[1]†, Kun Liu[1]†, Ruihua Wang[1]†, Guanglin Yang[1]*, Jiaying Lin[2]* and Xiaobing Liu[1,3]**

[1] Department of Vascular Surgery, Shanghai Ninth People's Hospital, Shanghai Jiao Tong University School of Medicine, Shanghai, China, [2] Department of Assisted Reproduction, Shanghai Ninth People's Hospital, Shanghai Jiao Tong University School of Medicine, Shanghai, China, [3] Department of Vascular Surgery, Fengcheng Hospital Affiliated to Shanghai Ninth People's Hospital, Shanghai Jiao Tong University School of Medicine, Shanghai, China

Chronic inflammation mediated by artery infiltrated macrophages plays critical role in artery restenosis after endovascular therapy. Evidence has demonstrated the potential ability of photothermal therapy (PTT) in eliminating chronic inflammation by targeting inflammatory cells including macrophages. Recently, increasing attention has been payed to copper chalcogenide nanocrystals doped of radiocontrast agent, e.g., bismuth (Bi) for computed tomography (CT) guided PTT. However, the application of imaging guided PTT in preventing artery restenosis is lacking and limited. Herein, a novel multifunctional $CuBiS_2$ nanoparticles ($CuBiS_2$ NPs) were synthesized for CT imaging guided PTT in artery re-stenosis prevention. The optimum amount and other conditions of $CuBiS_2$ NPs were optimized to exert the maximum ablation effect on macrophages with good biocompatibility. *In vivo* carotid injury model revealed that $CuBiS_2$ NPs exhibited promising therapeutic effect on inhibition of artery stenosis by eliminating macrophages with excellent CT imaging ability. The recent study highlights a new cost-effective metal nanostructures-based nanotechnology in prevention of artery restenosis after endovascular therapy.

Keywords: $CuBiS_2$ nanoparticles, computed tomography, photothermal therapy, arterial restenosis, endovascular treatment

OPEN ACCESS

Edited by:
Ming Ma,
Shanghai Institute of Ceramics (CAS), China

Reviewed by:
Shun Duan,
Beijing University of Chemical Technology, China
Jianqiang Liu,
Guangdong Medical University, China
Yanshuo Han,
Dalian University of Technology, China

***Correspondence:**
Xiaoyu Wu
wxy_cmu@aliyun.com
Guanglin Yang
yangglbs@hotmail.com
Jiaying Lin
13818761532@126.com
Xiaobing Liu
benny_liuxb@163.com

† *These authors have contributed equally to this work*

Specialty section:
This article was submitted to Biomaterials, a section of the journal Frontiers in Bioengineering and Biotechnology

Received: *21 July 2020*
Accepted: *18 September 2020*
Published: *21 October 2020*

Citation:
Wu X, Liu K, Wang R, Yang G, Lin J and Liu X (2020) Multifunctional $CuBiS_2$ Nanoparticles for Computed Tomography Guided Photothermal Therapy in Preventing Arterial Restenosis After Endovascular Treatment. Front. Bioeng. Biotechnol. 8:585631. doi: 10.3389/fbioe.2020.585631

INTRODUCTION

Atherosclerosis remains a devastating disease affecting cardio/cerebrovascular system with high morbidity and mortality (Toyohara et al., 2020). Although endovascular treatment i.e., percutaneous transluminal angioplasty (PTA) and stent implantation is somehow considered the treatment of choice when dealing with atherosclerotic stenosis or occlusion (Baumgartner et al., 2018), it would unavoidably lead to the injury of arterial endothelium, release of various cytokines and chemokines, and subsequent recruitment of circulating monocytes to the arterial wall (Koelwyn et al., 2018; Morley et al., 2018). Once activated, infiltrated monocytes differentiate

into macrophages, mediating chronic inflammation of the injured artery (Koelwyn et al., 2018). Evidence has been growing that inflammatory macrophages play crucial role in artery restenosis after endovascular treatment (Sun et al., 2016; Pei et al., 2019). Infiltrated macrophages secrete matrix metalloproteinase (MMP) to degrade extracellular matrix and pro-inflammatory cytokines to stimulate the proliferation and transformation of smooth muscle cell (SMC) via different signaling pathways, eventually leading to the negative remodeling of the artery, i.e., artery restenosis (Yamashita et al., 2015; Zhao et al., 2017). Therefore, depletion of local aggregated inflammatory macrophages would provide a powerful mean to prevent artery restenosis.

Due to excellent properties of tissue penetration and minimally invasive, near-infrared (NIR) light driven photothermal therapy (PTT) based on nanomaterials could induce apoptosis and cell death by targeting intracellular protein and DNA (Al-Barram, 2020; Zhang et al., 2020; Zhi et al., 2020). With the advantages above and novel nanoparticles being developed (such as modified/decorated metal-organic framework based nanomaterial), nanotech PTT has been shown to be greatly applied in the anti-tumor theranostics, cardiovascular diseases and nervous system diseases, etc. (Shan et al., 2018; Luo et al., 2019; Wang et al., 2019; Pan et al., 2020; Zhou et al., 2020). Using ZD2-engineered gold nanostar@ metal-oragnic framework nanoprobes, it has been reported that the nanoprobes based PTT was efficient in treating triple-negative breast cancer with good magnetic resonance imaging property (Zhang et al., 2018). Nevertheless, we have previously reported that other nanoparticles, e.g., $CuCo_2S_4$ nanocrystals, MoO_2 nanoclusters, Fe_3S_4 nanoparticles, polypyrrole nanoparticles, and gold nanorods as PTT agents, can effectively alleviate inflammation by eliminating inflammatory macrophages (Peng et al., 2015; Qin et al., 2015; Wang et al., 2019; Zhang et al., 2019). Collectively, growing evidence suggest that nanoparticles as PTT agents may be an attractive and promising therapeutic target for chronic inflammation, including artery re-stenosis. However, the potential use of nanoparticle-based PTT in preventing artery restenosis after endovascular intervention is still lacking.

Metal sulfides are kinds of ideal candidate materials for photothermal applications, but their band gaps are usually too large to absorb significant fractions of NIR light and it has been gathering interest that by means of combining Cu^+ and Bi^{3+}, the ternary sulfides $CuBiS_2$ is formed (Dufton et al., 2012). $CuBiS_2$ is a semiconductor material with an energy gap distributed between 1.5 and 2.1 eV with good light absorption capability. Askari and Askari (2019) reported that $CuBiS_2$ demonstrated good photothermal property and showed anticancer effect on AGS cancer cell line via apoptosis pathway *in vitro*. On one hand, due to non-carcinogenic or toxic properties, bismuth is considered safe in pharmaceutical application and some of its components or compounds as an anti-inflammatory, antiviral and antifungal agents are widely used in clinical treatment (Tiekink, 2002; Iuchi et al., 2008). Moreover, accumulating evidence has been reported that by doping of radiocontrast agent, e.g., bismuth, copper chalcogenide nanocrystals exhibited excellent property for CT guided PTT, which has attracted great attention (Liu et al., 2015). However, evidence of $CuBiS_2$ based PTT in preventing artery re-stenosis is lacking.

In current study, $CuBiS_2$ nanoparticles ($CuBiS_2$ NPs) were synthesized and characterized *in vitro*/*vivo* and photothermal properties of the nanoparticles were further evaluated. Moreover, the cytotoxicity and PTT effect of $CuBiS_2$ NPs on inflammatory macrophages were also assessed *in vitro*. Carotid inflammation/endothelium injury model was established by using 29G Syringe needle mimicking endothelia damage after endovascular intervention. After that, PTT was conducted based on local injection of $CuBiS_2$ NPs to the surrounding of the injured carotid artery. Of note, we specially evaluated the imaging ability of $CuBiS_2$ NPs for *in vivo* tracking by small animal CT device. Histologic analysis demonstrated the effect of PTT in attenuating artery wall inflammation and stenosis. Also, histologic analysis of major organs and blood examination were performed to evaluate the biocompatibility of $CuBiS_2$ NPs.

MATERIALS AND METHODS

Materials

Raw264.7 (mouse macrophage) was obtained from Fuheng Cell Bank, Fudan University (Shanghai, China) for the *in vitro* study. High glucose (4,500 mg^{-1} mL) Dulbecco's Modified Eagle's Medium (DMEM), penicillin/streptomycin and fetal bovine serum were purchased from Gibco (Carlsbad, CA, United States). The CD68 antibody and corresponding 2nd antibody were purchased from Thermo Fisher Scientific (United States). Cell Counting Kit-8 (CCK-8) and Calcein-AM/PI Double Stain Kit were purchased from Thermo Fisher Scientific (United States).

$CuBiS_2$ NPs Synthesis and Characterization

One-step hydrothermal process (Wang et al., 2019) was used for the synthesis of the $CuBiS_2$ NPs according to the method described previously. Briefly, 0.256 g $CuCl_2.2H_2O$ and 0.16 g $BiCl_3$ was mixed and stirred with 30 mL anhydrous alcohol and 50 mL glycerol by magnetic stirrer, during which thiourea resolution (i.e., 0.19 g thiourea dissolved in 10 mL anhydrous alcohol) was dropped and stirred together for 10 min. After that, the mixture solution was transferred to a flat flask for constant temperature water bath heating at 60°C for 1 h and moved to a Teflon lined autoclave to be heated at 160°C for 12 h. After centrifugation (5,000 r/min), the precipitate was then collected and washed with 75% ethanol and deionized water three times.

Scanning electron microscopy (SEM) characterized the size and morphology properties of the $CuBiS_2$ NPs. UV-vis absorption spectra were measured by Jasco V-7000 UV-visible-NIR spectrophotometer (Tokyo, Japan). X-ray diffractometer (XRD) analysis were conducted using Aeris X-ray diffractometer (Malvern, United Kingdom). Fourier transform infrared (FTIR) spectra were analyzed by KBr pellet methods using TruDefender^{TM} FTX/FTXi infrared spectrometer (Thermo Fisher Scientific; United States).

The power of 808 nm semiconductor laser (Hangzhou Qiulai Optoelectronics Technology Co. Ltd., China) could be externally

adjusted (average 1.5 W). Calibration of the output power of lasers was conducted by using a hand-held optical power meter (Newport model 1918-C, CA, United States).

Cell Culture and Characterization

Raw264.7 macrophages were cultured in DMEM medium (4,500 mg^{-1} mL glucose, with 10% FBS and 1% streptomycin/penicillin) and maintained at 37°C in a humidified 5% CO_2 atmosphere. Cellular immunofluorescence (IF) staining was performed to identify Raw264.7 macrophage properties by the fluorescence microscope (Olympus, Japan).

Cytotoxicity and Cell Viability

The cytotoxicity of $CuBiS_2$ NPs on macrophages was evaluated in the absence of PTT. Raw264.7 was co-cultured with $CuBiS_2$ NPs at different concentrations (0, 80, 160, 320 mg/mL) for 12 h. CCK-8 cell proliferation assay was used to measure the cell viability of macrophages after co-incubation with $CuBiS_2$ NPs, following which the safe concentration of $CuBiS_2$ NPs was determined and utilized for the subsequent *in vitro* or *in vivo* experiments. Next, the photothermal effects of $CuBiS_2$ NPs on macrophages was assessed. Raw264.7 was co-cultured with $CuBiS_2$ NPs at a predetermined concentration above for 12 h and subjected to 808 nm NIR laser irradiation for 5 min. After that, the irradiated macrophages stained with Calcein AM/PI (Calcein AM labeled-green, PI labeled-red, respectively) were observed under fluorescence microscope to discriminate living and dead cells. Flow cytometry (FCM) was performed to assess cell apoptosis analysis after Annexin V/PI staining following the procedures described previously (Wang et al., 2019).

Intracellular SEM

$CuBiS_2$ NPs engulfed by macrophages was observed by intracellular Transmission Electron Microscope (TEM; JEM-1400, Tokyo, Japan).

Animal Model and Photothermal Therapy

The animal experiment protocol was approved by Ethics Review Committee of Shanghai Ninth People's Hospital, Shanghai Jiao Tong University School of Medicine. Male, 8-week-old apolipoprotein E knockout mice ($ApoE^{-/-}$ mice; Shanghai Southern Model Biological Co., Ltd.) were raised under specific pathogen-free (SPF) conditions. The method for artery inflammation and endothelium injury mice model is briefly described as follows: First anesthetize the $ApoE^{-/-}$ mouse by intraperitoneal injection of pentobarbital sodium (40 mg/kg), after that the left common carotid artery (CCA) was dissected, and blocked by a blocking clamp at the proximal end, an incision was then made at the distal end of CCA, following which a 29G needle (BD Insulin Syringe Ultra-Fine®) was inserted to the CCA. To mimic the endothelium injury by endovascular treatment, the needle in CCA was rotated for three circles and pushed forward-back for three times. After closing the incision, the carotid artery was sheathed with a constrictive silica collar as previously descripted (Wang et al., 2019).

After 14 days, 100 mL (160 mg/mL) $CuBiS_2$ NPs were injected into the left carotid arteries, while the contralateral right carotid artery was sham-operated to serve as intra-animal control (without silica collar). Twelve hours after injection, all the necks were irradiated at 808 nm NIR laser with power density of 0.5 W cm^{-2} for 5 min. GX-300 photothermal medical device was used to record the temperature of full-body infrared thermal images dynamically.

Computed Tomography *in vivo*

Small animal CT scanning was used to determine the imaging ability of $CuBiS_2$ NPs. Endothelium injury model mice received CT scanning before and after perivascular injection with the $CuBiS_2$ NPs (160 mg/mL, 100 mL, per mouse). CT data were acquired using X-ray voltage biased to 50 kVp with a 670 μA anode current with projection angles of 720°. Afterward, 3-dimensional CT imaging was established to observe the distribution of $CuBiS_2$ NPs around the left carotid artery.

Tissue Histological Findings and Blood Examination

Fourteenth day after PTT, all the mice were sacrificed for histopathological examination. Both sham-operated and collared carotid arteries were harvested. The tissue infiltrating macrophages was stained for its surface maker CD68 and the immunofluorescent signal was detected by microscope which was further quantified using Image-Pro Plus software. The number of infiltrated macrophages were counted by two investigators blinded to group information. Hematoxylin-eosin (HE) staining was performed to determine the thickness of the intima-media of arteries by the Image-pro Plus software.

To assess the biocompatibility and toxicity of the $CuBiS_2$ NPs *in vivo*, major viscera, e.g., heart, liver, spleen, lung and kidney were made at 4–6 nm sections slides for HE staining. Five age-sex matched healthy $ApoE^{-/-}$ mice were sacrificed as control. Biochemical parameters of the blood samples were measured in Shanghai Research Center.

Statistics Analysis

Quantitative data was represented as means ± standard deviation (SD), and one-way *Annona* analysis was used to compare the difference among multiple groups. Student's *t*-test was used when appropriate. A P-value < 0.05 was considered statistically significant. All data are representative of at least three independent experiments.

RESULTS AND DISCUSSION

Characterization of $CuBiS_2$ NPs

$CuBiS_2$ NPs were synthesized according to one-step hydrothermal method described previously. **Figure 1A** shows the XRD pattern of the as-synthesized products. The pattern of the sample can be matched well with the emplectite $CuBiS_2$ phase (JCPDS no. 43-1473), without no other peaks. EDS analysis (**Supplementary Figure S1**) showed that the products was composed of three elements (i.e., Cu, Bi, and S), further indicating the high purity of the $CuBiS_2$ NPs. As

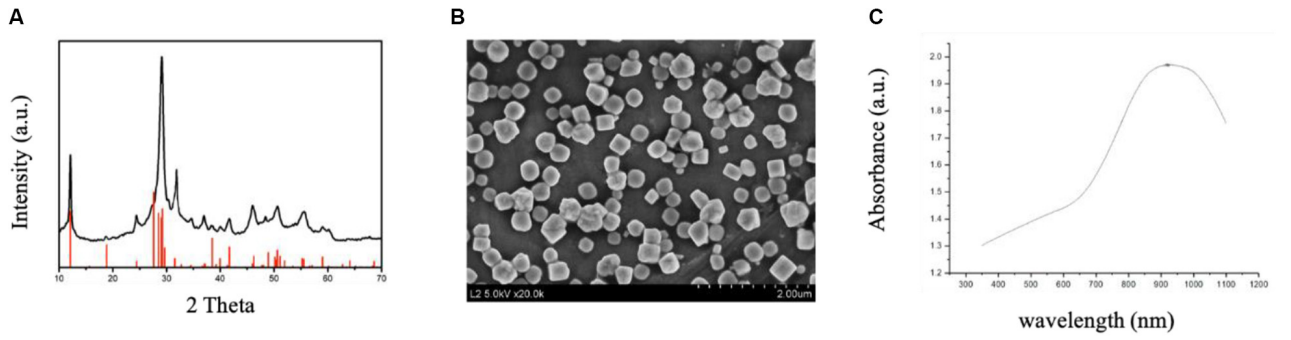

FIGURE 1 | Characterization of $CuBiS_2$ NPs. **(A)** XRD pattern and the corresponding standard pattern of $CuBiS_2$ NPs. **(B)** SEM images of $CuBiS_2$ NPs, Scale bars: 2 μm; **(C)** UV-vis-NIR absorption spectrum of $CuBiS_2$ NPs.

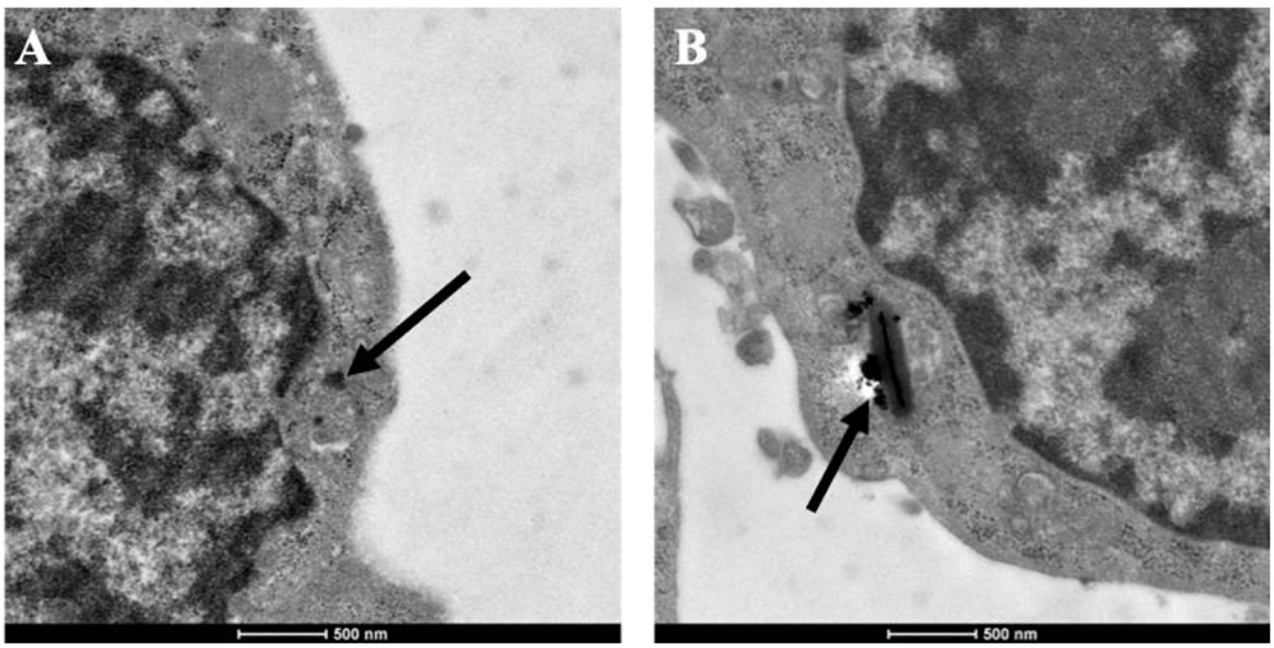

FIGURE 2 | Representative of TEM images of Raw264.7 co-incubated with $CuBiS_2$ NPs. Scale bar: 500 nm. **(A,B)** Macrophages incubated with 160 mg/mL $CuBiS_2$ NPs for 6 and 12 h, respectively. Scale Bar: 500 nm.

shown in **Figure 1B**, SEM results confirmed the products were nanoparticles with an average diameter of 240 nm (range from 180 to 400 nm). **Figure 1C** exhibits the UV-vis absorbance spectrum of the aqueous dispersion of $CuBiS_2$ NPs. It showed an intense absorption band centered at 910 nm. The strong NIR absorption made the nanoparticles possess the potential of to be PTT agents. Moreover, the zeta potential of $CuBiS_2$ NPs (160 mg/mL) was recorded by zeta potential analyzer (Nicomp Z3000) for 5 min, the result of which showed that the average zeta potential value was -1.86 mV.

As an important member of mononuclear phagocytic system, macrophages have powerful phagocytosis. Therefore, before determining the cytotoxicity and photothermal properties of $CuBiS_2$ NPs on Raw 264.7, we explored the phagocytosis of macrophages toward the $CuBiS_2$ NPs by TEM. The results showed efficient phagocytosis of $CuBiS_2$ NPs with no obvious accumulation or sever damage to other organelles of macrophages (**Figure 2**).

To evaluate the photothermal effect of $CuBiS_2$ NPs, the temperature evolution at different $CuBiS_2$ NPs concentration (0, 80, 160, 320 mg/mL) under continuous 808 nm wavelength laser irradiation for 300 s were recorded, showing that the temperature was elevated in dramatic and smooth pattern with increasement of $CuBiS_2$ NPs concentration (**Figure 3A**). Cytotoxicity of $CuBiS_2$ NPs on macrophages should be considered before other biomedical applications. To this end, Raw264.7 was co-cultured with $CuBiS_2$ NPs for 12 h in the absence of PTT. Subsequently, the CCK-8 assay was conducted to measure the concentration-dependent cytotoxic effect of $CuBiS_2$ NPs on Raw264.7 (**Figure 3B**). Finally, no

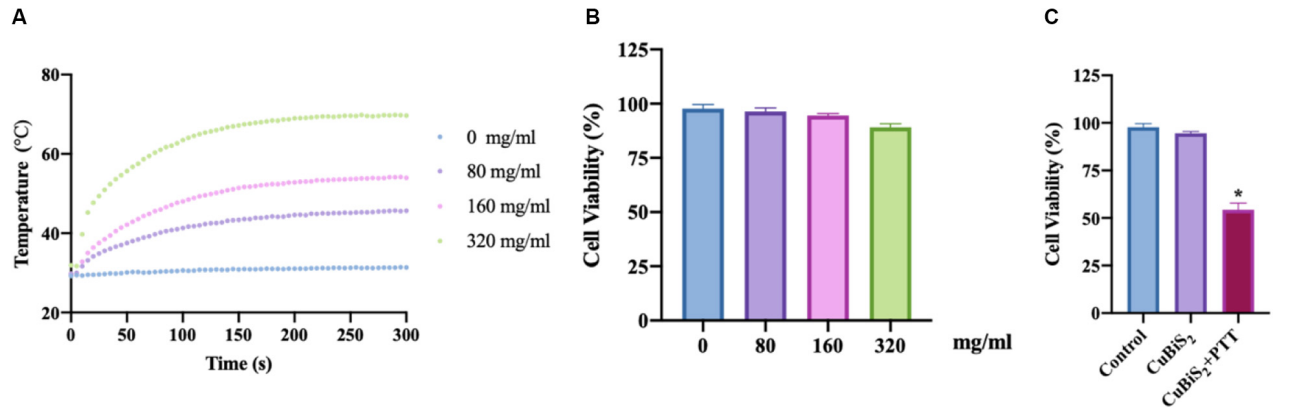

FIGURE 3 | Screening the optimal concentration of $CuBiS_2$ NPs for photothermal therapy. **(A)** *In vitro* photothermal effect of PBS and $CuBiS_2$ NPs in aqueous solution at different concentrations. **(B)** Relative cell viabilities of macrophages after co-incubation with $CuBiS_2$ NPs at different concentrations for 12 h without photothermal therapy. **(C)** Relative cell viabilities of macrophages after co-incubation with $CuBiS_2$ NPs at different concentrations for 12 h under photothermal therapy.

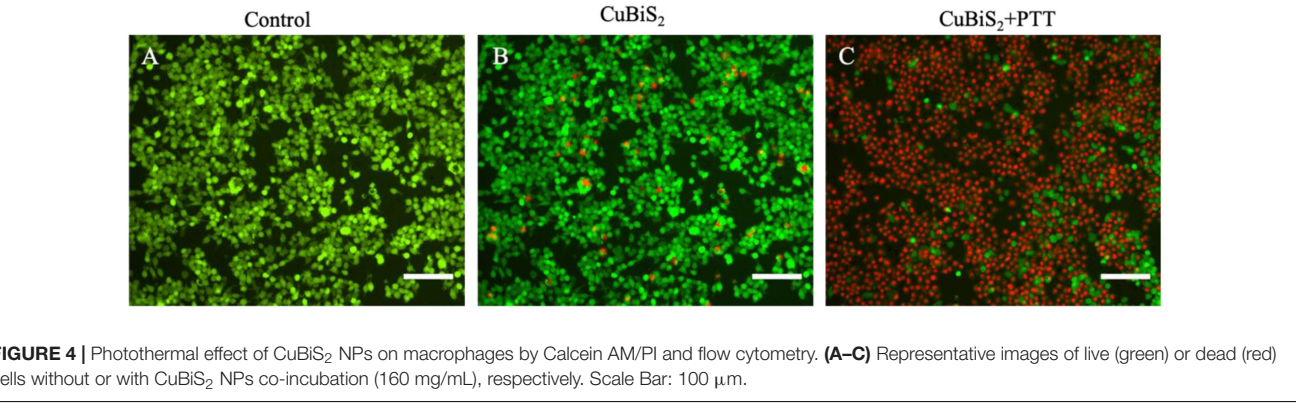

FIGURE 4 | Photothermal effect of $CuBiS_2$ NPs on macrophages by Calcein AM/PI and flow cytometry. **(A–C)** Representative images of live (green) or dead (red) cells without or with $CuBiS_2$ NPs co-incubation (160 mg/mL), respectively. Scale Bar: 100 μm.

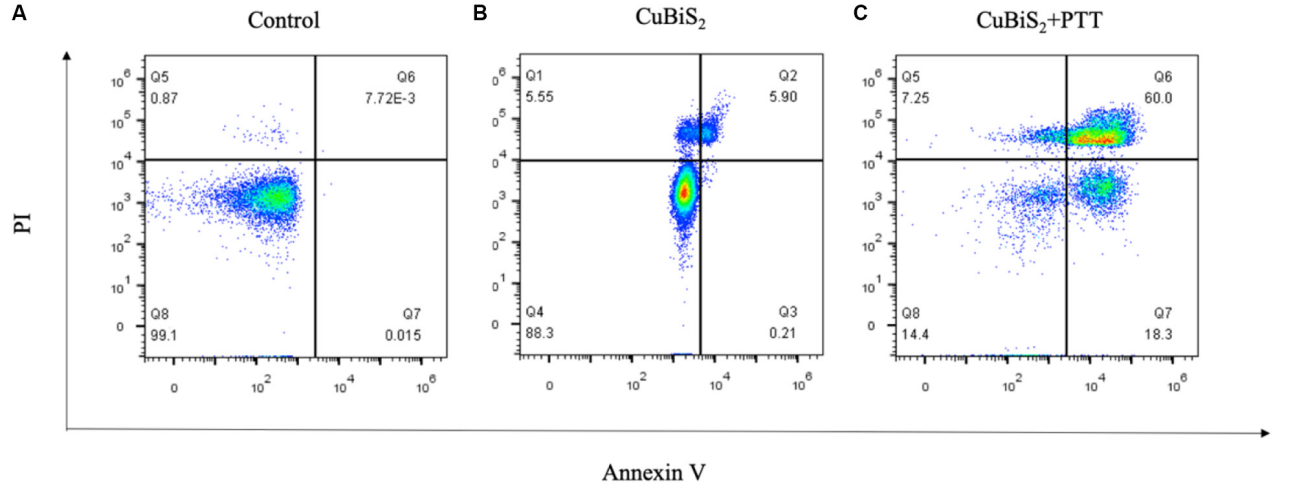

FIGURE 5 | $CuBiS_2$ NPs based PTT induced apoptosis of macrophages. Flow cytometry analysis of Raw264.7 apoptosis after different treatments: **(A)** Control; **(B)** $CuBiS_2$; **(C)** $CuBiS_2$ + PTT. Cell apoptosis was detected by flow cytometry with annexin-V-FITC and PI. $CuBiS_2$ NPs + PTT group showed higher early (Q7) and mid/late (Q6) apoptosis index than $CuBiS_2$ group.

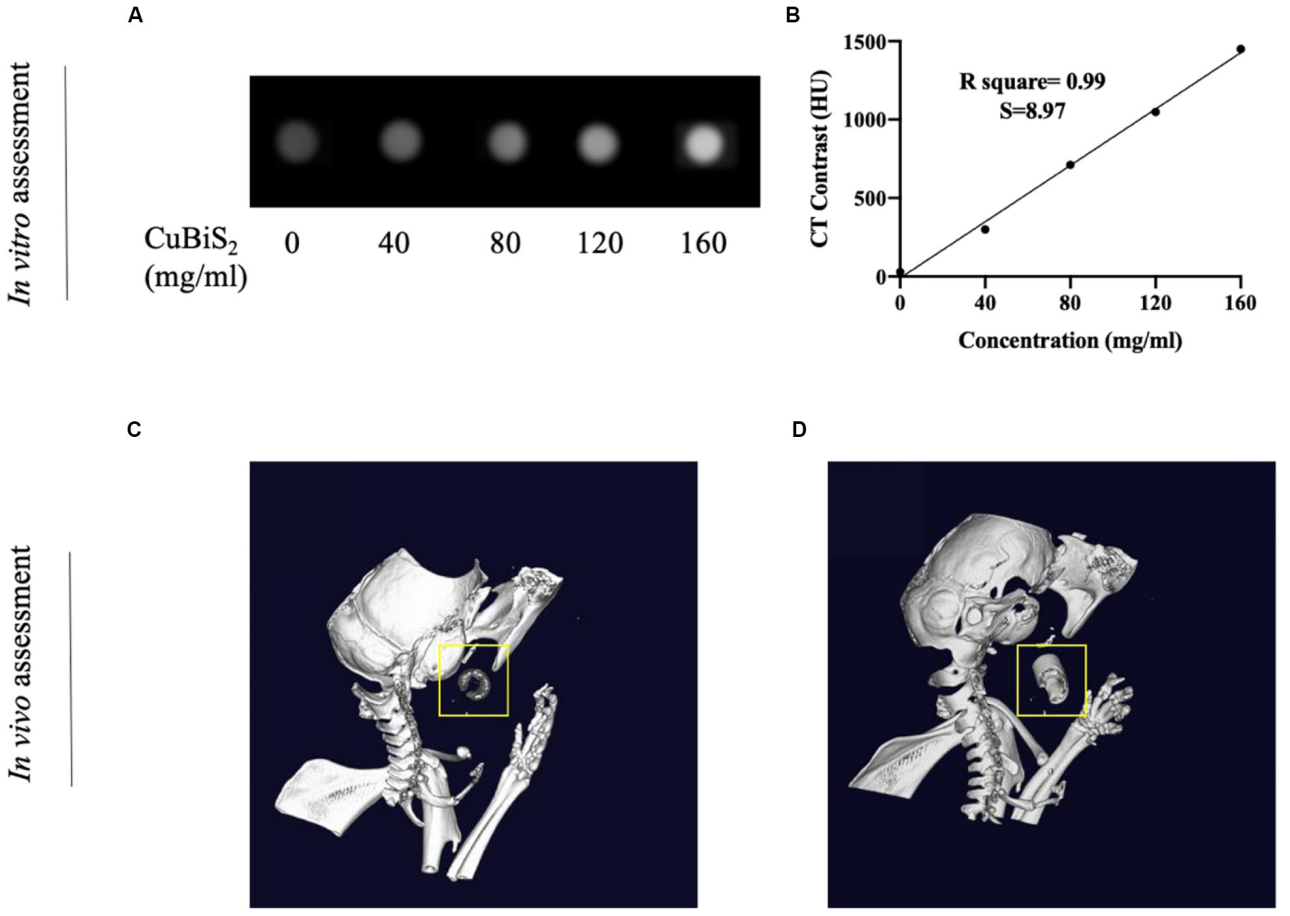

FIGURE 6 | Demonstration of computed tomography imaging property of $CuBiS_2$ *in vitro and in vivo*. **(A)** The CT signals intensity of different $CuBiS_2$ concentration *in vitro*. **(B)** CT value (HU) of the $CuBiS_2$ NPs as a function of the concentration of NPs. **(C,D)** 3-D CT imaging of mice without and with $CuBiS_2$ NPs being injected to the surrounding of the carotid artery, respectively.

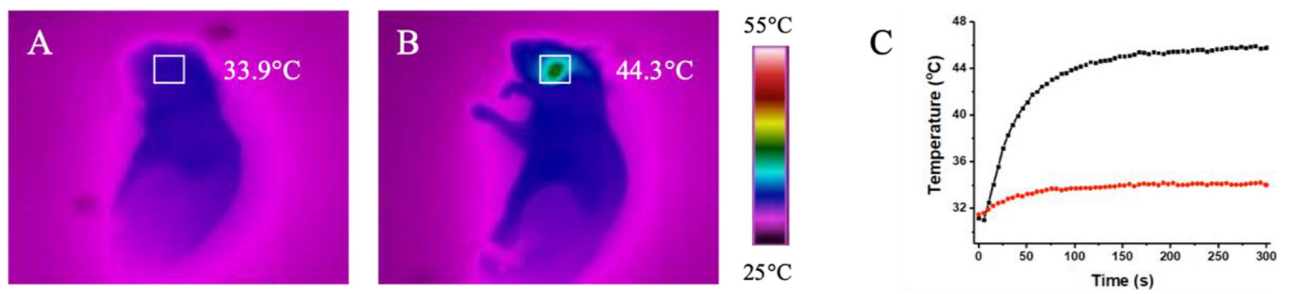

FIGURE 7 | *In vivo* thermal effect of $CuBiS_2$ NPs *in vivo*. **(A,B)** Representative of infrared thermal images of the mice after being injected with PBS or $CuBiS_2$ NPs under laser irradiation. **(C)** Temperature changes according to irradiation time in corresponding squared regions (red: PBS control; black: $CuBiS_2$ NPs group).

significant difference on cell cytotoxicity was identified between the $CuBiS_2$ NPs group and the control group below the concentration of 160 mg/mL, while significant cytotoxicity was observed when macrophages were co-incubated with $CuBiS_2$ NPs at concentration above 160 mg/mL, indicating that $CuBiS_2$ NPs exhibited good biocompatibility at concentration of 160 mg/mL (**Figure 3B**).

To investigate the applicability of $CuBiS_2$ NPs based PTT, *in vitro* evaluation of their photothermal efficacy was performed. Raw264.7 macrophages were co-cultured with $CuBiS_2$ NPs at 160 mg/mL for 12 h, and then subjected to 808 nm NIR irradiation (0.3 W/cm^2). Calcein AM/PI results demonstrated that few dead cells were observed in the control group, and $CuBiS_2$ NPs group (**Figures 4A,B**). While about 60% dead cells

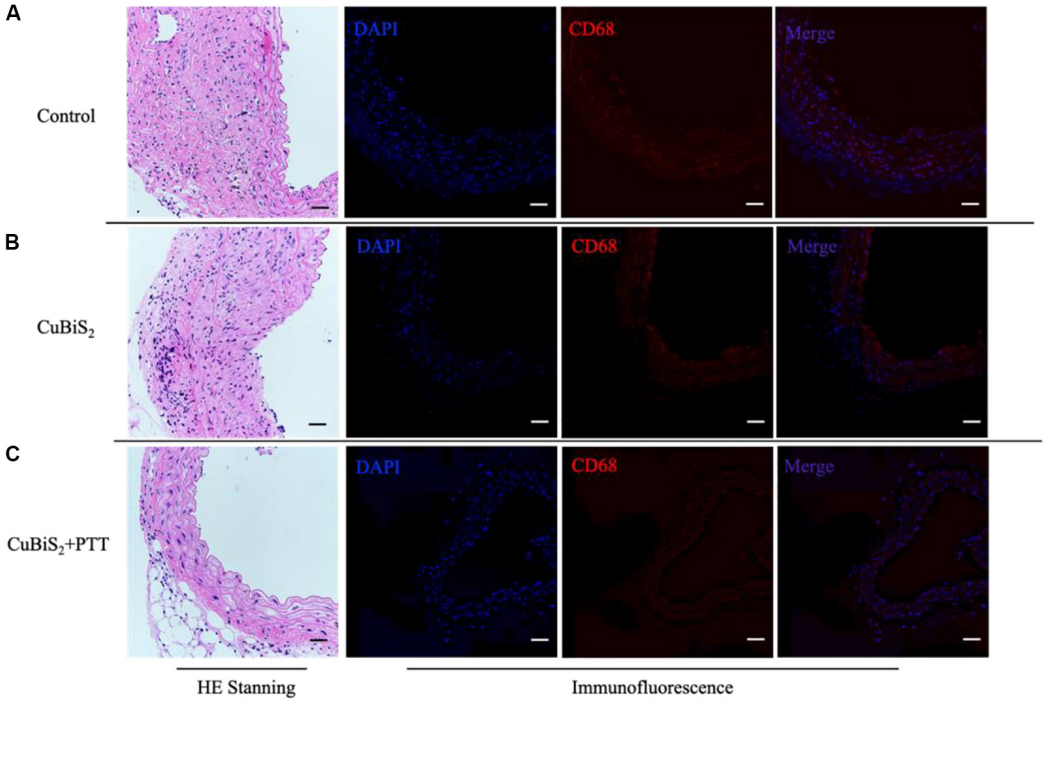

FIGURE 8 | $CuBiS_2$ NPs based PTT mitigated arterial inflammation *in vivo*. **(A–C)** Representative of HE and Immunofluorescence stanning of carotid artery from control group, $CuBiS_2$ group and $CuBiS_2$ + PTT group, respectively. **(D,E)** Representative of CD68 + macrophages positive area and artery wall thickness in each group, respectively. Scale bar: 50 μm.

were observed in the $CuBiS_2$ NPs + PTT group (**Figure 4C**). In accordance with Calcein AM/PI, the CCK-8 assay showed similar results (**Figure 3C**). The above results showed that $CuBiS_2$ NPs based PTT exhibited excellent photothermal property with remarkable macrophages death being observed.

Apoptosis is an important type of programmed cell death which can be induced by thermal effect, whether it is involved in $CuBiS_2$ NPs based PTT induced cell death is unknown. Annexin V/PI duo-stanning detects the signals of Annexin V and the impermeable nucleic acid dye, respectively, which can quantify the proportion of mid- and late-apoptotic cells, we used Annexin V/PI stanning to determine the $CuBiS_2$ NPs based PTT effect on macrophages and discriminate cell apoptosis and necrosis. Toward this end, FCM was performed showing that compared with $CuBiS_2$ NPs group, $CuBiS_2$ NPs + PTT group exhibited a significantly higher either early apoptosis (18.3 vs. 0.21%) or mid/late apoptosis (60 vs. 5.9%) index of macrophages with statistical difference (**Figure 5**). In contrast to programmed cell death, necrosis is the death process in which cells are subject to strong physical and chemical or biological factors that cause disordered changes in cells. As shown in **Figure 5**, the necrosis index of macrophages was identical between $CuBiS_2$ NPs group and $CuBiS_2$ NPs + PTT group, indicating that the type of $CuBiS_2$ NPs based PTT induced macrophages death was mainly apoptosis instead of necrosis. The above results demonstrated that $CuBiS_2$ NPs based PTT could ablate macrophages effectively by inducing cell apoptosis (**Figures 5A–C**), which possesses great potential to alleviate chronic inflammation mediated by macrophages.

CT Imaging Assessment and Photothermal Effect of $CuBiS_2$ NPs *in vivo*

Nanomaterials have drawn great attention over the decades and been widely utilized in biomedicine (Cole et al., 2015; Zhang et al., 2016). Nanoplatforms can integrate imaging moieties and therapeutic species flexibly, which has been widely applied in cancer diagnosis and treatment (Liu et al., 2007). Among numbers of investigations, CT imaging guided PTT has been widely reported and highly recognized. Conventional contrast agents have the disadvantages of short imaging time and potential nephrotoxicity, while new nanocrystal contrast agents such as Bi_2S_3, TaOx, and other nanoparticles (NPs) overcome the above shortcomings and has high absorption coefficient (Ai et al., 2011; Lee et al., 2012; Leeuwenburgh et al., 2013; Cheng et al., 2014). With high density (ρ) and atomic number (Z), Bi element was reported to possess high attenuation coefficient of X-ray (Elsabahy et al., 2015). With long vascular half-life, Bi_2S_3 nanoplates was reported to gain considerable potential to achieve enhanced CT efficacy with lower agent dose in future clinical use (Rabin et al., 2006). In addition to the

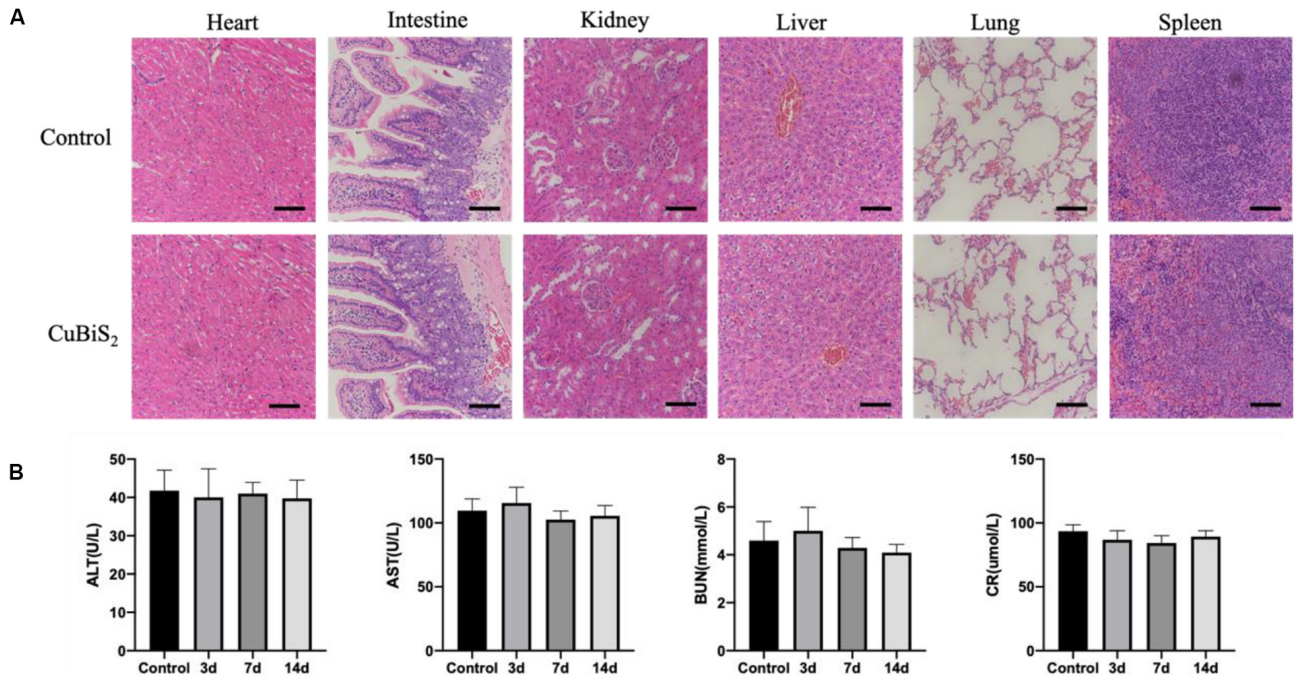

FIGURE 9 | *In vivo* biocompatibility test of $CuBiS_2$ NPs. **(A)** HE staining of major viscera showed no obvious histopathological changes in heart, intestine, kidney, liver, lung, or spleen between the control group and the $CuBiS_2$ group. Scale bar: 50 μm. **(B)** Laboratory blood test of control group and $CuBiS_2$ group at different time points (3, 7, 14 days) after $CuBiS_2$ NPs injection, including alanine aminotransferase (ALT), aspartate aminotransferase (AST), blood urea nitrogen (BUN), and creatinine (CR).

photothermal ablation ability, CT imaging property of $CuBiS_2$ NPs was further assessed *in intro* and *in vivo* on the bases of pre-determined concentration for cytotoxicity and cell viability evaluation *in vitro*. **Figure 6** presents the CT image of aqueous dispersions of the $CuBiS_2$ NPs with different concentration, showing that CT signal intensity enhanced with increased concentrations of the $CuBiS_2$ NPs. Meanwhile, the Hounsfield units (HU) values increased linearly with the concentration of the $CuBiS_2$ NPs. As shown in **Figures 6A,B**, $CuBiS_2$ NPs at concentration of 160 mg/ml exhibited excellent *in vitro* imaging property, which was further tested *in vivo* showing that distinct difference was observed in CT images of $CuBiS_2$ NPs surrounding inflammatory artery, demonstrating good CT imaging property of $CuBiS_2$ NPs (**Figures 6C,D**).

Endovascular repairs would unavoidably cause mechanical injury to endothelial cells and activates the endothelium to express massive adhesive molecules and chemokines, which promotes the recruitment of monocytes, accelerates differentiation of monocytes into macrophages and aggravate artery inflammation, leading the restenosis after endovascular treatment (Sun et al., 2016; Pei et al., 2019). According to above results, we speculate that the macrophages infiltrated in the injured lesion of artery endothelium engulf locally injected non-toxic $CuBiS_2$ NPs and provide opportunities for *in vivo* non-invasive PTT to attenuate arterial inflammation and stenosis. Toward this end, a carotid artery inflammation/endothelium injury model was conducted in $ApoE^{-/-}$ mice by mechanical injury to intima using a 29G Syringe needle mimicking endovascular treatment related endothelium injury to further validate the feasibility of $CuBiS_2$ NPs based PTT for inhibiting artery restenosis (**Supplementary Figure S2**). The mice received local injection of a solution of the $CuBiS_2$ NPs (160 mg/mL, 100 mL) around the left carotid artery and subjected to NIR laser irradiation (808 nm, 0.5 W cm^{-2}) 12 h. An equivalent volume of PBS was injected as control. The local temperatures of the left necks were recorded by an infrared thermal camera dynamically. In mice injected with $CuBiS_2$ NPs, the local surface temperature of the left neck gradually increased to 45°C rapidly within 5 min, while non-dramatic increase of the local surface temperature was recorded in the control group being injected PBS (**Figure 7**). After 14 days, the mice were sacrificed, and the carotid arteries were collected for HE staining and immunofluorescence examination.

The effectiveness of $CuBiS_2$ NPs based PTT for alleviating arterial inflammation was further assessed by IF (**Figures 8A–D**), the results of which showed that the artery-infiltrating macrophages in the $CuBiS_2$ NPs + PTT group reduced greatly. The HE staining exhibited that the thickness of arterial intima-media in the $CuBiS_2$ NPs + PTT group was much thinner than that of the $CuBiS_2$ NPs group and the control group (**Figure 8E**). However, there was no significant difference between the control group and the $CuBiS_2$ NPs group. Thus, the results suggested $CuBiS_2$ NPs as photothermal agents and 808 nm NIR PTT can effectively eliminate inflammatory macrophages infiltrated in the layer of artery to inhibit arterial inflammation and stenosis.

Biocompatibility of the $CuBiS_2$ Nanoparticles

Of note, favorable biocompatibility of NPs should be considered and guaranteed for living body. Mice from $CuBiS_2$ NPs group and control group (n = 4, each) were sacrificed 14 days after PTT. Paraffin-embedded sections (4 nm) of major organs were stained with hematoxylin-eosin (HE) dye. No obvious histopathological changes were found between the two groups (**Figure 9A**). No obvious cell degeneration and necrosis were observed in major viscera (**Figure 9A**). Blood samples were tested using Elisa method. Statistical difference was not gained between the two groups in terms of alanine aminotransferase (ALT), asparate aminotransferase (AST), blood urea nitrogen (BUN), or creatinine (Cr) (**Figure 9B**). As dysfunction of endothelial cells contributed to negative remodeling the artery (e.g., artery restenosis), Evan's Blue stanning of the carotid artery from each group was performed to test the potential side-effect of $CuBiS_2$ NPs on reendothelialization, showing that no difference was found between the groups (**Supplementary Figure S3**). These results show that $CuBiS_2$ NPs as PTT agents have no toxic effects on the major organ function, and thus are safe for use *in vivo*.

CONCLUSION

In summary, $CuBiS_2$ NPs were successfully synthesized by one-step hydrothermal method. The NPs showed intense NIR absorption due to the defect structure, thus were demonstrated excellent photothermal performance. Due to the High X-ray attenuation coefficient of bismuth, $CuBiS_2$ NPs possessed CT imaging ability. $CuBiS_2$ NPs based PTT could eliminate macrophages *in vitro* and *in vivo*, expanding the understanding of $CuBiS_2$ NPs as efficient PTT agents for arterial inflammation and restenosis after endovascular treatment.

DATA AVAILABILITY STATEMENT

All datasets generated for this study are included in the article/**Supplementary Material**.

ETHICS STATEMENT

The animal study was reviewed and approved by the Shanghai Ninth People's Hospital, Shanghai Jiao Tong University School of Medicine.

AUTHOR CONTRIBUTIONS

XW and XL contributed to the model development, code development, data generation and analysis, writing, and editing the manuscript. JL and GY contributed to the model development, data analysis, and editing the manuscript. KL and RW contributed to the model development, data analysis, writing, and editing the manuscript. All the authors contributed to discussion of the results.

FUNDING

This work was supported by the National Natural Science Foundation of China (Grant Nos. 81701801, 81971712, 81970405, and 81801526) and Clinical Research Program of Ninth People's Hospital, Shanghai Jiao Tong University School of Medicine (Grant No. JYLJ019).

SUPPLEMENTARY MATERIAL

The Supplementary Material for this article can be found online at: https://www.frontiersin.org/articles/10.3389/fbioe.2020.585631/full#supplementary-material

REFERENCES

Ai, K., Liu, Y., Liu, J., Yuan, Q., He, Y., and Lu, L. (2011). Large-scale synthesis of Bi(2)S(3) nanodots as a contrast agent for in vivo X-ray computed tomography imaging. *Adv. Mater.* 23, 4886–4891. doi: 10.1002/adma.201103289

Al-Barram, L. F. A. (2020). Laser enhancement of cancer cell destruction by photothermal therapy conjugated glutathione (GSH)-coated small-sized gold nanoparticles. *Lasers Med. Sci.* doi: 10.1007/s10103-020-03033-y [Epub ahead of print].

Askari, N., and Askari, M. B. (2019). Apoptosis-inducing and image-guided photothermal properties of smart nano CuBiS2. *Mater. Res. Express* 6:065404. doi: 10.1088/2053-1591/ab0c3e

Baumgartner, I., Norgren, L., Fowkes, F. G. R., Mulder, H., Patel, M. R., Berger, J. S., et al. (2018). Cardiovascular outcomes after lower extremity endovascular or surgical revascularization: the EUCLID trial. *J. Am. Coll. Cardiol.* 72, 1563–1572. doi: 10.1016/j.jacc.2018.07.046

Cheng, L., Liu, J., Gu, X., Gong, H., Shi, X., Liu, T., et al. (2014). PEGylated WS(2) nanosheets as a multifunctional theranostic agent for in vivo dual-modal CT/photoacoustic imaging guided photothermal therapy. *Adv. Mater.* 26, 1886–1893. doi: 10.1002/adma.201304497

Cole, L. E., Ross, R. D., Tilley, J. M., Vargo-Gogola, T., and Roeder, R. K. (2015). Gold nanoparticles as contrast agents in x-ray imaging and computed tomography. *Nanomedicine* 10, 321–341. doi: 10.2217/nnm.14.171

Dufton, J. T., Walsh, A., Panchmatia, P. M., Peter, L. M., Colombara, D., and Islam, M. S. (2012). Structural and electronic properties of CuSbS2 and CuBiS2: potential absorber materials for thin-film solar cells. *Phys. Chem. Chem. Phys.*14, 7229–7233. doi: 10.1039/c2cp40916j

Elsabahy, M., Heo, G. S., Lim, S. M., Sun, G., and Wooley, K. L. (2015). Polymeric nanostructures for imaging and therapy. *Chem. Rev.* 115, 10967–11011. doi: 10.1021/acs.chemrev.5b00135

Iuchi, K., Hatano, Y., and Yagura, T. (2008). Heterocyclic organobismuth(III) induces apoptosis of human promyelocytic leukemic cells through activation of caspases and mitochondrial perturbation. *Biochem. Pharmacol.* 76, 974–986. doi: 10.1016/j.bcp.2008.07.038

Koelwyn, G. J., Corr, E. M., Erbay, E., and Moore, K. J. (2018). Regulation of macrophage immunometabolism in atherosclerosis. *Nat. Immunol.* 19, 526–537. doi: 10.1038/s41590-018-0113-3

Lee, N., Cho, H. R., Oh, M. H., Lee, S. H., Kim, K., Kim, B. H., et al. (2012). Multifunctional Fe3O4/TaO(x) core/shell nanoparticles for simultaneous magnetic resonance imaging and X-ray computed tomography. *J. Am. Chem. Soc.* 134, 10309–10312. doi: 10.1021/ja3016582

Leeuwenburgh, M. M., Wiarda, B. M., Wiezer, M. J., Vrouenraets, B. C., Gratama, J. W., Spilt, A., et al. (2013). Comparison of imaging strategies with conditional contrast-enhanced CT and unenhanced MR imaging in patients suspected of having appendicitis: a multicenter diagnostic performance study. *Radiology* 268, 135–143. doi: 10.1148/radiol.13121753

Liu, J., Zheng, X., Yan, L., Zhou, L., Tian, G., Yin, W., et al. (2015). Bismuth sulfide nanorods as a precision nanomedicine for in vivo multimodal imaging-guided photothermal therapy of tumor. *ACS Nano* 9, 696–707. doi: 10.1021/nn506137n

Liu, Y., Miyoshi, H., and Nakamura, M. (2007). Nanomedicine for drug delivery and imaging: a promising avenue for cancer therapy and diagnosis using targeted functional nanoparticles. *Intern. J. Cancer* 120, 2527–2537. doi: 10.1002/ijc.22709

Luo, Z., Fan, S., Gu, C., Liu, W., Chen, J., Li, B., et al. (2019). Metal-organic framework (MOF)-based nanomaterials for biomedical applications. *Curr. Med. Chem.* 26, 3341–3369. doi: 10.2174/0929867325666180214123500

Morley, R. L., Sharma, A., Horsch, A. D., and Hinchliffe, R. J. (2018). Peripheral artery disease. *BMJ* 360:j5842. doi: 10.1136/bmj.j5842

Pan, Y., Luo, Z., Wang, X., Chen, Q., Chen, J., Guan, Y., et al. (2020). A versatile and multifunctional metal-organic framework nanocomposite toward chemo-photodynamic therapy. *Dalton Trans.* 49, 5291–5301. doi: 10.1039/c9dt04804a

Pei, C., Zhang, Y., Wang, P., Zhang, B., Fang, L., Liu, B., et al. (2019). Berberine alleviates oxidized low-density lipoprotein-induced macrophage activation by downregulating galectin-3 via the NF-κB and AMPK signaling pathways. *Phytother. Res.* 33, 294–308. doi: 10.1002/ptr.6217

Peng, Z., Qin, J., Li, B., Ye, K., Zhang, Y., Yang, X., et al. (2015). An effective approach to reduce inflammation and stenosis in carotid artery: polypyrrole nanoparticle-based photothermal therapy. *Nanoscale* 7, 7682–7691. doi: 10.1039/c5nr00542f

Qin, J., Peng, Z., Li, B., Ye, K., Zhang, Y., Yuan, F., et al. (2015). Gold nanorods as a theranostic platform for in vitro and in vivo imaging and photothermal therapy of inflammatory macrophages. *Nanoscale* 7, 13991–14001. doi: 10.1039/c5nr02521d

Rabin, O., Manuel Perez, J., Grimm, J., Wojtkiewicz, G., and Weissleder, R. (2006). An X-ray computed tomography imaging agent based on long-circulating bismuth sulphide nanoparticles. *Nat. Mater.* 5, 118–122. doi: 10.1038/nmat1571

Shan, D., Kothapalli, S. R., Ravnic, D. J., Gerhard, E., Kim, J. P., Guo, J., et al. (2018). Development of citrate-based dual-imaging enabled biodegradable electroactive polymers. *Adv. Funct. Mater.* 28:1801787. doi: 10.1002/adfm.201801787

Sun, J. Y., Li, C., Shen, Z. X., Zhang, W. C., Ai, T. J., Du, L. J., et al. (2016). Mineralocorticoid receptor deficiency in macrophages inhibits neointimal hyperplasia and suppresses macrophage inflammation through SGK1-AP1/NF-κB pathways. *Arterioscler. Thromb. Vasc. Biol.* 36, 874–885. doi: 10.1161/atvbaha.115.307031

Tiekink, E. R. (2002). Antimony and bismuth compounds in oncology. *Crit. Rev. Oncol.* 42, 217–224. doi: 10.1016/s1040-8428(01)00217-7

Toyohara, T., Roudnicky, F., Florido, M. H. C., Nakano, T., Yu, H., Katsuki, S., et al. (2020). Patient hiPSCs identify vascular smooth muscle arylacetamide deacetylase as protective against atherosclerosis. *Cell Stem Cell* 27, 178–180. doi: 10.1016/j.stem.2020.05.013

Wang, X., Wu, X., Qin, J., Ye, K., Lai, F., Li, B., et al. (2019). Differential phagocytosis-based photothermal ablation of inflammatory macrophages in Atherosclerotic disease. *ACS Appl. Mater. Interf.* 11, 41009–41018. doi: 10.1021/acsami.9b12258

Yamashita, T., Sasaki, N., Kasahara, K., and Hirata, K. (2015). Anti-inflammatory and immune-modulatory therapies for preventing atherosclerotic cardiovascular disease. *J. Cardiol.* 66, 1–8. doi: 10.1016/j.jjcc.2015.02.002

Zhang, L., Liu, C., Gao, Y., Li, Z., Xing, J., Ren, W., et al. (2018). ZD2-engineered gold nanostar@Metal-organic framework nanoprobes for T -weighted magnetic resonance imaging and photothermal therapy specifically toward triple-negative breast cancer. *Adv. Healthc. Mater.* 7:e1801144. doi: 10.1002/adhm.201801144

Zhang, R., Zhao, J., Han, G., Liu, Z., Liu, C., Zhang, C., et al. (2016). Real-time discrimination and versatile profiling of spontaneous reactive oxygen species in living organisms with a single fluorescent probe. *J. Am. Chem. Soc.* 138, 3769–3778. doi: 10.1021/jacs.5b12848

Zhang, X., Liu, J., Yang, X., He, G., Li, B., Qin, J., et al. (2019). CuCoS nanocrystals as a nanoplatform for photothermal therapy of arterial inflammation. *Nanoscale* 11, 9733–9742. doi: 10.1039/c9nr00772e

Zhang, Y., Feng, Y., Huang, Y., Wang, Y., Qiu, L., Liu, Y., et al. (2020). Tumor-targeted gene silencing ido synergizes ptt-induced apoptosis and enhances anti-tumor immunity. *Front. Immunol.* 11:968. doi: 10.3389/fimmu.2020.00968

Zhao, Q., Zhou, D., You, H., Lou, B., Zhang, Y., Tian, Y., et al. (2017). IFN-γ aggravates neointimal hyperplasia by inducing endoplasmic reticulum stress and apoptosis in macrophages by promoting ubiquitin-dependent liver X receptor-α degradation. *FASEB* 31, 5321–5331. doi: 10.1096/fj.201700327R

Zhi, D., Yang, T., O'Hagan, J., Zhang, S., and Donnelly, R. F. (2020). Photothermal therapy. *J. Control. Release* 325, 52–71. doi: 10.1016/j.jconrel.2020.06.032

Zhou, J., Ling, G., Cao, J., Ding, X., Liao, X., Wu, M., et al. (2020). Transcatheter intra-arterial infusion combined with interventional photothermal therapy for the treatment of hepatocellular carcinoma. *Intern. J. Nanomed.* 15, 1373–1385. doi: 10.2147/ijn.S233989

Conflict of Interest: The authors declare that the research was conducted in the absence of any commercial or financial relationships that could be construed as a potential conflict of interest.

frontiers in Bioengineering and Biotechnology

ORIGINAL RESEARCH
published: 26 October 2020
doi: 10.3389/fbioe.2020.599040

Facile Interfacial Synthesis of Densely Spiky Gold Nano-Chestnuts With Full Spectral Absorption for Photothermal Therapy

Zhiping Wan[1†], Jinmao Gu[1†], Yining Wang[2†], Jun Qian[1], Junle Zhu[1], Feng Chen[1], Haoheng Wang[1], Huairui Chen[1] and Chun Luo[1]**

[1] Department of Neurosurgery, Tongji Hospital, Tongji University School of Medicine, Shanghai, China, [2] Center of Reproductive Medicine, Shanghai Changzheng Hospital, Shanghai, China

The gold nanostructure is regarded as the most promising photothermal agent due to its strong localized surface plasma resonance (LSPR) effect. In particular, the gold nanostructures with sharp spikes on the surface have higher optical signal enhancement, owing to the sharp tips drastically enhancing the intense nanoantenna effect. However, current approaches for the synthesis of spiky gold nanostructures are either costly, complicated, or uncontrollable. Herein, we report a novel strategy to synthesize gold nano-chestnuts (SGNCs) with sharp spikes as an excellent photothermal agent. The SGNCs were prepared by a facile one-pot interfacial synthetic method, and their controllable preparation mechanism was acquired. The SGNCs exhibited ideal full-spectrum absorption and showed excellent photothermal effect. They have a photothermal conversion efficiency (η) as high as 52.9%, which is much higher than traditional photothermal agents. The *in vitro* and *in vivo* results show that the SGNCs could efficiently ablate the tumor cells. Thus, the SGNCs have great potential in photothermal therapy applied in malignant tumors.

Keywords: SGNCs, photothermal effect, malignant tumor, spike (S), spectral absorption

OPEN ACCESS

Edited by:
Bo Li,
Shanghai Jiao Tong University, China

Reviewed by:
Xijian Liu,
Shanghai University of Engineering Sciences, China
Guoying Deng,
Shanghai General Hospital, China

***Correspondence:**
Chun Luo
boyluochun@126.com
Huairui Chen
chen13761626536@163.com

[†]These authors have contributed equally to this work

Specialty section:
This article was submitted to Biomaterials, a section of the journal Frontiers in Bioengineering and Biotechnology

Received: *26 August 2020*
Accepted: *05 October 2020*
Published: *26 October 2020*

Citation:
Wan Z, Gu J, Wang Y, Qian J, Zhu J, Chen F, Wang H, Chen H and Luo C (2020) Facile Interfacial Synthesis of Densely Spiky Gold Nano-Chestnuts With Full Spectral Absorption for Photothermal Therapy. Front. Bioeng. Biotechnol. 8:599040. doi: 10.3389/fbioe.2020.599040

INTRODUCTION

Tumors, especially malignant tumors, have become one of the greatest threats to human health. Many strategies were devised for oncotherapy, and photothermal therapy (PTT) is the newest and most promising strategy among them, which uses PTT agents to convert the near-infrared (NIR) energy to heat for hyperthermia of tumors (Huang et al., 2017; Liu et al., 2019; Yang et al., 2019; Fernandes et al., 2020; Wang Y. et al., 2020; Zhang et al., 2020). Lots of PTT agents have been reported, such as semiconductors (transfer metal sulfide and transfer metal oxide), carbon materials (carbon nanotube), and noble metals (Liu et al., 2014, 2019; Huang et al., 2017). Among them, gold nanostructures (GNSs) are the most promising PTT agent, which could obtain strong localized surface plasma resonance (LSPR) due to their morphology and size (Cao et al., 2014; Furube and Hashimoto, 2017; Kong et al., 2020; Tabish et al., 2020). GNSs have also been proven not only as an efficient imaging agent for tumor diagnosis but also as a theranostic agent for thermal ablation of tumor cells, due to their excellent photothermal effect and tunable optical properties (Xia et al., 2011; Ren et al., 2015; An et al., 2017; D'Acunto, 2018; Norouzi et al., 2018). For *in vivo* applications,

the LSPR adsorption of GNSs must be optimized to the NIR region where light has high tissue transparency and penetration depth. To date, a variety of NIR-absorbing GNSs, such as nanorods (Xu et al., 2020), nanoshells (Xuan et al., 2016), nanocones (Zhang et al., 2013), nanocups (He et al., 2012), nanocages (Xia et al., 2011), and nanostars (Zhang et al., 2019), have been synthesized and widely explored for biomedical sensing, imaging, and therapy. As viable alternatives, GNSs with sharp spikes on the surface have emerged and attracted the most attention for a higher optical signal enhancement, owing to their sharp tips drastically enhancing an intense nanoantenna effect (de Silva Indrasekara et al., 2018). This feature leads to a high LSPR effect and strong adsorption for PTT. Currently, there are some reports on the synthesis of such spiky gold nanostructures (SGNSs), for example, peptide-modulated (Yuan et al., 2012; Yan et al., 2018) or seed-mediated (Sanchez-Gaytan and Park, 2010; de Silva Indrasekara et al., 2018) growth of SGNSs. However, these approaches are either tedious, complicated, or uncontrollable with low quality of spikes. Moreover, SGNSs synthesized by these methods do not exhibit full spectrum absorbance, although they are highly desired for photo-based therapy of ablating tumors.

In the current study, we report a novel, facile, scalable strategy for one-pot synthesis of uniform chestnut-like GNSs densely populated with sharp spikes on the surface (SGNCs). The SGNCs were obtained through facile reduction of a gold precursor (an aqueous solution of $HAuCl_4$) by 2-ethoxyaniline (EOA) at an oil/water interface to modulate the highly branched growth of GNSs (**Figure 1a**). The prepared SGNCs show strong absorption, from the UV to the NIR region (400–1000 nm) instead of mono- or bimodal absorption for traditional gold nanoparticles (GNPs), which is due to the dense surface coverage of spikes with varying diameters and lengths. Furthermore, the SGNCs exhibited excellent PTT effect, *in vitro* and *in vivo*, which can efficiently ablate tumors under the irradiation of an 808-nm laser. Thus, SGNCs have a great potential as an excellent PTT agent for tumor treatment.

EXPERIMENT

Materials

2-Ethoxyaniline, gold (III) chloride hydrate ($HAuCl_4$, 99.99%), and cyclohexane were purchased from Sigma-Aldrich and used as received. Dulbecco's modified Eagle's medium (DMEM), 2-(4-Amidinophenyl)-6-indolecarbamidine dihydrochloride (DAPI), and fluoresceinamine isomer I were obtained from Sigma-Aldrich. Fetal bovine serum (FBS), dimethyl sulfoxide (DMSO), trypsin-EDTA, and penicillin/streptomycin (5000 U ml) were purchased from Thermo Fisher Scientific.

Characterization

The SGNCs were imaged using a scanning electron microscope (SEM, S-4800) and a transmission electron microscope (TEM, JEM-2100F). The images of thermal results were recorded by an SC300 infrared camera (FLIR, VA, United States) and analyzed with IR images software (FL-IR).

Synthesis of SGNCs

In a typical synthesis, 2.04 mg of $HAuCl_4$ (6 μmol) was slowly dissolved in 5 ml of deionized water. Subsequently, 0.5 ml of an EOA cyclohexane solution (30 mM) was added dropwise to the above aqueous solution. The mixture was then treated with ultrasound. The SGNCs were collected by centrifugation and washed three times with deionized water. Then, the SGNCs were dispersed in DMF overnight. The SGNCs were further washed five times. Then, SH-PEG was mixed with the SGNCs overnight and then the PEG-modified SGNCs were collected by centrifugation.

Synthesis of GNPs

To prepare GNPs, 1 ml of a 20 mg/ml $HAuCl_4$ solution was injected into 500 ml of boiling water containing citrate under stirring, and then 3 ml of 10 mg/ml sodium citrate was added into the above solution. The temperature of solution was decreased to 85°C, after refluxing for 40 min. Furthermore, 1 ml of 20 mg/ml $HAuCl_4$ solution and 3 ml of 10 mg/ml sodium citrate solution was added to the above solution. Finally, GNPs were obtained by centrifugation and washing.

Photothermal Performances *in vitro*

The solutions of SGNCs and GNPs at a concentration of 300 μg/ml were irradiated with an 808-nm laser (1.0 W/cm^2). The temperature of the solutions was recorded by an infrared camera (FLIR, VA, United States). To estimate the cell mortality rate under laser irradiation, the MTT assay was used to evaluate it. U87MG cells were seeded in 96-well plates, and then these cells were incubated overnight at 37°C. Further, cells were rinsed with PBS solution (pH 7.4); the cells were incubated under different concentrations of SGNCs and GNPs for 4 h at 37°C under the same conditions. Then, PBS was used to rinse cells a second time and injected in 200 μl of new culture medium after being irradiated using an 808-nm laser with ∼1 W/cm^2 for 5 min. After the irradiation, cells were incubated for another 24 h in an incubator at 37°C. Procedures for the control group were identical to the experimental group except for the irradiation. To further identify the cell viability, Calcein AM and ethidium homodimer-1 were used to stain the cells to distinguish live (showing green) and dead (showing red) cells.

In vivo Photothermal Ablation and Therapy for Tumors

The mice for *in vivo* experiments were conducted following the protocols of the Shanghai Committee for the Accreditation of Laboratory Animal. All processes have been approved by the Shanghai Science and Technology Commission (Laboratory Animal Use Permit Number: SYXK2019-0005; Shanghai, China). All operations were performed after sodium pentobarbital anesthesia with all efforts made to minimize the suffering of mice.

When the tumor reached a size of ∼6 mm, the U87MG tumor-bearing mice were randomly divided into three groups (four mice per group): group I: Control, group II: GNPs, and group III: SGNCs. For group II and group III, GNPs and SGNCs with a dose of 5 mg/kg were i.t., injected. Mice in the control group

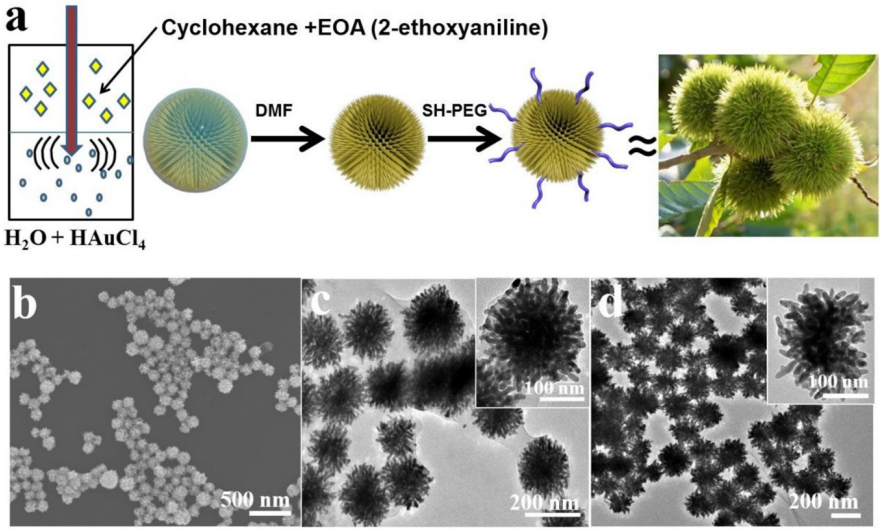

FIGURE 1 | (a) Schematic illustration for the synthesis of SGNCs. **(b)** SEM images of prepared SGNCs from EOA. **(c,d)** TEM images of SGNCs before and after washed by DMF.

were did not receive treatment. Mice in groups II and III were then irradiated by an 808-nm laser at a power density of 1 W/cm^2 for 8 min, and an infrared camera was applied to monitor the temperature changes. The mouse weights and tumor sizes were measured after treatment every 2 days for 14 days. At day 14, mice were all killed, and the major organs were isolated for slides. The slides were stained with hematoxylin/eosin and then observed with a microscope.

RESULTS AND DISCUSSION

The SGNCs were obtained by an aqueous solution of Au precursor ($HAuCl_4$) mixed with a solution of EOA in cyclohexane under moderate sonication. The redox reaction between Au^{3+} and EOA led to the concurrent polymerization of EOA into spherical poly(EOA) NPs and the formation of uniform SGNCs on the surface of poly(EOA) (**Figures 1b–d**). Over time, the resulting SGNCs detached from the poly(EOA) NPs, leaving a thin layer of poly(EOA) on the SGNC surface (**Figure 1c**). The poly(EOA) layer can be washed away using dimethylformamide (DMF), which is a good solvent for poly(EOA) (**Figure 1d**). The surface of the SGNCs is densely populated with sharp spikes with average widths and lengths of ∼12 nm and ∼40 nm, respectively (**Figures 1b,c**). The average particle size was measured to be ∼190 nm (**Supplementary Figure 1**). The surface of the SGNCs was subsequently modified with polyethylene glycol (PEG) to improve their biocompatibility in biological applications.

To understand the growth mechanism of spikes, we evaluated the time-dependent formation of SGNCs using TEM imaging and UV–vis spectroscopic analysis. As shown in **Figures 2a–d**, immediately after mixing the reactant solutions, bits of tiny spherical GNPs (∼10 nm in diameter) were rapidly formed on the surface of poly(EOA) NPs (∼60 nm in diameter). Approximately 5 min after mixing, many small GNPs presented on the surface of the polymer spheres, and the diameter of polymer spheres increased from 50 to 70 nm, suggesting the further reduction of Au^{3+} to Au^0 by EOA. The Au deposition continued, spiky gold thorn gradually grew on the poly(EOA) particles, while the smaller GNPs disappeared after 5 h. We presume that a ripening process occurred, leading to the dissolution of the small GNPs and re-deposition on a few seed GNPs immobilized on the polymer particles. The reaction was completed in ∼5 h to form a final product of SGNCs of ∼190 nm. UV–vis spectra at the corresponding time points show a gradual increase in the NIR absorption of the nanostructures as the reaction proceeded (**Figures 2e,f**). At the first stage of preparation of SGNCs, there are bits of GNPs in the poly(EOA) NPs; the absorption peak of ∼530 nm is due to the longitudinal LSPR properties of GNPs. With the growth of the GNPs, the LSPR peaks shifted to red and became broader due to plasmonic coupling between particles (Hu et al., 2006). Finally, when the SGNCs were prepared, the obvious longitudinal peak vanished and formed a broad bandwidth, which could be attributed to the increasing number of branches and lengths of GNSs (Cheng et al., 2012; de Silva Indrasekara et al., 2018). Thus, we deduce the preparation mechanism of SGNCs as in **Figure 2g**.

We further assessed the potential use of SGNCs as theranostic agents in PTT and thermal imaging. As shown in **Figure 3A**, SGNCs exhibited a significantly higher absorption in the NIR window (e.g., 808 nm) when compared with GNPs at the same concentration of Au element. To further investigate the photothermal performances of the SGNCs and GNPs, the dispersions of SGNCs and GNPs at a concentration of 300 μg/ml and pure water were irradiated under an 808-nm laser with an energy density of 1 W/cm^2. The temperature of the pure water had an insignificant rise, and a small increase (less than

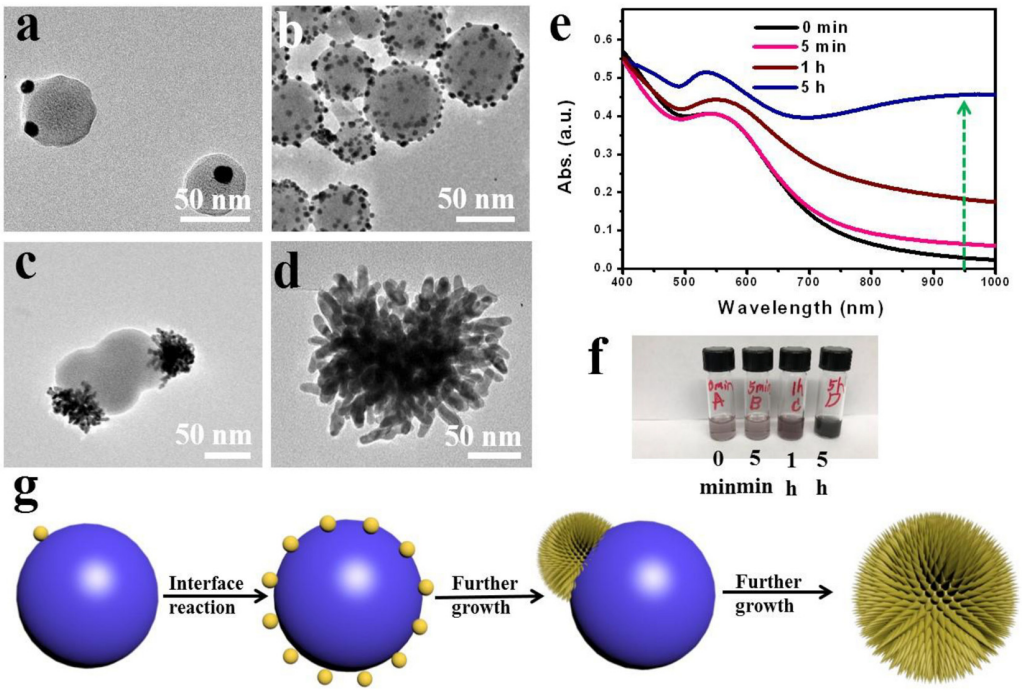

FIGURE 2 | Time-dependent growth of SGNCs. **(a–d)** TEM images of SGNCs obtained in the same reaction proceeded for 0 min **(a)**, 15 min **(b)**, 60 min **(c)**, and 5 h **(d)**, respectively. **(e,f)** The UV–vis spectra and digital picture of SGNCs in water at various reaction times: 0, 5, 60 min, and 5 h. **(g)** The mechanism of preparing SGNCs.

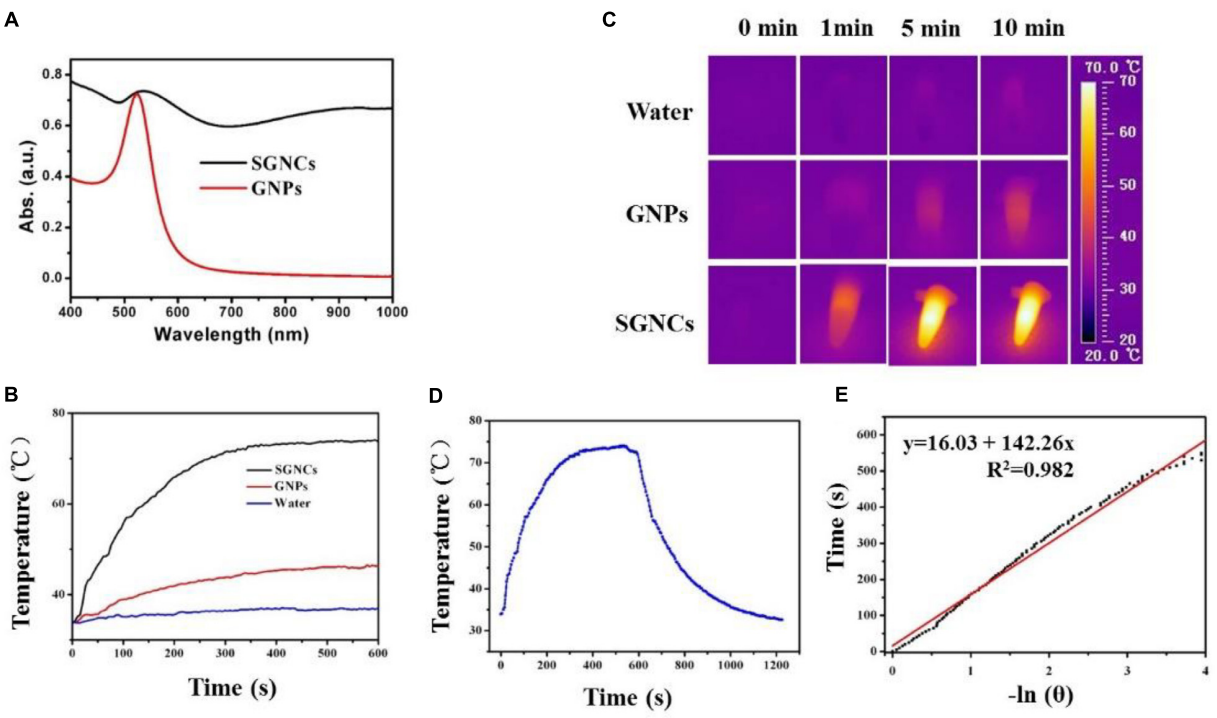

FIGURE 3 | (A) UV–vis-NIR absorbance spectra of GNPs and SGNCs. The temperature elevation **(B)** and thermal images **(C)** of water, GNPs, and SGNCs at a concentration of 300 μg/ml with time under the irradiation of an 808-nm laser with a power density of 1 W/cm^2. **(D)** The temperature change with irradiation for 10 min and nature cooling process. **(E)** Graph for negative natural logarithm versus cooling process to calculate the photothermal conversion efficiency (η).

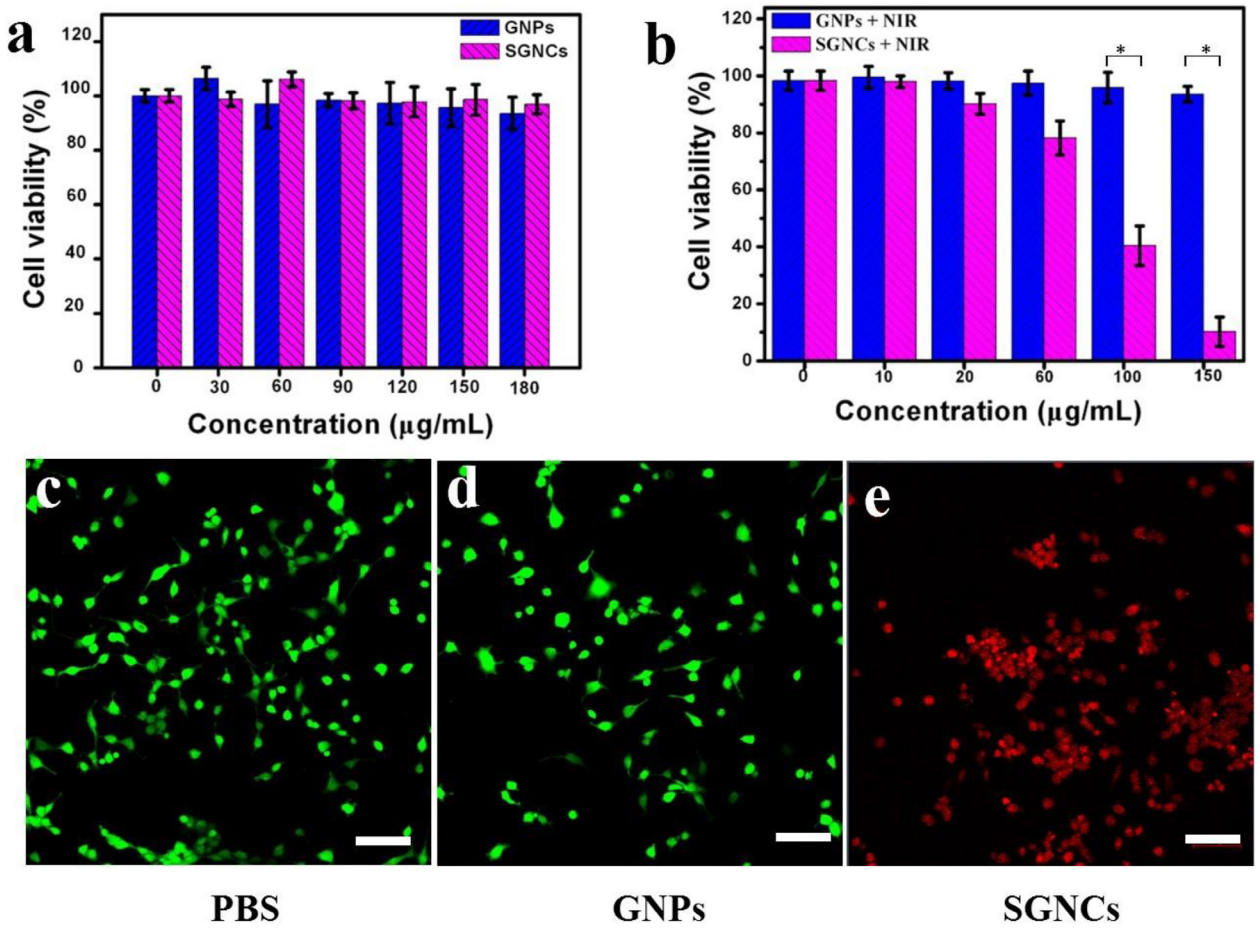

FIGURE 4 | In vitro cytotoxicity of GNPs and SGNCs to U87MG cells after incubation for 12 h **(a)** with no laser and **(b)** with laser irradiation. **(c)** Laser only and **(d,e)** incubation with GNPs and SGNCs and then irradiation with an 808-nm laser (1 W/cm^2 for 5 min) at a concentration of 150 μg/ml. Scale bar: 100 μm.

10°C) in temperature was observed for the GNP dispersion, while SGNC dispersion increased to 73.8°C within 600 s (**Figure 3B**). Owing to the enhanced LSPR adsorption, the temperature of SGNCs exhibited an approximately three-fold increase compared to that of GNPs. The higher photothermal effect of SGNCs than GNPs was visually observed by thermal images (**Figure 3C**). The photothermal conversion efficiency of the SGNCs was determined according to the previous method (Tian et al., 2011; Liu et al., 2014): $\eta = \frac{hs(T_{max}-T_{surr})-Q_{Dis}}{I(1-10^{-A808})}$.

After the temperature of the dispersion reached a steady state, the laser was turned off and the temperature variation was recorded (**Figure 3D**). The maximum steady temperature (T_{max}) minus environmental temperature (T_{Surr}) of the solution of the SGNCs was 41.5°C. The slope of the linear fitting curve acquired from the cooling process was used to calculate the τ_s (**Figure 3E**). The equation is $t = -\tau_s \ln[(T - T_{Surr})/(T_{max} - T_{Surr})]$. Then, the equation of $hs = (m_D C_D)/\tau_s$ was used to calculate the *hs*. Finally, the 808-nm laser heat conversion efficiency (η) of the SGNCs is calculated to be 52.9%, which is much higher than traditional photothermal agents, such as gold stars (40.1%) (Yu et al., 2020), gold nanorods (23.7%) (Tian et al., 2011), CuS (38.0%) (Liu et al., 2014), and Bi nanodots (30%) (Lei et al., 2017). Recent photothermal agents, such as FeCo@C-PEG nanoparticles (Song et al., 2020), Nano(O-Nonacene)-PEG (Yin et al., 2019), and upconverting covalent organic framework (COF) (Wang P. et al., 2020), are all ingeniously designed for PTT. However, the presented densely spiky gold nano-chestnuts are simply designed and showed excellent PTT effect for tumors. The SGNCs exhibit higher photothermal conversion efficiency (η) than other photothermal agents, which could be attributed to the strong spectral adsorption bandwidth in the NIR region. The SGNCs with dense SGNSs enhance the electromagnetic field for the tips of the branched particles, which leads to strong LSPR adsorption (Cheng et al., 2012; de Silva Indrasekara et al., 2018). These results showed that the SGNCs can be used as an excellent PTT agent.

The cytotoxicity of SGNCs and their performance in PTT of tumor cells were evaluated in vitro using U87MG cells. As illustrated in **Figure 4a**, the cell viability remained relatively high after incubation with GNPs or SGNCs with a concentration as high as 180 μg/ml, indicating good biocompatibility. The viability of cells incubated with Au nanostructures and exposed

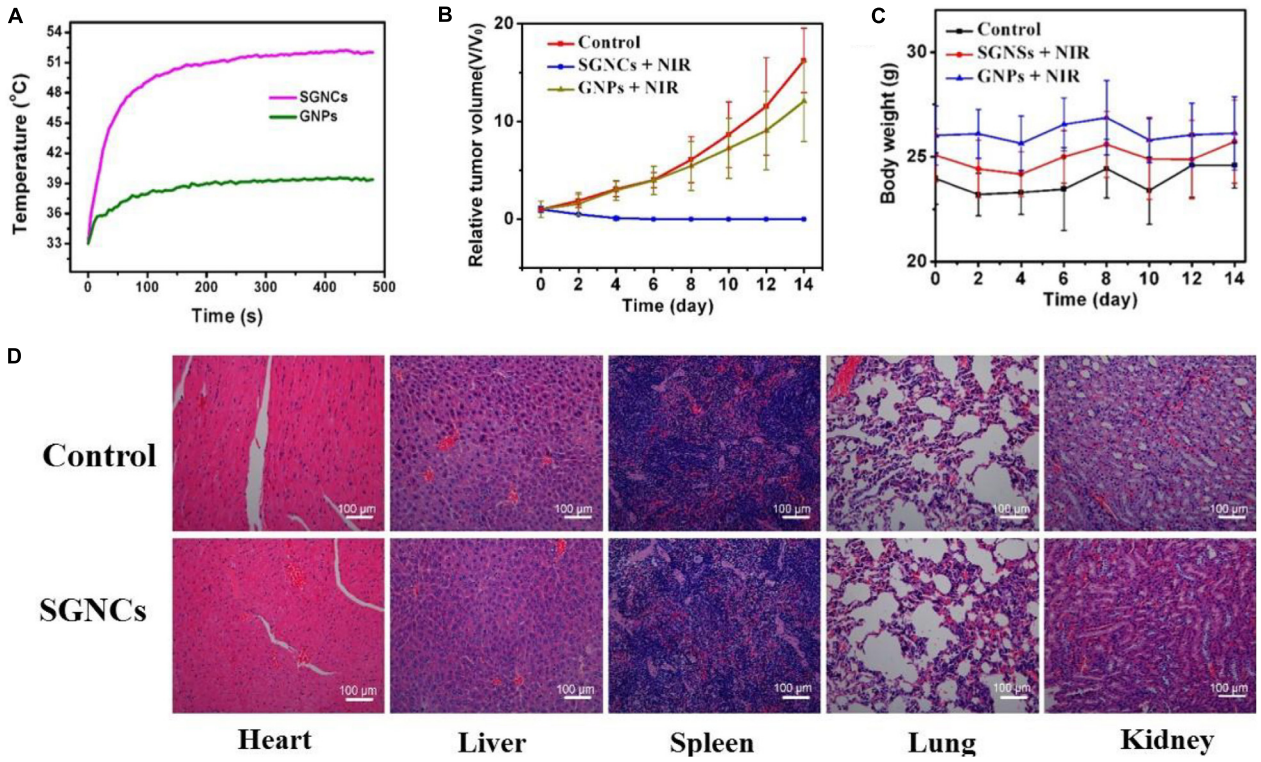

FIGURE 5 | (A) The U87MG tumor-bearing mice of the GNP and SGNC group were irradiated with NIR laser for 8 min. The volume change of tumors **(B)** as well as the body weight **(C)** of the tumor-bearing mice were measured every 2 days in different groups. **(D)** H&E-stained pictures of organs (heart, liver, spleen, lung, and kidney) of control group and SGNC group mice, showing no organ damage evidence contrast with the control group and the SGNC group.

to an 808-nm laser was further investigated using the MTT assay (**Figure 4b**). The cell viability of the GNP-treated groups showed no obvious divergence from control groups even at concentrations of ∼150 μg/ml. In contrast, the SGNC-treated group showed a significant reduction in cell viability with increasing SGNC concentration upon laser irritation. The PTT of tumor cells was further confirmed by staining living cells of the aforementioned groups (**Figures 4c–e**). Most of the cells were killed by the SGNC-treated group due to the excellent photothermal effect. Nevertheless, tumor cells' death was not significant in the GNP-treated groups and the control group. GNPs serve as robust PTT agents toward tumor therapy, which might trigger cancer cell death by a programmed apoptosis with the activation of the caspase-3 pathway (Ali et al., 2016; Wang et al., 2018).

The mice were separated into three groups casually (four mice for each group) to elevate the PTT effect. The mice in the control group received no treatment. The mice in the GNP and SGNC groups were intravenously injected with 100 μl of 5 mg/kg GNPs and 100 μl of 5 mg/kg SGNCs, respectively. Then, the GNP and SGNC groups were irradiated with NIR laser for 8 min at the tumor site. For the SGNC group, the tumor temperature rapidly reached 50°C, which is high enough to irreversibly kill the tumor cells. While the tumor temperature of the GNP group only increased to below 45°C (**Figure 5A**), which is not enough to kill tumor cells (Liu et al., 2020). After NIR irradiation, the volume change of tumors along with the body weight of the tumor-bearing mice were measured every 2 days. We found that the SGNC group obviously inhibited the growth of tumor cells, even completely ablating the tumor (**Supplementary Figure 2**), while tumor growth had no obvious difference between the GNP group and the control group (**Figure 5B**). Moreover, mice in the SGNC and GNP groups had no significant weight loss during treatment, implying negligible systemic toxicity of nanomaterials (**Figure 5C**). Furthermore, the pictures of organs' H&E stain show that tissue structure and cells had no obvious difference between the SGNC and the PBS group (**Figure 5D**), further proving the safety of SGNC treatment.

CONCLUSION

In summary, we have developed a novel facile approach for the preparation of SGNCs with high density of spikes and full-spectrum absorption and explored its controllable preparation mechanism. The SGNCs had a photothermal conversion efficiency as high as 52.9%. Moreover, the SGNCs could completely ablate the tumors under NIR irradiation of the 808-nm laser, showing better performance than GNPs due to the high density of spike structure. Therefore, SGNCs can serve as good PT agents for tumor therapy.

DATA AVAILABILITY STATEMENT

The original contributions presented in the study are included in the article/**Supplementary Material**, further inquiries can be directed to the corresponding author/s.

ETHICS STATEMENT

The animal study was reviewed and approved by Shanghai Committee for the Accreditation of Laboratory Animal; Shanghai Science and Technology Commission (The Laboratory Animal Use Permit Number: SYXK2019-0005' Shanghai, China).

AUTHOR CONTRIBUTIONS

ZW: data curation, and writing – original draft preparation. JG: conceptualization and investigation. YW: visualization. JQ: methodology. JZ: software. FC: investigation. HW: writing – reviewing. HC: supervision. CL: supervision and editing. All authors reviewed the manuscript.

FUNDING

This study was funded by the Shanghai Natural Science Foundation (Grant No. 18ZR1434500), the Shanghai Natural Science Foundation (Grant No. 19ZR1448900), and the Scientific Research Initial Funding of Shanghai Tongji Hospital (Grant No. RCQD1704).

SUPPLEMENTARY MATERIAL

The Supplementary Material for this article can be found online at: https://www.frontiersin.org/articles/10.3389/fbioe.2020.599040/full#supplementary-material

REFERENCES

Ali, M. R. K., Ali, H. R., Rankin, C. R., and El-Sayed, M. A. (2016). Targeting heat shock protein 70 using gold nanorods enhances cancer cell apoptosis in low dose plasmonic photothermal therapy. *Biomaterials* 102, 1–8. doi: 10.1016/j.biomaterials.2016.06.017

An, L., Wang, Y., Tian, Q., and Yang, S. (2017). Small gold nanorods: recent advances in synthesis. *Biol. Imaging Cancer Ther. Mater.* 10:1372. doi: 10.3390/ma10121372

Cao, J., Sun, T., and Grattan, K. T. V. (2014). Gold nanorod-based localized surface plasmon resonance biosensors: a review. *Sens. Actuator B* 195, 332–351. doi: 10.1016/j.snb.2014.01.056

Cheng, L.-C., Huang, J.-H., Chen, H. M., Lai, T.-C., Yang, K.-Y., Liu, R.-S., et al. (2012). Seedless, silver-induced synthesis of star-shaped gold/silver bimetallic nanoparticles as high efficiency photothermal therapy reagent. *J. Mater. Chem.* 22, 2244–2253. doi: 10.1039/c1jm13937a

D'Acunto, M. (2018). Detection of intracellular gold nanoparticles: an overview. *Materials* 11:882. doi: 10.3390/ma11060882

de Silva Indrasekara, A. S., Johnson, S. F., Odion, R. A., and Vo-Dinh, T. (2018). Manipulation of the geometry and modulation of the optical response of surfactant-free gold nanostars: a systematic bottom-up synthesis. *Acs Omega* 3, 2202–2210. doi: 10.1021/acsomega.7b01700

Fernandes, N., Rodrigues, C. F., Moreira, A. F., and Correia, I. J. (2020). Overview of the application of inorganic nanomaterials in cancer photothermal therapy. *Biomater. Sci.* 8, 2990–3020. doi: 10.1039/d0bm00222d

Furube, A., and Hashimoto, S. (2017). Insight into plasmonic hot-electron transfer and plasmon molecular drive: new dimensions in energy conversion and nanofabrication. *NPG Asia Mater.* 9:454.

He, J., Zhang, P., Gong, J., and Nie, Z. (2012). Facile synthesis of functional Au nanopatches and nanocups. *Chem. Commun.* 48, 7344–7346. doi: 10.1039/c2cc32070c

Hu, M., Chen, J., Li, Z.-Y., Au, L., Hartland, G. V., Li, X., et al. (2006). Gold nanostructures: engineering their plasmonic properties for biomedical applications. *Chem. Soc. Rev.* 35, 1084-1094.

Huang, X., Zhang, W., Guan, G., Song, G., Zou, R., and Hu, J. (2017). Design and functionalization of the NIR-responsive photothermal semiconductor nanomaterials for cancer theranostics. *Acc. Chem. Res.* 50, 2529–2538. doi: 10.1021/acs.accounts.7b00294

Kong, W., Wang, Q., Deng, G., Zhao, H., Zhao, L., Lu, J., et al. (2020). Se@SiO2@Au-PEG/DOX NCs as a multifunctional theranostic agent efficiently protect normal cells from oxidative damage during photothermal therapy. *Dalton Trans.* 49, 2209–2217. doi: 10.1039/c9dt04867g

Lei, P., An, R., Zhang, P., Yao, S., Song, S., Dong, L., et al. (2017). Ultrafast synthesis of ultrasmall Poly(Vinylpyrrolidone)-protected bismuth nanodots as a multifunctional theranostic agent for in vivo dual-modal CT/photothermal-imaging-guided photothermal therapy. *Adv. Funct. Mater.* 27:1702018. doi: 10.1002/adfm.201702018

Liu, X., Li, B., Fu, F., Xu, K., Zou, R., Wang, Q., et al. (2014). Facile synthesis of biocompatible cysteine-coated CuS nanoparticles with high photothermal conversion efficiency for cancer therapy. *Dalton Trans.* 43, 11709–11715. doi: 10.1039/c4dt00424h

Liu, X., Zhang, M., Yan, D., Deng, G., Wang, Q., Li, C., et al. (2020). A smart theranostic agent based on Fe-HPPy@Au/DOX for CT imaging and PTT/chemotherapy/CDT combined anticancer therapy. *Biomater. Sci.* 8, 4067–4072. doi: 10.1039/d0bm00623h

Liu, Y., Bhattarai, P., Dai, Z., and Chen, X. (2019). Photothermal therapy and photoacoustic imaging via nanotheranostics in fighting cancer. *Chem. Soc. Rev.* 48, 2053–2108. doi: 10.1039/c8cs00618k

Norouzi, H., Khoshgard, K., and Akbarzadeh, F. (2018). In vitro outlook of gold nanoparticles in photo-thermal therapy: a literature review. *Lasers Med. Sci.* 33, 917–926. doi: 10.1007/s10103-018-2467-z

Ren, Q.-Q., Bai, L.-Y., Zhang, X.-S., Ma, Z.-Y., Liu, B., Zhao, Y.-D., et al. (2015). Preparation, modification, and application of hollow gold nanospheres. *J. Nanomater.* 2015, 1-7.

Sanchez-Gaytan, B. L., and Park, S.-J. (2010). Spiky gold nanoshells. *Langmuir* 26, 19170–19174. doi: 10.1021/la1038969

Song, G., Kenney, M., Chen, Y. S., Zheng, X., Deng, Y., Chen, Z., et al. (2020). Carbon-coated FeCo nanoparticles as sensitive magnetic-particle-imaging tracers with photothermal and magnetothermal properties. *Nat. Biomed. Eng.* 4, 325–334. doi: 10.1038/s41551-019-0506-0

Tabish, T. A., Dey, P., Mosca, S., Salimi, M., Palombo, F., Matousek, P., et al. (2020). Smart gold nanostructures for light mediated cancer theranostics: combining optical diagnostics with photothermal therapy. *Adv. Sci.* 7:1903441. doi: 10.1002/advs.201903441

Tian, Q., Jiang, F., Zou, R., Liu, Q., Chen, Z., Zhu, M., et al. (2011). Hydrophilic Cu9S5 nanocrystals: a photothermal agent with a 25.7% heat conversion efficiency for photothermal ablation of cancer cells in vivo. *ACS Nano* 5, 9761–9771. doi: 10.1021/nn203293t

Wang, J., Zhou, Z., Zhang, F., Xu, H., Chen, W., and Jiang, T. (2018). A novel nanocomposite based on fluorescent turn-on gold nanostars for near-infrared photothermal therapy and self-theranostic caspase-3 imaging of glioblastoma tumor cell. *Colloids Surf. B Biointerfaces* 170, 303–311. doi: 10.1016/j.colsurfb.2018.06.021

Wang, P., Zhou, F., Guan, K., Wang, Y., Fu, X., Yang, Y., et al. (2020). In vivo therapeutic response monitoring by a self-reporting upconverting covalent organic framework nanoplatform. *Chem. Sci.* 11, 1299–1306. doi: 10.1039/c9sc04875h

Wang, Y., An, L., Lin, J., Tian, Q., and Yang, S. (2020). A hollow Cu9S8 theranostic nanoplatform based on a combination of increased active sites and photothermal performance in enhanced chemodynamic therapy. *Chem. Eng. J.* 385:123925. doi: 10.1016/j.cej.2019.123925

Xia, Y., Li, W., Cobley, C. M., Chen, J., Xia, X., Zhang, Q., et al. (2011). Gold nanocages: from synthesis to theranostic applications. *Acc. Chem. Res.* 44, 914–924. doi: 10.1021/ar200061q

Xu, C., Zhang, T., Lu, G., Chen, K., Tao, J., Zhang, Y., et al. (2020). Disulfiram-gold-nanorod integrate for effective tumor targeting and photothermal-chemical synergistic therapy. *Biomater. Sci.* 8, 3310–3319. doi: 10.1039/d0bm00062k

Xuan, M., Shao, J., Dai, L., Li, J., and He, Q. (2016). Macrophage cell membrane camouflaged au nanoshells for in vivo prolonged circulation life and enhanced cancer photothermal therapy. *ACS Appl. Mater. Interf.* 8, 9610–9618. doi: 10.1021/acsami.6b00853

Yan, F., Liu, L., Walsh, T. R., Gong, Y., El-Khoury, P. Z., Zhang, Y., et al. (2018). Controlled synthesis of highly-branched plasmonic gold nanoparticles through peptoid engineering. *Nat. Commun.* 9, 1–8.

Yang, Y., Chen, M., Wu, Y., Wang, P., Zhao, Y., Zhu, W., et al. (2019). Ultrasound assisted one-step synthesis of Au@Pt dendritic nanoparticles with enhanced NIR absorption for photothermal cancer therapy. *Rsc Adv.* 9, 28541–28547. doi: 10.1039/c9ra04286e

Yin, B., Wang, Y., Zhang, C., Zhao, Y., Wang, Y., Teng, L., et al. (2019). Oxygen-embedded quinoidal acene based semiconducting chromophore nanoprobe for amplified photoacoustic imaging and photothermal therapy. *Anal. Chem.* 91, 15275–15283. doi: 10.1021/acs.analchem.9b04429

Yu, X., Zhong, Y., Sun, Y., and Chen, Y. (2020). Controllable preparation of plasmonic gold nanostars for enhanced photothermal and SERS effects. *Chem. Res. Chin. Univ.* 137, 10460-10463.

Yuan, H., Fales, A. M., and Vo-Dinh, T. (2012). TAT peptide-functionalized gold nanostars: enhanced intracellular delivery and efficient NIR photothermal therapy using ultralow irradiance. *J. Am. Chem. Soc.* 134, 11358–11361. doi: 10.1021/ja304180y

Zhang, L., Yang, X.-Q., Wei, J.-S., Li, X., Wang, H., and Zhao, Y.-D. (2019). Intelligent gold nanostars for in vivo CT imaging and catalase-enhanced synergistic photodynamic & photothermal tumor therapy. *Theranostics* 9, 5424–5442. doi: 10.7150/thno.33015

Zhang, M., Liu, X., Luo, Q., Wang, Q., Zhao, L., Deng, G., et al. (2020). Tumor environment responsive degradable CuS@mSiO2@MnO2/DOX for MRI guided synergistic chemo-photothermal therapy and chemodynamic therapy. *Chem. Eng. J.* 389:124450. doi: 10.1016/j.cej.2020.124450

Zhang, P., He, J., Ma, X., Gong, J., and Nie, Z. (2013). Ultrasound assisted interfacial synthesis of gold nanocones. *Chem. Commun.* 49, 987–989. doi: 10.1039/c2cc37713f

Conflict of Interest: The authors declare that the research was conducted in the absence of any commercial or financial relationships that could be construed as a potential conflict of interest.

frontiers in Bioengineering and Biotechnology

ORIGINAL RESEARCH
published: 19 November 2020
doi: 10.3389/fbioe.2020.590518

$CuGeO_3$ Nanoparticles: An Efficient Photothermal Theragnosis Agent for CT Imaging-Guided Photothermal Therapy of Cancers

Jiawu Wang[1] *and Chengyao Zhang*[2]*

[1] *Department of Urology, The Second Affiliated Hospital of Chongqing Medical University, Chongqing, China,* [2] *Department of Head and Neck Cancer Center, Chongqing University Cancer Hospital & Chongqing Cancer Institute & Chongqing Cancer Hospital, Chongqing, China*

OPEN ACCESS

Edited by:
Bo Li,
Shanghai Jiao Tong University School of Medicine, China

Reviewed by:
Jichun Liu,
Jianghuai Military Region Rear Hospital, China
Yong Gao,
The First Affiliated Hospital of Bengbu Medical College, China

***Correspondence:**
Chengyao Zhang
cczhangcy@163.com

Specialty section:
This article was submitted to Biomaterials, a section of the journal Frontiers in Bioengineering and Biotechnology

Received: *01 August 2020*
Accepted: *11 September 2020*
Published: *19 November 2020*

Citation:
Wang J and Zhang C (2020) $CuGeO_3$ Nanoparticles: An Efficient Photothermal Theragnosis Agent for CT Imaging-Guided Photothermal Therapy of Cancers. Front. Bioeng. Biotechnol. 8:590518. doi: 10.3389/fbioe.2020.590518

The photothermal agents have been widely developed due to the minimally invasive treatment for targeted tumor photothermal therapy, which is considered to have great potential for antitumor bioapplications. The development of multifunctional photothermal agents is extremely challenging. This work presents a novel photothermal theragnosis agent, i.e., $CuGeO_3$ nanoparticles (CGO NPs), showing intense absorption in the near-infrared (NIR) window and excellent ability of CT imaging. Due to the strong NIR absorption, CGO NPs exhibit excellent photothermal effect with a photothermal conversion efficiency of 59.4%. Moreover, because of the high X-ray attenuation coefficient of germanium, the CGO NPs have a great potential of CT imaging diagnosis in clinical application. Additionally, the CGO NPs show negligible cytotoxicity *in vitro* and *in vivo*, indicating that it can be served as an outstanding contrast and anticancer agent in a biosafe way. Our work opens the way for the development of bimetallic copper-based oxides used in photothermal diagnostic agents for cancer treatment.

Keywords: photothermal theragnosis agent, multifunction, CT imaging, photothermal therapy, $CuGeO_3$ nanoparticles

INTRODUCTION

With the development of medical sciences, the average life expectancy of humans has been significantly improved, but cancer still remains a major threat. Early treatment of cancer, such as complete resection of the positive edge of the tumor, has a negative impact on health. Thus, the development of novel therapeutic methods is of great significance for improving cancer therapy (Lee et al., 2012; Liu et al., 2017). An ideal cancer treatment approach should be with low side effect, non-invasive, and targeting (Li and Pu, 2019). A large number of nanomaterials with low toxicity have been reported to efficiently promote photothermal therapy (PTT) for *in vivo* tumor ablation (Zhang et al., 2020). The interior properties of nanoparticles, including intrinsic optical and electrical properties, can be effective for PTT. The compounds of transition metal elements, which

have a large atomic number and a variety of valences could attribute to strong absorption in the NIR region. Some of them also have a large X-ray attenuation coefficient, such as FeS, WO_x, and Bi_2S_3 (Nam et al., 2019). Compared with metallic photothermal agents such as Au nanostructures (Lee et al., 2019), Ag nanoparticles, and Pt-based nanostructures (Huang et al., 2011), transition-metal nanoparticles possessing intense optical properties that are low cost, and have low cytotoxicity can serve as effective candidates for photothermal therapy of cancers (Chen et al., 2013).

The ternary semiconductor nanomaterials can inherit the performance of the corresponding binary semiconductors (Li et al., 2015, 2017; Wang et al., 2015). A series of studies have reported that ternary nanomaterials based on copper-based chalcogenide photosensitizers [for example, $CuCo_2S_4$ nanocrystals (Zhang et al., 2019), $CuFeS_2$ nanoplates (Ding et al., 2017), or copper bismuth sulfide (Li et al., 2015)] could show several exciting properties such as strong absorption in the NIR region, excellent photothermal effect, and good photothermal stability. For example, copper–bismuth–sulfur nanostructures (such as Cu_3BiS_3) are usually p-type semiconductors. On the one hand, these nanomaterials may have many carrier concentrations due to copper defects and exhibit NIR absorption properties similar to binary copper-based chalcogenides (Li et al., 2015). On the other hand, the copper–bismuth–sulfur nanostructures can be used as efficient CT contrast agents like the Bi_2S_3 nanostructure due to the high X-ray attenuation coefficient of bismuth that has been extensively used for CT imaging (Ai et al., 2011). In theory, ternary copper-based semiconductor nanomaterials can show NIR absorption property and CT imaging ability. $CuGeO_3$ nanoparticles have recently made some progresses in morphology and crystal phase control (Fu et al., 2018; O'Neal et al., 2018), but no $CuGeO_3$ (CGO) nanoparticles with strong near-infrared absorption are synthesized (Bassi et al., 1996), which probably resulted from the low carrier concentration caused by monovalent copper ions (Tian et al., 2011). However, the concentration of the carriers in a semiconductor can be adjusted by doping and crystal defects (Li et al., 2014). These properties make the defect-structured CGO nanoparticles a new type of photothermal diagnostic agent.

In this work, CGO nanoparticles were designed and synthesized as biocompatible agents for photothermal therapy by a facile solvothermal method, which showed a favorable application in photothermal therapy (PTT) due to their small size, good dispersion, strong near-infrared (NIR) absorption, and excellent photothermal effect. In the CGO nanoparticles, the coexistence of different valences of copper ions attributes to the obvious absorption in the NIR region that resulted from the d-d energy band transition of Cu^{2+} (Tian et al., 2011; Li et al., 2015). As we expected, CGO nanoparticles showed an amazing photothermal effect with a photothermal conversion efficiency of 59.4%. $CuGeO_3$ nanoparticles were first used as the photothermal agents for cancer treatment. When CT imaging was combined with photothermal therapy, $CuGeO_3$ nanoparticles could enhance antitumor therapy due to the CT imaging-guided photothermal therapy. In addition, the good biocompatibility performance of Ge and Ge-containing compounds makes it possible to be used as dietary supplements (Gao et al., 2019; Song and Kazarian, 2020).

MATERIALS AND METHODS

Synthesis of CGO Nanoparticles

CGO nanoparticles were synthesized via a simple solvothermal route. Normally, 0.7248 g of $Cu(NO_3)_2{\cdot}3H_2O$ and 0.3139 g of GeO_2 was fully dissolved in dehydrated ethanol (35 ml) with magnetic stirring at room temperature until the mixture solution completely dissolved. After 30 min of stirring, the NaOH solution (2 M, 100 μl) should be gently added into the ethanol dispersion of $Cu(NO_3)_2$ and GeO_2 drop by drop. In this period, the magnetic stirrer should remain stirring for at least 20 min to make sure of a sufficient reaction. Next, the homogeneous solution was transferred into a Teflon-lined autoclave (50 ml in volume). The temperature of the electric oven should be 140°C, and the whole reaction may take 24 h. After the reaction, the Teflon-lined autoclave should cool down to room temperature, and the products were obtained by centrifuge and washing with deionized water. Finally, the as-prepared CGO nanoparticles were redispersed for further modification. In order to improve the compatibility of CGO NPs, 1 mg of PVP was added to the obtained CGO NP solution with a concentration of 1.25 mg/ml as a mixture solution. Similar with previous processes, the resulting solution should be centrifuged and washed twice with ethanol.

Characterization

The transmission electron microscope (TEM) was used to determine the morphology, size, and microstructure of CGO nanoparticles. The UV-vis absorbance performance was determined by a UV-visible-NIR spectrophotometer at room temperature. The crystal structure of the samples was obtained by X-ray powder diffraction (XRD). X-ray photoelectron spectroscopy (XPS) was used for element composition and chemical state analysis in CGO nanoparticles. The concentration of germanium ions was determined by inductively coupled plasma atomic emission spectroscopy (ICP-AES). NIR lasers (808 nm) and an infrared thermal imager were used to obtain the infrared thermal images of dispersions to evaluate the photothermal effects of CGO nanoparticles. The power density of the infrared thermal imager could be adjusted from 0 to 2 W/cm^2. The handheld optical power meter was used to calibrate the output power of the lasers independently.

Photothermal Effect

The photothermal performance of the CGO nanoparticles has been measured by laser irradiation experiment. The gradient concentrations of CGO nanoparticle aqueous dispersion were irradiated under an 808 nm laser (0.5 W cm^{-2}) for 5 min. The infrared thermal camera was used to monitor and record the temperature change in CGO nanoparticle dispersion.

In order to calculate the photothermal conversion efficiency (η) of CGO nanoparticles, we dispersed the CGO nanoparticles into deionized water, which was exposed to an 808 nm NIR laser (0.5 W cm^{-2}, 5 min). The temperature curve during laser on and

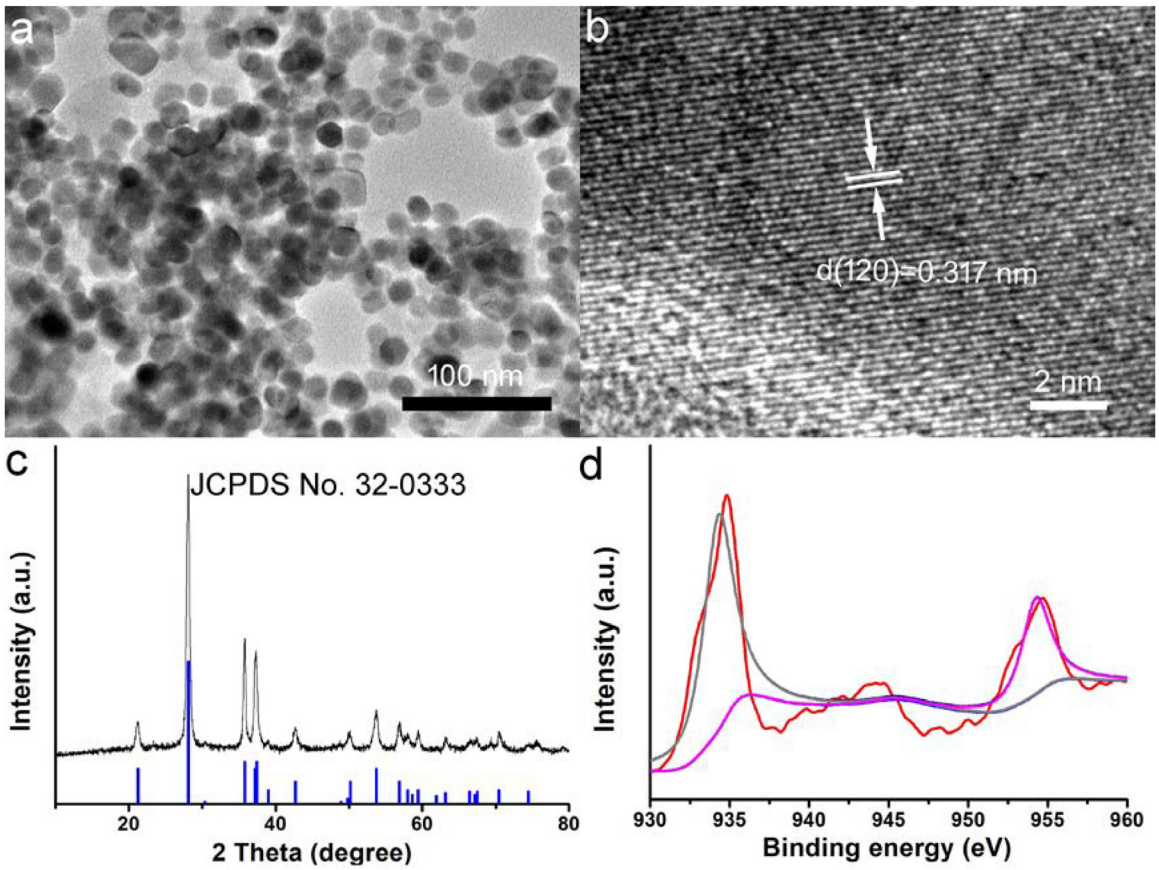

FIGURE 1 | (a) Transmission electron microscope (TEM) image of as-prepared $CuGeO_3$ nanoparticles (CGO NPs). **(b)** CGO NP microstructure under a high-resolution TEM. **(c)** X-ray powder diffraction (XRD) patterns of synthesized CGO and standard CGO on a JCPDS card (no. 32-0333). **(d)** X-ray photoelectron spectroscopy (XPS) spectrum for copper ion in the CGO nanoparticles.

off was recorded. The photothermal conversion efficiency can be calculated by referring to the following equations:

$$\eta = \frac{hA(\Delta T_{\max} - \Delta T_{\max,\text{water}})}{I(1 - 10^{-A_{808}})} \quad (1)$$

$$\tau_s = \frac{m_D c_D}{hA} \quad (2)$$

where I is the NIR laser power, and A_{808} stands for the absorbance of dispersion at 808 nm. The value of hA can be calculated from Eq. 2 by using the system time constant τ_s with the help of the mass (m_D) and the heat capacity (C_D) of deionized water. $\Delta T_{\max}$ and $\Delta T_{\max,\text{water}}$ are the temperature change in CGO nanoparticle dispersion and pure water.

Cell Culture

The Cell Counting Kit-8 (CCK-8) has been used to evaluate the *in vitro* cytotoxicity of the CGO nanoparticles. CAL-27 cells were seeded into 96-well culture plates with a density of 1.5×10^4 cells per well at 37°C with the presence of 5% CO_2 for 24 h. Then, the various concentrations of the CGO nanoparticles (0–320 ppm) was added to each well and incubated for 24 h. Next, 10 μl of CCK-8 solution was added to each well of the plate for another 2 h incubation. Each sample was measured three times to reduce the sampling error.

Photothermal Therapy *in vivo*

CAL-27 tumor-bearing nude mice were randomly divided into three groups: (a) mice with no treatments (Control); (b) mice injected with PBS injection and then irradiated with 808 nm laser irradiation with power density of 0.5 W/cm^2 (PPS + NIR); (c) mice injected with CGO nanoparticle and then irradiated with 808 nm laser irradiation with power density of 0.5 W/cm^2 (CGO + NIR). After the indicated treatment, the tumor size (~100 mm^3 before treatment) and body weights were measured every 2 days for 2 weeks. The calculation of the tumor volume and the relative tumor volume was determined by V/V_0 (Gao et al., 2019).

CT Imaging

The micro-CT imaging system was used to obtain the CT images of the various concentrations of CGO nanoparticles (0, 0.5, 1.0, 2.0, and 4.0 mg/ml). First, the prepared solution of CGO nanoparticles was directly scanned using a micro-CT imaging

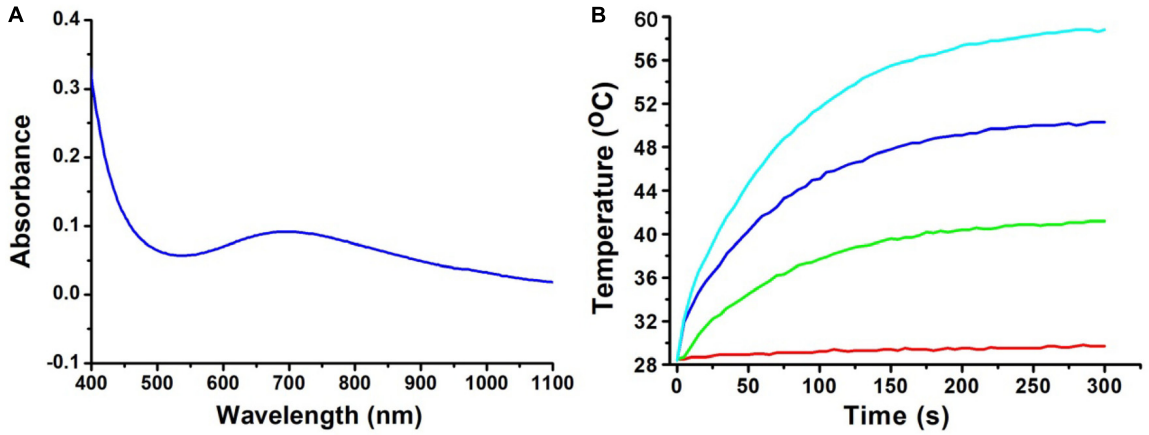

FIGURE 2 | (A) UV-vis absorption spectrum for $CuGeO_3$ NPs with a wide range of 400–1,000 nm. **(B)** Temperature elevation of the $CuGeO_3$ nanoparticle solution with different concentrations under irradiation with an 808 nm laser (0.5 W/cm^2, 300 s).

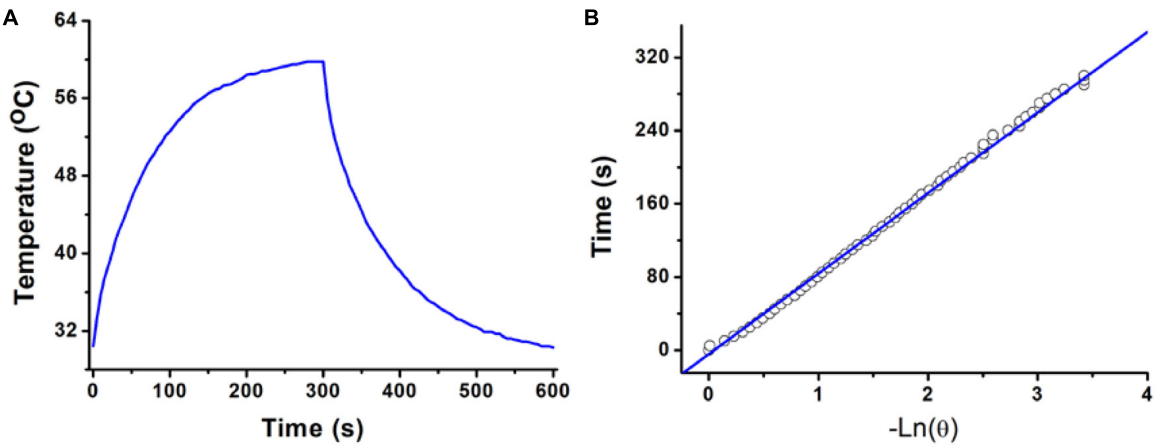

FIGURE 3 | (A) Photothermal effect of a $CuGeO_3$ NP aqueous solution (50 ppm) irradiated under an 808 nm laser with a power density of 0.5 W/cm^2, in which the process lasted for 5 min, and the laser was then shut off after irradiation. **(B)** Time constant for heat transfer from the system, determined to be τ_s = 93.1 s.

system to measure the CT signal of resulting products at 100 kV. The manufacturer-supplied software was used to evaluate the CT values on the same workstation.

All animal experiments were carried out in accordance with the guidelines of the Institutional Animal Care and Use Committee of the Second Affiliated Hospital of Chongqing Medical University. CAL-27 tumor-bearing mice were also divided into two groups: a. intratumoral injection of PBS (100 μl) and b. intratumoral injection of the CGO nanoparticles (4 mg/ml, 100 μl), and the mice were anesthetized before CT scanning. Thirty minutes after injection, CT scanning was performed with parameters similar to those for *in vitro* experiments.

Long-Term Toxicity *in vivo*

H&E analysis was conducted to evaluate the effect of CGO on the main organs (including the heart, liver, lungs, spleen, and kidneys) after the intravenous administration of CGO nanoparticles. The contents of nanocrystals accumulated in the main organs at different time points (i.e., 1, 5, 10, 15 days) were also evaluated to study the biodistribution.

RESULTS AND DISCUSSION

CGO nanoparticles were synthesized by a simple solvothermal method and subsequently modified the surface by PVP. The transmission electron microscopy (TEM) image of CGO nanoparticles is shown in **Figure 1a**. It exhibits that the resulting products have an irregular morphology and dimensions of around 25 nm (**Supplementary Figure S1**). Obviously, the as-prepared CGO nanoparticles was non-aggregated in the TEM image (**Figure 1a**), showing very good dispersion. The small size of CGO nanoparticles can be considered perfect for photothermal agents as the nanoparticles with this size could have relatively long blood circulation. More microstructure information is shown in **Figure 1b** from the high-resolution TEM (HRTEM). The lattice spacing from the HRTEM was determined to be

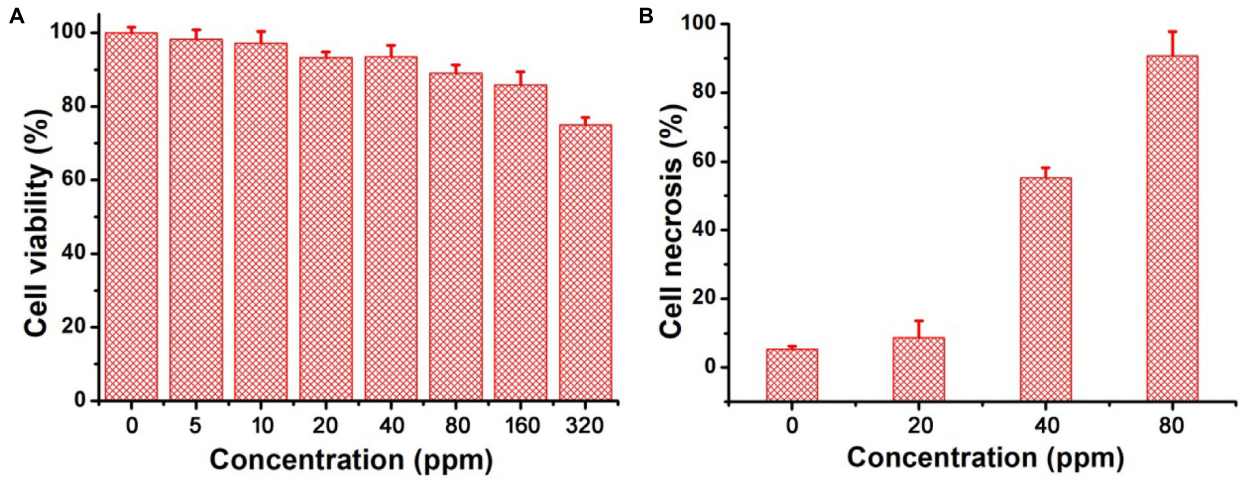

FIGURE 4 | (A) *In vitro* cytotoxicity of CGO nanoparticles on CAL-27 cells. **(B)** Relative cell necrosis of CAL-27 cells after an 808 nm laser irradiating with different concentrations of CGO nanoparticles.

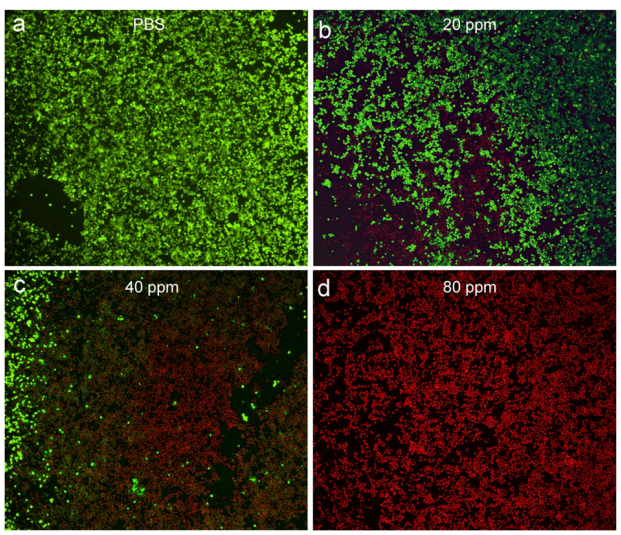

FIGURE 5 | Confocal microscopy images of CAL-27 cells after incubation with various concentrations of CGO nanoparticles for phototherapy: **(a)** PBS, **(b)** 20 ppm, **(c)** 40 ppm, and **(d)** 80 ppm. The CAL-27 cells were costained with propidium iodide (red, dead cells) and calcein-AM (green, live cells). Magnification: 200×.

0.317 nm, assigned to (120) planes of orthorhombic structured $CuGeO_3$. The XRD analysis of the CGO products shown in **Figure 1c** revealed that the obtained products have a high crystallinity for pure CGO because all of the main reflection peaks of CGO nanoparticles can be matched well with the standard cards JCPDS file no. 32-0333, indicating the formation of the orthorhombic structured of $CuGeO_3$. In **Figure 1d**, a high resolution of XPS spectrum for Cu 2p in the CGO nanoparticles was analyzed to verify the existence of non-equivalent valency state of copper ions in CGO NPs. There are three sharp peaks that can be observed in **Figure 1d**. The peaks at 932.7 and 952.6 eV indicated the presence of Cu^{+} in as-prepared $CuGeO_3$ nanoparticles; the peaks at 935.1, 941.6, and 955.2 eV belonged to Cu^{2+} in $CuGeO_3$ nanoparticles (Lv et al., 2016; Suriyawong et al., 2016). The XPS spectrum demonstrated that there was a coexistence of copper ions with different valences in synthesized $CuGeO_3$ nanoparticles, probably resulting in intense NIR absorption due to d-d electron transition. As reported before, the existence of different valency ions in transition metal-based photothermal agents could result in ionized free carriers, thus contributing to NIR absorption (Li et al., 2014).

The optical properties of the CGO nanoparticles were investigated by a UV-vis-NIR spectrophotometer in a range from 400 to 1,000 nm. The spectrum of the CGO nanoparticle aqueous dispersion displayed high absorption in both the visible and near-infrared regions, as shown in **Figure 2A**. The absorbance value was high enough in the NIR region from 600 to 1,100 nm, which showed the typical absorption properties of ternary copper-based compounds (Li et al., 2015; Yuan et al., 2020). By determining the concentration of CGO nanoparticles via ICP-AES, the extinction coefficient of the CGO nanoparticles at 808 nm was measured to be 11.3 L g^{-1} cm^{-1}. We then investigated the photothermal performance of $CuGeO_3$ NPs. The as-prepared CGO NPs with gradient concentrations of 0, 20, 40, 80 ppm were irradiated by an 808 nm laser (0.5 W cm^{-2}) for 5 min. In **Figure 2B**, we can see that the temperature change showed an obvious difference between the CGO nanoparticle aqueous dispersion and pure water in the photothermal effect experiment. The temperature can easily reach to ∼55°C in 5 min, which was high enough to kill tumor cells for CGO nanoparticle aqueous solution with low concentration (80 ppm). However, the temperature of pure water, as a control, remained almost unchanged (less than 2°C). According to a previous report, the reproduction and growth of tumor cells can be suppressed at temperatures of 40–44°C because a high temperature can result in DNA damage, protein denaturation, and disruption of the cellular membrane, leading to eradication of tumor tissues (Nam et al., 2019).

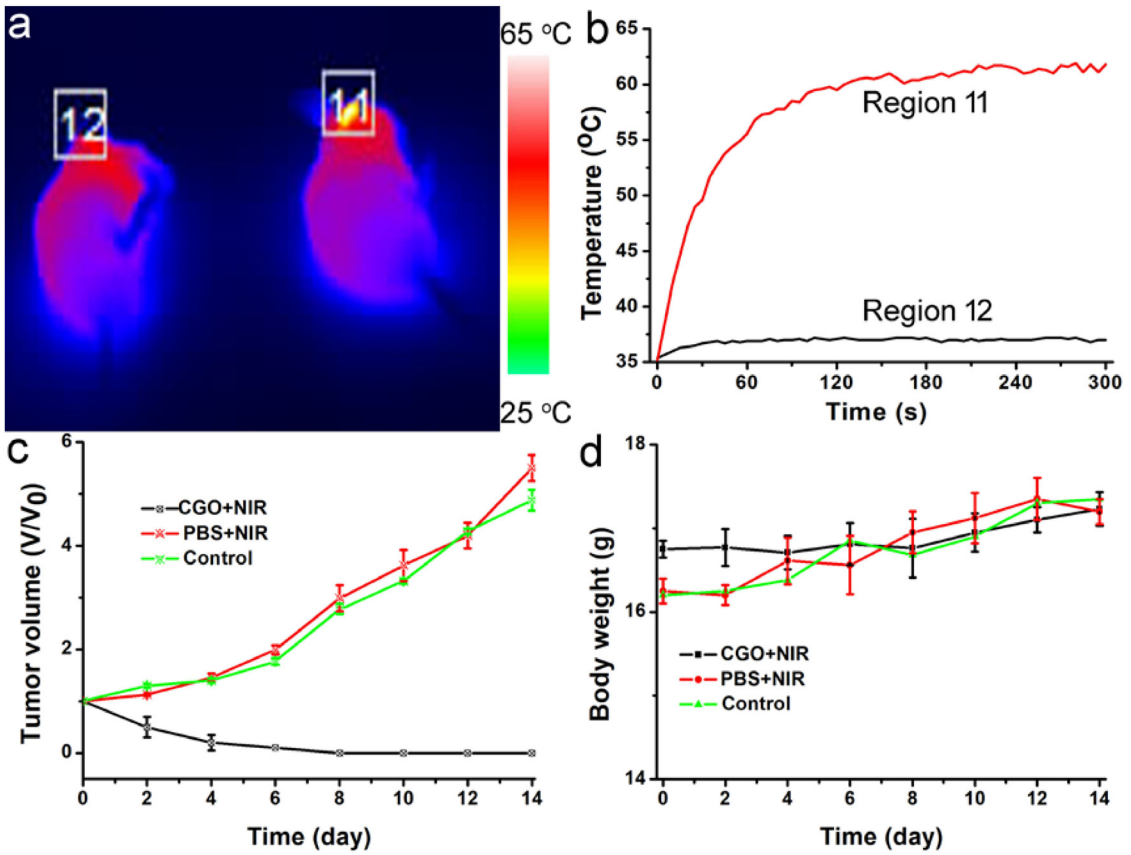

FIGURE 6 | (a) Infrared thermal imaging pictures of mice treated with PBS (left) and CGO nanoparticles (right), then irradiated by 808 nm lasers with a power density of 0.5 W cm^{-2} for 300 s. **(b)** The temperature change curve of a local tumor with different treatments for 5 min. **(c)** Tumor growth curves in each group of mice after treatments. **(d)** Body weight changes in the mice in each group after the treatments.

The photothermal conversion efficiency of copper-based agents has great influences on their photothermal performance. To further explore the optical performance of the CGO nanoparticles, the photothermal conversion efficiency was measured following Tian's report (Tian et al., 2013). With the continuous irradiation of the 808 nm laser (0.5 W/cm^2, 300 s), the temperature change in the solution (80 ppm) was recorded until the temperature reached a steady-state condition (**Figures 3A,B**). Obviously, temperature elevation of the solution (50 ppm) reached to 51.3°C (the highest point) under irradiation for 5 min. The temperature of the solution was decreased to room temperature with time extending after the laser was shut off. Based on the obtained data, the heat conversion efficiency, η, of $CuGeO_3$ NPs driven by an 808 nm laser can reach to about 59.4%. Thus, we supposed that the high photothermal conversion efficiency of these nanoparticles resulted from intense absorbance in the NIR region, which makes it possible for photothermal therapy of cancers.

The excellent photothermal performance of CGO nanoparticles motivated us to further evaluate the potential of these nanoparticles *in vivo*. Prior to the bioapplication, the cytotoxicity *in vitro* of CGO nanoparticles on cells was carried out by a CCK-8 assay. The cell viability remained at a high level (over 85% when the concentration was increased to 160 ppm) after incubation for 24 h (**Figure 4A**), indicating the excellent biocompatibility of CGO nanoparticles. Furthermore, the photothermal therapy effect *in vitro* on CAL-27 cells was evaluated by the combination of CGO nanoparticles and 808 nm lasers. The cell viability after the treatment was investigated by a standard CCK-8 evaluation. Lasers (808 nm) with a power density of 0.5 W cm^{-2} were used to irradiate CAL-27 cells with varied concentrations of CGO nanoparticles. As shown in **Figure 4B**, CGO nanoparticles (80 ppm) that mediated NIR irradiation could induce over 85% cancer cell death at a low power density of irradiation for 10 min (0.8 W/cm^2), indicating the excellent photothermal therapy effect *in vitro*.

After costaining with propidium iodide and calcein-AM, the live/dead staining cells can be obviously observed under the confocal microscopy, which can help to evaluate photothermal effect *in vitro* using CGO nanoparticles due to the distinct chromatic aberration between live (green fluorescence) and dead (red fluorescence) staining cells. PBS buffer can be used as a control experiment. As can be seen in **Figure 5a**, only live cell staining (green) was present in the untreated cells. With the increasing concentration of CGO nanoparticle dispersion, massive cell death occurred as expected (**Figures 5b–d**). The

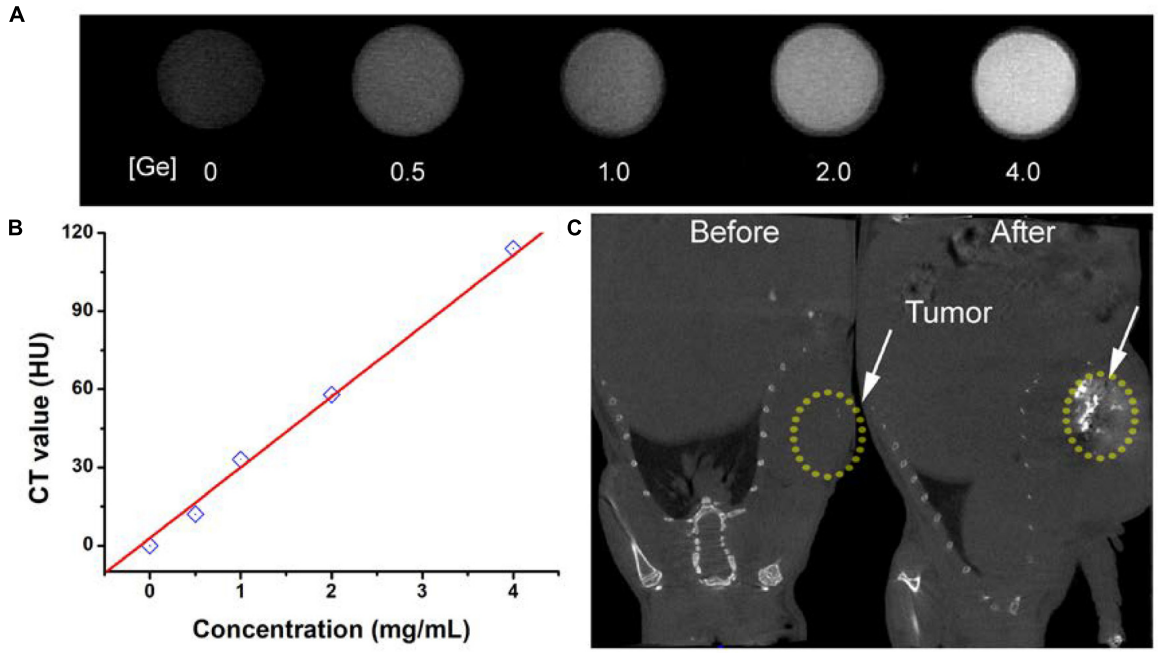

FIGURE 7 | (A) *In vitro* CT images of CGO nanoparticles with different concentrations. **(B)** CT values as a function of the concentrations of CGO nanoparticles. **(C)** CT images *in vivo* of mice before and after the injection of CGO nanoparticles.

cell mortality rate after the treatment could reach to ∼90% (**Figure 5d**), when CGO nanoparticles (80 ppm) was combined with the irradiation of an 808 nm laser, further certifying the efficient photothermal effect *in vitro*.

Photothermal therapy *in vivo* using CGO nanoparticles was then carried out. The mice were randomly divided into three groups: (a) Control group; (b) PBS + 808 nm laser irradiation with power density of 0.5 W/cm^2 (PBS + NIR); (c) CGO nanoparticle injection + 808 nm laser irradiation (CGO + NIR). The temperature change in mice was monitored with a thermal imaging camera during the whole treatment. As expected, the temperature raised rapidly in the experiment group (a), in sharp contrast to group (b) without injection of CGO. As shown in **Figure 6a**, the tumor site in the experiment group (injected with CGO nanoparticles) was much brighter than that of the control group (injected with PBS). That is to say that only mice injected with CGO nanoparticles can contribute to the above fantabulous photothermal effects *in vivo*. Tumor surface temperature curves (**Figure 6b**) revealed that the surface temperature of mice injected with CGO nanoparticles could dramatically increase to about 60°C with the role of an 808 nm laser, while the surface temperature of mice injected with CGO nanoparticles was still kept at room temperature. Then, the relative tumor volumes have been recorded to evaluate the antitumor efficiency for 14 days (**Figure 6c**). The tumor growth significantly disappeared in the mice of group (c) sharply compared to the two other control groups. Evidently, there was no reoccurrence observed in group (c) after 14 days of treatment, which means that the tumor cells of mice have disappeared completely, while continuous tumor development was found in the control groups. The difference in tumor changes after the treatments at the 14th day after treatments (**Supplementary Figure S2**) was matched well with the tumor growth curves in **Figure 6c**. After the treatment, the tumors from the three groups were also analyzed by H&E staining analysis (**Supplementary Figure S3**). Tumor cells in the CGO + NIR group were significantly damaged (nuclear shrinkage and nuclear dissolution), while tumor cells in the control group and the PBS + NIR group showed almost no changes. In addition, the side effect of the photothermal therapy could be evaluated by measuring the body weight change in the mice after the treatment. **Figure 6d** displayed that the body weight among the three groups of mice did not show notable differences, suggesting the limited biotoxicity of CGO at the given conditions.

The early diagnosis of cancer remains a big challenge for antitumors. CT imaging, as a powerful diagnostic tool, has been widely used in clinics. It has been reported that a great deal of metallic elements have been developed as promising CT contrast agents, such as iodine, bismuth, lanthanides, gold, and so on. Germanium, as a typical metallic element, has a relatively high attenuation coefficient; thus, we believe that CGO nanoparticles also have great potential to become a contrast agent for CT imaging, so we evaluated the contrast efficacy of CGO nanoparticles. As displayed in **Figures 7A,B**, with the increase in Ge content, the CT signal enhanced fast (dark to light), and the signal intensity (Hounsfield units, HU) exhibited linear growth behavior. These results demonstrated that CGO nanoparticles could be an efficient CT contrast agent for cancer diagnosis. All the advantages above motivated us to further investigate the CT imaging diagnosis application of CGO nanoparticles *in vitro*.

As depicted in **Figure 7C**, first, before intratumoral injection of CGO nanoparticles, the tumor appeared as a relatively dark image. After intratumoral injection, the tumor turned to full brightness at 2 h, demonstrating that CGO can be effective for imaging diagnosis.

Finally, we evaluated the long-term toxicity *in vivo* of CGO nanoparticles. After the intravenous administration of CGO nanoparticles, H&E analysis was conducted to evaluate the effect of CGO on the main organs. From the H&E staining of the major organs (including the heart, liver, lungs, spleen, and kidneys), no changes in the size, shape, and number of cells were observed (**Supplementary Figure S4**). The contents of nanocrystals accumulated in main organs at different time points were also evaluated. It showed (**Supplementary Figure S5**) that the CGO nanoparticles mainly accumulated at the kidneys and the spleen, indicating that CGO nanoparticles could be eliminated in the body through the kidneys and the spleen.

CONCLUSION

In summary, $CuGeO_3$ nanoparticles have great potential to be a novel bifunctional photothermal agent due to their small size (∼25 nm), good compatibility and dispersion, excellent photothermal effect, and CT imaging capability, which can be easily prepared by a simple solvothermal process and, subsequently, a surface modification process. The $CuGeO_3$ nanoparticle solution reveals an intense and strong absorption band in the NIR region due to the existence of different valence states of copper ions and the excellent photothermal effect. The photothermal conversion efficiency of $CuGeO_3$ nanoparticles was calculated to be 59.4%. Moreover, $CuGeO_3$ nanoparticles can be used as CT contrast agents for CT imaging both *in vitro* and *in vivo* due to the high attenuation coefficient of germanium. Therefore, the $CuGeO_3$ nanoparticles have great potential as a bifunctional agent with both high photothermal efficiency and CT imaging.

DATA AVAILABILITY STATEMENT

All datasets presented in this study are included in the article/**Supplementary Material**.

ETHICS STATEMENT

The animal study was reviewed and approved by the Second Affiliated Hospital of Chongqing Medical University.

AUTHOR CONTRIBUTIONS

JW and CZ designed the project and wrote the manuscript. JW carried out the experiment and performed the experimental data analysis. Both authors contributed to discussion of the results.

FUNDING

This work was financially sponsored by the Cancer Research Youth Science Foundation of the Chinese Anti-Cancer Association (CAYC18A49), Chongqing Science and Technology Commission Research Institute Performance Incentive Program of China (2017jxjl30022).

SUPPLEMENTARY MATERIAL

The Supplementary Material for this article can be found online at: https://www.frontiersin.org/articles/10.3389/fbioe.2020.590518/full#supplementary-material

REFERENCES

Ai, K., Liu, Y., Liu, J., Yuan, Q., He, Y., and Lu, L. (2011). Large-scale synthesis of Bi2S3Nanodots as a contrast agent for in vivo X-ray computed tomography imaging. *Adv. Mater.* 23, 4886–4891. doi: 10.1002/adma.201103289

Bassi, M., Camagni, P., Rolli, R., Samoggia, G., Parmigiani, F., Dhalenne, G., et al. (1996). Optical absorption of CuGeO3. *Phys. Rev. B Condens. Matter* 54, R11030–R11033. doi: 10.1103/physrevb.54.r11030

Chen, Z., Wang, Q., Wang, H., Zhang, L., Song, G., Song, L., et al. (2013). Ultrathin PEGylated W18O49Nanowires as a new 980 nm-laser-driven photothermal agent for efficient ablation of cancer cells in vivo. *Adv. Mater.* 25, 2095–2100. doi: 10.1002/adma.201204616

Ding, B., Yu, C., Li, C., Deng, X., Ding, J., Cheng, Z., et al. (2017). cis-Platinum pro-drug-attached CuFeS2 nanoplates for in vivo photothermal/photoacoustic imaging and chemotherapy/photothermal therapy of cancer. *Nanoscale* 9, 16937–16949. doi: 10.1039/c7nr04166g

Fu, L., Zheng, X., Huang, L., Shang, C., Lu, K., Zhang, X., et al. (2018). Synthesis and investigation of CuGeO3 nanowires as anode materials for advanced sodium-ion batteries. *Nanoscale Res. Lett.* 13:193. doi: 10.1186/s11671-018-2609-z

Gao, Y., Wang, S., Yang, C., An, N., Liu, Z., Yan, M., et al. (2019). A near-infrared responsive germanium complex of Ge/GeO2 for targeted tumor phototherapy. *J. Mater. Chem. B* 7, 5056–5064. doi: 10.1039/c9tb00548j

Huang, X., Tang, S., Liu, B., Ren, B., and Zheng, N. (2011). Enhancing the photothermal stability of plasmonic metal nanoplates by a core-shell architecture. *Adv. Mater.* 23, 3420–3425. doi: 10.1002/adma.201100905

Lee, D.-E., Koo, H., Sun, I.-C., Ryu, J. H., Kim, K., and Kwon, I. C. (2012). Multifunctional nanoparticles for multimodal imaging and theragnosis. *Chem. Soc. Rev.* 41, 2656–2672. doi: 10.1039/c2cs15261d

Lee, S. B., Lee, J. E., Cho, S. J., Chin, J., Kim, S. K., Lee, I. K., et al. (2019). Crushed gold shell nanoparticles labeled with radioactive iodine as a theranostic nanoplatform for macrophage-mediated photothermal therapy. *Nano Micro Lett.* 11:36. doi: 10.1007/s40820-019-0266-0

Li, B., Wang, Q., Zou, R., Liu, X., Xu, K., Li, W., et al. (2014). Cu7.2S4 nanocrystals: a novel photothermal agent with a 56.7% photothermal conversion efficiency for photothermal therapy of cancer cells. *Nanoscale* 6, 3274–3282. doi: 10.1039/c3nr06242b

Li, B., Ye, K., Zhang, Y., Qin, J., Zou, R., Xu, K., et al. (2015). Photothermal theragnosis synergistic therapy based on bimetal sulphide nanocrystals rather than nanocomposites. *Adv. Mater.* 27, 1339–1345. doi: 10.1002/adma.201404257

Li, B., Yuan, F., He, G., Han, X., Wang, X., Qin, J., et al. (2017). Ultrasmall CuCo2S4Nanocrystals: all-in-one theragnosis nanoplatform with magnetic resonance/near-infrared imaging for efficiently photothermal therapy of tumors. *Adv. Funct. Mater.* 27:1606218. doi: 10.1002/adfm.201606218

Li, J., and Pu, K. (2019). Development of organic semiconducting materials for deep-tissue optical imaging, phototherapy and photoactivation. *Chem. Soc. Rev.* 48, 38–71. doi: 10.1039/c8cs00001h

Liu, J. N., Bu, W., and Shi, J. (2017). Chemical design and synthesis of functionalized probes for imaging and treating tumor hypoxia. *Chem. Rev.* 117, 6160–6224. doi: 10.1021/acs.chemrev.6b00525

Lv, G., Guo, W., Zhang, W., Zhang, T., Li, S., Chen, S., et al. (2016). Near-infrared emission CuInS/ZnS quantum dots: all-in-one theranostic nanomedicines with intrinsic fluorescence/photoacoustic imaging for tumor phototherapy. *ACS Nano* 10, 9637–9645. doi: 10.1021/acsnano.6b05419

Nam, J., Son, S., Park, K. S., Zou, W., Shea, L. D., and Moon, J. J. (2019). Cancer nanomedicine for combination cancer immunotherapy. *Nat. Rev. Mater.* 4, 398–414. doi: 10.1038/s41578-019-0108-1

O'Neal, K. R., Al-Wahish, A., Li, Z. Q., Dhalenne, G., Revcolevschi, A., Chen, X. T., et al. (2018). Charge and bonding in CuGeO3 nanorods. *Nano Lett.* 18, 3428–3434. doi: 10.1021/acs.nanolett.8b00407

Song, C. L., and Kazarian, S. G. (2020). Micro ATR-FTIR spectroscopic imaging of colon biopsies with a large area Ge crystal. *Spectrochim. Acta A Mol. Biomol. Spectrosc.* 228:117695. doi: 10.1016/j.saa.2019.117695

Suriyawong, N., Aragaw, B., Shi, J. B., and Lee, M. W. (2016). Ternary CuBiS2 nanoparticles as a sensitizer for quantum dot solar cells. *J. Colloid Interface Sci.* 473, 60–65. doi: 10.1016/j.jcis.2016.03.062

Tian, Q., Hu, J., Zhu, Y., Zou, R., Chen, Z., Yang, S., et al. (2013). Sub-10 nm Fe3O4@Cu(2-x)S core-shell nanoparticles for dual-modal imaging and photothermal therapy. *J. Am. Chem. Soc.* 135, 8571–8577. doi: 10.1021/ja4013497

Tian, Q. W., Jiang, F. R., Zou, R. J., Liu, Q., Chen, Z. G., Zhu, M. F., et al. (2011). Hydrophilic Cu9S5 nanocrystals: a photothermal agent with a 25.7% heat conversion efficiency for photothermal ablation of cancer cells in vivo. *ACS Nano* 5, 9761–9771. doi: 10.1021/nn203293t

Wang, F., Li, Q., Lin, L., Peng, H., Liu, Z., and Xu, D. (2015). Monodisperse copper chalcogenide nanocrystals: controllable synthesis and the pinning of plasmonic resonance absorption. *J. Am. Chem. Soc.* 137, 12006–12012. doi: 10.1021/jacs.5b05591

Yuan, L., Hu, W. W., Zhang, H., Chen, L., Wang, J. Y., and Wang, Q. (2020). Cu5FeS4 nanoparticles with tunable plasmon resonances for efficient photothermal therapy of cancers. *Front. Bioeng. Biotechnol.* 8:21. doi: 10.3389/fbioe.2020.00021

Zhang, M., Wang, W., Wu, F., Zheng, T., Ashley, J., Mohammadniaei, M., et al. (2020). Biodegradable Poly(gamma-glutamic acid)@glucose oxidase@carbon dot nanoparticles for simultaneous multimodal imaging and synergetic cancer therapy. *Biomaterials* 252:120106. doi: 10.1016/j.biomaterials.2020.120106

Zhang, X., Liu, J., Yang, X., He, G., Li, B., Qin, J., et al. (2019). CuCo2S4 nanocrystals as a nanoplatform for photothermal therapy of arterial inflammation. *Nanoscale* 11, 9733–9742. doi: 10.1039/c9nr00772e

Conflict of Interest: The authors declare that the research was conducted in the absence of any commercial or financial relationships that could be construed as a potential conflict of interest.

frontiers in Materials

ORIGINAL RESEARCH
published: 15 January 2021
doi: 10.3389/fmats.2020.591281

Photothermal Therapy Based on CuS Nanoparticles for Alleviating Arterial Restenosis Induced by Mechanical Injury of Endovascular Treatment

Xiaoyu Wu[1], Kun Liu[1], Qun Huang[1], Qin Zhang[2], Xinrui Yang[1]*, Xiaobing Liu[1]* and Ruihua Wang[1]**

[1]Department of Vascular Surgery, Shanghai Ninth People's Hospital, Shanghai Jiao Tong University School of Medicine, Shanghai, China, [2]Institute of Translational Medicine, Shanghai University, Shanghai, China

OPEN ACCESS

Edited by:
Guanjie He,
University of Lincoln, United Kingdom

Reviewed by:
Jingyi Zhu,
Nanjing Tech University, China
Shilei Ni,
Jilin University, China
Yong Gao,
The First Affiliated Hospital of Bengbu Medical College, China

***Correspondence:**
Qin Zhang
sabrina_1985@shu.edu.cn
Xinrui Yang
Cinder_13@126.com
Xiaobing Liu
benny_liuxb@163.com
Ruihua Wang
wangruihua0330@sina.com

Specialty section:
This article was submitted to Biomaterials, a section of the journal Frontiers in Materials

Received: 04 August 2020
Accepted: 12 October 2020
Published: 15 January 2021

Citation:
Wu X, Liu K, Huang Q, Zhang Q, Yang X, Liu X and Wang R (2021) Photothermal Therapy Based on CuS Nanoparticles for Alleviating Arterial Restenosis Induced by Mechanical Injury of Endovascular Treatment. Front. Mater. 7:591281. doi: 10.3389/fmats.2020.591281

CuS nanoparticles (NPs) as an effective near-infrared absorption agent have been widely applied in the photothermal therapy (PTT) of cancer. However, little is known about the application of CuS NP-based PTT in alleviating arterial inflammation and restenosis, which affects the long-term prognosis of endovascular treatment. In this study, CuS NPs were synthesized and used as PTT nanoplatform for ameliorating arterial inflammation induced by mechanical injury of endovascular treatment. The macrophages possess powerful phagocytosis toward CuS NPs is evidenced by intracellular transmission electron microscopic imaging. As illustrated from Cell Counting Kit-8 assay and calcein AM/PI staining, an efficient depletion of macrophages by CuS NPs coculture combined with the irradiation with a 915-nm near-infrared laser was achieved. The endarterium injury/inflammation model was established by insertion of a 29G needle (BD Insulin Syringe Ultra-Fine®) to the left common carotid artery of an apolipoprotein E knockout mouse to mimic endarterium damage after endovascular treatment. Local injection of CuS NPs around the left common carotid artery followed by irradiation with a 915-nm INR laser significantly depleted infiltrated macrophages and alleviated arterial stenosis. This work emphasizes the role of CuS NPs as a PTT agent in post-injury remodeling of the arterial wall and provides an attractive target macrophage that can be depleted to alleviate arterial restenosis.

Keywords: CuS nanoparticles, computed tomography, photothermal therapy, arterial restenosis, macrophage

INTRODUCTION

Atherosclerosis obliterans of the extracranial carotid artery accounts for 15–20% of ischemic strokes (Li et al., 2015). Combination of percutaneous transluminal angioplasty and stent implantation has become alternative to endarterectomy partly because it has the advantages of shorter operation time, less invasion, and quick recovery (Beckman et al., 2020). Regardless of refinements of the endovascular technique, the mechanical injury to the endarterium is unavoidable, and subsequent arterial inflammation and restenosis are still incompletely understood and entirely unpredictable or unpreventable (Hong and Lee, 2020).

The negative remodeling of the arterial wall mediated by arterial inflammation is a hallmark of restenosis (Williams et al., 2019). Mechanical injury of endovascular treatment wrecks the integrity and continuity of the endarterium, which triggers the release of a number of cytokines from

endothelial cells, neutrophils, and platelets (Arakawa et al., 2005) and recruits massive circulating monocytes to the arterial intima (Koelwyn et al., 2018). Via serious signaling pathways (Tong et al., 2020), recruited monocytes differentiate into macrophages, which mediates the chronic inflammation of the injured artery (Koelwyn et al., 2018). After penetrating into the lesion site, macrophages contribute to the secretion of matrix metalloproteinase to degrade the extracellular matrix and release of pro-inflammatory chemokines to stimulate the transformation and proliferation of smooth muscle cells, ultimately leading to arterial restenosis (Jinnouchi et al., 2020; Tong et al., 2020). Thus, depletion of abnormal infiltrated macrophages provides novel insights into alleviating restenosis after endovascular treatment.

Photothermal therapy (PTT) using nanoparticles as near-infrared (NIR) absorption agents has been widely applied in medicine, especially cancer therapy (Wang et al., 2020). The principal mechanism of its therapeutic effect is converting light energy into thermal energy, which results in degeneration of DNAs and proteins of target cells (de Melo-Diogo et al., 2017). Taking advantage of this feature, we have effectively developed this procedure using $CuCo_2S_4$ nanocrystals (Zhang et al., 2019), MoO_2 nanoclusters (Wang et al., 2019), polypyrrole nanoparticles (Peng et al., 2015), and gold nanorods (Qin et al., 2015) to alleviate arterial inflammation by eliminating macrophages. As typical semiconductor materials, copper chalcogenides, especially CuS NPs, have many unique advantages as new photothermal conversion materials owing to strong NIR absorbance, photostability, and low toxicity (Zhou et al., 2010; Cheng et al., 2014; Yang et al., 2016). With strong absorption in the NIR (700–1,400 nm), copper chalcogenides were first reported as photothermal reagents by Li et al. (2000), who found that thioglycolate-coated copper sulfide nanoparticle exhibited good laser-induced photothermal effect in eliminating cancer cells. CuS NPs, nanoplatforms with dual photoacoustic/magnetic resonance imaging, and PTT are being widely studied in the anticancer field (Poudel et al., 2019). *In vivo* experiments confirmed evident accumulation of CuS NPs with both imaging and therapeutic functions in breast cancer, and cancer growth was inhibited markedly through synergistic photodynamic/PTT (Zhou et al., 2010; Hu X. et al., 2020). Despite wide utilization of copper-based nanoparticle–based PTT on cancer treatment with promising results, it is currently unknown whether PTT using CuS NPs as NIR absorption reagent can ameliorate negative remodeling of arterial wall that is, restenosis after endovascular treatment by eliminating artery infiltrating macrophages.

Toward this end, CuS NPs were synthesized, and their characterization and photothermal properties were measured. The cytotoxicity and PTT effect on macrophages were evaluated *in vitro*. The endarterium injury/inflammation model was established by insertion of a 29G needle (BD Insulin Syringe Ultra-Fine®) to the left common carotid artery of the apolipoprotein E knockout mouse to mimic endarterium damage after endovascular treatment. PTT therapy based on the local administration of CuS NPs was subsequently carried out. Of note, we specially evaluated the imaging property of CuS NPs for *in vivo* tracking by small animal CT device. Histopathological examination was conducted to assess the effect of PTT in alleviating arterial restenosis. This work emphasized the novelty of CT-guided therapy based on CuS NPs in prevention and treatment of arterial restenosis after mechanical injury of the endarterium.

MATERIALS AND METHODS

Materials

$CuCl_2$, sodium citrate, and Na_2S were purchased from Sinopharm Chemical Reagent Co., Ltd. (Shanghai, China) and used without purification. Mouse macrophage cell line, Raw 264.7, was purchased from the Beijing Cell Bank, the Chinese Academy of Medical Sciences (Beijing, China). Dulbecco's modified Eagle's medium (DMEM, with high glucose 4,500 mg ml^{-1}), fetal bovine serum, trypsin-EDTA (0.25%), and penicillin/streptomycin were purchased from Thermo Fisher (New York, United States). The primary CD68 antibody and relevant second antibody were purchased from Thermo Fisher (New York, United States). The Cell Counting Kit-8 (CCK-8) and Calcein-AM/PI Double Stain Kit were purchased from Dojindo (Kumamoto, Japan).

Synthesis of CuS Nanoparticles

The CuS NPs were synthesized according to the method described previously (Zhou et al., 2010). To 1,000 ml of aqueous solution of sodium citrate (0.2 g, 0.68 mmol) and $CuCl_2$ (0.1345 g, 1 mmol), 1 ml of sodium sulfide solution (Na_2S, 1 M) was added under magnetic stirring at room temperature. Ten minutes later, the mixture was heated to 90°C and stirred until dark green color appeared, and then the mixture was transferred to ice-cold water. The Cit-CuS NPs were obtained and stored at 4°C for further use.

Characterization of CuS Nanoparticles

Scanning electron microscopy (JEM-2010F; Japan) was used to determine the size, microstructure, and morphological properties of the CuS NPs. X-ray diffractometer analysis was conducted on a BT-X X-ray diffractometer (Olympus, Tokyo, Japan). UV-vis absorption spectra and diffuse reflectance spectra were recorded by using a TP720 UV-vis-NIR spectrophotometer (Olympus, Tokyo, Japan) from 400 to 1,000 nm. Fourier transform infrared spectra were measured by using KBr pellet methods using an infrared spectrometer (IRPrestige-21; Japan). Contents of ions released from the synthesized CuS NPs were determined by inductively coupled plasma atomic emission spectroscopy (Thermo Fisher, New York, United States). A 915-nm semiconductor laser (Thorlabs, United States) could be adjusted externally (0–2 W). Calibration of the output power of lasers was conducted by using a handheld optical power meter (OLP-35, VIAVI, United States). To measure the photothermal property, 100 μl of CuS NPs at different concentrations were irradiated with a 915-nm semiconductor laser device at a power density of 0.5 W cm^{-2} for 5 min. To evaluate the photostability of CuS NPs, the solution was irradiated with a 915-nm laser for 5 min, followed by natural cooling without irradiation for 5 min. The procedure was repeated five times. The temperature was recorded

and imaged simultaneously with a thermal imaging camera (FLIR A300, United States).

Cell Culture and Characterization

Raw 264.7 macrophages were cultured in Dulbecco's modified Eagle's medium (4500 mg ml^{-1} glucose), supplemented with 10% fetal bovine serum and 1% streptomycin/penicillin, and maintained at 37°C in a humidified 5% CO_2 atmosphere. The Raw 264.7 macrophages were stained with CD68 and DAPI and observed using a fluorescence microscope (Olympus, Japan).

Cytotoxicity, Cell Viability Assay, and Intracellular Transmission Electron Microscopy

To evaluate the cytotoxicity properties of CuS NPs on macrophages in the absence of PTT, Raw 264.7 was seeded in a 96-well plate (1×10^5 per well) and cocultured with CuS NPs at different concentrations (0, 20, 40, 80, 120, 200, 400, and 800 μg ml^{-1}) for 12 h. CCK-8 cell proliferation assay was conducted to measure the viability of macrophages after cocultured with CuS NPs according to the manufacturer's instructions. Then, the safe concentration of CuS NPs was confirmed and used for the subsequent experiments. To assess the photothermal effects of CuS NPs, Raw 264.7 was cocultured with CuS_2 NPs at safe concentration for 12 h and then irradiated with a 915-nm NIR laser at different power densities (0, 0.3, 0.5, and 1.0 W cm^{-2}). After that, the irradiated macrophages were stained with calcein AM/PI to discriminate living and dead cells (Calcein AM-green fluorescence, PI-red fluorescence) and observed using an inverted fluorescence microscope (Olympus, Japan). For the intracellular TEM, CuS NPs engulfed by macrophages were observed using an intracellular transmission electron microscope (TEM; JEM-1450, Tokyo, Japan).

Animal Model and Photothermal Therapy

Male, 8-week-old apolipoprotein E knockout mice were enrolled in the present study. The animal protocol was approved by the Ethics Review Committee for Animal Experimentation of Shanghai Ninth People's Hospital, Shanghai Jiao Tong University School of Medicine.

The mice were anaesthetized by intraperitoneal injection of 40 mg/kg pentobarbital sodium, and then the left common carotid artery was skeletonized. The LCA was blocked by cross-clamping at the proximal end, and an incision was then made at the distal end of the LCA. A 29G needle (BD Insulin Syringe Ultra-Fine®) was inserted to the LCA, rotated, and pushed forward and backward for three times. After closing the incision, left carotid arteries were wrapped with a constrictive silica collar. After 14 days, 100 μl (80 μg ml^{-1}) CuS NPs were injected into the constrictive silica collar under the guidance of small animal ultrasonic instrument, while the contralateral right carotid arteries were sham-operated to serve as the intra-animal control. The procedure is shown in **Supplementary Figure S1**. Then, 12 h after injection, all groups were subjected to 915-nm NIR laser irradiation at a power density of 0.5 W cm^{-2} for 5 min.

In Vivo Computed Tomography

Small animal CT scanning (SkyScan1278, Brooke, German) was used to determine the imaging property of CuS NPs. The operated mice (intra-collar injection with 100 μl of CuS NPs, 80 μg ml^{-1}) were subjected to CT scanning. 3-dimensional CT imaging was reconstructed to track the distribution of CuS NPs around the LCA.

Histological Analysis and Blood Examination

On the 14th day after PTT, all the mice were sacrificed for histopathological examination. Both collared and sham-operated carotid arteries were harvested. The arteries were stained with macrophage surface marker CD68 and DAPI, and the immunofluorescent signal was detected by using a microscope which was further quantified by ImageJ 1.8.0 software. The number of cells of CD68-positive macrophages was then counted by two investigators who were blinded to group information. The thickness of the intima and media of the arteries was observed by using a microscope after routine HE staining of slides from the carotid arteries and calculated by ImageJ 1.8.0. To observe the restoration of integrity and continuity of the post-injury endarterium, Evans blue staining was performed following the standard protocol.

To assess the *in vivo* toxicity and biocompatibility of CuS NPs, the major viscera, heart, liver, spleen, lung, kidney, and intestine were made to 4- to 6-nm sections for HE staining, and the histopathological changes were observed. Seven age-matched healthy mice were sacrificed as control. All the bloods biochemical parameters were measured in Shanghai Ninth People's Hospital Research Center for Model Organisms.

Statistics Analysis

Parametric data are represented as means ± standard deviation, and comparisons among groups were analyzed by one-way analysis of variance followed by Bonferroni correction for *post hoc* test. The number of macrophages was analyzed by using the Kruskal–Wallis test with Bonferroni correction. P-value <0.05 was considered statistically significant. All data are representative of at least three independent experiments. SPSS, version 25.0 (IBM-SPSS, Inc., Armonk, NY), was used to perform statistical analysis. The comparison results between groups labeled with * for $p < 0.05$ and ** for $p < 0.01$.

RESULTS AND DISCUSSION

Synthesis and Characterization of CuS Nanoparticles

Hydrophilic CuS NPs were prepared by a one-step hydrothermal synthesis method in the presence of sodium citrate. The crystal phase of the products is characterized by using an X-ray diffractometer (XRD). **Figure 1A** shows the XRD pattern of the as-synthesized products. The pattern of the sample can be matched well with the hexagonal CuS phase (JCPDS no. 43-1473), with no other peaks. EDS analysis (**Supplementary Figure S2**) showed that the products were composed of two elements (Cu and S), indicating the high purity of

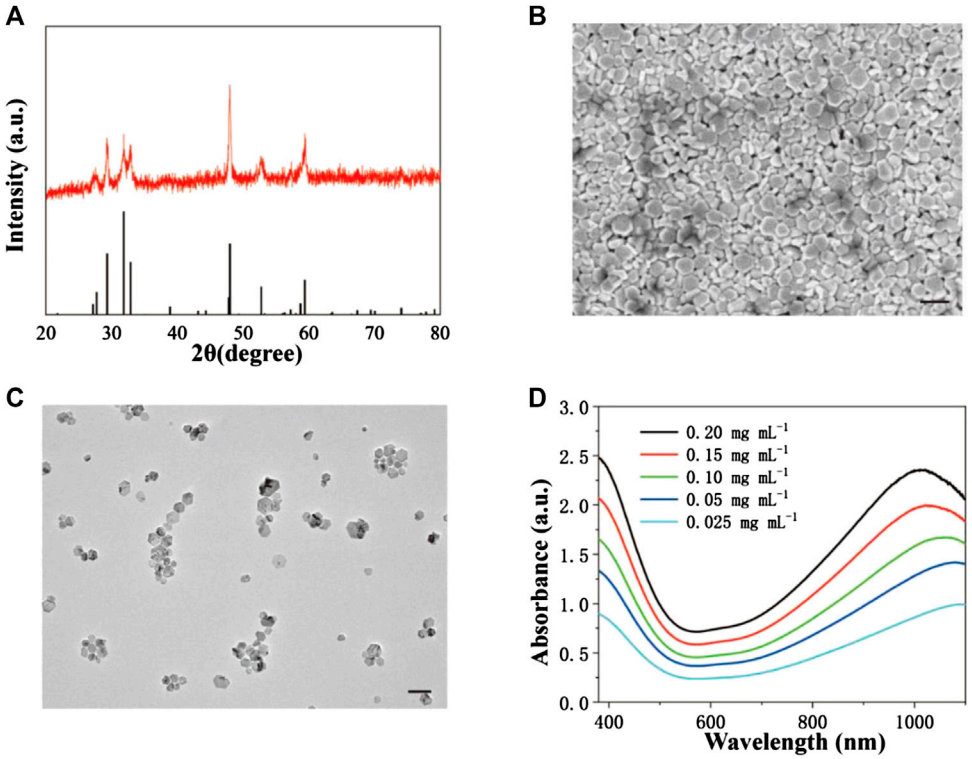

FIGURE 1 | Synthesis and characterization of CuS NPs. **(A)** XRD pattern of CuS NPs. **(B)** SEM image of CuS NPs. Scale bar: 50 nm. **(C)** TEM image of CuS NPs. Scale bar: 50 nm. **(D)** UV-vis-NIR absorption spectrum of CuS NPs at room temperature.

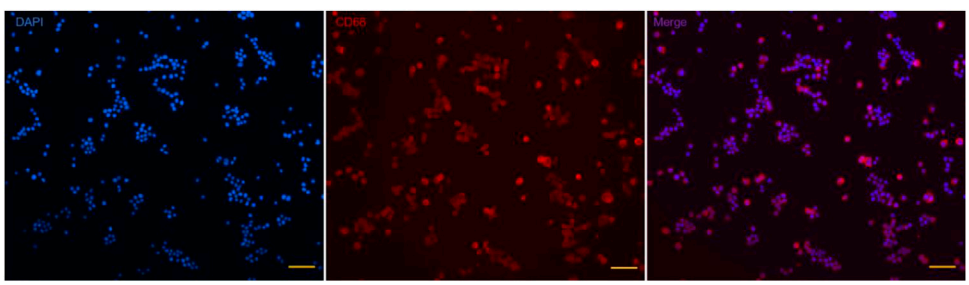

FIGURE 2 | Identification specific surface antigen of Raw 264.7. Nuclear is stained with DAPI (blue); specific surface antigen is positive for CD68 (red). Scale bar: 100 μm.

the CuS NPs. As shown in **Figures 1B,C**, SEM and TEM images confirmed that the products were nanoparticles with a size of 50 nm, showing good dispersion. **Figure 1D** exhibits the UV-vis absorbance spectrum of the aqueous dispersion of CuS NPs. It showed an intense absorption band centered at 1,010 nm. The strong NIR absorption made the CuS NPs an ideal candidate as PTT agents.

Identification of Macrophages and Intracellular Uptake

As an important member of the mononuclear phagocytic system, macrophages own the characteristics of strong phagocytosis and rapid growth. Raw 264.7 has been widely applied to study the function and characteristics of macrophages. Raw 264.7 was identified by cell immunofluorescence to determine the specific surface antigen of macrophages. Cellular immunofluorescence (**Figure 2**) demonstrated that Raw 264.7 was positive for CD68 (red), and nuclear staining with DAPI (blue).

Macrophages are known to be the principal participants in the chronic remodeling of the arterial wall. To detect the possibility of applying PTT using CuS NPs in ablating macrophages, we evaluated the phagocytosis of macrophages toward the CuS NPs using TEM. The intracellular TEM images

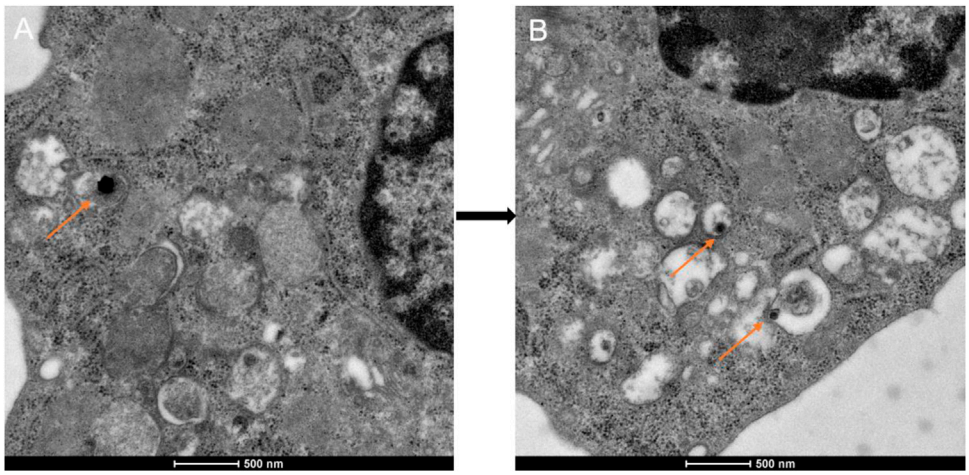

FIGURE 3 | Representative TEM images of phagocytosis of the CuS NPs. **(A)** Raw 264.7 incubated with the CuS NPs for 12 h. **(B)** Karyolysis and cytolysis of Raw 264.7 after incubation with the CuS NPs for 12 h and NIR laser for 5 min at a power density of 0.5 W cm^{-2}. The orange arrows indicate the CuS NPs engulfed by lysosomes.

of Raw 264.7 showed efficient phagocytosis toward the CuS NPs without obvious damage to organelles (**Figure 3A**). However, after coculturing with CuS NPs at a concentration of 80 μg ml^{-1} for 12 h and then undergoing 915-nm NIR laser irradiation at a power density of 0.5 W cm^{-2} for 5 min, significant blebbing, karyolysis, and cytolysis were observed (**Figure 3B**), all indicating that macrophages were induced to apoptosis and/or necrosis after PTT treatment. Thus, the present PTT using CuS NPs as photothermal agents demonstrates a potential application for ablating macrophages to alleviate chronic inflammation.

Cytotoxicity and Photothermal Effect of the CuS Nanoparticles on Macrophages

To evaluate the photothermal effect of CuS NPs, the temperature evolution at different CuS NP concentrations (0, 20, 40, and 80 μg ml^{-1}) under continuous 915-nm wavelength laser irradiation for 300 s was recorded, showing that the temperature elevated in a dramatic and smooth pattern with increment of CuS NP concentration (**Supplementary Figure S3**). Biomedical safety is prerequisite for any clinical application, and the cytotoxicity of the CuS NPs should be assessed. After incubating with the CuS NPs for 12 h, the CCK-8 assay was conducted to detect the concentration-dependent cytotoxicity of the CuS NPs on Raw 264.7. No significant difference was observed in cell viability at the concentrations under 80 μg ml^{-1}. When the concentration reached 120 μg ml^{-1}; the viability of Raw 264.7 was slightly affected (**Figure 4A**). Therefore, CuS NPs below a concentration of 80 μg ml^{-1} were selected for being cocultured with macrophages in subsequent *in vitro* and *in vivo* experiments.

To study the photothermal effect of CuS NPs on macrophages, Raw 264.7 was cocultured with CuS NPs of 80 μg ml^{-1} for 12 h and then exposed to 915-nm laser at different power densities (0, 0.25, 0.5, and 1.0 W cm^{-2}) for 5 min. The CCK-8 assay was conducted to detect the power density–dependent cytotoxicity of the CuS NPs on Raw 264.7. The viability of Raw 264.7 reduced slightly at a power density of 0.25 W cm^{-2}. However, when the power density reached 0.5 W cm^{-2}, the viability of Raw 264.7 reduced markedly (**Figure 4B**). Considering the results above, laser power (0.5 W cm^{-2}) was chosen to mimic the treatment *in vitro*.

Next, Raw 264.7 was incubated with CuS NPs of 80 μg ml^{-1} for 12 h and then exposed to 915-nm laser (0.5 W cm^{-2}) for 5 min. Subsequently, Raw 264.7 cells were stained with calcein AM/PI for discriminating living (green) cells and dead (red) cells. Calcein AM/PI results (**Figure 4C**) showed that no dead cells were observed in the control group (**Figure 4C,a**), and about 25% were dead cells in the CuS NPs group (**Figure 4C,b**), while about 95% cells were dead in the CuS NPs + PTT group (**Figure 4C,c**). The CCK-8 assay showed results consistent with calcein AM/PI results (**Figure 4C,d**). Those results demonstrated that PTT using CuS NPs as NIR absorption agents could eliminate macrophages effectively and may provide great potential to alleviate arterial stenosis.

As an important type of programmed cell death, apoptosis could be induced by the thermal effect of nanoparticles; however, whether it is involved in CuS-based PTT-induced macrophage death is currently unknown. To this end, we performed annexin V/PI staining of macrophages from control, CuS NPs, and CuS NPs + PTT groups, and the flow cytometry analysis showed that the necrosis index of macrophages was slightly higher in the CuS NPs group than in the control group and difference in the apoptosis index was not found between the two groups. In contrast, the CuS NPs + PTT group exhibited a significantly higher either early apoptosis (24.9% vs. 1.97%) or mid/late apoptosis (32.5% vs. 0.76%) index of macrophages than the CuS NPs group (**Figure 5**). However, the necrosis index of the macrophages was similar between CuS NPs and CuS NPs + PTT

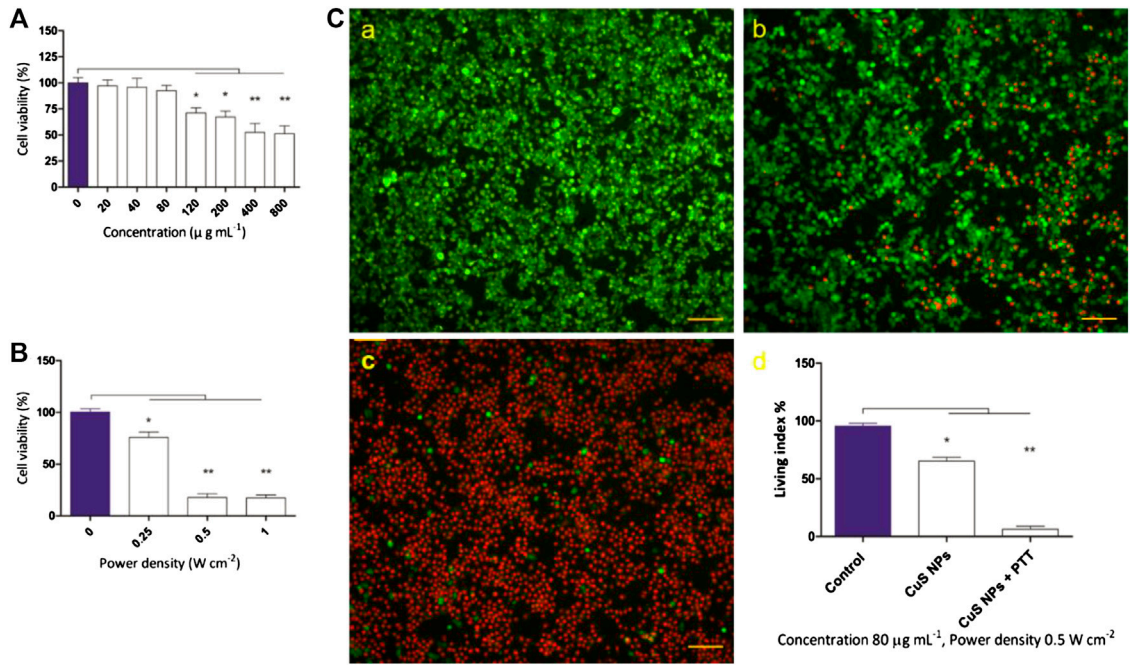

FIGURE 4 | Cytotoxicity of CuS NPs and its thermal effect on macrophages. **(A)** The cell viability of macrophages after cocultured with different concentrations of CuS NPs. **(B)** The cell viability of macrophages cocultured with CuS NPs (80 μg ml^{-1}) exposed to 915 nm NIR laser at different power density for 5 min. **(C)** Representative images of live (green) and dead (red) cells with CuS NPs (80 μg ml^{-1}, 0.5 W cm^{-2}) in the control group, CuS NPs group, CuS NPs + PTT group, respectively. Scale bar: 100 μm.

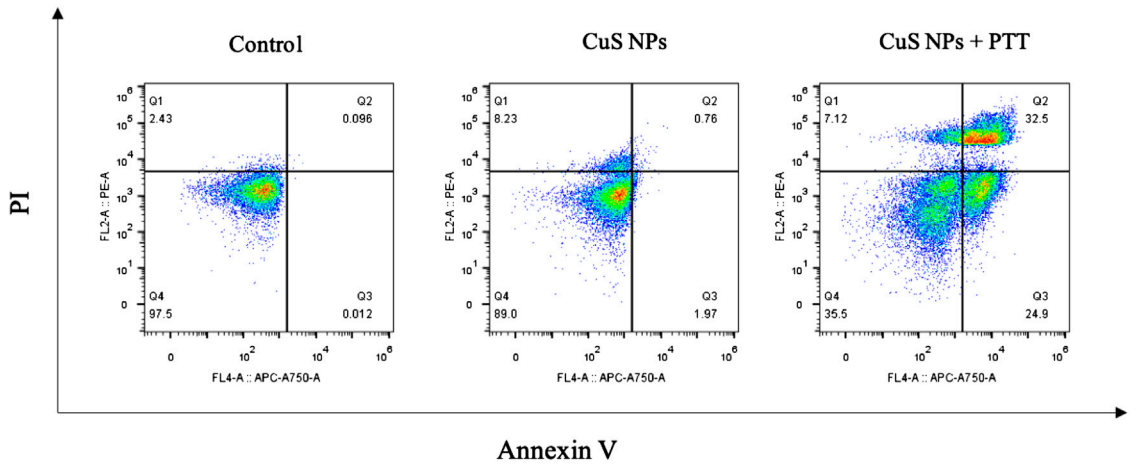

FIGURE 5 | Annexin V/PI duostaining of macrophages. CuS NPs + PTT group exhibited a significantly higher either early apoptosis (Q3) or mid/late apoptosis (Q2) index of macrophages than the CuS NPs group.

groups, indicating that the macrophage cell death induced by the CuS NPs–based photothermal effect was mainly apoptosis, rather than necrosis.

In Vivo Computed Tomography Imaging

In addition to their powerful therapeutic effect, the imaging function of nanomaterials has drawn great attention. Targeted delivery of imaging nanomaterials provides a promising approach for precious location of lesions and accurate diagnosis of diseases (Ge et al., 2020). The binding of Cu^{2+} to black phosphorus not only enhances photothermal stability and accelerates degradation, which makes Cu^{2+}-based nanomaterials the best photothermal agents (Wicki et al., 2015) but also provides *in vivo* real-time and quantitative tracking positron emission tomography–computed tomography (PET-CT) imaging (Hu K. et al., 2020). Moreover, it was reported that

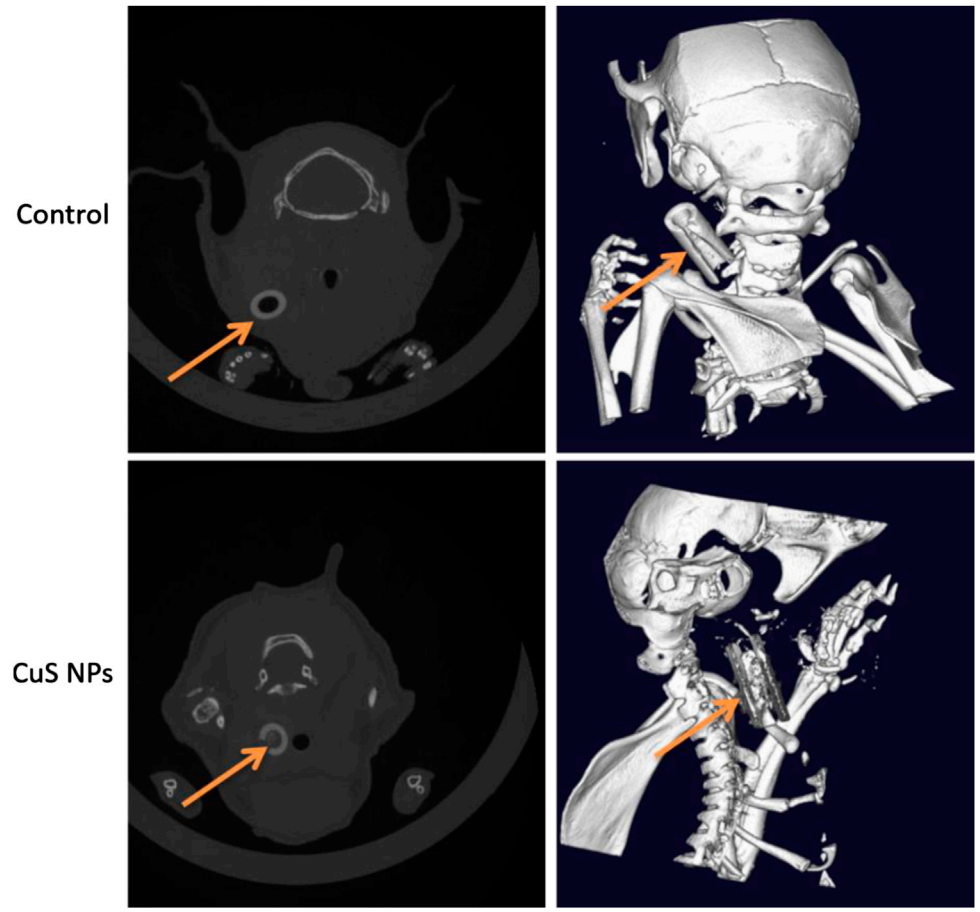

FIGURE 6 | Demonstration of 2D-CT and 3D-CT imaging property of CuS NPs *in vivo*. The orange arrows indicate the CuS NPs and the constrictive silica collars.

chelator-free ^{64}CuS nanoparticles are suitable for PET-CT imaging and robust photothermal ablation (Zhou et al., 2010). In the progression of atherosclerosis, increased accumulation of ^{64}Cu-labeled vMIP-II comb was confirmed by PET-CT imaging and was consistent with histopathological characterization of plaque including increased macrophage number and enlarged size (Luehmann et al., 2016). Collective data have indicated that Cu-based nanomaterials are suitable for CT imaging of tumor and inflammation. As demonstrated in 2D-CT and 3D-CT (**Figure 6**), flocculent and high-density imaging of CuS NPs was confined in the constrictive silica collar that wrapped the common carotid artery, indicating excellent CT imaging property of CuS NPs. Moreover, only little diffusion of CuS NPs to the surrounding tissues and organs was observed, which indicates that the CuS NPs can be accurately located around the lesion and play a role in PTT without causing any side effect.

Photothermal Effect on Carotid Artery Inflammation Induced by Mechanical Injury to Endarterium

PTA or stent implantation in mechanical injury to the endarterium is inevitable (Ng et al., 2017). Post-injury platelet/endothelium interaction promotes penetration of circulating monocytes through the injured endarterium with the regulation of cytokines (Arakawa et al., 2005), microRNAs (Gareri et al., 2016), and adhesion molecules (Hytonen et al., 2016), resulting in the transformation from monocytes to macrophages. Accumulating evidence indicate that activated macrophages surrounding the arterial wall triggers an overproduction of pro-inflammatory factors, which leads to severe hyperplasia of smooth muscle cells and arterial restenosis (Hoare et al., 2019). Therefore, it is plausible that macrophages are the target of ablation by which PTT using CuS NPs alleviates arterial inflammation after mechanical injury to the endarterium and mediates a protective effect on the endarterium. Apo E knockout mice were used to conduct the endarterium injury model and to mimic the mechanical injury of endovascular treatment. According to different treatment procedures, they were divided into control group, CuS NP group, and CuS NP + PTT group. After 14 days, the left carotid arteries were harvested for HE staining and immunofluorescence staining. The results showed that compared with the control group and the CuS NP group, the number of macrophages in the CuS NP + PTT group reduced greatly (**Figures 7A,B**). This suggests that PTT using CuS NPs

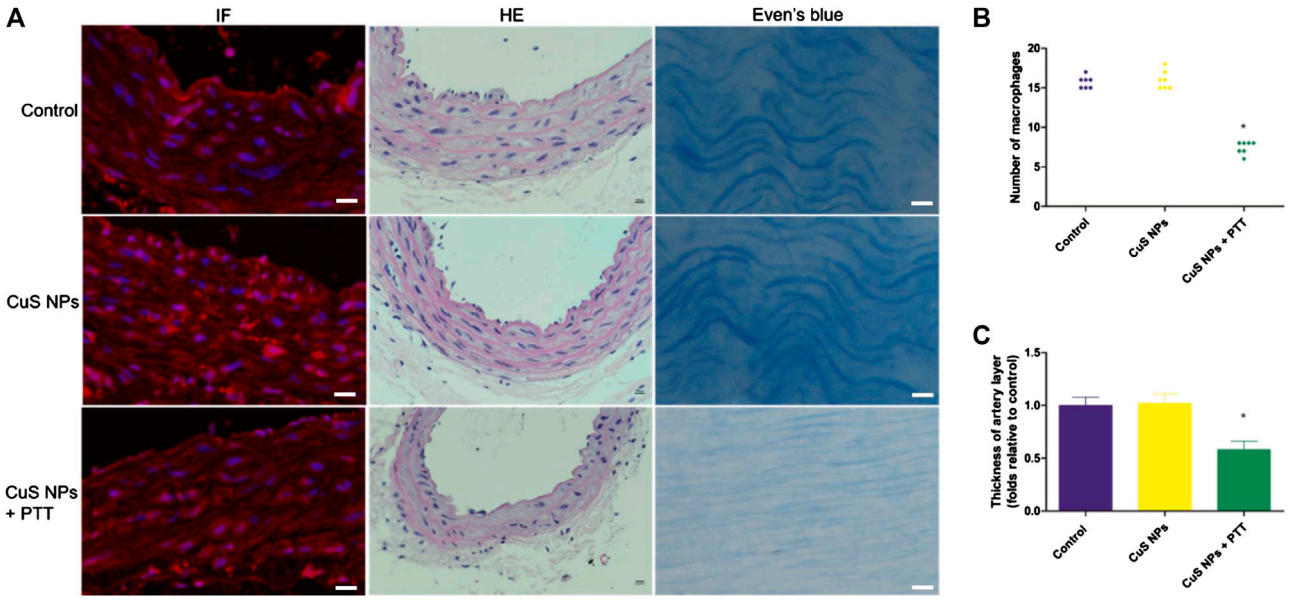

FIGURE 7 | Representative immunofluorescence images of the carotid artery. **(A)** Representative of HE, immunofluorescence (IF) staining, and Evans blue staining of carotid artery from the control group, CuS NP group, and CuS NP + PPT group, respectively. **(B)** Representative of the number of $CD68^{+}$ macrophages in each group. **(C)** Representative of the artery wall thickness in each group. Scale bar: 200 μm.

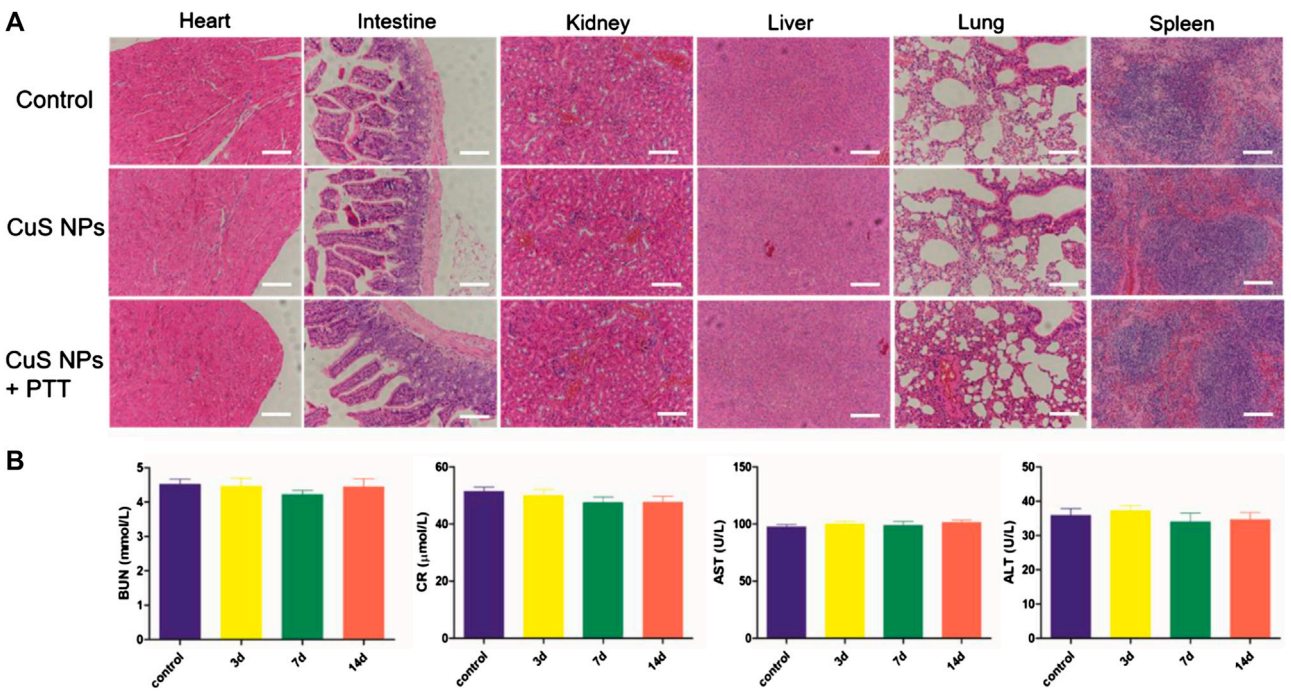

FIGURE 8 | Biocompatibility assay of CuS NPs *in vivo*. **(A)** HE staining of major viscera. No significant pathologic changes were observed in the heart, intestine, kidney, liver, lung, and spleen in the three groups. Scale bar: 200 μm. **(B)** Blood biomedical results of the control group and the CuS NP group at different time points (3, 7, and 14 days) after injection.

can ablate macrophages effectively. What is more, HE staining demonstrated that the thickness of the intima and media in the CuS NP + PTT group was much thinner than that in the control group and the CuS NP group (**Figures 7A,C**). The number of macrophages was revealed to be reduced in the media of the artery in our study, which confirmed the essential role of PTT

using CuS NPs in the ablation of macrophages. Another important finding revealed by the present study was that the thickness of the intima and media was thinnest after the PTT using CuS NPs, which might be associated with 1) apoptosis and necrosis of SMCs induced by higher temperature and 2) inhibition of SMC proliferation through eliminating macrophages. As either percutaneous balloon angioplasty or stent transplantation would unavoidably lead to the injury of the arterial endothelium and endothelial dysfunction, re-endothelialization of the injured arteries after endovascular treatment greatly affects later artery restenosis and patency. Results from Evans blue staining revealed that compared to the control group and the CuS NP group, re-endothelialization of the endarterium in the CuS NP + PTT group restored excellently after PTT as evidenced by more intact and continuous endarterium (**Figure 6A**).

Biocompatibility of the CuS Nanoparticles

Favorable biocompatibility of NPs should be considered and guaranteed for living bodies. Mice from the three groups (n = 7, each) were sacrificed 14 days after PTT, and major viscera were harvested for histopathological examination. Paraffin-embedded sections (4 nm) of major viscera (heart, intestine, kidney, liver, lung, and spleen) were stained with hematoxylin–eosin dye. Compared with the control group, no obvious pathological changes such as cell denaturation and necrosis were observed in the other two groups (**Figure 8A**). Blood samples were tested using the ELISA method. Statistical difference was not found between the three groups in terms of alanine aminotransferase, aspartate aminotransferase, blood urea nitrogen, or creatinine (**Figure 8B**). These results illustrate that CuS NPs as PTT agents have no side effects and are safe for use in the living body.

Limitations

However, several limitations of the work should be merited comment. Macrophage necrosis and apoptosis are the key cellular events in alleviating the negative remodeling of post-injury endarterium. It is not known whether photothermal effects against macrophages, rather than other cells, such as fibroblasts or endothelial cells, contribute to the restoration of post-injury endarterium. The mechanisms by which PTT induces macrophage apoptosis have not been investigated fully. Further investigation is needed to identify the signal pathways regulating macrophage apoptosis.

CONCLUSION

In conclusion, nontoxic and biocompatible CuS NPs can be engulfed by macrophages so that efficient photothermal depletion of macrophages was achieved *in vitro* and *in vivo*. Intra-collar injection of CuS NPs exhibits excellent CT imaging property and no diffusion to the surrounding tissue, which provides precise positioning and targeted therapy. The therapeutic effects of CuS NPs based PTT is proved by the decrease in the number of macrophages and arterial intima/media thickness. To our knowledge, this is the first report that CuS NP-based PTT plays an important role in alleviating arterial restenosis by targeting macrophages. The current study further expanded the understanding of CuS NPs as PTT agent against carotid arterial restenosis after endovascular treatment, which may improve the long-term prognosis of ischemic strokes.

DATA AVAILABILITY STATEMENT

The original contributions presented in the study are included in the article/**Supplementary Material**, further inquiries can be directed to the corresponding authors.

ETHICS STATEMENT

The animal study was reviewed and approved by Ethics Review Committee for Animal Experimentation of Shanghai Ninth People's Hospital, Shanghai Jiao Tong University School of Medicine.

AUTHOR CONTRIBUTIONS

XW, KL, and QH and contributed equally to this work. XW, KL, and QH contributed to experimental operations, statistical analysis, and manuscript writing. QZ contributed to the synthesis of CuS nanoparticles and measurement of the morphology features and the photothermal characteristics. XY, XL, and RW contributed to experimental design, manuscript proofreading, and communication.

FUNDING

This work was supported by the National Natural Science Foundation of China (Grant 81701801, 81971712, and 81870346), Clinical Research Program of Ninth People's Hospital, Shanghai Jiao Tong University School of Medicine (JYLJ019) and Shanghai Municipal Health Bureau Project (202040434).

SUPPLEMENTARY MATERIAL

The Supplementary Material for this article can be found online at: https://www.frontiersin.org/articles/10.3389/fmats.2020.591281/full#supplementary-material.

REFERENCES

Arakawa, H., Qian, J. Y., Baatar, D., Karasawa, K., Asada, Y., Sasaguri, Y., et al. (2005). Local expression of platelet-activating factor-acetylhydrolase reduces accumulation of oxidized lipoproteins and inhibits inflammation, shear stress-induced thrombosis, and neointima formation in balloon-injured carotid arteries in nonhyperlipidemic rabbits. *Circulation* 111 (24), 3302–3309. doi:10.1161/CIRCULATIONAHA.104.476242

Beckman, J. A., Ansel, G. M., Lyden, S. P., and Das, T. S. (2020). Carotid artery stenting in asymptomatic carotid artery stenosis: JACC Review topic of the week. *J. Am. Coll. Cardiol.* 75 (6), 648–656. doi:10.1016/j.jacc.2019.11.054

Cheng, L., Wang, C., Feng, L., Yang, K., and Liu, Z. (2014). Functional nanomaterials for phototherapies of cancer. *Chem. Rev.* 114 (21), 10869–10939. doi:10.1021/cr400532z

de Melo-Diogo, D., Pais-Silva, C., Dias, D. R., Moreira, A. F., and Correia, I. J. (2017). Strategies to improve cancer photothermal therapy mediated by nanomaterials. *Adv. Healthc. Mater.* 6 (10), 1700073. doi:10.1002/adhm.201700073

Gareri, C., De Rosa, S., and Indolfi, C. (2016). MicroRNAs for restenosis and thrombosis after vascular injury. *Circ. Res.* 118 (7), 1170–1184. doi:10.1161/CIRCRESAHA.115.308237

Ge, J., Zhang, Q., Zeng, J., Gu, Z., and Gao, M. (2020). Radiolabeling nanomaterials for multimodality imaging: new insights into nuclear medicine and cancer diagnosis. *Biomaterials* 228, 119553. doi:10.1016/j.biomaterials.2019.119553

Hoare, D., Bussooa, A., Neale, S., Mirzai, N., and Mercer, J. (2019). The future of cardiovascular stents: bioresorbable and integrated biosensor technology. *Adv. Sci.* 6 (20), 1900856. doi:10.1002/advs.201900856

Hong, M. K., and Lee, S. Y. (2020). Differential effects of drug-coated balloon angioplasty for in-stent restenosis. *J. Am. Coll. Cardiol.* 75 (21), 2679–2681. doi:10.1016/j.jacc.2020.04.005

Hu, K., Xie, L., Zhang, Y., Hanyu, M., Yang, Z., Nagatsu, K., et al. (2020). Marriage of black phosphorus and Cu(2+) as effective photothermal agents for PET-guided combination cancer therapy. *Nat. Commun.* 11 (1), 2778. doi:10.1038/s41467-020-16513-0

Hu, X., Lu, Y., Zhou, L., Chen, L., Yao, T., Liang, S., et al. (2020). Post-synthesis strategy to integrate porphyrinic metal-organic frameworks with CuS NPs for synergistic enhanced photo-therapy. *J. Mater. Chem. B* 8 (5), 935–944. doi:10.1039/c9tb02597a

Hytonen, J., Leppanen, O., Braesen, J. H., Schunck, W. H., Mueller, D., Jung, F., et al. (2016). Activation of peroxisome proliferator-activated receptor-delta as novel therapeutic strategy to prevent in-stent restenosis and stent thrombosis. *Arterioscler. Thromb. Vasc. Biol.* 36 (8), 1534–1548. doi:10.1161/ATVBAHA.115.306962

Jinnouchi, H., Guo, L., Sakamoto, A., Torii, S., Sato, Y., Cornelissen, A., et al. (2020). Diversity of macrophage phenotypes and responses in atherosclerosis. *Cell. Mol. Life Sci.* 77 (10), 1919–1932. doi:10.1007/s00018-019-03371-3

Koelwyn, G. J., Corr, E. M., Erbay, E., and Moore, K. J. (2018). Regulation of macrophage immunometabolism in atherosclerosis. *Nat. Immunol.* 19 (6), 526–537. doi:10.1038/s41590-018-0113-3

Li, L., Yiin, G. S., Geraghty, O. C., Schulz, U. G., Kuker, W., Mehta, Z., et al. (2015). Incidence, outcome, risk factors, and long-term prognosis of cryptogenic transient ischaemic attack and ischaemic stroke: a population-based study. *Lancet Neurol.* 14 (9), 903–913. doi:10.1016/s1474-4422(15)00132-5

Li, Y., Lu, W., Huang, Q., Huang, M., Li, C., and Chen, W.(2000). Copper sulfide nanoparticles for photothermal ablation of tumor cells. *Nanomedicine (Lond.)* 5 (8), 1161–1171. doi:10.2217/nnm.10.85

Luehmann, H. P., Detering, L., Fors, B. P., Pressly, E. D., Woodard, P. K., Randolph, G. J., et al. (2016). PET/CT imaging of chemokine receptors in inflammatory atherosclerosis using targeted nanoparticles. *J. Nucl. Med.* 57 (7), 1124–1129. doi:10.2967/jnumed.115.166751

Ng, J., Bourantas, C. V., Torii, R., Ang, H. Y., Tenekecioglu, E., Serruys, P. W., et al. (2017). Local hemodynamic forces after stenting: implications on restenosis and thrombosis. *Arterioscler. Thromb. Vasc. Biol.* 37 (12), 2231–2242. doi:10.1161/ATVBAHA.117.309728

Peng, Z., Qin, J., Li, B., Ye, K., Zhang, Y., Yang, X., et al. (2015). An effective approach to reduce inflammation and stenosis in carotid artery: polypyrrole nanoparticle-based photothermal therapy. *Nanoscale* 7 (17), 7682–7691. doi:10.1039/c5nr00542f

Poudel, K., Gautam, M., Jin, S. G., Choi, H. G., Yong, C. S., and Kim, J. O. (2019). Copper sulfide: an emerging adaptable nanoplatform in cancer theranostics. *Int. J. Pharm.* 562, 135–150. doi:10.1016/j.ijpharm.2019.03.043

Qin, J., Peng, Z., Li, B., Ye, K., Zhang, Y., Yuan, F., et al. (2015). Gold nanorods as a theranostic platform for *in vitro* and *in vivo* imaging and photothermal therapy of inflammatory macrophages. *Nanoscale* 7 (33), 13991–14001. doi:10.1039/c5nr02521d

Tong, Y., Cai, L., Yang, S., Liu, S., Wang, Z., and Cheng, J. (2020). The Research progress of vascular macrophages and atherosclerosis. *Oxid. Med. Cell Longev.* 2020, 7308736. doi:10.1155/2020/7308736

Wang, J., Wu, X., Shen, P., Wang, J., Shen, Y., Shen, Y., et al. (2020). Applications of inorganic nanomaterials in photothermal therapy based on combinational cancer treatment. *Int. J. Nanomedicine* 15, 1903–1914. doi:10.2147/IJN.S239751

Wang, X., Wu, X., Qin, J., Ye, K., Lai, F., Li, B., et al. (2019). Differential phagocytosis-based photothermal ablation of inflammatory macrophages in atherosclerotic disease. *ACS Appl. Mater. Interfaces* 11 (44), 41009–41018. doi:10.1021/acsami.9b12258

Wicki, A., Witzigmann, D., Balasubramanian, V., and Huwyler, J. (2015). Nanomedicine in cancer therapy: challenges, opportunities, and clinical applications. *J. Control Release* 200, 138–157. doi:10.1016/j.jconrel.2014.12.030

Williams, J. W., Huang, L. H., and Randolph, G. J. (2019). Cytokine circuits in cardiovascular disease. *Immunity* 50 (4), 941–954. doi:10.1016/j.immuni.2019.03.007

Yang, W., Guo, W., Le, W., Lv, G., Zhang, F., Shi, L., et al. (2016). Albumin-bioinspired Gd:CuS nanotheranostic agent for in vivo photoacoustic/magnetic resonance imaging-guided tumor-targeted photothermal therapy. *ACS Nano* 10 (11), 10245–10257. doi:10.1021/acsnano.6b05760

Zhang, X., Liu, J., Yang, X., He, G., Li, B., Qin, J., et al. (2019). CuCo2S4 nanocrystals as a nanoplatform for photothermal therapy of arterial inflammation. *Nanoscale* 11 (19), 9733–9742. doi:10.1039/c9nr00772e

Zhou, M., Zhang, R., Huang, M., Lu, W., Song, S., Melancon, M. P., et al. (2010). A chelator-free multifunctional [64Cu]CuS nanoparticle platform for simultaneous micro-PET/CT imaging and photothermal ablation therapy. *J. Am. Chem. Soc.* 132 (43), 15351–15358. doi:10.1021/ja106855m

Conflict of Interest: The authors declare that the research was conducted in the absence of any commercial or financial relationships that could be construed as a potential conflict of interest.

Advantages of publishing in Frontiers

OPEN ACCESS
Articles are free to read for greatest visibility and readership

FAST PUBLICATION
Around 90 days from submission to decision

HIGH QUALITY PEER-REVIEW
Rigorous, collaborative, and constructive peer-review

TRANSPARENT PEER-REVIEW
Editors and reviewers acknowledged by name on published articles

Frontiers
Avenue du Tribunal-Fédéral 34
1005 Lausanne | Switzerland

Visit us: www.frontiersin.org
Contact us: frontiersin.org/about/contact

REPRODUCIBILITY OF RESEARCH
Support open data and methods to enhance research reproducibility

DIGITAL PUBLISHING
Articles designed for optimal readership across devices

FOLLOW US
@frontiersin

IMPACT METRICS
Advanced article metrics track visibility across digital media

EXTENSIVE PROMOTION
Marketing and promotion of impactful research

LOOP RESEARCH NETWORK
Our network increases your article's readership